The Synthesis of Novel Polymeric Materials for Application in Inkjet Printing

A thesis submitted in part fulfilment of the degree of Doctor of Philosophy

Jessica Godleman

Department of Chemistry

Supervised by: Prof. W. Hayes, Prof. H. M. Colquhoun,

Dr. P. Cranwell and Dr. J. Harries

November 2019

Declaration of Original Authorship

I confirm that this is my own work and the use of all material from other sources has been properly and fully acknowledged.

Jessica Godleman

Acknowledgements

There are many people who deserve thanks towards their input, big or small, towards my PhD over the past four years. Firstly, I would like to thank my supervisors at the University of Reading- Prof. Wayne Hayes, Prof. Howard Colquhoun and Dr. Philippa Cranwell. Without their help and expertise this thesis would not have been achieved. I would also like to thank my industrial supervisor, Dr. Josie Harries for her support and advice and for making me feel welcome and included during my placements at Domino.

My industrial placements were always enjoyable and much of that is because of the friendly and enthusiastic people who helped me during my visits. A special thanks goes to Dr. Julian Philpott, Andrew Kyriacou, Dr. Stuart Molloy, Dr. Stuart Reynolds, Dr. Martin Thompson, Dr. Phil Woolston for sharing their vast knowledge and answering my (many) questions. I have learnt such a great deal from everyone at Domino and am grateful to have worked with such a kind and clever group of people.

The past four years have definitely been made more bearable by the members of the Hayes and Colquhoun groups. Undoubtedly, I owe my sanity to Dr. Hannah Bowden who has been the best friend I could've asked for or needed through both the good and bad times during my PhD. The same goes to Dr. Oli Balmford for the coffee breaks, biscuits, and advice. I also owe thanks to Dr's: Kate Lim, Tahkur Babra, Lewis Hart, Marcus Knappert, Ben Baker, Priya Singh, Corinne McEwan, Karine Hakobayan, Flavien Leroux and Ashfaq Afsar, as well as the soon to be doctors Sara Salimi, Adam O'Donnell and Alex Gavriel, all of whom have contributed to an enjoyable work- and pub-environment.

There are also many people outside of the research groups who have contributed to my PhD experience- Prof. Matthew Almond for his continued support and advice, Dr. Nick Michael for finding my mass ion peaks without fail, Heather and Barbara for their entertaining chats and keeping the department going, Dr. Radek Kowalcyzk for maintaining the NMR machines, Dr. Pedro Rivas-Ruiz for keeping the CAF lab in good order and Phil Mason for putting up with our many trips to stores. Alongside the staff I've also been lucky to share a PhD office with a great bunch of people, particularly those in the little office- Charlotte, Jess and Sara who never held back on the gossip, laughter or entertainment.

Finally, and most importantly, I would like to thank my family for their endless support and encouragement. A special thank you goes to Jack White for constantly reminding me what I am capable of and to my mum, Helen Waites, as I truly would not have achieved any of this without her.

Synopsis

Several novel polymeric systems have been designed and synthesised as functional materials for inkjet printing purposes. The polymers described in this thesis are aimed towards three separate chemistries for inkjet printing: i) self-assembling polymer networks through π-stacking interactions, ii) UV-curable anthracene-capped polymers and iii) soluble poly(fluorocarbinol) (PFO) materials as hydrophobic polymers.

The investigation into self-assembling polymer networks involved the synthesis and characterisation of a novel π-electron rich anthracene-capped poly(ethyleneglycol) (PEG) polymer and a π-electron deficient naphthalene diimide polymer. The supramolecular assembly of the π-electron rich anthracene and π-electron deficient naphthalene diimide moieties was studied using both computational modelling and ^{1}H NMR spectroscopic binding constant measurements to predict the interaction of the polymeric systems. The interaction of the complementary π-systems within the polymer architecture was also investigated using UV-vis and ^{1}H NMR spectroscopic analysis to reveal a weak π-interaction between the aromatics of the polymer blends. The formulation and deposition of the polymers using a Dimatix™ drop-on-demand (DOD) printer was also undertaken to determine that both polymeric systems were printable using DOD inkjet printing and produced clear, neat images.

The synthesis of novel linear and branched anthracene-capped PEG polymers for the assessment of these materials as UV-curable ink formulations was investigated. A linear anthracene-capped PEG was employed as a model compound for solution state analysis using UV-vis and ^{1}H NMR spectroscopies and confirmed the dimerisation of anthracene units upon irradiation with UV light. An analogous branched system formed an insoluble material, post-irradiation, as a result of the formation of a cross-linked material and therefore the end-group dimerisation process was characterised using lap shear tests, rheology and dielectric cure measurements, which all demonstrated the transition of the branched polymer from a viscous oil to an elastic material. The suitability of both polymers as inkjet formulations for DOD printing was then studied and the suitability of the branched anthracene-capped PEG as a UV-curable polymer component for inkjet formulations investigated. The materials were readily deposited using inkjet printing and exhibited UV-curing of the prints even with the inclusion of dye compounds in the formulations.

Finally, poly(fluorocarbinol)s (PFO)s ranging in molecular weights (11,500–114,500 g mol^{-1}) were synthesised successfully to yield soluble, hydrophobic polymeric materials for use in inkjet formulations. The hydrophobic properties of the polymer films were investigated using contact angle measurements to determine their suitability as hydrophobic coatings and revealed hydrophobic surfaces with water contact angles of 88–89°. The printability of the PFO materials was determined using a Dimatix™ DOD inkjet printer and studies involving two lower molecular weight PFOs

(11,500 and 25,200 g mol^{-1}) were undertaken to determine the rheological behaviour of the polymers in the printhead, revealing Newtonian or near-Newtonian behaviour of the materials at high shear. The deposition of the materials using a Domino Printing Sciences Ax-series continuous inkjet printer was also investigated, producing sharp prints with no apparent satellite droplets.

Abbreviations

appt	Apparent
9-BBN	9-Borabicyclo[3.3.1]nonane
CAB	Cellulose acetate butyrate
CAM	Contact angle measurement
CIJ	Continuous Inkjet
d	doublet
Đ	Polydispersity
DCC	*N*,*N*'-dicyclohexylcarbodiimide
dd	Double doublet
DHB	Dihydroxybenzoic acid
DLS	Dynamic Light Scattering
DMAc	Dimethylacetamide
DMAP	4-Dimethylaminopyridine
DMF	Dimethylformamide
DNA	Deoxyribonucleic acid
DOD	Drop-on-demand
DSC	Differential Scanning Calorimetry
EFSA	European food safety authorisation
ESI	Electrospray ionisation
FATRIFE	2,2,2-Trifluoroethyl α-fluoroacrylate
FT-IR	Fourier Transform Infrared
G′	Storage modulus
G″	Loss modulus
GPC	Gel Permeation Chromatography
HCl	Hydrochloric acid
HMBC	Heteronuclear Multiple Bond Correlation
IR	Infrared
K	Constant of free space within a polymer
K_a	Association constant
LCD	Liquid Crystalline Display
LDPE	Low density poly(ethylene)
LED	Light emitting diode
LEP	Light Emitting Polymer
m	Multiplet
m/*z*	Mass/charge ratio
MAF	2-(Trifluoromethyl)acrylic acid
MALDI-TOF	Matrix Assisted Laser Desorption Time of Flight
MeI	Methyl iodide

MEK	Methylethyl ketone
M_n	Number average molecular weight
M.p.	Melting point
MS	Mass spectroscopy
M_w	Weight average molecular weight
NDI	Naphthalene Diimide
NDIT	Naphthalene diimide tweezer
NMP	*N*-methyl-2-pyrrolidone
NMR	Nuclear magnetic resonance
OPV	Organic photovoltaic
OWRK	Owens, Wendt, Rabel, Kaelble (method for surface energy calculations)
PAEM	Poly(2-aminoethylacrylate)
PDDA	Poly(diallylmethylammonium chloride)
PEDOT	Poly(3,4-ethylenedioxythiophene)
PEG	Poly(ethylene glycol)
PEGDA	Polyethylene glycol diacrylate
PEK	Poly(ether ketone)
PEKK	Poly(etherketoneketone)
PET	Poly(ethyleneterephthalate)
PFO	Poly(fluorocarbinol)
Phe	Phenylalanine
PIJ	Piezoelectric Inkjet
PLED	Polymer light emitting diode
PLGA	Poly(lactic-*co*-glycolic acid)
PP	Poly(propylene)
PSE	Poly(trifluoromethyltrimethylsilyl ether)
PSS	Polystyrene sulfonic acid
PTFE	Poly(tetrafluoroethylene)
r	Ratio of monomers
RGB	Red, green, blue
s	Singlet
SEM	Scanning Electron Microscopy
TBAF	Tetra-*n*-butyl ammonium fluoride
t_c	Relaxation time of fluid
TFA	Trifluoroacetic acid
TFT	Thin film transistors
T_g	Glass transition temperature
THF	Tetrahydrofuran
TIJ	Thermal Inkjet
TLC	Thin layer chromatography

T_m	Melting temperature
t_p	Observation time of system
UPy	Ureidopyrimidone
UV	Ultraviolet
UV-vis	Ultraviolet/visible
VROC®	Viscometer-rheometer-on-a-chip
$\overline{X}$	Degree of polymerisation
γ_{LV}	Liquid-vapour interface
γ_{SL}	Solid-liquid interface
γ_{SV}	Solid-vapour interface
γ^{tot}	Surface free energy
ν	Velocity
ε'	Permittivity
ρ	Density
ρ_{DC}	Log ion viscosity
σ	Surface tension
$\dot{\gamma}$	Shear rate
μ	Viscosity

Contents

Chapter 1- Introduction

Chapter 2- Anthracene-Capped PEG as a Supramolecular Polymer for Inkjet Printing

Chapter 1

Introduction

1.1 Introduction to Inkjet Printing

Inkjet printing technology is used extensively on an international basis, with a valuation of the global inkjet printing market estimated to be £56.6 billion ($69.6 billion) in 2018 and predicted to rise to £88.6 billion ($109 billion) by 2023.[1] The industrial applications of inkjet printing include graphics, coding and marking, direct mail, books, newspapers, labels, ceramic tile printing, printing of textiles and microfabrication.[2] Inkjet printing is also commonplace in day-to-day life with the prevalence of inkjet printers in offices and homes, following the initial introduction of inkjet printing to the high throughput industrial sector over 40 years ago.[3]

Despite the fact that inkjet printing was only introduced commercially in the late 1970's, the behaviour of liquid jets passing through an orifice has been long understood. In 1833, Savart *et al*. reported[4] that a liquid stream falling from an orifice formed uniform droplets upon the application of acoustic energy. Despite the pioneering discovery by Savart, it was over a decade later in 1848 that Plateau reported[5] that the formation of instabilities and droplets from a jet stream was a surface tension driven phenomena. A further mathematical insight into the instability of fluid jets was reported by Rayleigh *et al*. in 1879, who derived fundamental equations[6–8] to explain the fluid dynamics of the instability of jet streams.

The application of the instability of jet streams was in fact exploited for inkjet purposes before Rayleigh had derived the fundamental equations that explained the behaviour of the fluids. In 1869 Thomson (later Lord Kelvin) designed a Siphon recorder which used a fluid stream of droplets to record incoming telegraph messages as a line of ink on a roll of paper.[9] Despite the pioneering use of inkjet technology by Thomson, inkjet products were not introduced on the commercial scale until the development of a medical chart recorder by Siemens.[10] Since then, digital inkjet printing has seen a significant growth, with the introduction of digital inkjet printing for the low cost and high throughput coding and marking of food and medicine packaging in the 1970's.[3,11]

The expansion of inkjet printing can be attributed to the number of practical advantages of using the technology. The non-contact nature of inkjet printing is extremely useful for printing onto rough or uneven surfaces and the technology can be adapted to print onto a range of substrates. The digital input of the image signal creates and deposits each droplet, meaning each print can be reproduced with precision or easily altered to produce a different image.[2] Therefore inkjet printing permits the deposition of limitless designs that can be changed frequently with minimal effort. This freedom of

design was not possible using more traditional screen printing, which requires fabrication of stencils for each design to be printed.[12] Further advantages include the high production rates, scalable print quality, precise control of ink volume and the reduced ink consumption,[12] all of which contribute to the popularity of inkjet printing in modern society.

1.1.1 Types of Inkjet Deposition

The success of inkjet printing relies on the controlled deposition of ink droplets onto a substrate,[3] a process that can be achieved using different inkjet mechanisms. Inkjet printing mechanisms can be divided into two main categories; drop-on demand (DOD) inkjet printing and continuous inkjet (CIJ) printing, both of which allow the controlled deposition of droplets onto a substrate, but using different drop generation techniques. DOD systems are more commonly used in home or office printing owing to their smaller size, lower cost and the reduced amount of maintenance required when compared to CIJ printers.[13]

In DOD printing, ink droplets are only ejected when they are required to form part of the image or structure. The deposition of droplets using the DOD mechanism is achieved by the creation of a pressure pulse which forces a controlled volume of fluid out of the cartridge and onto the substrate. DOD printing can be further divided into two mechanisms, thermal inkjet (TIJ) and piezoelectric inkjet (PIJ), both of which differ in the way that the drop ejection is achieved from the printhead.[3]

In TIJ printing, a pressure pulse is created by rapidly heating a thin resistive element located in a small ink chamber near the nozzle. The resistive element is typically heated to 350–400 °C for a few microseconds causing the surrounding ink to vaporise and form a small bubble.[3] The bubble then collapses creating a pressure pulse and forcing a controlled volume of ink out of the nozzle (Figure 1). The utilisation of a TIJ-DOD printhead can be advantageous if very small drop volumes are required, e.g. for compact devices, however the limitations of this technique are significant.

Firstly, the carrier solvent employed in the formulation needs to be something that can be vaporised, but is not too volatile (generally an aqueous solution), and secondly all components of the formulation are required to withstand very high local temperatures. These factors eliminate a wide range of materials from use in TIJ printhead systems, as heating polymers and functional materials, such as dyes to very high temperatures can result in degradation. If the components of the ink formulation are not stable at these temperatures, build-up of material on the heating element will occur, reducing its efficiency and the lifetime of the printhead.[3]

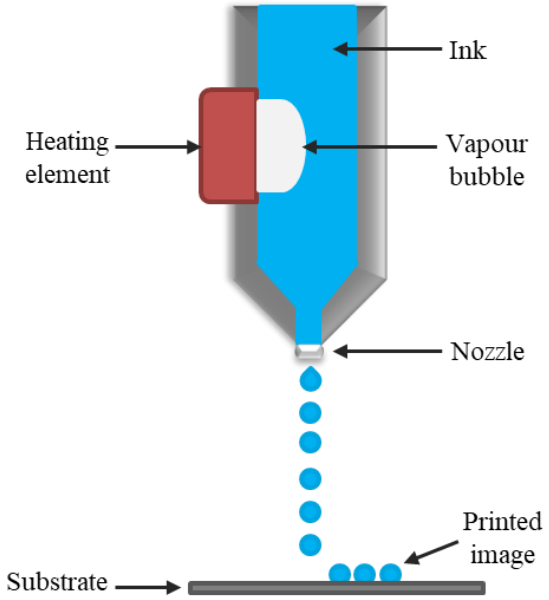

Figure 1-Thermal Inkjet (TIJ) drop-on-demand printhead, showing the formation of a vapour bubble following rapid heating of the resistive element.

PIJ technology involves the creation of a pressure pulse by application of a voltage to the ink chamber, which is composed of a piezoelectric material. The applied voltage deforms the chamber and decreases its internal volume, creating a pressure wave, which breaks the surface tension of the ink and forces a controlled volume of ink out of the nozzle (Figure 2).[14] DOD systems employing PIJ technologies allow the largest amount of ink development freedom, as a wide range of formulations with a range of different physical properties can be deposited.[3]

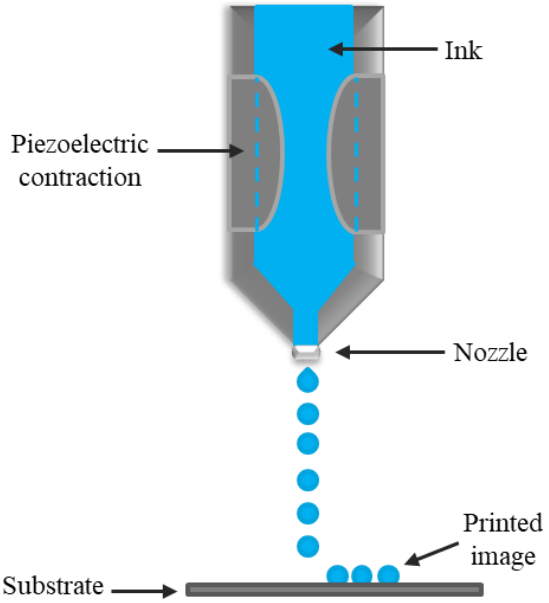

Figure 2- Piezoelectric Inkjet (PIJ) drop-on-demand printhead, indicating the piezoelectric contraction of the cartridge with the neutral state of the cartridge indicated by the blue dashed lines.

Both subcategories of DOD printers deposit droplets onto the substrate by movement of the printer nozzle over the substrate, depositing droplets at specific locations that are determined by the digital image used as an input. The droplet generation rate for DOD printers ranges between 1 and 20 kHz,[15] with an average droplet diameter of 20–50 µm.[16]

CIJ printers exhibit larger drop diameters than DOD systems, forming droplets with an average diameter of 100 µm at a higher drop frequency that can exceed 100 kHz.[17] These properties allow rapid printing onto fast moving substrates, hence the commonplace application of CIJ printers in high throughput industrial applications, such as coding and marking.[3,16,17] CIJ printers eject a continual stream of evenly sized ink droplets,[14] most of which are not used for printing, but are recirculated through the printer. The evenly sized droplets are formed by a vibrating piezoelectric actuator that breaks up the stream of ink as a result of the Rayleigh instability.[7] As the droplets leave the inkjet nozzle a charge is imparted on them by a charge electrode allowing control of their deposition via electrostatic deflection. The droplets are either deflected by the electrostatic deflection plates and deposited at a specific location on the substrate, or allowed to continue without deflection to a collection gutter for re-circulation (Figure 3).[14]

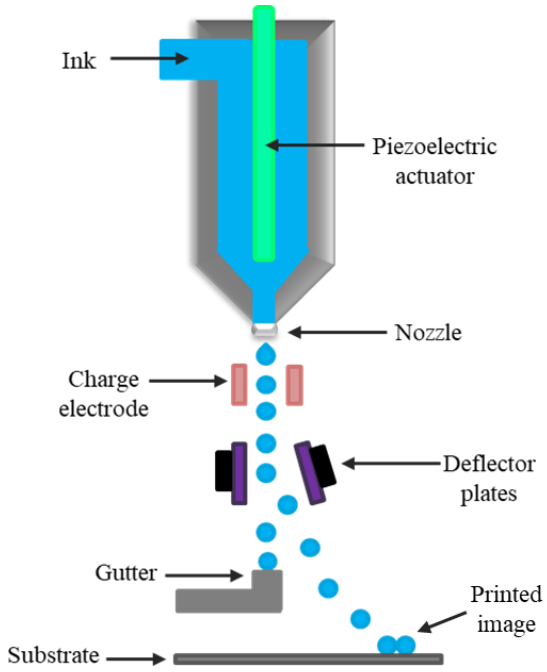

Figure 3- Schematic representation of a continuous inkjet (CIJ) printer, showing both the deflection of droplets onto the substrate and the collection of droplets in the gutter for re-use.

In order to achieve successful deflection of droplets onto the substrate, ink formulations for CIJ often require the inclusion of a charged species, e.g. conducting salts or charged dyes, in order for a charge to be imparted upon the droplets as they pass the charge electrode. Only then can the charged droplets of ink be deflected to a specific location, determined by the digital image, onto the moving substrate.

1.1.2 Inkjet Formulation Properties

The different mechanisms of droplet generation (DOD and CIJ) described in Section 1.1.1 require distinct formulation properties in order to produce high quality printed images.[18] The most distinct difference between inkjet formulations for DOD and CIJ printers is the volatility of the solvents used. DOD systems are confronted with the need for the solvent to dry on the substrate, but not at the nozzle, where the ink is held until droplets are required. DOD systems therefore require ink formulations that contain lower volatility solvents that will not evaporate at the printhead. In contrast, CIJ formulations are recycled continuously through the printer system reducing the risk of nozzle blockage, and therefore CIJ systems can employ both volatile (MEK) or non-volatile solvents (water) in their inkjet formulations.

The surface tension and viscosity of ink formulations are important factors in producing high quality printed images. Most liquids of practical interest for inkjet printing have surface tensions within the range of 20-70 mN m^{-1}, with most organic solvents exhibiting lower surface tensions 20-40 mN m^{-1} and water exhibiting a higher surface tension of 72 mN m^{-1}.[16] In DOD systems, the ink formulations require substantial surface tension to prevent the ink from undesirably exiting the nozzle, whereas in CIJ systems the correct surface tension is required for sufficient drop formation. The viscosity required for ink formulations varies according to the printhead to be used: TIJ require low viscosity inks (3 cP) to permit vaporisation of the ink, CIJ systems print more effectively with inks in the viscosity range of 3-6 cP, whereas PIJ systems exhibit a wider range of versatility and can print inks in the viscosity range of 1-25 cP.[3,16]

1.1.3 Types of Inkjet Formulations

The type of printhead employed in deposition is, however, only one of the factors considered when formulating an inkjet ink. Inkjet printing has been developed for use in a variety of applications, from date-coding to the direct writing of biological, electronic, metallic and polymeric devices.[19] The final application of the printed material and the consumer specifications define the components required for the inkjet formulation and the properties of the final print.

Inkjet formulations are designed to deposit a functional material such as a colourant, UV curable monomer, biological cell or electronically conducting material onto a substrate. These functional materials are additives which make up the composition of the ink alongside liquids (as carrier solvents) and often polymers to aid in binding the ink to the substrate.[3] The types of inks used can be split into four classes: i) phase-change, ii) UV-curable, iii) water-based and iv) solvent-based,[20] all of which are liquid at the time of printing. The main difference between these ink categories is the manner in which the functional material adheres to the substrate.

i) Phase change inks are stored as solids, but are melted to form a liquid before introduction to the inkjet printer. They are usually composed of resins, waxes and dyes or pigments, with common resins used including urethane, acrylic, ethylene vinyl acetate, polyester or polyamide resin.[21] The melted ink is deposited onto the substrate where it solidifies rapidly, which prevents spreading and increases the precision of deposition (Figure 4). Although phase-change inks are advantageous for their short setting times, they often suffer from low durability and abrasion resistance.[3]

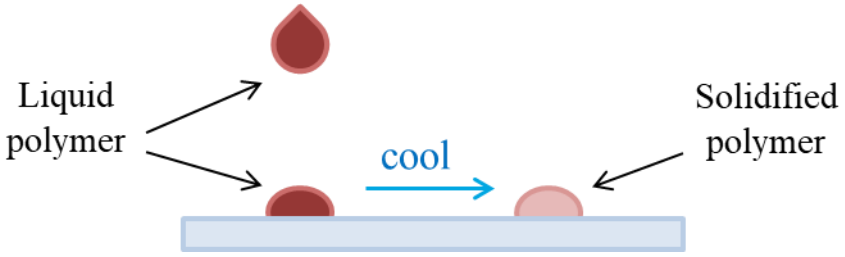

Figure 4- Diagram of the deposition of a phase change ink showing the transition from the liquid polymer (left) to the solidified polymer (right).

ii) UV-curable inks are composed of acrylic monomers, oligomers, photoinitiators and pigments or dyes.[2,22] Monomer based inks often do not require a solvent, as the monomers themselves are liquid. The components of the UV ink remain in the liquid form until the activation of a cross-linking reaction, upon irradiation with UV light (>350 nm). The cross-linking reaction of the monomers is triggered by the photoinitiators present in the inkjet formulation, which absorb UV light and disintegrate into free radicals to initiate the polymerisation of the unsaturated double bonds of the monomers. The cross-linking reaction forms a solid, high molecular weight polymer network, fixing any functional materials to the surface of the substrate without the need for additional polymer binders (Figure 5). UV-curable inks benefit from very fast drying times, good adhesion to a variety of substrates and the production of a strong cross-linked polymeric network post-irradiation.

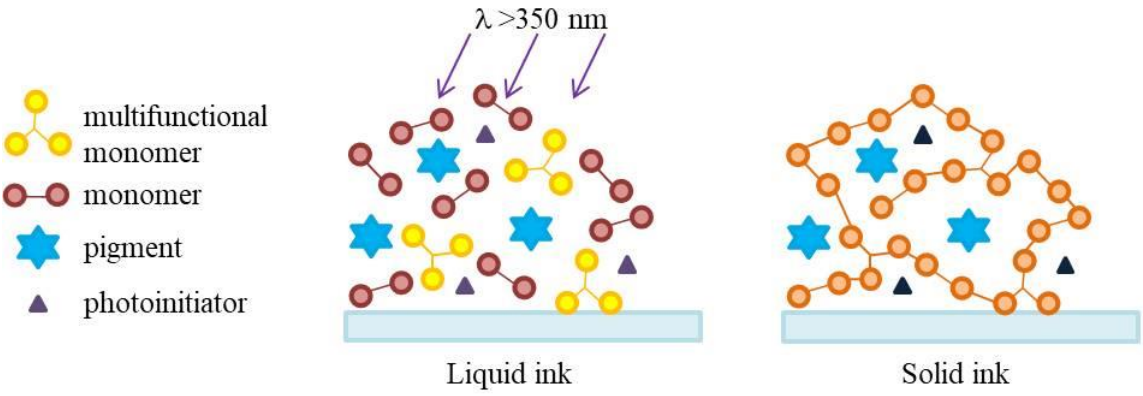

Figure 5- Diagram showing the components of a UV ink (left) and the polymerised structure produced (right) following irradiation with UV light, which results in the adhesion of the functional compounds (light blue) to the substrate.

iii and *iv*) Both water and solvent-based inks involve the deposition of a solution onto the substrate followed by rapid evaporation of the carrier solvent, leaving the functional molecule adhered to the substrate.[3] The successful deposition of water-based formulations requires the use of porous or pre-treated substrates as poor wetting is often observed with non-porous surfaces, resulting in poor adhesion of the ink and thus limiting their industrial application (Figure 6). Aqueous solvents also exhibit slow evaporation times, due to the low volatility of the water.

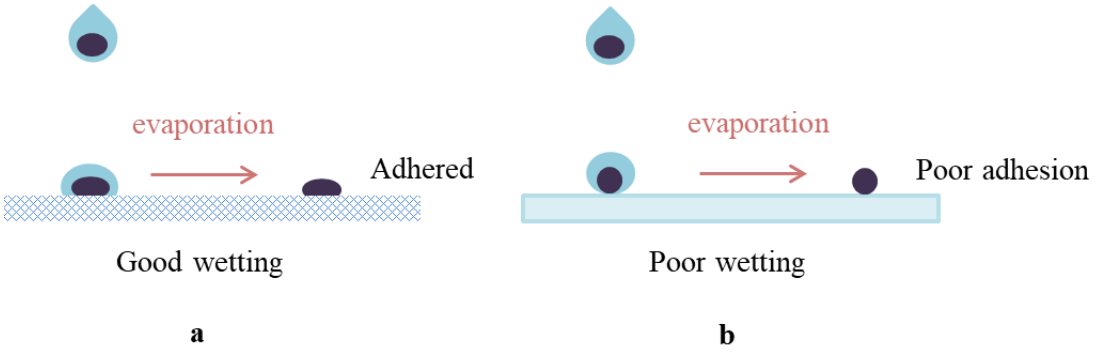

Figure 6- Deposition of an aqueous ink showing: a) deposition onto a porous or pre-treated substrate, showing good wetting of the solvent and adhesion of the functional material (purple) and b) deposition onto a non-porous substrate showing poor wetting and poor adhesion of the functional material (purple) to the substrate.

Solvent-based formulations, however, benefit from faster drying times and good wetting of a variety of porous and non-porous substrates, indicating the potential for good adhesion to a wide range of materials.[3] The improved wetting and faster drying times of the solvent-based materials render them more suitable for the high throughput process used in the coding and marking of materials.

1.2 The Role of Polymers in Inkjet Printing

With the expansion of inkjet printing into a wide range of technologies and applications, consumer demand now requires high throughput inkjet deposition onto a wider variety of substrates including a large amount of non-porous substrates, such as plastics. Both aqueous and solvent-based inks often require the inclusion of polymer additives to aid the binding of the functional materials and improve the permanence of prints. Successful binders exhibit good dye or pigment fixation as well as improved permanence,[23] abrasion and water resistance.[24,25] Commonly used binders include poly(vinyl alcohol)s,[26] cellulosic polymers[27] and poly(ethylene glycol)s (PEG)s,[28] which have also been included in inkjet formulations as viscosity modifiers.[27,28] The viscosity of the inkjet formulation is an important factor; too low viscosity can result in droplet break up, resulting in satellite droplet formation, which reduces the overall quality of the print,[28] whereas too high a viscosity can result in nozzle blockage or even ink build-up in the printer.[3] Polymers have also been included in inkjet formulations to aid droplet formation,[29] pigment dispersion[30] and as functional materials.[31–33]

1.2.1 Rheological Behaviour of Polymer Solutions

Despite the many advantages afforded by the inclusion of polymers in inkjet formulations, their addition also adds some complexity to the printing process as they often exhibit non-Newtonian behaviour. This behaviour is a result of the polymer chains disentangling, aligning and stretching, and can produce formulations with complex rheological properties.[31,33–35] The behaviour of liquid droplets can be characterised by dimensionless numbers, which are ratios that can be used to compare and contrast different formulation systems in order to provide valuable information about the print characteristics of fluids.[35] The three most useful dimensionless numbers for a fluid jet are the Reynolds (*Re*), Weber (*We*) and Ohnesorge (*Oh*) numbers- these are calculated by Equations 1–3, see below.

$$Re = \frac{\rho v L}{\mu} \quad \text{(Equation 1)}$$

$$We = \frac{\rho v^2 L}{\sigma} \quad \text{(Equation 2)}$$

$$Oh = \frac{\sqrt{We}}{Re} \quad \text{(Equation 3)}$$

These dimensionless numbers consider the density (ρ), viscosity (μ), surface tension (σ), velocity (ν), and characteristic length (L) (e.g. diameter of the liquid) in the determination of printability of a fluid. The Reynolds number represents the ratio between the inertial and viscous forces of the fluid, whereas the Weber number contrasts the inertial forces and surface tension. The Ohnesorge number considers all three properties, without the influence of velocity and is therefore considered to be independent of driving conditions. The Ohnesorge number is the closest representation to the formation of a droplet from a DOD nozzle and thus is often used to determine the suitability of a fluid for inkjet purposes.[35,36] For Newtonian fluids, successful droplet formation without the evolution of satellite droplets is achieved with Ohnesorge numbers in the range of 0.1–1.[35]

The three dimensionless numbers considered thus far are predominately aimed at fluids that exhibit Newtonian behaviour. The inclusion of polymeric additives into the formulation adds complexity to the rheological behaviour of the ink and can produce formulations that exhibit non-Newtonian or viscoelastic behaviour. Two further dimensionless numbers are employed in these cases; the Deborah number (*De*) (Equation 4) and the Weissenberg number (*Wi*) (Equation 5).

$$De = \frac{t_c}{t_p} \quad \text{(Equation 4)}$$

$$Wi = \lambda \dot{\gamma} \quad \text{(Equation 5)}$$

The Deborah number relates the relaxation time (t_c) of the fluid, which is affected by the inclusion of polymers, and the observation time (t_p) of the system, which in inkjet printing is microseconds. A Deborah number of above 1 can result in solid-like behaviour of the ink, which is unfavourable for inkjet deposition. The Weissenberg number relates the relaxation time (λ) of the fluid to the shear rate ($\dot{\gamma}$), at steady shear and is used to determine the viscoelastic response of a fluid. In the case of formulations containing polymers in extensional flow, a Weissenberg number that exceeds 0.5 indicates a transition from a random coil to a highly stretched state known as the coil-stretch transition of the polymer (Figure 7).[37–41]

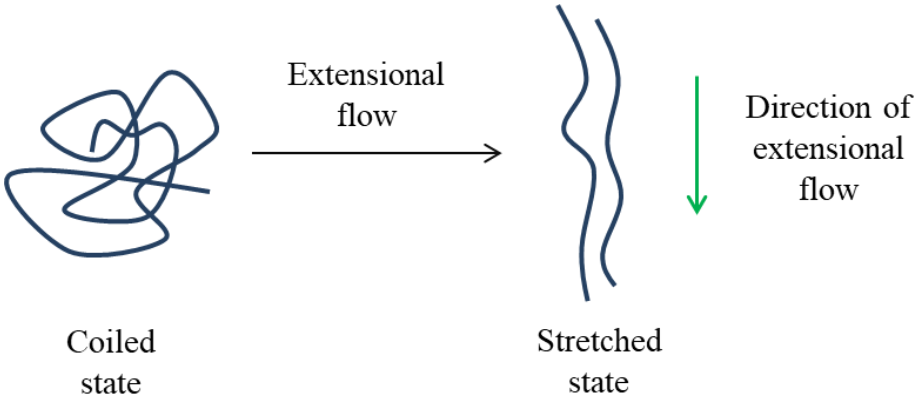

Figure 7- The coil-stretch transition often observed as a result of extensional flow in formulations containing polymers. The coil-stretch transition is observed for formulations that exhibit a Weissenberg number of above 0.5 because the elastic forces dominate over the viscous forces.

In CIJ printing, the inkjet formulations are passed through the printer nozzle at high shear rates and therefore the coil-stretch transitions of the polymeric components are very likely to occur.[34,42] The behaviour of the polymer at high shear rates can affect the viscosity of the formulation, leading to complications in printing and sometimes failure of print.

The viscous response of formulations at high shear rates can be investigated pre-deposition using shear rheology and can aid in predicting the behaviour of the materials during CIJ printing. Shear rheology employs a microfluidic device with a series of sensors that record the viscosity of the formulation at increasing shear rates. Newtonian fluids exhibit a consistent viscosity that is independent of shear rates. However, formulations that contain polymers often behave as non-Newtonian fluids, meaning that the viscosity is not independent of shear rates. For these formulations, high shear rates can lead to shear thinning (decrease in viscosity) or shear thickening (increase in viscosity) of the formulation (see Figure 8).

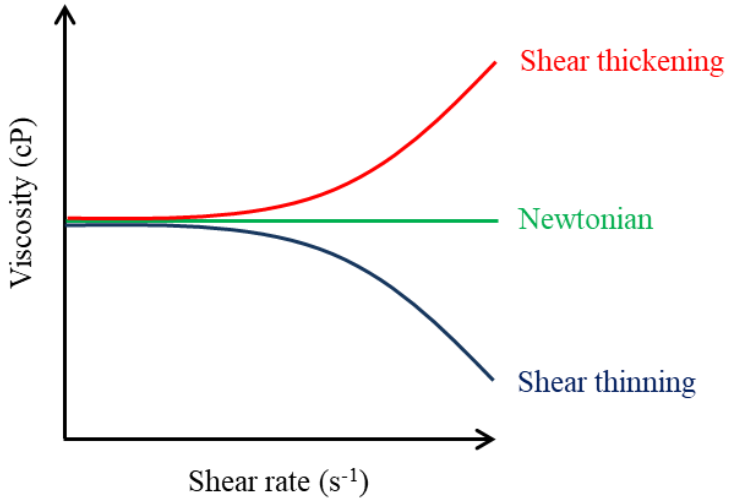

Figure 8- A model graph showing the viscous response of Newtonian (green) and non-Newtonian (red and blue) fluids with increasing shear rates.

The viscoelastic response of polymers can also be investigated using microrheology, which is used to record the change in complex viscosity of a formulation with increasing angular frequency. This technique reveals information about the relaxation of the polymeric microstructure under a small strain. Microrheology can be achieved by using dynamic light scattering (DLS) to monitor the movement of tracer particles in a sample of the polymer solution at increasing angular frequencies.[43] The tracer particles are buffeted in solution by solvent molecules, resulting in random motion (Brownian motion) which imparts randomness on scattered light to form constructive or deconstructive interference. The scattering of light can, therefore, be used to determine the extent of movement of the tracer particles in the presence of polymeric structures (Figure 9).

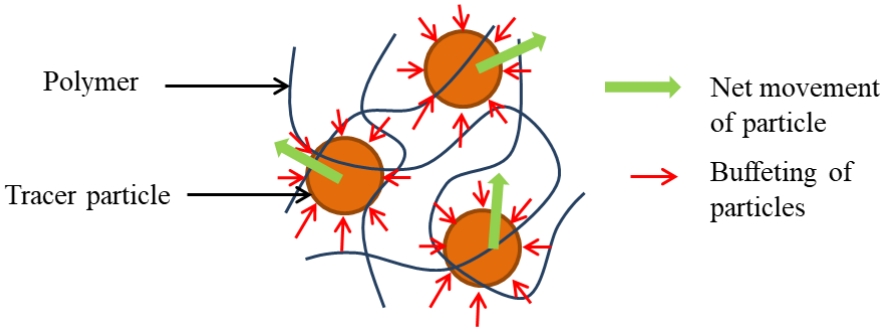

Figure 9- Schematic of the buffeting (red arrows) of tracer particles (orange) dispersed in a polymer solution (blue) causing the random motion of the particles, which can be traced using dynamic light scattering techniques.

For Newtonian fluids the movement of the tracer particles is not limited, but often for non-Newtonian polymer solutions the movement of the tracer particles is often limited at higher frequencies (shorter timeframes) because the polymer microstructure has had insufficient time to return to the relaxed state and exhibits a more viscoelastic nature.

1.3 Functional Polymeric Materials for Inkjet Printing

Despite the complexities often observed by the introduction of even small quantities of polymeric materials into inkjet formulations, the potential of polymeric materials as functional components of inkjet inks is vast.[31] In order to overcome the rheological constraints described, careful selection of the molecular weight, chain length and viscosity of the polymer is required. Studies have been undertaken to determine the effects of each of these factors on the printability of polymer solutions.[19,29,32,41,44–48] The benefits of employing polymers in the microfabrication of devices include the flexibility of the materials, ease of processability, low manufacturing costs and in some cases low cytotoxicity of the materials.[49]

1.3.1 Inkjet printing of Polymer Electronics

Functional polymers have been applied in the field of electronics as dielectric materials, conductors, semiconductors, sensors and light emitting materials all of which require the precise deposition of materials to produce high resolution microarrays.[50] Polymeric light emitting diodes (PLED)s employ a polymer film which acts as the emissive electroluminescent layer. Upon application of an electric current the film emits light of a specific wavelength to produce a coloured light.[51] PLEDs consist of a series of layers on a glass display. Firstly an anode layer (commonly indium tin oxide (ITO)) is deposited onto the substrate, followed by a hole conducting (p-type) polymer, a light emitting polymer (LEP), a cathode material (low work function metal e.g. Ca, Ba) and finally a layer of conductive metal (e.g. Al or Ag)[50] (Figure 10).

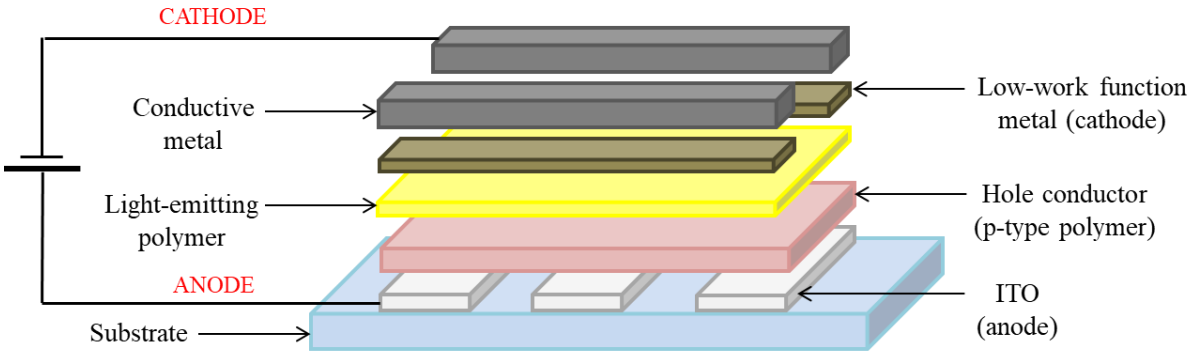

Figure 10- Diagram showing the components used to produce a polymer light emitting diode. The substrate is usually transparent e.g glass, particularly for application in screen technologies.

When a voltage is applied to the PLED assembly, electrons are injected from the cathode and holes are injected from the anode into the LEP, where they combine to form an exciton. Colour is produced following decay of the exciton to the ground state, with emission of light of a characteristic wavelength. Monochromatic PLED displays can be produced using spin-coating to deposit the polymeric layers, but for the production of multicolour displays a precise micro-patterning technique is required to deposit a red, green and blue colour set.[32]

Bharathan and Yang were the first to report[52] the use of inkjet printing in the fabrication of a PLED device, depositing a semiconducting poly(3,4-ethylenedioxythiophene) (PEDOT) ink from aqueous solution to produce several well-defined images. An electroluminescent polymer buffer layer consisting of poly(2-methoxy-5-2'-ethylhexyloxy-1,4-phenylene vinylene) was then spin-coated on top of the images, with only the PEDOT layer forming an emissive region. Since the development of the first inkjet-printed PLED, several investigations towards improving the resolution, wetting and uniformity of films have been undertaken.[53–57]

A further electronic application that employs inkjet deposition to produce polymer arrays is that of thin film transistors (TFT)s, which are used in liquid-crystal displays (LCD)s. TFTs are used to regulate the current and act as a switch for electrical signals. TFTs consist of source and drain electrodes on the substrate, which is usually glass as well as a coating of semiconducting material, an insulating material and finally the gate electrode on top (Figure 11).

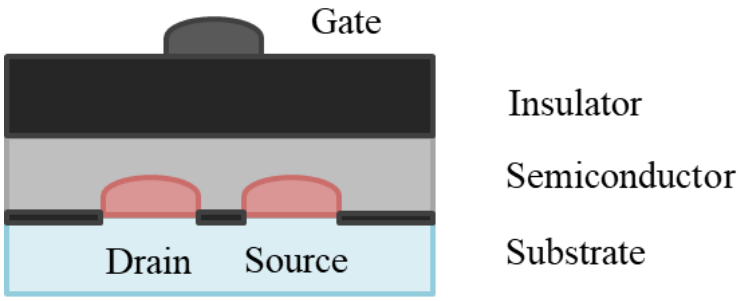

Figure 11- Schematic diagram of a thin film transistor used to regulate the current and act as a switch for electronic signals.

In 2000, Sirringhaus *et al*. successfully utilised piezoelectric inkjet printing to deposit PEDOT doped with poly(styrene sulfonic acid) (PSS) to produce an all polymer TFT.[58] Polymer source-drain electrode channel lengths of 5 μm were achieved by the precise inkjet deposition of aqueous polymer solutions onto pre-etched hydrophilic channels on the hydrophobic surface of the substrate. The same approach, was later used by Sele *et al*. to produce 250 nm channels of PEDOT:PSS electrodes.[59] Further work by this group[59] eradicated the need for pre-etching of the substrate, by firstly depositing a solution containing a surfactant and PEDOT:PSS followed by a solution containing solely PEDOT:PSS. The second solution was partially overprinted onto the first solution and was repelled by the surfactant-containing droplets, forcing it to one side of the first series of droplets to form a self-aligned channel (Figure 12).

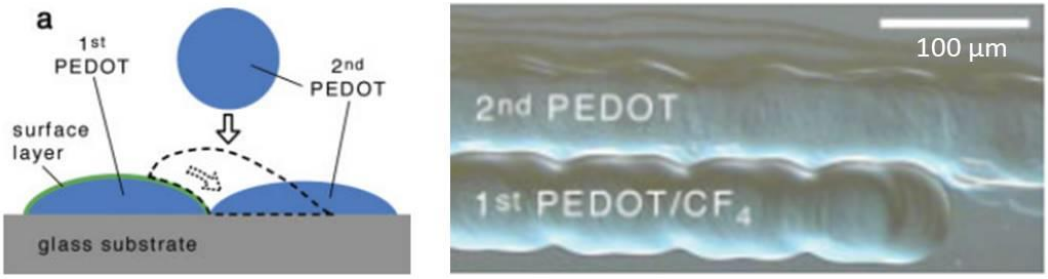

Figure 12- Schematic representation of the overprinting technique used by Sele *et al*. and b) optical microscopic image of the PEDOT electrodes, which are in close proximity.[59] Figure reproduced with kind permission from reference 59.

PEDOT:PSS is a popular polymeric component for electronics and has also been employed to produce transparent touch sensing devices. Ma *et al*. produced,[60] for the first time, a fully inkjet-printed touch sensor using DOD printing. Orthogonal layers of transparent, conductive PEDOT:PSS were deposited via inkjet printing with dielectric poly(methyl siloxane) separators in between (Figure 13).

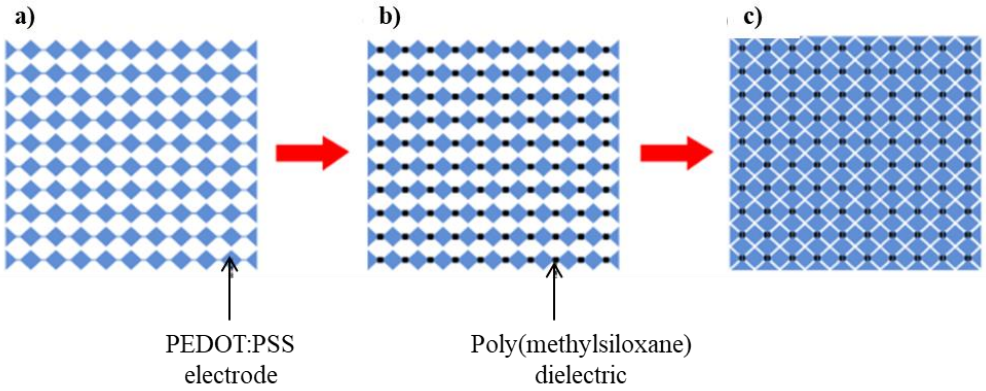

Figure 13- Schematic showing the layer by layer deposition of the transparent touch sensing device produced in the work of Ma *et al*.[60] The construction of the device involved the deposition of diamond shaped PEDOT:PSS layer followed by a dielectric poly(methylsiloxane) spacer and another layer of PEDOT:PSS. Figure adapted with kind permission from reference 60.

The sensors were deposited onto both borosilicate glass and polyethylene terephthalate (PET). Upon a touch event, the two PEDOT:PSS electrodes come into contact, resulting in a change of resistance allowing the facile location of the touch event. It was concluded that the sensors demonstrated industrially viable potential for the inkjet deposition of sensors on rigid and flexible substrates for a variety of sensing applications.[60]

1.3.2 Inkjet Printing of Polymers for Biological Applications

Inkjet deposition techniques have also been implemented for the precise deposition of polymeric and pharmaceutical materials for controlled drug delivery devices.[61] The benefits of employing inkjet

printing for the preparation of pharmaceuticals includes the ability to accurately control the spatial deposition of low volumes, and to produce complex geometries.[62] Wu *et al*. realised the effects of the composition and microstructure of drug delivery devices on the release rate of drug components and investigated[63] several simple drug delivery frameworks by the inkjet deposition of polycapralactone and PEG materials. The study involved the controlled release of two model 'drug' compounds, methylene blue and alizann yellow, from the polymer microstructure and it was found that variation of the polymer microstructure and position of the model 'drug' resulted in different release rates, showing potential for the use of a single polymer structure for release of more than one drug at differing rates.

Kook-Lee *et al*. displayed a similar approach in their investigation into drug delivery systems, producing a variety of different geometries of polymer-drug microparticles.[64] The research involved the successful deposition of paclitaxel (pharmaceutical drug) loaded poly(lactic-*co*-glycolic acid) (PLGA) to produce circle, ring, grid and honeycomb geometries (Figure 14) which showed an increasing release rate of the drug as a result of an increased surface area of the printed polymer and drug structure.

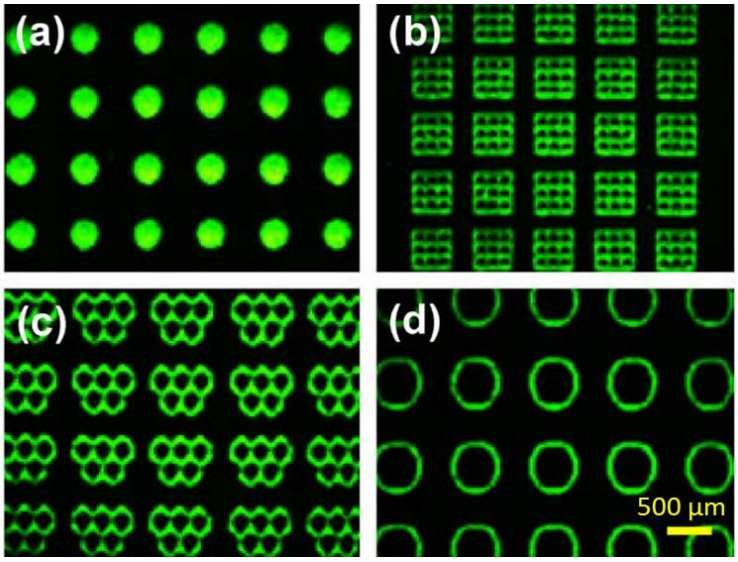

Figure 14- The different geometries of paclitaxel loaded PLGA deposited using inkjet printing in the studies described by Kook-Lee *et al*. showing a) circle, b) grid, c) honeycomb and d) ring geometries.[64] Figure reproduced with kind permission from reference 64.

Hauschild *et al*. also investigated[65] the application of inkjet printing for the deposition of materials intended for drug delivery. The study exploited inkjet printing techniques to directly deposit block co-polymers (poly(2-vinylpyridine-*b*-ethyleneglycol)) from ethanol directly into water to produce vesicle assemblies. The vesicles were characterised using DLS and cryo-transmission electron microscopy which revealed co-polymer vesicle diameters of *ca*. 130 nm. Initial encapsulation studies of the vesicles were performed using fluorescein as a model drug compound using two different approaches.

The first approach consisted of deposition of the co-polymers into an aqueous solution, whereas the second approach involved the injection of a solution of co-polymer with fluorescein into water. The latter method revealed an encapsulation concentration over three times higher than the first approach used, indicating much better suitability towards drug encapsulation.

1.3.3 Inkjet Printing of Hydrophobic Polymer Coatings

Hydrophobic polymer coatings are extremely useful for the production of easy clean, water repellent surfaces such as Teflon™, a polytetrafluoroethylene coating used to produce non-stick cookware. Polymers containing fluorine groups are known to exhibit segregation of fluoroalkyl units at the air-interface, resulting in polymer films with low-surface energies and hydrophobic properties.[66] As well as water-resistant and self-cleaning properties, the production of hydrophobic surfaces can also be advantageous in controlling the size of ink droplets deposited by inkjet printing technologies as a result of decreased wetting of the substrate.

Park *et al*. exploited[67] the hydrophobic properties of fluoropolymers to restrict the surface wetting of a silver-based ink (Ag nanoparticles in tetradecane) to produce high resolution, silver printed patterns for potential applications in electronics. A hydrophobic surface was produced by spin coating a commercially available polyfluorosilane (EGC-1720, 3A). The polyfluorosilane coating exhibited a water contact angle of 113° whereas the silver ink demonstrated a contact angle of 68°, both of which were decreased by plasma treatment with O_2 or Ar to control the droplet diameter and thus the width of deposited silver nanoparticles (Figure 15).

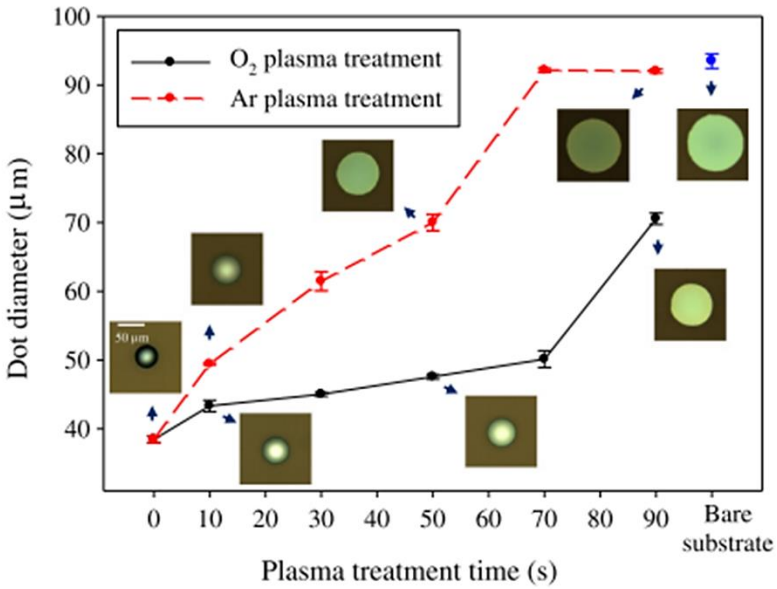

Figure 15- Graph showing the change in diameter of ink droplets with increasing plasma treatment time. The smallest drop diameter was observed for the sample that was not treated (0 hours).[67] Figure reproduced with kind permission from reference 67.

Despite the extensive investigations into fluoropolymer-based hydrophobic coatings,[66,68–72] efforts have also been aimed towards the production of fluorocarbon-free hydrophobic coatings.[73,74] Yu *et al*. have developed[75] a printable, hydrophobic textile coating which has been employed to modify the surface properties of polyester and polyamide fabrics. A commercially available amino-functionalised methyl polysiloxane (M_w = 70,000 g mol^{-1}) dispersion in water was deposited as a solid square onto the textiles using inkjet printing to produce flexible, hydrophobic coatings that demonstrated good self-cleaning and stain-repellent properties. The water contact angles of the treated textiles were recorded using the sessile drop method with an optical tensiometer and revealed an increase in the water contact angle of the textiles from less than 90° for untreated samples to 136° and 137° for treated polyester and polyamide, respectively.

1.4 Formation of Polymer Networks Post-inkjet Deposition

Depending on the final application of the inkjet-printed polymer, it is often desirable to deposit a high molecular weight, strong material to enhance adhesion and permanence of the print. However, the rheological complexities observed when depositing high molecular weight polymers often render them unprintable[29,41,45,46] and therefore alternative routes to the production of high molecular weight polymer films are required. One alternative is to produce high molecular weight polymer networks from lower molecular weight derivatives, which can form supramolecular networks[76–79] or covalent[80-82] bonds by the application of a stimulus.

1.4.1 Inkjet Printing of UV-Curable Polymers

The use of UV-curable materials in inkjet printing has become increasingly popular because of the ability to form high molecular weight polymeric materials by the UV curing of low molecular weight, unsaturated monomers. The benefits of UV-curing inkjet formulations are the rapid curing times, high resolution of the image plus space and energy efficiency, when applied at industrial scales.[83]

The most commonly used UV-curable inks contain mono, di, tri and/or tetra-functional acrylate monomers, which exhibit low molecular weight (M_n = 128–352 g mol^{-1})[83] and viscosity allowing facile deposition using inkjet printing. Acrylates also benefit from high reactivity i.e. short reaction times, (often fractions of a second) to afford high molecular weight polymers. Acrylate inkjet formulations consist of acrylate monomers and oligomers as well as photoinitiators, which break down with UV light to form radicals. The radicals then initiate the polymerisation process of the acrylate monomers to form a polymeric material (Scheme 1).

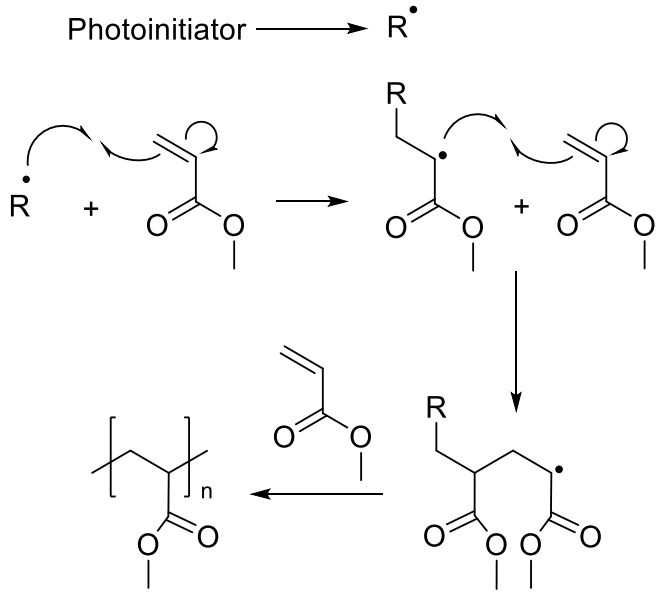

Scheme 1- An example of the radical polymerisation of an acrylate monomer (methyl acrylate) to produce a polymeric network poly(methyl acrylate). The polymerisation process is initiated by radicals, which are produced following UV irradiation of the photoinitiator.

The example given in Scheme 1 shows the radical polymerisation of a mono-functional monomer, leading to the production of a linear polymer, however, most UV-curable formulations contain a mixture of mono- di- and tri-functional monomers, as well as oligomers to promote cross-linking during polymerisation. One of the major advantages of employing acrylate monomers in UV cross-linking is the high speed (< 1 second) at which a cross-linked network is formed, however, many acrylate monomers are irritants, toxic or suspected carcinogens.[83] The use of small monomer compounds also poses a risk for unreacted monomers to undesirably migrate to the surface of the print, or through packaging if employed in coding and marking applications. More recently polymers containing UV-active acrylates have been investigated, to produce polymeric networks without the use of low molecular weight (M_n = 128–352 g mol^{-1}) acrylates.

Sangermano and Chiolerio *et al*. have exploited the use of UV curing to produce UV-cured conductive inks for microelectronic devices.[84,85] Both studies employed an aqueous dispersion of silver nanoparticles with poly(ethylene glycol) diacrylate (PEGDA) as a UV-curable polymer matrix. The materials were deposited as a solution in water and upon UV-irradiation formed a solid material, with suitability as a microelectronic device. Saleh *et al*. also investigated[86] the use of a UV-curable resin alongside PEGDA in inkjet formulations to produce solid structures that show potential for use in additive manufacturing. The formulations investigated contained varying amounts of iron oxide nanoparticles, producing UV-cured materials with tuneable electromagnetic properties.

A more recent study[87] by Invernizzi *et al*. details the successful inkjet deposition of methacrylate terminated-polycapralactones and ureidopyrimidones from chloroform and the subsequent UV cross-

linking of the materials with the aid of 2,4,6-trimethylbenzoyl-diphenyl-phosphine oxide as a photoinitiator to form an insoluble polymeric film. The materials demonstrated remarkable shape memory, exhibited by the production of an L-shaped film to mimic an opposable thumb geometry. The material was able to fold fully in half, before recovering the original shape, indicating suitability towards human-machine interactions and soft robotics.[87]

Despite the ability to produce UV-curable polymeric networks by employing acrylate polymers in place of monomers, the studies described required the presence of photoinitiators in order for polymerisation to take place. Photoinitiator-free reactions of polymers that form extended covalently bonded networks following UV irradiation have been described[81,82,88] with several of the studies employing polymers that are functionalised with UV-active anthracene,[89–101] coumarin[88,101–111] and cinnamate ester[112–116] groups. The polymer end groups form dimers upon irradiation with UV via a [4+4] (anthracene[117–119]) or [2+2] (coumarins and cinnamate ester[115]) photocycloaddition processes (Scheme 2).

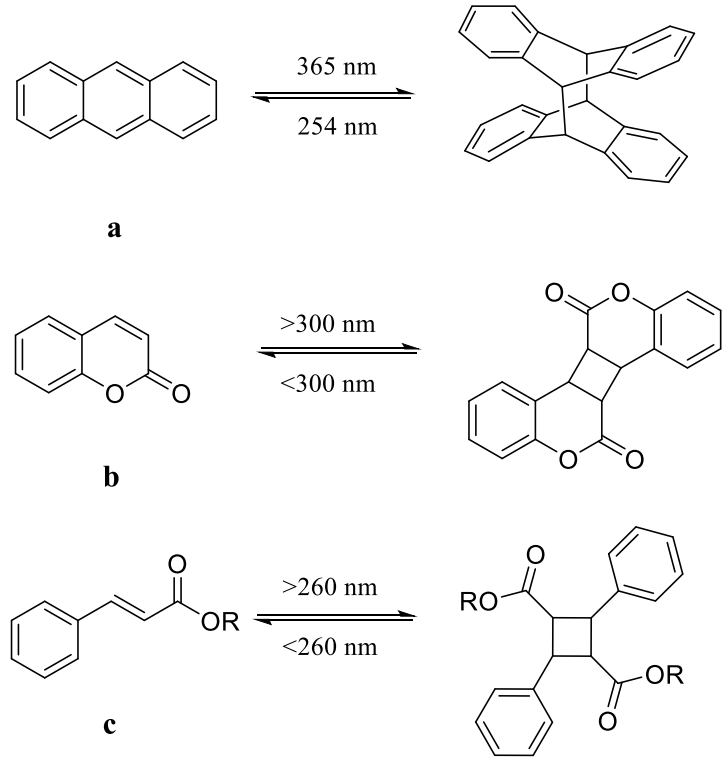

Scheme 2- The reversible photodimerisation of a) anthracene, b) coumarin* and c) cinnamate ester. *Only one conformation is shown (head-to-tail) for b, but a head-to-head conformation is also possible.

Despite the extensive research undertaken in this field, polymers containing the UV-dimerisable end-groups described have not yet been investigated in the field of inkjet printing. However, they may provide a useful alternative to UV monomers and polymers that require photoinitiators in order to

form a cross-linked polymer network. The reversibility of the dimerisation process would also be useful for the facile removal of ink upon the recycling of used packaging.

1.4.2 Inkjet Printing of Supramolecular Polymers

The use of supramolecular polymeric materials in inkjet printing formulations can provide a further alternative approach to the production of high molecular weight materials, post-inkjet deposition. Supramolecular materials can be described as 'chemical species of higher complexities, held together by intermolecular (non-covalent) binding interactions'.[120] The exploitation of these weak non-covalent interactions, either within or between molecules, allows the production of large complex networks, in which smaller subunits self-assemble without the need for difficult or elaborate synthetic procedures.

Non-covalent interactions are weaker than covalent bonds, with their strength varying according to the type of interaction observed. Weaker, non-covalent interactions such as van der Waals forces display an interaction energy of <5 kJ mol^{-1}, whereas interaction energies of up to 250 kJ mol^{-1} are observed in ion-ion electrostatic interactions.[77] In recent years, various studies have been undertaken, broadening the field of supramolecular materials to include applications in drug delivery,[121–124] molecular recognition,[125–128] healable materials,[15,77,129–131] catalysis and transport processes.[120] The formation of a supramolecular motif can occur through various types of non-covalent interactions, within or between residues. These interactions include electrostatic interactions, hydrogen bonding and π-π stacking interactions.

1.4.2.1 Electrostatic Supramolecular Polymers

Electrostatic interactions occur as a result of coulombic attraction between opposite charges and include ion-ion, ion-dipole and dipole-dipole interactions.[132] Dipole-dipole interactions exhibit binding energies ranging between[133] 5-50 kJ mol^{-1}. The interaction energy is low as dipoles are weakly charged and therefore only a weak interaction between molecules is observed. The interaction between a polar molecule and a charged molecule is known as an ion-dipole electrostatic interaction. This type of interaction is of a higher energy than dipole-dipole bonding, ranging from 50-200 kJ mol^{-1}.[133]

Ion-ion interactions are the strongest type of non-covalent force and are observed between positively charged cations and negatively charged anions. The strength of ion-ion interactions are between 200-350 kJ mol^{-1} which is comparable with the strength of single covalent bonds.[133,134] An example of ion-ion interactions that result in the formation of a supramolecular polymer network is described by Cross *et al*.[135] The study described the development of different cationic polymers using poly(2-aminoethyl methacrylate) (PAEM) (RNH_3^+ as cationic functionality) to functionalise linear and star PEGs, which were combined with hyaluronic acid anions ($RCOO^-$ as anionic functionality) to produce a precipitate (linear PEG) and hydrogel (branched PEG) as a result of electrostatic interactions (Figure 16).

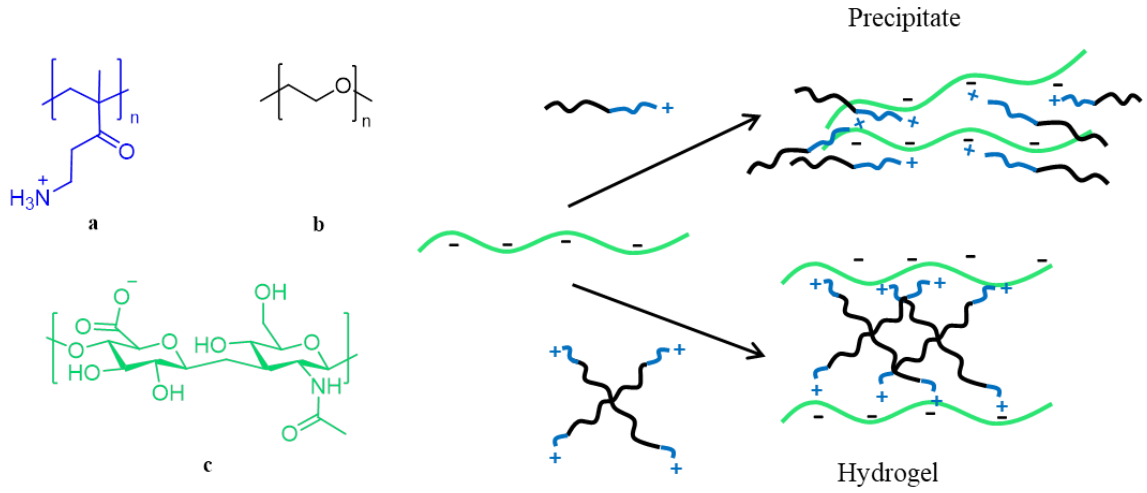

Figure 16- The polymeric components employed by Cross *et al.*, showing a) the cationic PAEM end-group that is attached to b) PEG backbones. The cationic components interact with hyaluronic anionic compound c) to form either a precipitate (linear cationic polymer) or a hydrogel assembly (star cationic polymer).[135] Figure adapted with kind permission from reference 135.

The exploitation of electrostatic interactions to produce polymer networks has been investigated by Parker *et al.*[136] in the formation of microcapsules using a combination of electrostatic interactions and host-guest chemistry. A microfluidic device was used to effectively mix an aqueous emulsion using two inlets that combined at a flow-focusing junction. The aqueous phase contained a macrocyclic host, curcurbit[8]uril as well as negatively charged fluorescein-functionalised polyacrylamides and positively charged stilbene-functionalised polyvinyl alcohols (Figure 17), which aggregated at the aqueous-oil interface with the aid of positively and negatively charged dopants (amine terminated poly(hexafluoropropylene oxide) and carboxylate terminated Krytox, respectively).

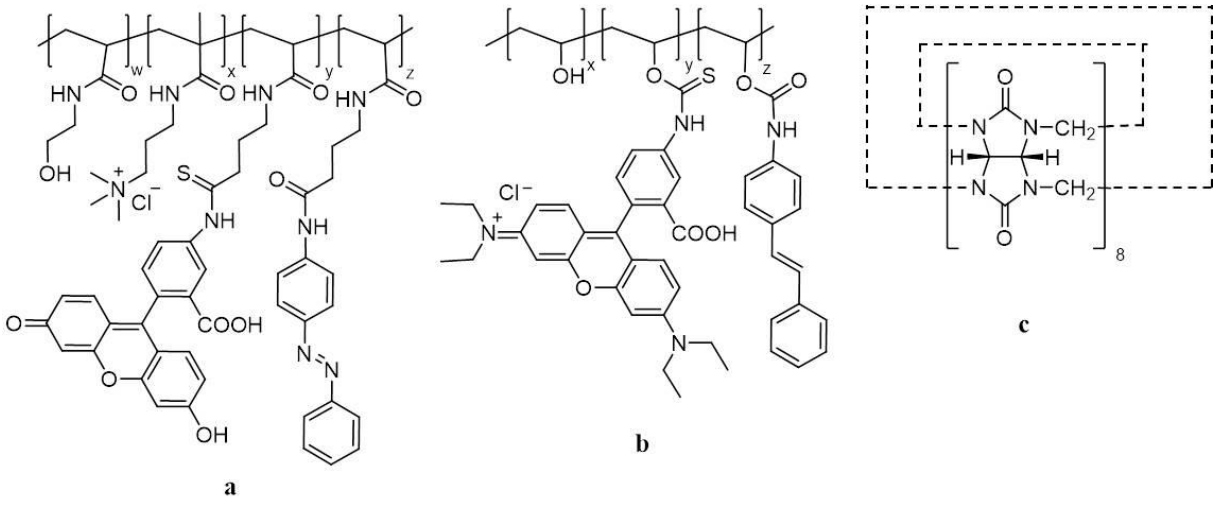

Figure 17- The structures of the complementary charged polymers a) fluorescein-functionalised polyacrylamide and b) stilbene-functionalised polyvinyl alcohol as well as c) curcurbit[8]uril host macrocycle.[136]

The electrostatic copolymers aggregated at the aqueous-oil interface where they were then able to form host-guest complexes with the curcurbit[8]uril host, encapsulating the aqueous phase in a microcapsule structure. The microcapsules developed[136] by Parker *et al*. were able to undergo a series of dehydration and rehydration cycles, without affecting their structure, indicating their potential for synergistic storage or release of biochemical cargos.

Limem *et al*. have incorporated the use of inkjet printing into the formation of electrostatically driven supramolecular polymer networks.[137,138] Initial studies[138] involved the deposition of alternate layers of poly(diallylmethylammonium chloride) (PDDA) and poly(vinylaminesulfonate) with an anthrapyridone chromophore as cationic and anionic polymers, respectively, to form self-assembled ionic complexes. The study also investigated a similar approach to the inkjet deposition of polypeptides. Solutions of polyglutamic acid and polylysine hydrobromide (0.25%w/v) in sodium chloride solution (0.25% w/v) were deposited alternately to form supramolecular, ionic complexes that were insoluble in water.

Subsequent studies[137] by Limem et *al*. involved the inkjet deposition of alternating layers of the polyelectrolytes poly(sodium-4-styrene sulfonate) and PDDA. The polyelectrolytes were deposited from a mixture of water and ethylene glycol, and washed post-deposition to remove the counter ions. The printing of alternating layers resulted in the formation of an ionic gel, which became insoluble in water, indicating the formation of an extended network by electrostatic interactions. The formation of the supramolecular network was further confirmed using scanning electron microscopy with electron dispersive spectroscopy, which demonstrated the presence of only a small percentage of counter ions on the surface of the polymer gels after washing (Figure 18).

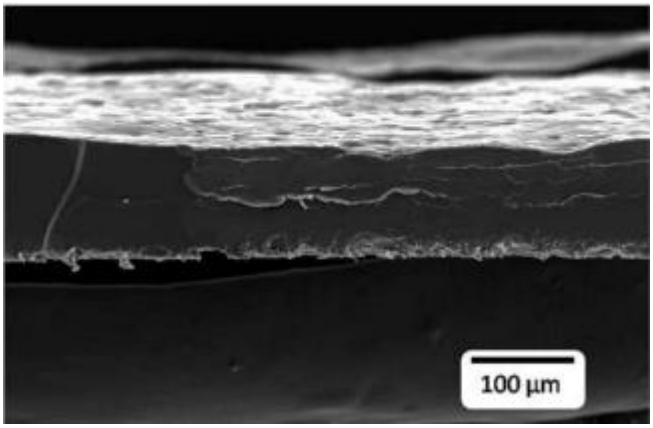

Figure 18- Scanning electron microscopy image of a film of 335 alternating layers of PDDA and poly(sodium-4-styrene sulfonate) on a glass substrate.[137] Figure reproduced with kind permission from reference 137.

1.4.2.2 Hydrogen Bonding Supramolecular Polymers

Hydrogen bonding can be described as a highly directional, attractive interaction between positive dipole charges on hydrogen atoms and negative dipole charges on electronegative atoms.[139] The hydrogen bond donor involved in the hydrogen bonding must be covalently bonded to an electronegative heteroatom, which induces a dipole moment to create a partial positive charge on the hydrogen atom. The partially charged hydrogen atom interacts with the partial negative charge of an electronegative heteroatom, known as the hydrogen bond acceptor (Figure 19).

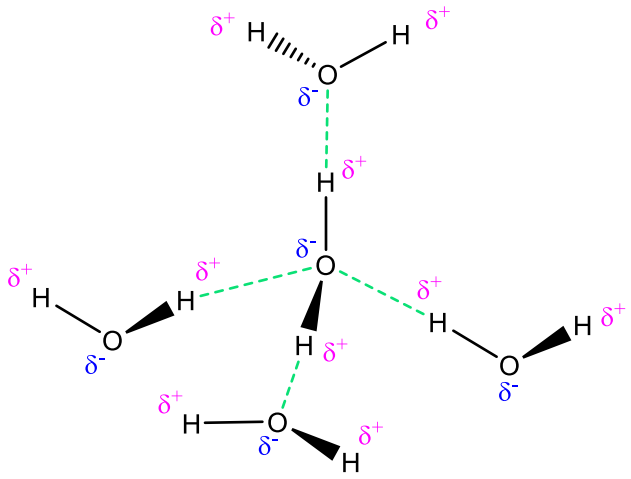

Figure 19- Hydrogen bonding interactions between water molecules, showing partial positive charges (pink) on the hydrogen atoms and partial negative charges (blue) on the oxygen atoms resulting in the formation of hydrogen bonds (green).

The strength of a single hydrogen bond ranges from 4–120 kJ mol^{-1} and depends largely on the electronegativity of the heteroatoms involved. Hydrogen bonded polymers have also been employed in inkjet applications.

Peng *et al*. have produced[140] a series of fluorophore-functionalised bis-ureidopyrimidone (UPy) monomers that interact via quadruple hydrogen bonding motifs to form a supramolecular polymer network and the subsequent formation of nanoparticles. The materials were deposited as aqueous dispersions using DOD inkjet technologies and it was found that variation of the fluorophore resulted in the formation of red, green and blue fluorescent images. Combining the different monomers in a variety of ratios, using a tricolour cartridge permitted the production of an expanded colour palette to produce well defined multi-coloured images, which were clearly visible using a UV lamp (365 nm) (Figure 20).

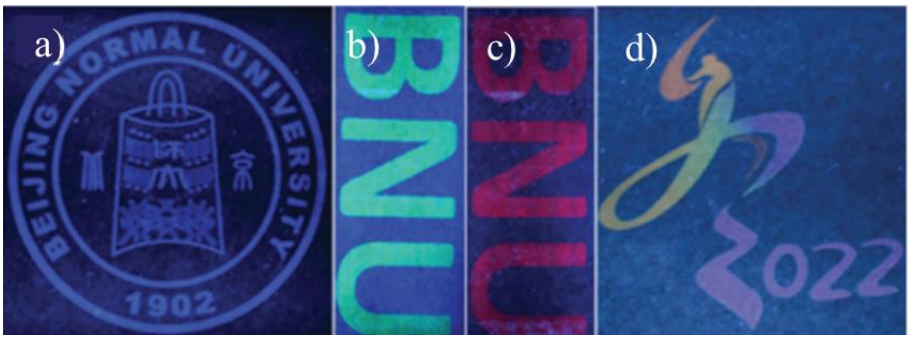

Figure 20- Inkjet-printed images produced[140] in the work of Peng *et al*. illuminated with a 365 nm UV lamp, showing a) blue-emissive nanoparticles, b) green-emissive nanoparticles and c) red-emissive nanoparticles as well as d) the multi-coloured image produced using a tricolour inkjet cartridge. Figure reproduced with kind permission from reference 140.

Zhang *et al*. also produced[141] a hydrogen-bonded polymer network using inkjet deposition. The study describes the development of a biodegradable polyurethane with sulfonic acid functionalities incorporated into the polymer backbone. Careful control of the pH of polymer solutions permitted the transition of the polymer from water soluble (pH > 8.7) to water insoluble (pH < 8.7). The structure of the hydrogen-bonded network formed was controlled by inkjet deposition of acetic acid:water solution (50% v/v) onto a solution of polyurethane in water (pH 8.7) (2% w/v) to form precise precipitated structures of the hydrogen-bonded polyurethane (Figure 21).

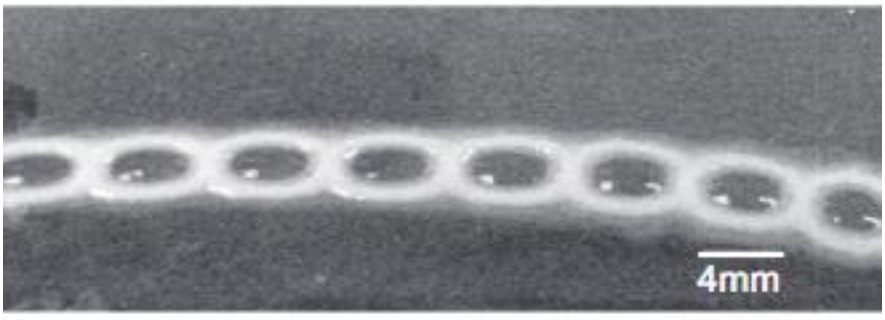

Figure 21- Hydrogen-bonded polyurethane structure produced[141] in the work of Zhang *et al.* by the inkjet deposition of acetic acid solution (50% v/v) onto a glass substrate coated with a weakly basic solution of polyurethane in water. Figure reproduced with kind permission from reference 141.

The polyurethane materials demonstrated good mechanical properties as well as the potential to re-dissolve the polymeric material using mild base when its end use has been achieved. Zhang *et al*. further investigated the use of the polymer as a biological scaffold and revealed that although the sulfonate-polyurethane was non-toxic, it demonstrated a lower level of cell attachment than for the control polyurethane without sulfonic acid groups.[141]

1.4.2.3 π–π Stacking Supramolecular Polymers

Supramolecular aromatic interactions are pervasive in nature and contribute to the stability of Deoxyribonucleic acid[142,143] (DNA), the 3-dimensional structure and function of proteins[142–146] and the packing of aromatics in the crystalline state.[146] Aromatic π-stacking interactions occur in three different ways; edge-to-face (so-called 'T-type' interactions), offset face-to-face or face-to-face stacking of aromatic systems.[147] Edge-to-face π-stacking involves the perpendicular interaction of an electropositive hydrogen atom with the centre of the π-electron cloud of the other aromatic system. Offset face-to-face interactions involve the partial overlapping of aromatic rings, where the centre of the electron cloud of one aromatic interacts with the σ-framework of the other aromatic. Face-to-face π-stacking interactions (also known as donor-acceptor π-stacking) occur between electronically complementary π-electron deficient and π-electron rich aromatic systems. The different π-stacking geometries described are depicted in Figure 22.

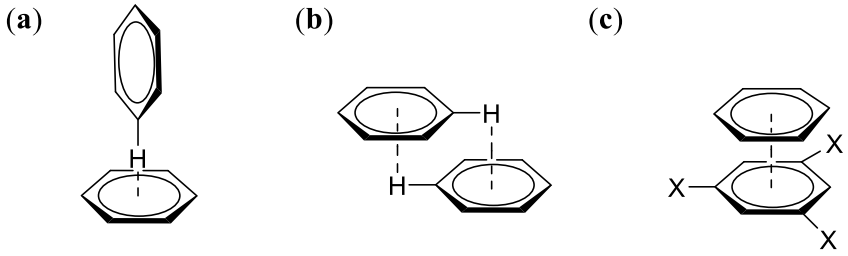

Figure 22- Aromatic π-stacking geometries, showing a) edge-to-face, b) offset face-to-face and c) face-to-face stacking (X = electron withdrawing group).

The self-assembling nature of donor-acceptor aromatic π-stacking has received a lot of interest in the production of complex supramolecular networks including small compound interactions,[148–152] macrocyclic structures[153] and polymeric assemblies.[130,152,154–161] Inkjet printing of π-π-stacking materials has been investigated for small compounds[162] and polymer systems.[149,156,157,163] In 2008, Adler-Abromovich used[162] inkjet deposition techniques to control the patterning of aromatic peptide assemblies that self-assembled through π-π-stacking interactions to form nanostructures. The study involved the production of two different formulations of the amine substituted phenylalanine (Phe) peptide tertbutoxycarbonyl-Phe-Phe, each of which produced different nanostructures of the self-assembled peptide. A stock solution of peptide in ethanol (10 mg mL^{-1}) was diluted in distilled water to produce a solution of peptide (5 mg mL^{-1}) that formed nanospheres following inkjet deposition, whereas employing a stock solution of peptide in heaxafluoro-2-propanol (100 mg mL^{-1}), and diluting with deionised water resulted in a peptide solution (2 mg mL^{-1}) that formed nanotube structures following inkjet deposition (Figure 23).

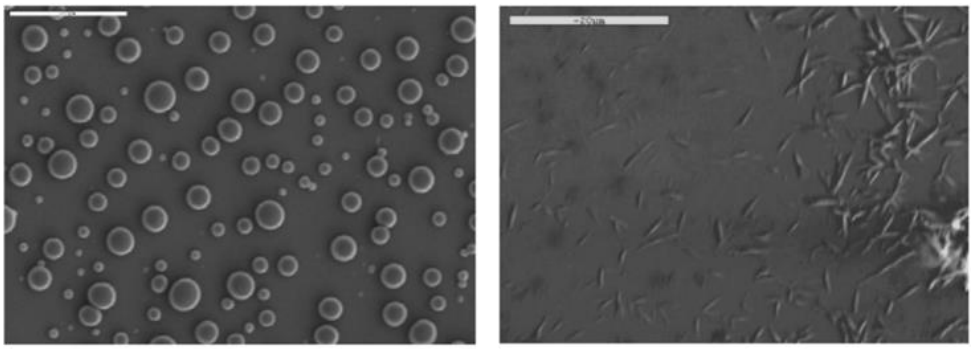

Figure 23- Scanning electron microscopy (SEM) images exhibiting the different nanostructures formed by the self-assembling phenylalanine peptide in the work of Adler-Abromovich *et al.*[162] The SEM images show the nanosphere structure (left) and nanotube structure (right) observed in the study. Figure reproduced with kind permission from reference 162.

Inkjet printing techniques have also been employed in the deposition of polymeric blends that exhibit π-π-stacking behaviour. Hart *et al*. reported[149,157,164] the deposition of electronically complementary, low molecular weight, functionalised PEGs to precisely control the deposition of self-assembling polymeric networks. The polymers developed by Hart *et al*. contained either π-electron rich (pyrene or perylene) or π-electron deficient (naphthalene diimide (NDI)) groups which, when over-printed, spontaneously self-assembled via aromatic stacking interactions and produced coloured charge transfer complexes between the π-electron deficient and the π-electron rich moieties. The self-coloured red (pyrene) and green (perylene), polymeric assemblies provided an alternative approach to producing coloured images without the requirement for dyes or pigments in the inkjet formulation (Figure 24).

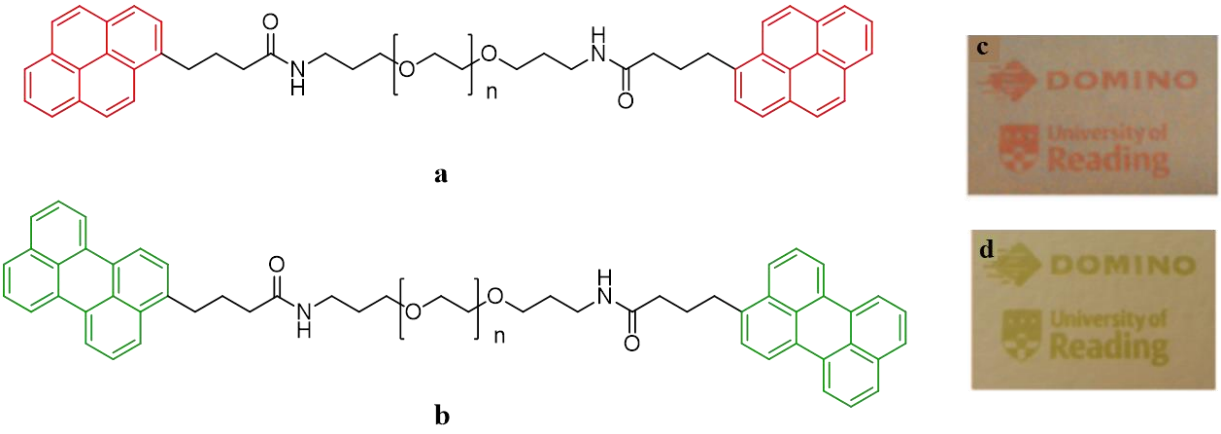

Figure 24- Inkjet deposited images (c and d) produced by Hart *et al.*[157] by the overprinting of a) perylene-capped PEG and b) pyrene-capped PEG with a naphthalene diimide containing π-electron deficient polymer. Figure reproduced with kind permission from reference 157.

1.5 Project Aims

This project was focused towards the design, synthesis and characterisation of novel, functional polymeric systems for inkjet deposition applications, including supramolecular materials, UV-curable polymers and surface-active hydrophobic polymeric films.

The development of supramolecular polymer systems was to be achieved by the synthesis and investigation of polymers with complementary π-π stacking motifs as self-assembling polymer networks that can be deposited using inkjet printing. The polymers would be low molecular weight (M_n <10,000 g mol^{-1}) to ensure ease of inkjet deposition and contain either π-electron rich or π-electron deficient aromatic moieties.

UV-curable polymer systems were to be synthesised using non-toxic, soluble PEG backbones with photodimerisable end-groups that do not require photoinitiators to form carbon-carbon bonds. The UV-curing process of the materials was to be investigated using spectroscopic techniques as well as physical techniques and finally the materials were to be tested for their suitability as inkjet inks. The effect of dyes on the UV-curing of the polymer would also be investigated to determine its suitability as a UV-curing component for inkjet formulations.

Polymers that exhibit hydrophobic film properties were also to be synthesised and their hydrophobic properties investigated. The molecular weight of the polymers would be controlled to produce materials that are suitable for inkjet deposition and the hydrophobic materials would also be tested for use in a high throughput CIJ printer and their rheological properties under high shear were to be analysed.

1.6 References

1 Smithers, *Inkjet Printing Market Value*, 2019, https://www.smithers.com/en-gb/resources/2018/oct/inkjet-printing-builds-towards-$100-billion-market. [Accessed: 27/09/19].

2 I. M. Hutchings and G. D. Martin, *Inkjet Technology for Digital Fabrication*, John Wiley and Sons Ltd., Chichester, UK, 2013.

3 S. Magdassi, *The Chemistry of Inkjet Inks*, World Scientific Publishing, Singapore, 2010.

4 F. Savart, *Ann. Chim. Phys.*, 1833, **53**, 337–386.

5 J. Plateau, *Experimental and Theoretical Statics of Liquids Subject to Molecular Forces Only* Gauthier-Villars, Paris, 1873, 1–427.

6 Lord Rayleigh, *Proceedings R. Soc. London*, 1879, **5**, 71–98.

7 Lord Rayleigh, *Proc. London Math. Soc.*, 1878, **10**, 4–13.

8 Lord Rayleigh, *Philos. Mag. J. Sci.*, 1892, **34**, 145–154.

9 W. Thomson, *Improvements in Receiving or Recording Instruments for Electric Graphs*, UK Patent 2147, 1867.

10 R. Elmqvist, *Measuring Instrument of the Recording Type*, US Patent 2655443, 1949.

11 R. G. Sweet, *Fluid Droplet Recorder*, US Patent 3,596,275, USA, Siemens, 1971.

12 W. Zapka, *Handbook of Industrial Inkjet Printing*, Wiley VCH, Weinheim, Germany, 2017.

13 J. G. Korvink, P. J. Smith and D. Shin, in *Inkjet-Based Micromanufacturing*, Wiley, Weinheim, 2012.

14 J. S. R. Wheeler, S. W. Reynolds, S. Lancaster, V. S. Romanguera and S. G. Yeates, *Polym. Degrad. Stab.*, 2014, **105**, 116–121.

15 L. R. Hart, Supramolecular Polymer Networks: Novel Healable and Printable Materials, PhD Thesis, University of Reading, 2014.

16 R. Waasdorp, O. van den Heuvel, F. Versluis, B. Hajee and M. K. Ghatkesar, *RSC Adv.*, 2018, **8**, 14765–14774.

17 O. A. Basaran, *AIChE. J.*, 2002, **48**, 1842–1848.

18 P. Calvert, *Chem. Mater.*, 2001, **13**, 3299–3305.

19 G. D. Martin, S. D. Hoath and I. M. Hutchings, *J. Phys. Conf. Ser.*, 2008, **105**, 1–14.

20 Z. Pan, Y. Wang, H. Huang, Z. Ling, Y. Dai and S. Ke, *Ceram. Int.*, 2015, **41**, 12515–12528.

21 A. Pekarovicova, H. Bhide, D. Paul and F. Iii, *J. Coatings Technol.*, 2003, **75**, 65–72.

22 Z. W. Wicks Jr, F. N. Jones, S. P. Pappas and D. A. Wicks, *Organic Coatings: Science and Technology*, John Wiley and Sons, Hoboken, 3rd Edn., 2007.

23 Z. Zołek-Tryznowska and J. Izdebska, *Dyes Pigm.*, 2013, **96**, 602–608.

24 X. J. Tang and L. H. Li, *Inf. Rec. Mater.*, 2009, **10**, 32–36.

25 Y. Zhang, Z. Liu, Y. Cao, R. Li and Y. Jing, *BioResources*, 2015, **10**, 1462–1476.

26 S. Sousa, A. M. de Sousa, B. Reis and A. Ramos, *Mater. Sci. Medzg.*, 2014, **20**, 55–60.

27 DuPont, Industrial Cellulosics, https://www.industrialcellulosics.com/products/ethocel, 2019, [Accessed: 01/10/19].

28 S. Hoath, *Fundamentals of Inkjet Printing: The Science of Inkjet and Droplets*, Wiley, Weinheim, Germany, 2016.

29 D. Xu, V. Sanchez-Romaguera, S. Barbosa, W. Travis, J. De Wit, P. Swan and S. G. Yeates, *J. Mater. Chem.*, 2007, **17**, 4902–4907.

30 J. Merrington, S. G. Yeates, P. Hodge and P. Christian, *J. Mater. Chem.*, 2008, **18**, 182–189.

31 J. S. R. Wheeler and S. G. Yeates, *Polymers in Inkjet Printing*, In:*Fundamentals of Inkjet Printing: The Science of Inkjet and Droplets*, Wiley, Weinheim, Germany, 2016, pp. 117–140.

32 B. J. de Gans, P. C. Duineveld and U. S. Schubert, *Adv. Mater.*, 2004, **16**, 203–213.

33 O. A. Basaran, H. Gao and P. P. Bhat, *Annu. Rev. Fluid Mech.*, 2013, **45**, 85–113.

34 I. Delaby, R. Muller and B. Ernst, *Rheol. Acta*, 1995, **34**, 525–533.

35 B. Derby, *Annu. Rev. Mater. Res.*, 2010, **40**, 395–414.

36 C. Clasen, P. M. Phillips, L. Palangetic and J. Vermant, *AIChE J*, 2012, **58**, 3242–3255.

37 P. G. De Gennes, *J. Chem. Phys.*, 1974, **60**, 5030–5042.

38 R. G. Larson and J. J. Magda, *Macromolecules*, 1989, **22**, 3004–3010.

39 E. J. Hinch, *Colloq. Int. du C.N.R.S. Polym. Lubrif.*, 1974, 233, 241–247.

40 M. J. Miles and A. Keller, *Polymer*, 1980, **21**, 1295–1298.

41 Z. Du, X. Yu and Y. Han, *Chinese Chem. Lett.*, 2018, **29**, 399–404.

42 S. J. Haward, G. H. Mckinley and A. Q. Shen, *Nat. Sci. Rep.*, 2016, **6**, 1–18.

43 Malvern Pananlytical, *Microrheology*, 2019, https://www.malvernpanalytical.com/en/products/measurement-type/microrheology. [Accessed: 08/10/19].

44 B. J. De Gans, E. Kazancioglu, W. Meyer and U. S. Schubert, *Macromol. Rapid Commun.*, 2004, **25**, 292–296.

45 A. S. Johns and C. D. Bain, *ACS Appl. Mater. Interfaces*, 2017, **9**, 22918–22926.

46 S. D. Hoath, O. G. Harlen and I. M. Hutchings, *J. Rheol.*, 2012, **56**, 1109–1127.

47 A. V. Bazilevskii, J. D. Meyer and A. N. Rozhkov, *Fluid Dyn.*, 2005, **40**, 376–392.

48 H. J. Shore and G. M. Harrison, *Phys. Fluids*, 2005, **17**, 331041–331047.

49 E. Tekin, P. J. Smith and U. S. Schubert, *Soft Matter*, 2008, **4**, 703–713.

50 E. I. Haskal, M. Büchel, P. C. Duineveld, A. Sempel and P. van De Weijer, *MRS Bull.*, 2002, 864–869.

51 K. P. Bhuvana, R. J. Bensingh, M. Abdul Kader and S. K. Nayak, *Polym. - Plast. Technol. Eng.*, 2018, **57**, 1784–1800.

52 Y. Yang and J. Bharathan, *Light. Diodes Res. Manuf. Appl. II*, 1998, **72**, 2660–2662.

53 J. Ha, J. Park, J. Ha, D. Kim, S. Chung, C. Lee and Y. Hong, *Org. Electron. Physics, Mater.*

Appl., 2015, **19**, 147–156.

54 P. Wilson, C. Lei, C. Lekakou and J. F. Watts, *Org. Electron. Physics, Mater. Appl.*, 2014, **15**, 2043–2051.

55 R. Xing, T. Ye, Y. Ding, Z. Ding, D. Ma and Y. Han, *Chinese J. Chem.*, 2013, **31**, 1449–1454.

56 F. Ely, C. O. Avellaneda, P. Paredez, V. C. Nogueira, T. E. A. Santos, V. P. Mammana, C. Molina, J. Brug, G. Gibson and L. Zhao, *Synth. Met.*, 2011, **161**, 2129–2134.

57 T. Cheng, Y. Z. Zhang, J. P. Yi, L. Yang, J. D. Zhang, W. Y. Lai and W. Huang, *J. Mater. Chem. A*, 2016, **4**, 13754–13763.

58 H. Sirringhaus, T. Kawase and R. H. Friend, *MRS Bull.*, 2001, **26**, 539–543.

59 C. W. Sele, T. von Werne, R. H. Friend and H. Sirringhaus, *Adv. Mater.*, 2005, **17**, 997–1001.

60 S. Ma, F. Ribeiro, K. Powell, J. Lutian, C. Müller, T. Large and J. Holbery, *ACS Appl. Mater. Interfaces*, 2015, **7**, 21628–21633.

61 G. K. Eleftheriadis, P. K. Monou, N. Bouropoulos and D. G. Fatouros, *Materials*, 2018, **11**, 1–14.

62 L. K. Prasad and H. Smyth, *Drug Dev. Ind. Pharm.*, 2016, **42**, 1019–1031.

63 B. M. Wu, S. W. Borland, R. A. Giordano, L. G. Cima, E. M. Sachs and M. J. Cima, *J. Control. Release*, 1996, **40**, 77–87.

64 B. K. Lee, Y. H. Yun, J. S. Choi, Y. C. Choi, J. D. Kim and Y. W. Cho, *Int. J. Pharm.*, 2012, **427**, 305–310.

65 S. Hauschild, U. Lipprandt, A. Rumplecker, U. Borchert, A. Rank, R. Schubert and S. Förster, *Small*, 2005, **1**, 1177–1180.

66 A. Hirao, K. Sugiyama and H. Yokoyama, *Prog. Polym. Sci.*, 2007, **32**, 1393–1438.

67 H. Y. Park, B. J. Kang, D. Lee and J. H. Oh, *Thin Solid Films*, 2013, **546**, 162–166.

68 S. Banerjee, B. V. Tawade, V. Ladmiral, L. X. Dupuy, M. P. MacDonald and B. Améduri, *Polym. Chem.*, 2017, **8**, 1978–1988.

69 Y. Patil and B. Ameduri, *Prog. Polym. Sci.*, 2013, **38**, 703–739.

70 M. Damaceanu, C. Constantin, A. Nicolescu, M. Bruma, N. Belomoina and R. S. Begunov, *Eur. Polym. J.*, 2014, **50**, 200–213.

71 M. Tamura, R. Chaiwattananone and A. Sekiya, *Polym. J.*, 1992, **24**, 1307–1309.

72 B. Liu, G. Wang, W. E. I. Hu, Y. Jin, C. Chen, Z. Jiang, W. Zhang, Z. Wu and Y. E. N. Wei, *J. Polym. Sci. Part A Polym. Chem.*, 2002, **40**, 3392–3398.

73 A. K. Singh and J. K. Singh, *New J. Chem.*, 2017, **41**, 4618–4628.

74 Z. H. Zhang, H. J. Wang, Y. H. Liang, X. J. Li, L. Q. Ren, Z. Q. Cui and C. Luo, *Sci. Rep.*, 2018, **8**, 1–12.

75 J. Yu, S. Seipel and V. A. Nierstrasz, *J. Mater. Sci.*, 2018, **53**, 13216–13229.

76 L. R. Hart, J. L. Harries, B. W. Greenland, H. M. Colquhoun and W. Hayes, *Polym. Chem.*, 2013, **4**, 4860–4870.

77 S. Burattini, B. W. Greenland, D. Chappell, H. M. Colquhoun and W. Hayes, *Chem. Soc. Rev.*, 2010, **39**, 1973–1985.

78 L. Yang, X. Tan, Z. Wang and X. Zhang, *Chem. Rev.*, 2015, **115**, 7196–7239.

79 X. Yan, F. Wang, B. Zheng and F. Huang, *Chem. Soc. Rev.*, 2012, **41**, 6042–6065.

80 D. Abliz, Y. Duan, L. Steuernagel, L. Xie, D. Li and G. Ziegmann, *Polym. Polym. Compos.*, 2013, **21**, 341–348.

81 R. J. Wojtecki, M. A. Meador and S. J. Rowan, *Nat. Mater.*, 2011, **10**, 14–27.

82 D. Habault, H. Zhang and Y. Zhao, *Chem. Soc. Rev.*, 2013, **42**, 7244–7256.

83 C. Mendes-Felipe, J. Oliveira, I. Etxebarria, J. L. Vilas-Vilela and S. Lanceros-Mendez, *Adv. Mater. Technol.*, 2019, **4**, 1–16.

84 M. Sangermano, A. Chiolerio, G. Marti and P. Martino, *Macromol. Mater. Eng.*, 2013, **298**, 607–611.

85 A. Chiolerio and M. Sangermano, *Mater. Sci. Eng. B Solid-State Mater. Adv. Technol.*, 2012, **177**, 373–380.

86 E. Saleh, P. Woolliams, B. Clarke, A. Gregory, S. Greedy, C. Smartt, R. Wildman, I. Ashcroft, R. Hague, P. Dickens and C. Tuck, *Addit. Manuf.*, 2017, **13**, 143–148.

87 M. Invernizzi, S. Turri, M. Levi and R. Suriano, *Eur. Polym. J.*, 2018, **101**, 169–176.

88 S. R. Trenor, A. R. Shultz, B. J. Love and T. E. Long, *Chem. Rev.*, 2004, **104**, 3059–3077.

89 J.van Damme, O. van den Berg, J. Brancart, L. Vlaminck, C. Huyck, G. van Assche, B. van Mele and F. Du Prez, *Macromolecules*, 2017, **50**, 1930–1938.

90 Y. K. Song, K. H. Lee, W. S. Hong, S. Y. Cho, H. C. Yu and C. M. Chung, *J. Mater. Chem.*, 2012, **22**, 1380–1386.

91 Y. Zheng, M. Micic, S. V. Mello, M. Mabrouki, F. M. Andreopoulos, V. Konka, S. M. Pham and R. M. Leblanc, *Macromolecules*, 2002, **35**, 5228–5234.

92 L. López-Vilanova, I. Martínez, T. Corrales and F. Catalina, *Eur. Polym. J.*, 2014, **56**, 69–76.

93 X. A. Trinh, J. Fukuda, Y. Adachi, H. Nakanishi, T. Norisuye and Q. Tran-Cong-Miyata, *Macromolecules*, 2007, **40**, 5566–5574.

94 X. Zhang, Y. Gao, Y. Lin, J. Hu and Y. Ju, *Polym. Chem.*, 2015, **6**, 4162–4166.

95 J. T. Goldbach, T. P. Russell and J. Penelle, *Macromolecules*, 2002, **35**, 4271–4276.

96 S. Paul, W. Knoll and K. Mullen, *Acta Polym.*, 1994, **45**, 235–243.

97 J. F. Xu, Y. Z. Chen, L. Z. Wu, C. H. Tung and Q. Z. Yang, *Org. Lett.*, 2013, **15**, 6148–6151.

98 M. Coursan, J. P. Desvergne and A. Deffieux, *Macromol. Chem. Phys.*, 1996, **197**, 1599–1608.

99 P. Froimowicz, H. Frey and K. Landfester, *Macromol. Rapid Commun.*, 2011, **32**, 468–473.

100 L. A. Connal, R. Vestberg, C. J. Hawker and G. G. Qiao, *Adv. Funct. Mater.*, 2008, **18**, 3315–3322.

101 L. Kan, H. Cheng, B. Li, X. Zhang, Q. Wang, H. Wei and N. Ma, *New J. Chem.*, 2019, **43**, 2658–2664.

102 Y. Chen and C. Jean, *J. Appl. Polym. Sci.*, 1996, **64**, 1759–1768.

103 Y. Chen and J. L. Geh, *Polymer*, 1996, **37**, 4473–4480.

104 E. Sato, S. Nagai and A. Matsumoto, *Prog. Org. Coatings*, 2013, **76**, 1747–1751.

105 P. O. Jackson, M. O'Neill, L. W. Duffy, P. Hindmarsh, S. M. Kelly and G. J. Owen, *Chem. Mater.*, 2001, **13**, 694–703.

106 R. H. Huyck, S. R. Trenor, B. J. Love and T. E. Long, *J. Macromol. Sci. Part A Pure Appl. Chem.*, 2008, **45**, 9–15.

107 Y. Chujo, K. Sada and T. Saegusa, *Macromolecules*, 1990, **23**, 2693–2697.

108 Y. Chen and C. Chou, *J. Polym. Sci. Part A Polym. Chem.*, 1995, **33**, 2705–2714.

109 Y. Chen and K. H. Chen, *J. Polym. Sci. Part A Polym. Chem.*, 1997, **35**, 613–624.

110 Y. Chen and J. L. Geh, *Polymer*, 1996, **37**, 4481–4486.

111 D. Gindre, K. Iliopoulos, O. Krupka, M. Evrard, E. Champigny and M. Sallé, *Molecules*, 2016, **21**, 1–13.

112 L. M. Minsk, J. G. Smith, W. P. van Deusen and J. F. Wright, *J. Appl. Polym. Sci.*, 1959, **11**, 302–307.

113 P. Gupta, S. R. Trenor, T. E. Long and G. L. Wilkes, *Macromolecules*, 2004, **37**, 9211–9218.

114 J. M. Rochette and V. S. Ashby, *Macromolecules*, 2013, **46**, 2134–2140.

115 A. C. Fonseca, M. S. Lima, A. F. Sousa, A. J. Silvestre, J. F. J. Coelho and A. C. Serra, *Polym. Chem.*, 2019, **10**, 1696–1723.

116 X. Hu, X. Chen, H. Cheng and X. Jing, *J. Polym. Sci. Part A Polym. Chem.*, 2009, **47**, 161–169.

117 H.-D. Becker, *Chem. Rev*, 1993, **93**, 145–172.

118 G. W. Breton and X. Vang, *J. Chem. Educ.*, 1998, **75**, 81–82.

119 H. Bouas-Laurent, A. Castellan, J. P. Desvergne and R. Lapouyade, *Chem. Soc. Rev.*, 2001, **30**, 248–263.

120 J. M. Lehn, *Angew. Chem. Int. Ed. Engl.*, 1990, **29**, 1304–1319.

121 Y. Li, Y. Lai, X. Xu, X. Zhang, Y. Wu, C. Hu and Z. Gu, *Nanomedicine Nanotechnology, Biol. Med.*, 2016, **12**, 355–364.

122 C. Cheng, F. Chang, W. Kao, S. Hwang and L. Liao, *Acta Biomater.*, 2016, **33**, 194–202.

123 S. Ho, J. P. K. Tan, F. Nederberg, K. Fukushima, J. Colson, C. Yang, A. Nelson, Y. Yang and J. L. Hedrick, *Biomaterials*, 2010, **31**, 8063–8071.

124 Q. Zhang, L. Zhang, P. Wang and S. Du, *J. Pharm. Sci.*, 2014, **103**, 643–651.

125 X. Dang, C. Hu, H. Chen, J. Huang and D. Zheng, *Sensors Actuators B. Chem.*, 2016, **228**, 709–715.

126 F. Ahmed, K. Shah, I. Zubair and M. Raza, *Ecotoxicol. Environ. Saf.*, 2016, **129**, 103–108.

127 H. M. Chawla, P. Goel and P. Munjal, *Tetrahedron Lett.*, 2015, **56**, 682–685.

128 S. Li, G. Yin, X. Wu, C. Liu and J. Luo, *Electrochim. Acta*, 2016, **188**, 294–300.

129 L. M. De Espinosa, G. L. Fiore, C. Weder, E. J. Foster and Y. C. Simon, *Prog. Polym. Sci.*, 2015, **49**–**50**, 60–78.

130 S. Burattini, H. M. Colquhoun, J. D. Fox, D. Friedmann, B. W. Greenland, P. J. F. Harris, W. Hayes, M. E. Mackay and S. J. Rowan, *Chem. Commun.*, 2009, 6717–6719.

131 E. B. Murphy and F. Wudl, *Prog. Polym. Sci.*, 2010, **35**, 223–251.

132 P. D. Beer, P. A. Gale and D. K. Smith, *Supramolecular Chemistry*, Oxford University Press, Oxford, 1999.

133 J. W. Steed, *Core Concepts in Supramolecular Chemistry and Nanochemistry*, John Wiley and Sons Ltd., Chichester, 1st edn., 2007.

134 J. Steed and J. L. Atwood, *Supramolecular Chemistry*, John Wiley and Sons Ltd., Chichester, 2nd edn., 2009.

135 D. Cross, X. Jiang, W. Ji, W. Han and C. Wang, *Macromol. Biosci.*, 2015, **15**, 668–681.

136 R. M. Parker, J. Zhang, Y. Zheng, R. J. Coulston, C. A. Smith, A. R. Salmon, Z. Yu, O. A. Scherman and C. Abell, *Adv. Funct. Mater.*, 2015, **25**, 4091–4100.

137 S. Limem, D. McCallum, G. G. Wallace, M. Panhuis and P. Calvert, *Soft Matter*, 2011, **7**, 3818–3826.

138 S. Limem, D. Li, S. Iyengar and P. Calvert, *J. Macromol. Sci. Part A Pure Appl. Chem.*, 2009, **46**, 1205–1212.

139 A. Harada, *Supramolecular Polymer Chemistry*, John Wiley and Sons, Weinhein, Germany, 2012.

140 H. Q. Peng, C. L. Sun, L. Y. Niu, Y. Z. Chen, L. Z. Wu, C. H. Tung and Q. Z. Yang, *Adv. Funct. Mater.*, 2016, **26**, 5483–5489.

141 C. Zhang, X. Wen, N. R. Vyavahare and T. Boland, *Biomaterials*, 2008, **29**, 3781–3791.

142 K. E. Riley and P. Hobza, *Acc. Chem. Res.*, 2013, **46**, 927–936.

143 C. R. Martinez and B. L. Iverson, *Chem. Sci.*, 2012, **3**, 2191–2201.

144 S. K. Burley and G. A. Petsko, *Science*, 1985, **229**, 23–28.

145 G. B. McGaughey, M. Gagné and A. K. Rappé, *J. Biol. Chem.*, 1998, **273**, 15458–15463.

146 C. A. Hunter, *Chem. Soc. Rev.*, 1994, 101–109.

147 C. A. Hunter and J. K. M. Sanders, *J. Am. Chem. Soc.*, 1990, **112**, 5525–5534.

148 B. W. Greenland, S. Burattini, W. Hayes and H. M. Colquhoun, *Tetrahedron*, 2008, **64**, 8346–8354.

149 L. R. Hart, N. A. Nguyen, J. L. Harries, M. E. Mackay, H. M. Colquhoun and W. Hayes, *Polymer*, 2015, **69**, 293–300.

150 H. M. Colquhoun, Z. Zhu, C. J. Cardin, Y. Gan and M. G. B. Drew, *J. Am. Chem. Soc.*, 2007, **129**, 16163–16174.

151 P. M. Alvey, J. J. Reczek, V. Lynch and B. L. Iverson, *J. Org. Chem.*, 2010, **75**, 7682–7690.

152 R. S. Lokey and B. L. Iverson, *Nature*, 1995, **375**, 303–305.

153 Z. Zhu, C. J. Cardin, Y. Yan and H. Colquhoun, *Nat. Chem.*, 2010, **2**, 653–660.

154 B. W. Greenland, M. B. Bird, S. Burattini, R. Cramer, R. K. O'Reilly, J. P. Patterson, W. Hayes, C. J. Cardin and H. M. Colquhoun, *Chem. Commun.*, 2013, **49**, 454–456.

155 M. R. Molla and S. Ghosh, *Chem. A. Eur. J.*, 2012, **18**, 9860–9869.

156 L. R. Hart, J. L. Harries, B. W. Greenland, H. M. Colquhoun and W. Hayes, *Polym. Chem.*, 2015, **6**, 7342–7352.

157 L. R. Hart, J. L. Harries, B. W. Greenland, H. M. Colquhoun and W. Hayes, *ACS Appl. Mater. Interfaces*, 2015, **7**, 8906–8914.

158 S. Burattini, B. W. Greenland, D. H. Merino, W. Weng, J. Seppala, H. M. Colquhoun, W. Hayes, M. E. MacKay, I. W. Hamley and S. J. Rowan, *J. Am. Chem. Soc.*, 2010, **132**, 12051–12058.

159 M. S. Cubberley and B. L. Iverson, *J. Am. Chem. Soc.*, 2001, **123**, 7560–7563.

160 J. Q. Nguyen and B. L. Iverson, *J. Am. Chem. Soc.*, 1999, **121**, 2639–2640.

161 P. M. Alvey, R. J. Ono, C. W. Bielawski and B. L. Iverson, *Macromolecules*, 2013, **46**, 718–726.

162 L. Adler-Abromovich and E. Gazit, *J. Pept. Sci.*, 2008, **14**, 217–223.

163 L. R. Hart, S. Li, C. Sturgess, R. Wildman, J. R. Jones and W. Hayes, *ACS Appl. Mater. Interfaces*, 2016, **8**, 3115–3122.

164 L. R. Hart, J. L. Harries, A. Clifton, H. M. Colquhoun and W. Hayes, *Inkjet Composition*, W02014111722A1, UK, Domino Printing Sciences PLC, University of Reading, 2014.

Chapter 2

Anthracene-Capped PEG as a Supramolecular Polymer for Inkjet Printing

Abstract

In this chapter the synthesis of a novel bis-anthryl poly(ethylene glycol) (M_n = 1995 g mol^{-1}) as a π-electron donor for complementary π-π-stacking polymers is described. Binding studies between anthracene and the π-electron deficient naphthalene diimide (NDI) units were performed using model compounds to reveal a binding constant (K_a = 4 M^{-1}) that was much smaller than those of the analogous pyrene and perylene derivatives (K_a = 50 and 227 M^{-1}, respectively). Despite the interaction between the two stacking moieties observed by ^{1}H NMR spectroscopy, solutions containing the naphthalene diimide tweezer and anthracene did not produce a charge transfer colour, which was not surprising considering the weak binding constant observed between the two compounds.

In parallel, analogous poly(ethylene glycol) (PEG) polymers containing NDI or anthracene units within the polymer architecture were synthesised, characterised, and their π-stacking interaction investigated. ^{1}H NMR spectroscopy of the blend of the two polymers revealed a small change in chemical shift of both anthracene (0.03 ppm) and NDI (0.02 ppm) proton resonances, indicating a weak interaction between the two π-stacking moieties. UV-vis spectroscopic analysis also revealed the absence of a charge transfer complex in the polymer derivatives as a result of a combination of (i) the weak binding constant between the π-motifs and (ii) the natural tendency of the polymer chains to favour the unbound, mobile state. The inkjet printability of the polymers was also investigated, and both polymers were readily formulated as 100 mg mL^{-1} solutions in THF:hexanediol and deposited successfully using a Dimatix™ drop-on-demand printhead to produce clear, sharp images.

2.1 Introduction

Polymeric materials produced through covalent interactions are of great importance across a wide range of fields including drug delivery, prosthetic limbs, lightweight composites, surface coatings, injection moulded structures and textiles.[1] However, within the past two decades, great advances have been observed in the field of supramolecular polymer chemistry.[2] This field of chemistry exploits the use of non-covalent bonds to allow the controlled assembly and disassembly of polymeric structures upon application of a stimulus such as temperature, pH, UV or mechanical stress.[3,4] The inclusion of non-covalent supramolecular interactions within polymer networks has yielded dynamic, reversible polymeric networks that can be employed to produce processable, healable materials.[2] Supramolecular interactions between polymer chains include ionic interactions, hydrogen bonding, guest/host interactions and π-π stacking.[1–8]

In the inkjet printing industry, polymeric materials have been employed in formulations for a range of applications including coatings for polymer light-emitting diodes (PLED)s,[9] precise printing of thin film transistors[10] and 3D printing of ceramics using polymer solutions as polymeric binders in powder bed printing.[11]

In order to achieve adhesion, strength, toughness and durability of a printed material, it is preferable to employ high molecular weight, viscous polymers. However, in inkjet printing these characteristics are unfavourable, because high molecular weight polymers can contribute to nozzle blockage in the printhead over time and failure to print.[12] The exploitation of supramolecular polymer chemistries in inkjet formulations has afforded lower molecular weight and viscosity inks, which are better suited to inkjet printing. The polymers employed also maintain a high molecular weight supramolecular network post deposition as a result of non-covalent self-assembly on the substrate.[13–22]

Pataky *et al*. have reported[16] the deposition of alginate polysaccharide solutions (0.8 wt % in deionised water) using a 50 μm microdrop nozzle to produce a hydrogen-bonded hydrogel post deposition, of which the structure can be carefully controlled to produce tissue-like geometries. Highley *et al*. also investigated[17] the inkjet deposition of hydrogel-forming polysaccharides, instead using hyaluronic acids that were modified with adamantane or β-cyclodextrin. The functionalised hyaluronic acid materials, upon interaction on the substrate, formed supramolecular host-guest assemblies to produce a healable hydrogel.[17]

The deposition of a series of metallo-copolymers have also been investigated in the work of Wild *et al*. and Friebe *et al*. as printable, photoluminescent supramolecular polymers aimed towards organic photovoltaic (OPV) and PLED applications.[18,19] Friebe *et al*. reported, in a short communication, the synthesis, printing and photoluminescent properties of bisterpyridines with different central chromophores that formed metallo-copolymers upon complexation with Zn^{II} (Figure 1). The different supramolecular complexes were deposited by inkjet as thin films (150–200 nm) to produce a variety of photoluminescent colours.[19]

Wild *et al*. later reported the production of a series of bisterpyridine-capped polymers that consisted of a central dye unit (bis(thiazole), benzothiadiazole or quinoxaline) surrounded by thiophene donor moieties.[18] These polymers produced extended metallo-copolymers upon complexation of the terpyridine functionalities with Zn^{II}, and produced red, green and blue photoluminescence complexes, which were combined in different ratios to produce an extended colour palette, including a white photoluminescent complex for potential in PLED applications.

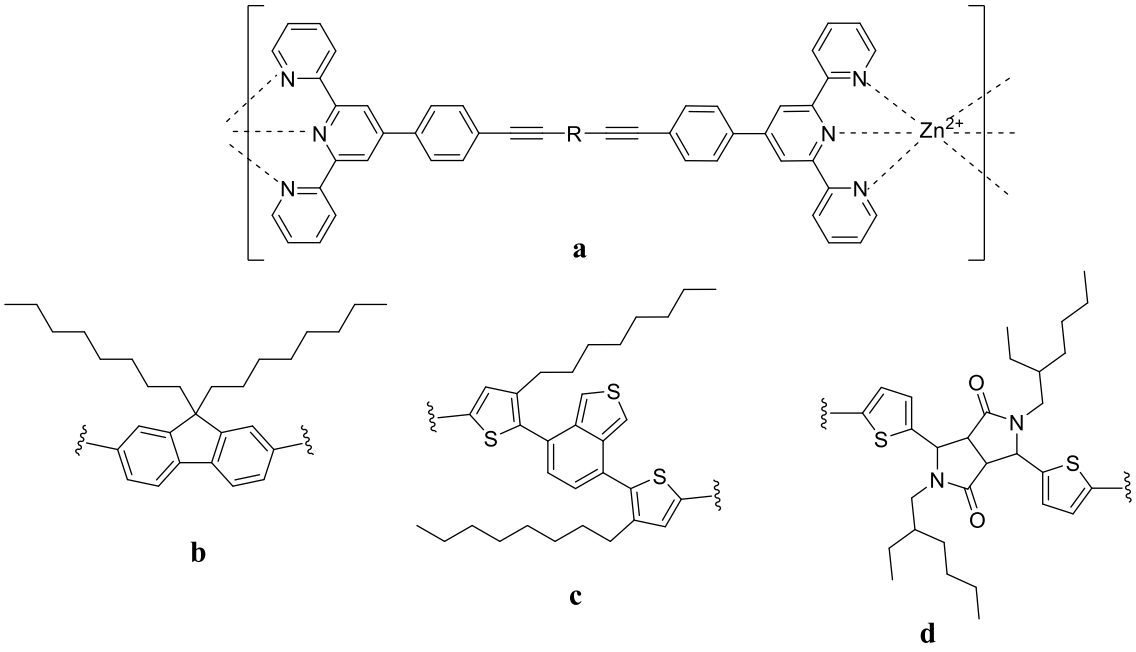

Figure 1- The photoluminsecent metallo-copolymers developed[18,19] by Friebe *et al*. depicting a) the structure of the metallo-copolymer formed with central chromophore R and b-d) the different chromophores (R) investigated.

In more recent work, Hart *et al*. have investigated both 3D and 2D inkjet deposition of supramolecular polymer networks.[13–15,23] The most recent work details the synthesis of a series of biocompatible poly(caprolactone)-derived (M_n > 2000 g mol^{-1}) polymers with ureidopyrimidinone hydrogen bonding motifs and their corresponding silica composite blends. The materials produced were non-toxic and readily deposited using a drop-on-demand printer to produce 3D cubes and a more complex 3D twisted pyramid structure. The suitability of the printable, non-toxic materials to produce more complex structures highlighted the potential application for the materials as supramolecular polymer based scaffolds for regenerative medicine.[14]

Hart *et al*. also reported the deposition of electronically complementary, low molecular weight, functionalised PEGs to produce robust, self-colouring images.[13,15,23] These polymers contained complementary π-electron rich and π-electron deficient groups which self-assembled on the substrate to produce charge transfer interactions between the naphthalene diimide unit in the π-electron deficient polymer and the pyrenyl and perylenyl moieties of the constituent π-electron rich polymers.[13,15,23]

The π-electron rich materials produced in this work produced two of the three colours (red and green) in the red, green, blue (RGB) colour set for inkjet inks (Figure 2). Alteration of the π-electron rich end-capping group resulted in a change in the colour of the final blend, and it was suggested that the employment of anthracene as a π-electron rich end-capping group would produce a blue charge transfer complex.[13]

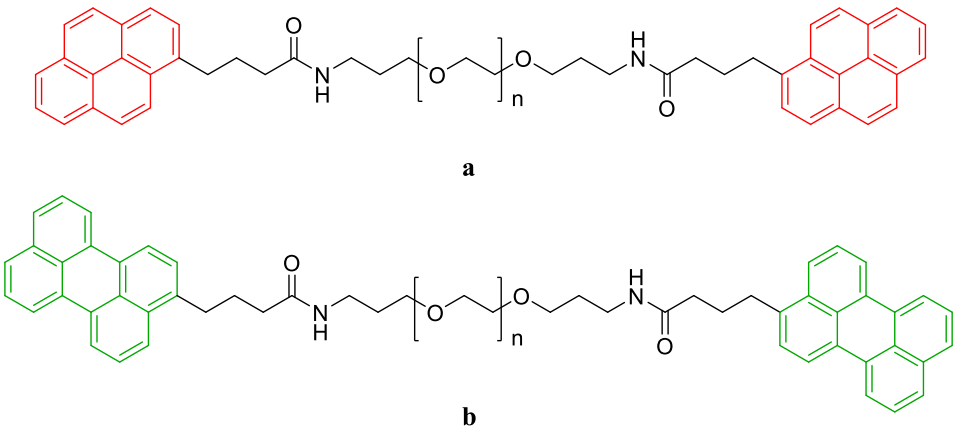

Figure 2- The π-electron rich polymers used in the work of Hart *et al.* showing a) the pyrene-capped PEG and b) the perylene-capped PEG.[13]

The synthesis of an electronically complementary polymer blend that produced a blue charge transfer complex would complete the RGB colour set, providing access to an entire colour palette of inks, without the requirement for dyes or pigments. It was suggested that anthracene end-groups would produce a blue charge transfer complex with naphthalene diimide moieties.

In this chapter, the analogous anthracene-capped π-electron rich polymer has been synthesised, its interaction with the π-electron deficient chainfolding naphthalene polydiimide has been analysed, and the suitability of both polymers towards inkjet printing investigated.

2.2 Results and Discussion

2.2.1 Computational Modelling of Anthracene as a Potential π-electron Donor

Naphthalene diimide compounds are known to form tweezer-like structures upon complexation with π-electron rich compounds such as pyrene.[23–25] A computational modelling study (charge-compensated molecular mechanics, using custom version of the Dreiding II force field, Cerius 3.5, Accelrys Inc.) of a simplified NDI tweezer **1** and 9-anthracene butyl amide **2** was undertaken to predict the π-stacking interaction of anthracenyl compounds with naphthalene diimide units. The computational modelling indicated partial overlap of the host **1** and guest **2**, with two of the anthracenyl aromatic rings situated between the aromatic segments of the NDI tweezer.

The modelling suggested that ~66% of the aromatic region (equivalent to ~2 aromatic rings) in the anthracenyl compound **2** would be located between the two naphthalene diimide units of **1**, and that the complex would exhibit a 1:1 (host:guest) arrangement (Figure 3(c)).

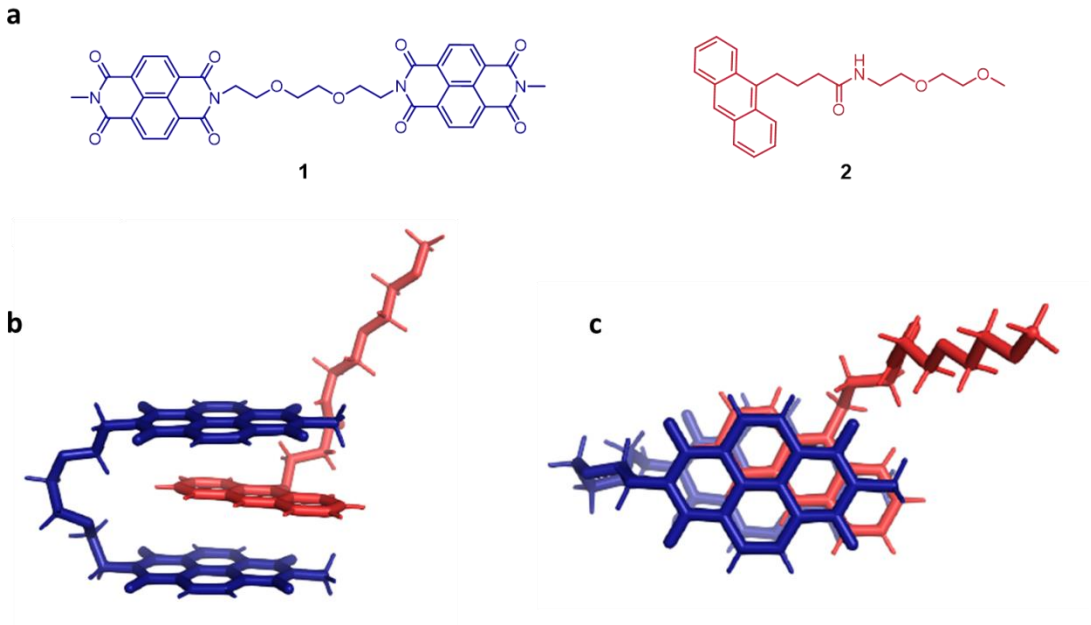

Figure 3- (a) The structure of theoretical π-electron deficient **1** (blue) and π-electron rich **2** (red) model compounds. (b) The energy minimised model of 'tweezer' complexation between the NDI tweezer (blue) and anthracene (red) and (c) a top-down view of the complex showing partial overlap of the aromatic systems.

Computational results reported previously[23,26] for the analogous perylene and pyrene complexes formed with the NDI tweezer, showed a similar stacking interaction with 1:1 stoichiometry. However, in the case of perylene, ~60% of the total aromatic system (equivalent to ~3 aromatic rings) was situated between the NDI moieties and ~75% of the aromatic rings of pyrene (equivalent to ~3 aromatic rings) were located between the NDI moieties. In the model complex formed between NDI tweezer **1** and 9-anthracene butyl amide **2**, it was predicted that only 2 aromatic rings of the π-electron rich moiety would be situated within the tweezer units. This result could indicate a weaker π-stacking interaction between anthracene compounds *cf.* pyrene and perylene as a result of the availability of fewer π-orbitals to contribute to π-π*-orbital overlapping and the subsequent formation of a charge-transfer complex.

2.2.2 Synthesis of a π-electron Deficient Tweezer as a Model Compound

Previous studies within the Colquhoun and Hayes research groups have exploited the use of a naphthalene diimide tweezer (NDIT) compound **3** to investigate the π-π-stacking interaction with different aromatic compounds, such as pyrene and perylene.[23,24] In this study, the NDIT **3** was synthesised and employed as a model π-electron deficient unit to investigate the donor acceptor π-π-stacking interaction of **3** with anthracene. The synthesis of **3** was achieved in this study using a two-step approach reported by Greenland *et al.*[24] The first step entailed the pH controlled (pH 6.3) mono-substitution of 1,4,5,8-naphthalene tetracarboxylic acid **4** with 2-ethylhexylamine **5** to produce

ethylhexylimide diacid **6** in moderate yield (62%). Diacid **6** was then combined with 2,2'-ethylenedioxybis(ethylamine) **7** and heated at 135 °C to produce tweezer complex **3** (Scheme 1).

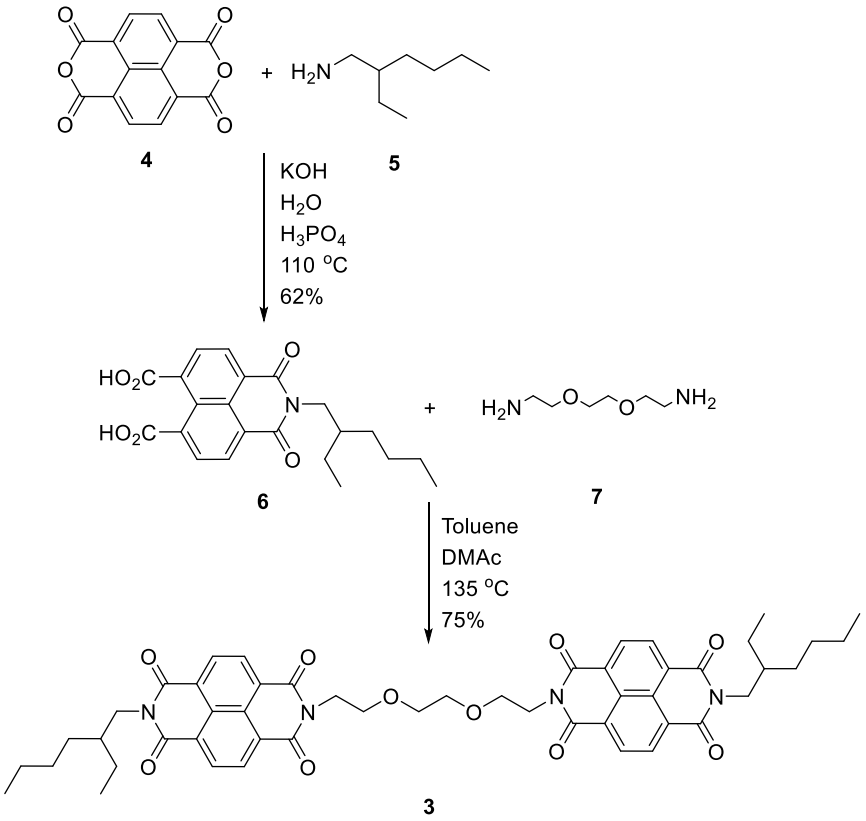

Scheme 1- The synthetic route used to obtain naphthalene imide diacid **6** by the pH controlled reaction between naphthalene tetracarboxylic acid **4** and 2-ethylhexylamine **5** followed by the subsequent reaction of **6** with 2,2'-ethylenedioxybisethylamine **7** to produce naphthalene diimide tweezer **3**.

2.2.3 Binding Constant Studies Using ^{1}H NMR Spectroscopy

The supramolecular π-stacking interaction between the π-electron rich guest [G] (e.g. anthracene) and π-electron deficient host [H] (e.g. NDIT) moieties can be analysed to calculate an association constant (K_a) for the supramolecular complex [HG] formed (Equation 1).[27,28]

$$K_a = \frac{[HG]}{[H][G]} \qquad \text{(Equation 1)}$$

The association constant is related to the kinetics of the particular system, and therefore $K_a = k_1/k_{-1}$ where k_1 is the 'on' (complexed) rate and k_{-1} is the 'off' (non-complexed) rate. [HG] and [H][G] cannot be measured directly, but titration experiments can be used to indirectly determine the concentration of [HG] that can then be used to calculate a binding constant using data analysis software, such as Bindfit.[29]

To begin to assess the π-stacking interactions between π-electron rich anthracene **8** and π-electron deficient NDIT **3**, a titration experiment was performed using ^{1}H NMR spectroscopy to determine the binding ratio of the host guest complex. The titration was performed using a total compound concentration of 3.0×10^{-3} M, with ^{1}H NMR spectra collected from 100% NDIT **3** to 100% anthracene **8** altering the ratio of **3** and **8** in increments of 10%. The ^{1}H NMR titration spectra revealed that increasing the concentration of anthracene resulted in a small upfield shift of the NDIT resonance originating at 8.71 ppm. A similar trend was observed with the anthracene resonances (8.43, 8.01 and 7.46 ppm), which also revealed a small upfield shift upon increasing the concentration of NDIT **3** (Figure 4).

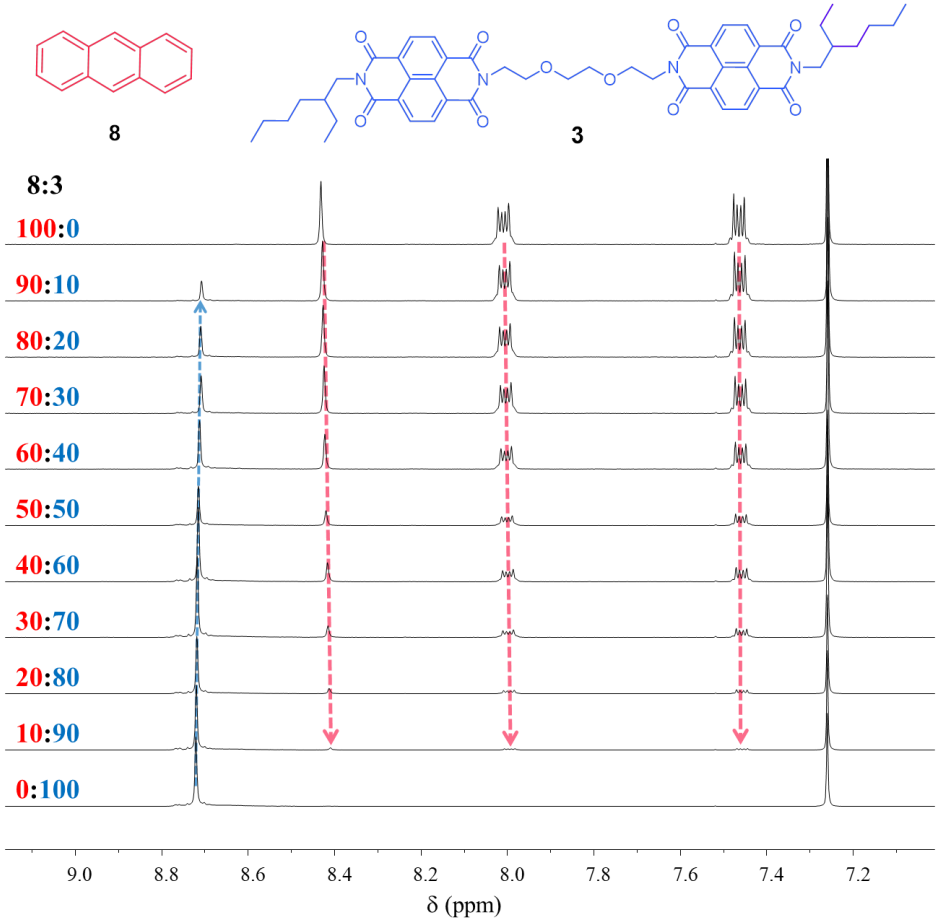

Figure 4- Stacked ^{1}H NMR spectroscopic titration of 3×10^{-3} M concentrations of naphthalene diimide tweezer **3** (blue) and anthracene **8** (red) in $CDCl_3$ revealing a minor upfield complexation shift for both sets of resonances (8.71 and 8.43 ppm).

Overall shifts of 0.01 and 0.02 ppm of the chemical shifts upon complexation were observed, for the NDIT **3** (8.71 ppm) and anthracene **8** (8.43ppm) resonances, respectively, indicating minor interaction between the aromatic units, as predicted by the molecular modelling studies (see Section 2.2.1). The observed changes in the chemical shift values of these key proton resonances upon complexation of the NDIT and anthracene are drastically smaller than the complexation shifts of the naphthalene

diimide resonance observed in the presence of pyrene and perylene which, in previous studies,[23] were determined to be 0.2 ppm (20 times larger) and 0.5 ppm (50 times larger), respectively, at the same overall solution concentration of 3×10^{-3} M.

The upfield shift of the naphthalene diimide resonance was plotted against the increasing concentration of the π-electron rich guest, anthracene, to produce a Job plot.[30] The Job plot reveals the favoured stacking ratio between the host **3** and guest **8**, and in the case of anthracene revealed an equimolar stacking ratio for π-electron deficient and π-electron rich moieties, with the Job plot peaking at 0.5 molar fractions (or 1 molar equivalent of the two compounds). The data was in accordance with the π-stacking ratio determined in previous studies for perylene and pyrene which also demonstrated a 1:1 host-guest stoichiometry (Figure 5).

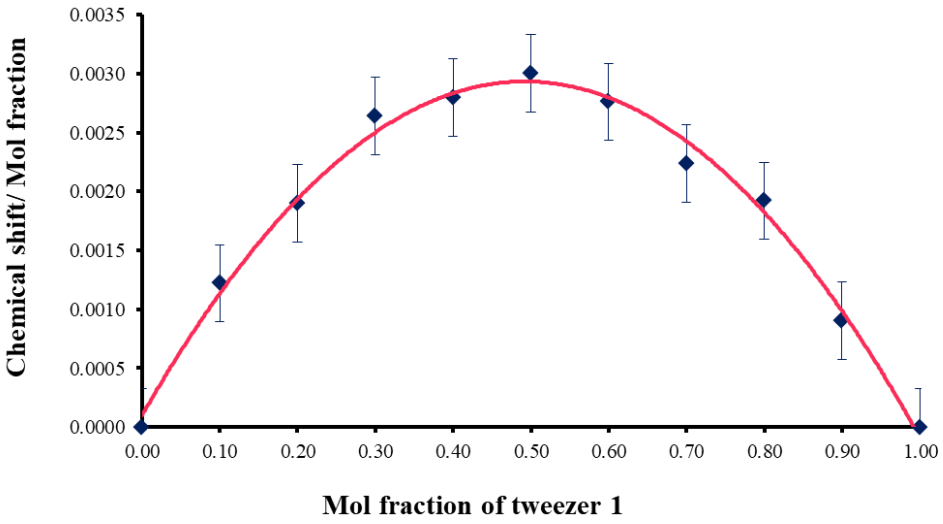

Figure 5- The Job plot produced from the ^{1}H NMR titration results, showing the binding between NDIT **3** and anthracene **8**, with a Job plot peak at 0.5 mol fraction, indicating that the binding between **3** and **8** is equimolar (1:1) with respect to binding motifs.

Once the binding ratio had been confirmed, the binding association constant, K_a, for the 1:1 naphthalene diimide tweezer and anthracene complex could be determined. Firstly, ^{1}H NMR spectroscopy was used to analyse the host-guest π-stacking interaction between the two compounds. The analysis was performed by the preparation of several samples containing a set concentration (7.5×10^{-3} M) of the host compound **3**, but increasing molar equivalents of the guest compound **8** and the ^{1}H NMR spectra of the mixed solutions were then recorded. The study revealed an upfield complexation shift of the naphthalene diimide resonance, and splitting of the resonance with the introduction of increasing equivalents of anthracene (i.e. 2 equivalents and above). Despite the change in chemical shift observed for the tweezer complex **3**, it was noted that the chemical shift values of the

resonances attributed to the anthracene moiety **8** did not change, despite the addition of up to four equivalents of the guest when compared to the concentration of the tweezer host **3** (Figure 6).

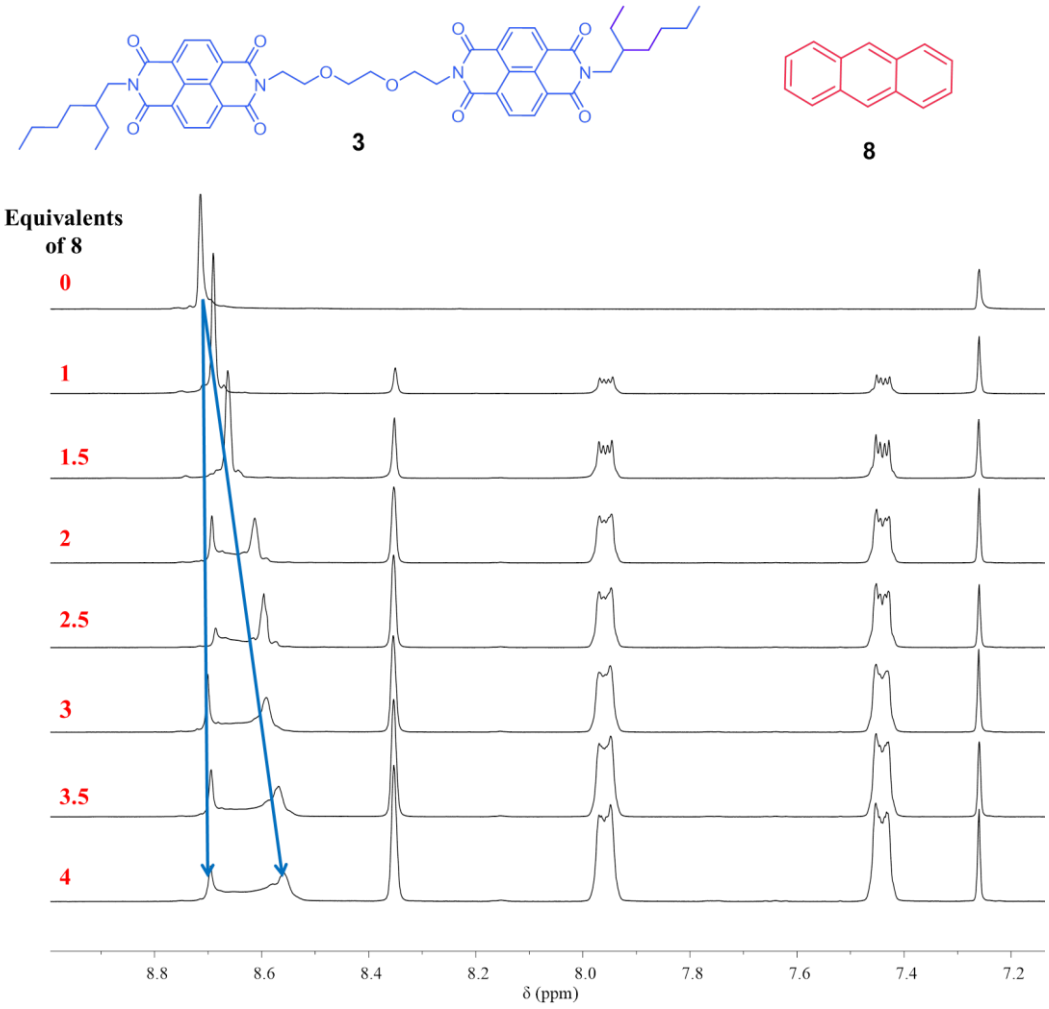

Figure 6- Stacked ^{1}H NMR spectroscopic analysis of host-guest interaction between NDIT **3** and anthracene **8**. The spectroscopic analysis was performed in $CDCl_3$ at 25 °C adding increasing molar equivalents of anthracene to a constant concentration of tweezer **3** (7.5×10^{-3} M).

The change in the chemical shift of the NDIT **3** resonance with increasing concentration of anthracene was utilised to calculate a binding constant for the π-stacking complex using the online binding constant calculation technique BindFit.[27,29] The binding calculator produced a binding fit using the experimental data, to reveal that the 1:1 host-guest complex demonstrated a very weak binding constant of only K_a = 4 M^{-1} (±6% error).[31] The binding constant calculated was 12.5 times (K_a = 50 M^{-1}) and 57 times (K_a = 227 M^{-1}) weaker when compared to the complexes formed by pyrene and perylene, respectively, and correlates with the weak interaction between π-complexes observed in the titration studies (see Figure 4).[23]

The weak interaction between the π-electron rich and π-electron deficient moieties was also indicated by the absence of a coloured charge-transfer complex in solution (Figure 7); the analogous pyrene and perylene complexation solutions were red and green, respectively.[23,32]

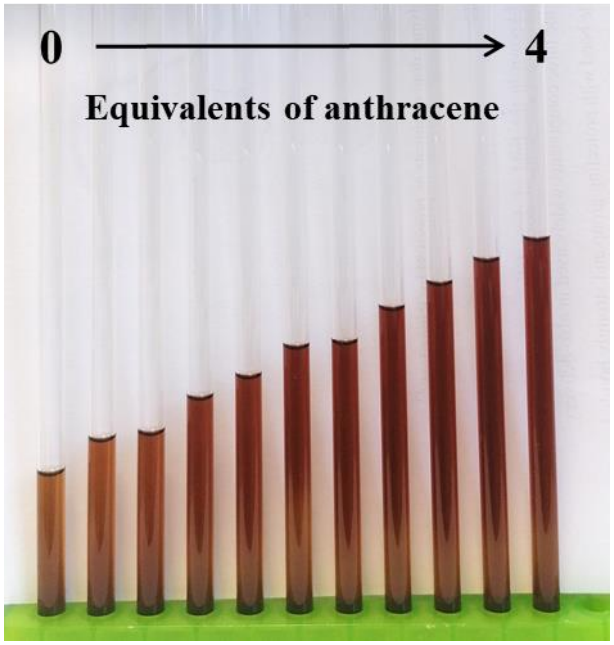

Figure 7- ^{1}H NMR spectroscopy samples of naphthalene diimide tweezer **3** (7.5×10^{-3} M) and anthracene **8** (in increasing molar equivalents from 0–4) revealed minimal charge transfer colour in solution ($CDCl_3$).

The absence of a charge transfer colour is likely to be the result of the small binding constant observed for anthracene, which can be attributed to the decrease in the total surface area of the π-electron rich aromatic system within the π-electron deficient NDI moieties, when compared to pyrene and perylene (see Figure 3). The decreased area of π-electron density of anthracene *cf*. pyrene and perylene can also lead to faster on/off (k_1/k_{-1}) rates of complexation, which alongside the weak binding interaction can result in the formation of a weaker complex between **3** and **8**.

2.2.4 Synthesis of Chain-folding Naphthalene Diimide Polymer 9

In parallel to the binding studies, efforts were also focused on the development of analogous polymeric components for use in the formulation and deposition studies of new inkjet inks featuring anthracene-naphthalene diimide complexes. Poly(ethylene glycol) (PEG) was selected as the polymer backbone for both the host and guest polymer inkjet inks because of its good solubility in common organic solvents, such THF and MEK, rendering it a suitable material for inkjet deposition. PEG is also non-toxic, meaning that its application as a polymer backbone for self-assembling polymeric inks for the coding and marking of food packaging would pose minimal risk to human health.

A π-electron deficient polymer **9** consisting of a PEG backbone and naphthalene diimide units linked with a short ethylenedioxy spacer unit was synthesised following the protocol reported[32] by Hart *et al.*

to produce a polymeric version of the naphthalene diimide tweezer **1** (see Scheme 1). Polymer **9** was synthesised by a condensation polymerisation reaction between 1,4,5,8-naphthalene tetracarboxylic dianhydride **4**, ethylenedioxybisethylamine **7** and bis(3-aminopropyl) terminated PEG **10** to produce a dark brown solid in good yield (69%) (Scheme 2). The chainfolding polymer demonstrated number and weight average molecular weights M_n = 6,700 g mol^{-1}, M_w = 12,500 g mol^{-1}, respectively, and a polydispersity $Đ$ = 1.87. The glass transition and melting temperature of the dark brown material were confirmed by differential scanning calorimetry to be T_g = 145 °C and T_m = 36 °C, in good agreement with the previously reported literature.[15,32]

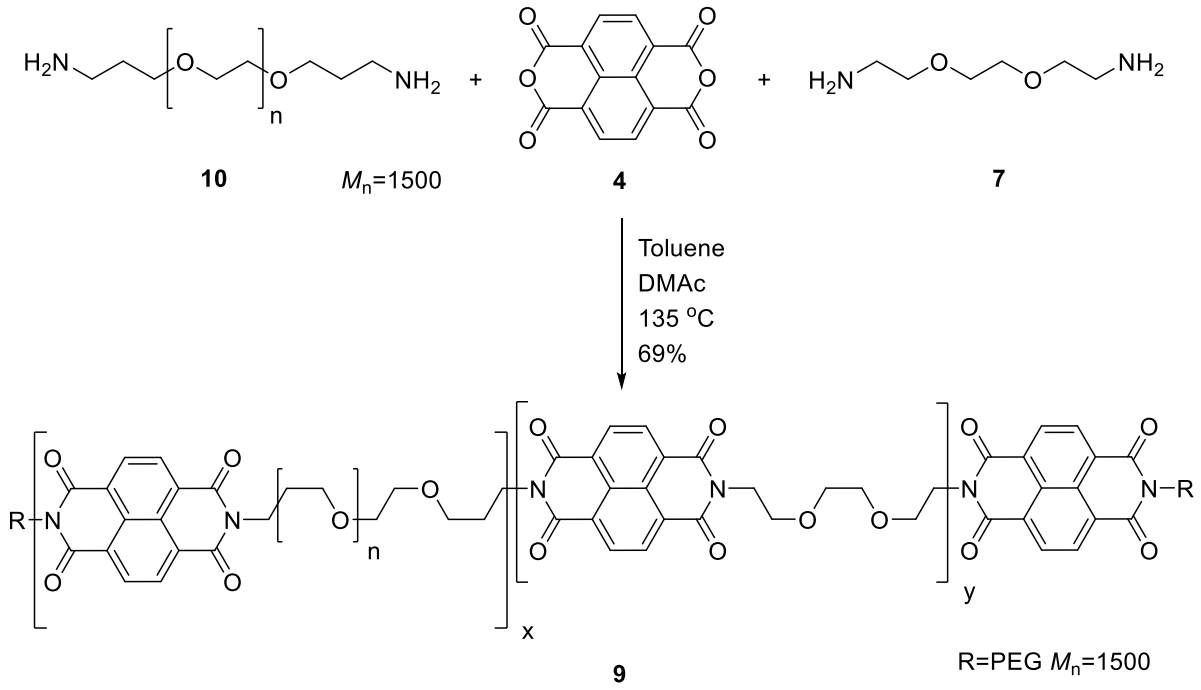

Scheme 2- The synthetic route used to produce chainfolding naphthalene diimide polymer **9**. The synthesis involves the random polycondensation of 1,4,5,8-naphthalenetetracarboxylic acid **4** and amine terminated compounds **7** and **9**.[13,15]

The formation of imide groups in the synthesis of polymer **9** was evident in the IR spectrum, which revealed a (C=O) stretch at 1705 cm^{-1} that was attributed to the carbonyl groups of the imide functionalities. ^{1}H NMR spectroscopic analysis of chainfolding NDI polymer **9** also revealed the successful formation of imide units from 1,4,5,8-naphthalenetetracarboxylic dianhydride **4** and the amine-terminated linker groups **7** and **9**, with the presence of methylene proton resonances at 4.40–4.35 ppm that were attributed to the methylene groups bonded to the imide nitrogen. Naphthalene diimide proton resonances at 8.85–8.60 ppm were also observed, alongside proton resonances at 4.00–3.39 ppm that were attributed to the methylene protons of the ethylene glycol residues (Figure 8).

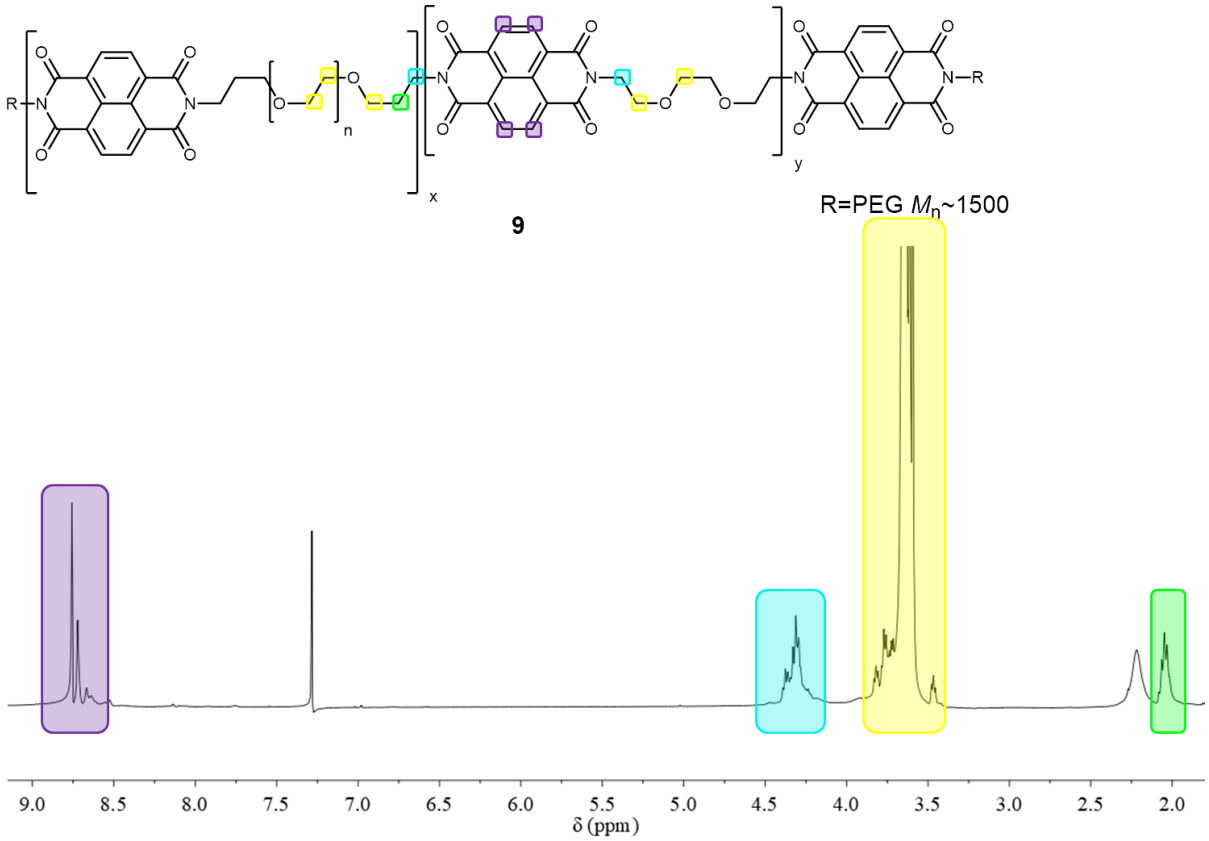

Figure 8-^{1}H NMR spectroscopic analysis of chainfolding naphthalene diimide polymer **9**, highlighting the proton resonances of the methylene groups adjacent to the imide (shown in blue), the methylene protons adjacent to those previously described in the PEG linker (shown in green), the ethylene glycol proton resonances (shown in yellow) and the proton resonances attributed to the naphthalene diimide protons (shown in purple).

2.2.5 Synthesis of π-electron Rich Anthracenyl Polymer 16

In order to synthesise an anthracene end-capped PEG that was structurally analogous to the perylene and pyrene derivatives described by Hart *et al.*,[15,23,32] it was first necessary to synthesise an anthracene end group with an alkyl spacer and an acid functionality. The synthesis of 9-anthracene pentanoic acid **11** was achieved using a three-step procedure adapted from a protocol described by Esteban *et al.*[33] Firstly, methyl-4-pentenoate ester **12** was produced by the esterification of 4-pentenoic acid **13**. Secondly, a Suzuki-Miyaura palladium cross-coupling between methyl-4-pentenoate ester **12** and 9-bromoanthracene **14** was performed to produce the 9-anthracene methyl ester **15** in an isolated yield of 68%. The subsequent hydrolysis of the 9-anthracene methyl ester **15** using KOH/EtOH, followed by acidification, produced 9-anthracene pentanoic acid **11** as the targeted polymer end-group (Scheme 3).

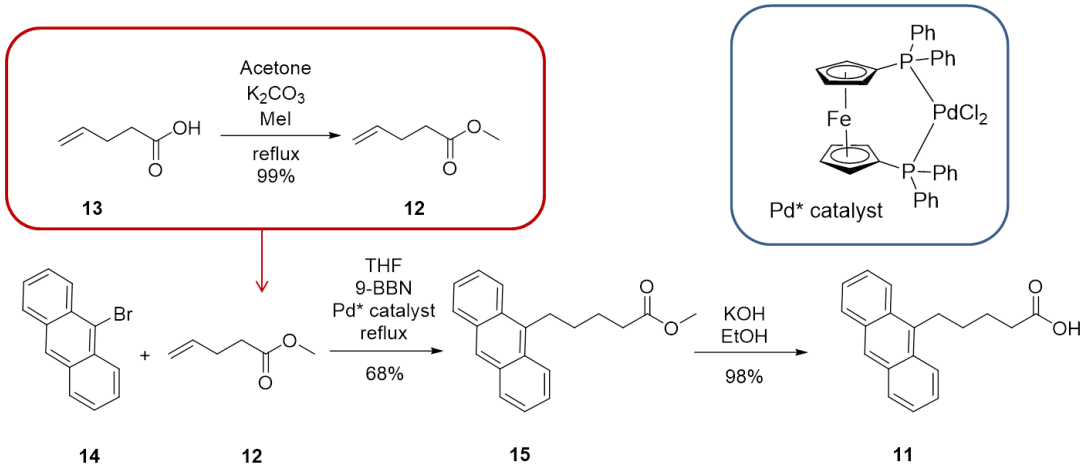

Scheme 3- The synthetic routes used to obtain 9-anthracene pentanoic acid **11** for use as a polymer end group. The synthesis of precursor 9-anthracene methyl ester **15** was achieved via a Suzuki-Miyaura palladium cross-coupling using [1,1'-bis(diphenylphosphino)ferrocene]dichloropalladium(II)] (shown in the blue box) as the catalyst.

The formation of the carbon–carbon bond between the 9-bromoanthracene **14** and the 4-methyl pentenoate ester **12** was confirmed by ^{1}H-^{13}C heteronuclear multiple bond correlation (HMBC) spectroscopy. Multiple bond correlation was observed between three of the quaternary carbons (shown in pink and yellow (Figure 9) of anthracene and the methylene proton resonance of the pentanoate alkyl chain.

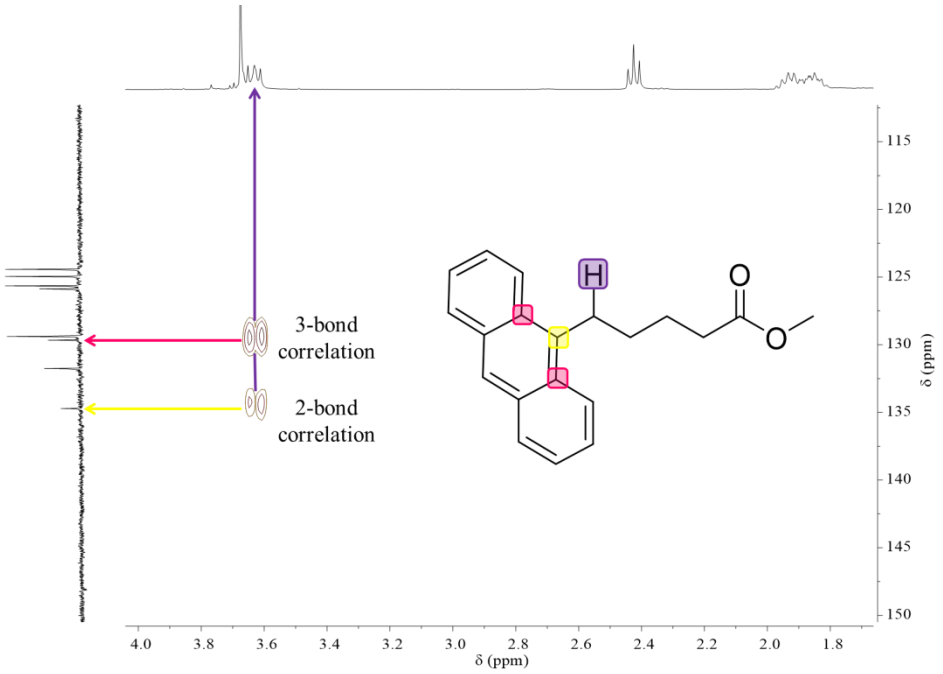

Figure 9- ^{1}H-^{13}C heteronuclear multiple bond correlation spectroscopic analysis of 9-anthracene pentenoate ester **15**, showing the correlation between anthracenyl quaternary carbons (shown in pink and yellow) and the adjacent methylene proton (shown in purple) nuclei, indicating the formation of a carbon–carbon bond in the reaction between 9-bromoanthracene **14** and 4-methyl pentenoate ester **12**.

Following the synthesis and purification of 9-anthracene pentenoate ester **15** the material was converted to the carboxylic acid derivative by saponification of the ester, using a solution of KOH in ethanol, followed by protonation using acid, to produce 9-anthracene pentanoic acid **11** in excellent yield (98%). The conversion of the ester functionality in **15** to an acid derivative in **11** was evident from the changes observed in the carbonyl IR-absorption frequencies, which showed a shift from 1737 cm^{-1} to 1715 cm^{-1} for **15** and **11**, respectively. The hydrolysis of the methyl group was further confirmed using ^{1}H NMR spectroscopy, which revealed the absence of the characteristic methyl ester resonance at 3.69 ppm in the spectrum of the carboxylic acid derivative **11** (Figure 10).

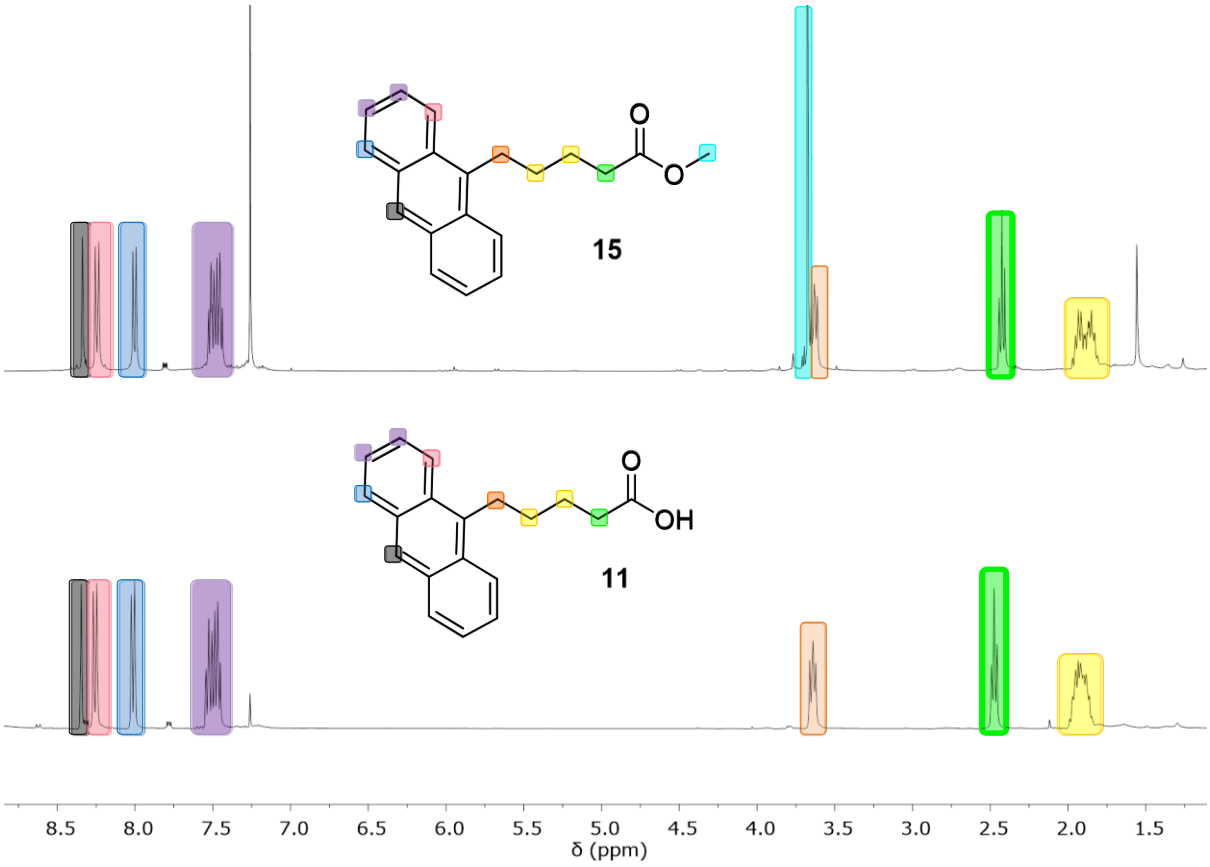

Figure 10- Stacked ^{1}H NMR spectra of compounds **10** and **13** indicating the absence of the methyl proton resonance at 3.68 ppm following hydrolysis of the methyl ester.

In a similar approach to the synthesis of pyrene and perylene capped PEGs developed by Hart *et al.*[23,32] the 9-anthracene pentanoic acid **11** produced was coupled to bis(3-aminopropyl) terminated PEG **9** via dicyclohexylcarbodiimide (DCC)-mediated coupling to yield bis-anthryl polymer **16** (Scheme 4).

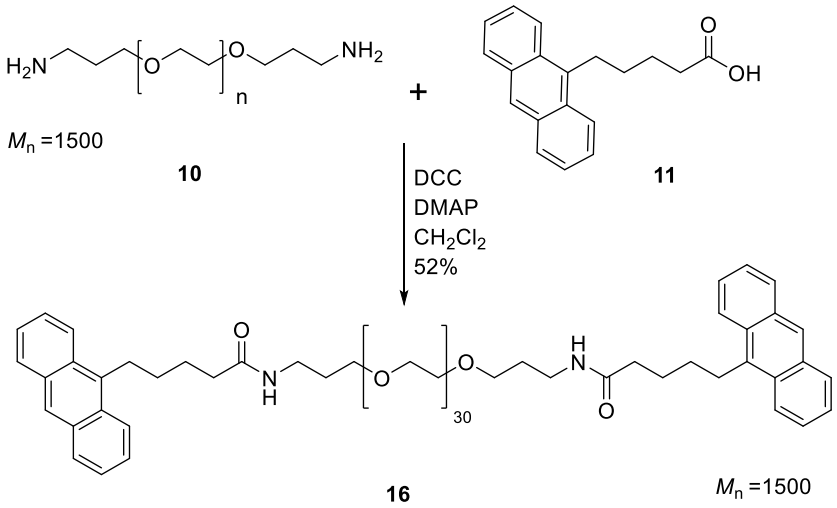

Scheme 4- Synthesis of bis-anthryl PEG **16** via the DCC-mediated coupling of bis(3-amino propyl)-terminated PEG **10** and 9-anthracene pentanoic acid **11**.

The DCC coupling proceeded more slowly than for the analogous pyrene and perylene derivatives synthesised by Hart *et al.*[23,32] with a total reaction time of 120 hours required to produce a light brown, waxy solid with a glass transition temperature and crystalline melting temperature at T_g = 31 °C and T_m = 47 °C, respectively. The synthesis of polymer **16** was further confirmed by ^{1}H NMR spectroscopic analysis, which showed a novel amide proton resonance at 6.25 ppm as well as the absence of the characteristic PEG methylene resonance at 2.80 ppm attributed to the methylene groups adjacent to the terminal amine groups (Figure 11).

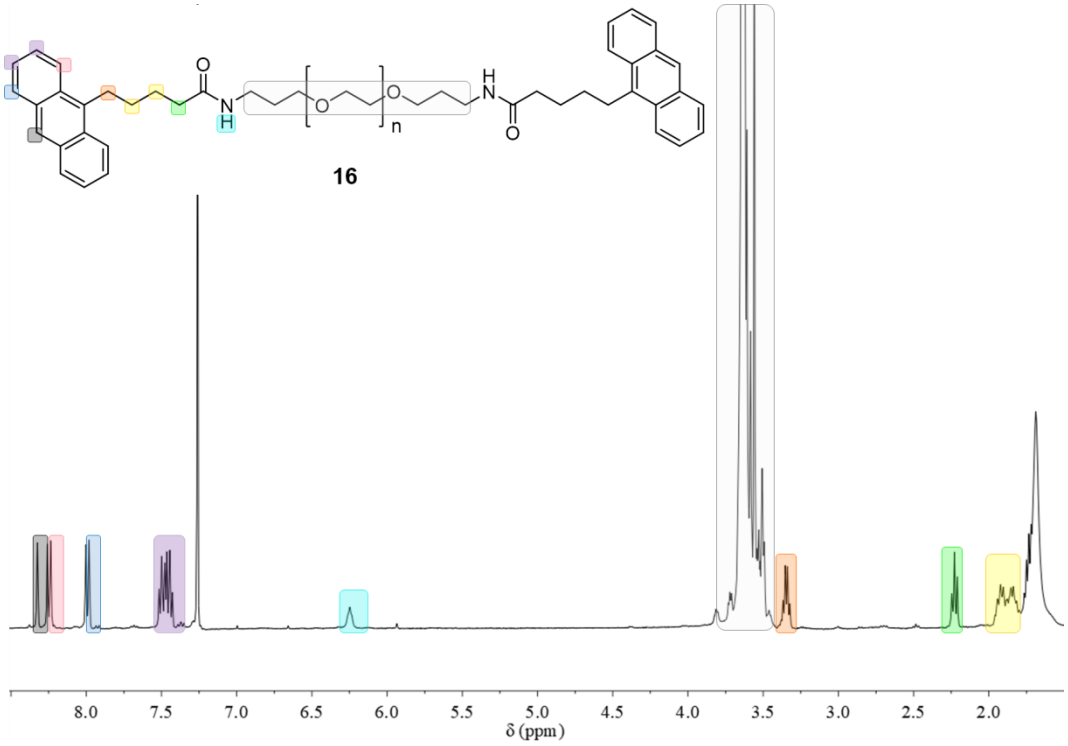

Figure 11- ^{1}H NMR spectroscopic analysis of polymer **16**, revealing a novel amide resonance at 6.25 ppm and the disappearance of the characteristic methylene resonance (2.80 ppm) of the starting PEG **10**.

The formation of an amide bond was also evident in IR spectroscopic analysis, with the presence of an absorbance band at 3325 cm^{-1} attributed to the N–H amide stretch and a shift in the absorption band of the carbonyl group *cf*. the 9-anthracene pentanoic acid (1715 cm^{-1}) to 1677 cm^{-1} upon conversion to an amide.

MALDI-TOF mass spectroscopic analysis of **16** was performed, revealing a highest-abundance mass ion at 1995.93 Da which corresponded to the sodiated species $[C_{104}H_{168}N_2O_{33}Na]^+$ which has an expected mass ion of 1996.14 Da. The MALDI-TOF mass spectrum demonstrated spacing of 44 Da, which corresponds to one ethylene glycol repeat unit (Figure 12).

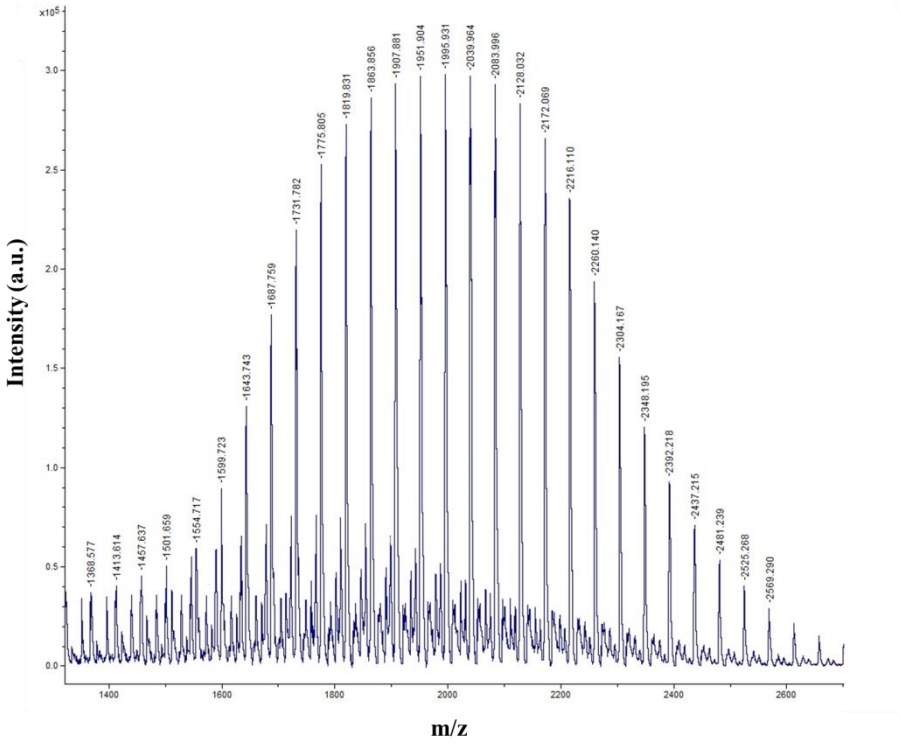

Figure 12- MALDI-TOF mass spectroscopic analysis of bis-anthryl polymer **16** revealing a mass ion at 1995.93 Da with a spacing of 44 Da, equal to that of one ethylene glycol unit. The mass ion is attributed to the sodiated species of bis-anthryl PEG with 30 repeat ethylene glycol units. MALDI-TOF samples were prepared in a DHB matrix at a concentration of 0.25 mg mL^{-1}.

2.2.6 Solution Complexation Studies of π-donor and π-acceptor Polymers

In order to investigate the supramolecular interactions between the π-electron deficient polymer **9** and the π-electron rich polymer **16**, equimolar solutions of the two individual polymers and the polymer blend (**9**+**16**) were combined and analysed using ^{1}H NMR spectroscopy. The samples were prepared in deuterated chloroform at concentrations of 3×10^{-3} M, as in the previous studies,[23,32] to allow direct

comparison of the results. Both the naphthalene diimide chainfolding polymer **9** and bis-anthryl polymer **16** proton resonances exhibited small upfield shifts (0.02 and 0.03 ppm, respectively) upon complexation (Figure 13) as expected following the initial complexation studies performed between the naphthalene diimide tweezer complex **3** and anthracene **8** (see Figure 4).

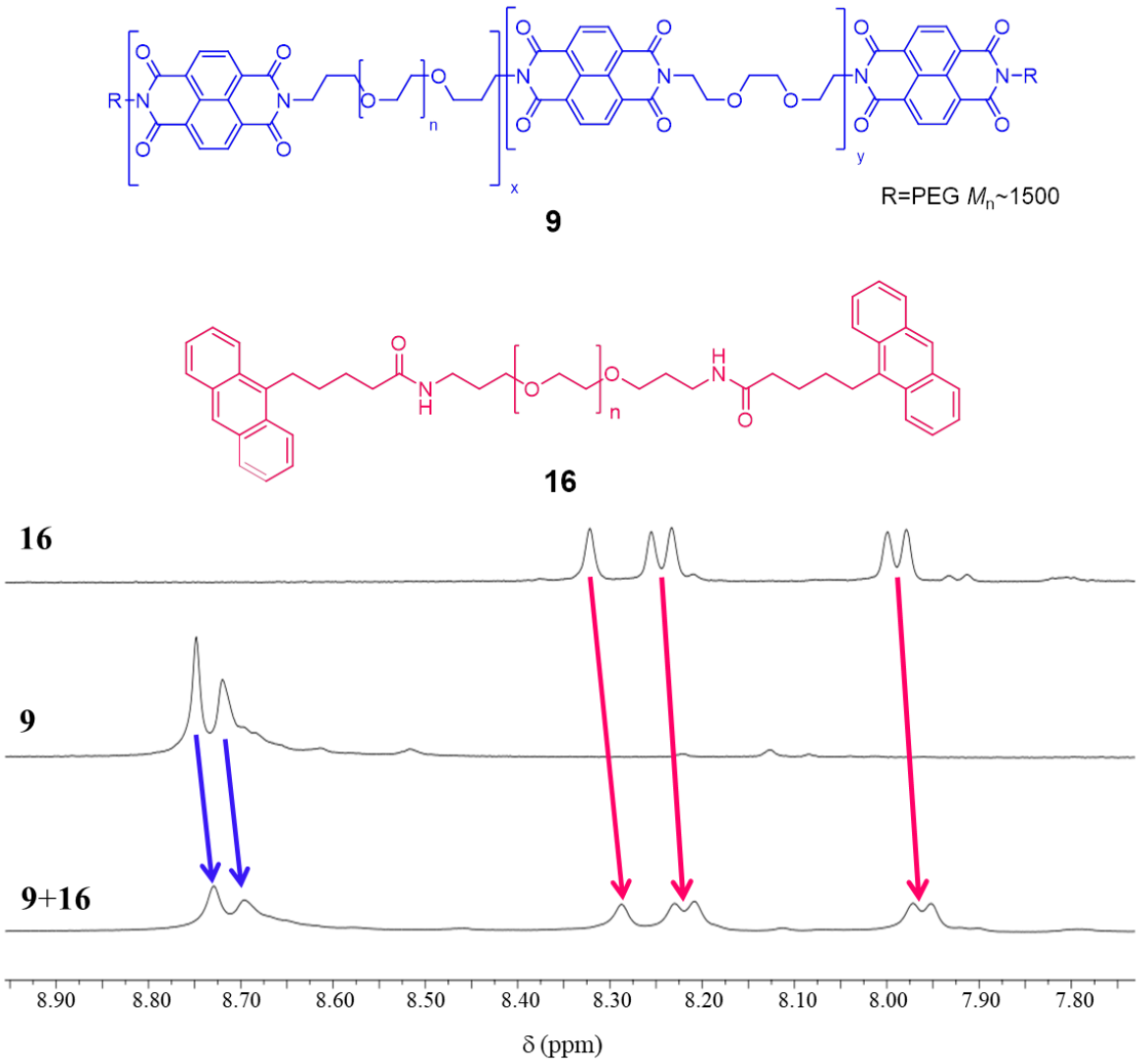

Figure 13- ^{1}H NMR spectroscopic analysis of the polymeric blend (**9**+**16**) of the π-electron deficient polymer **9** and the π-electron rich polymer **16** revealing small upfield complexation shifts for both polymers **9** and **16**.

The bis-anthryl polymer **16** was colourless in solution and the chainfolding naphthalene diimide polymer **9** was pale brown in colour. The blend of bis-anthryl polymer **16** and NDI polymer **9** was also very pale brown in colour and showed no indication of a charge-transfer complex. However, fluorescence quenching was observed in the blend which confirmed that the two polymer systems were interacting with one another to form a weak supramolecular polymer network (Figure 14).

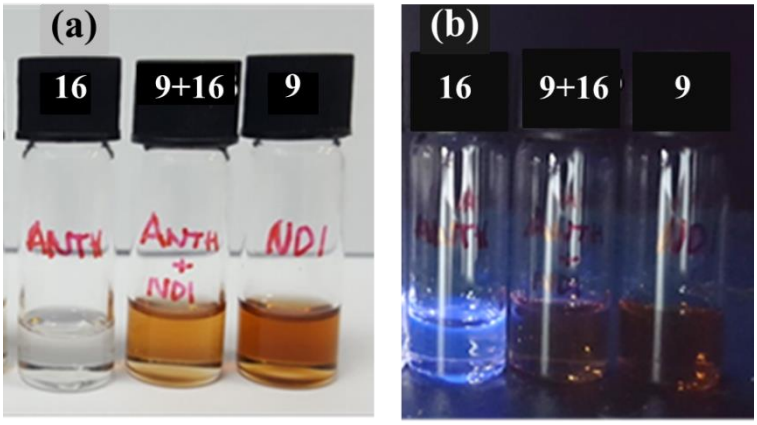

Figure 14- Solutions of polymers **9** and **16** and their subsequent blend under (a) visible light, showing the pale brown solution formed upon blending the polymers (**9**+**16**) and (b) UV light (254 nm) showing the fluorescence quenching of the blend (**9**+**16**) when compared to the bis-anthryl polymer **16**.

The absence of a charge-transfer absorption was further confirmed using UV-vis spectroscopy, in which the visible region of the spectrum can be analysed for potential charge-transfer absorptions (400–800 nm). The blend did not show an absorption band in the visible region of the spectrum, thus confirming the visual observation of an absence of charge-transfer between the two polymers (**9**+**16**) (Figure 15).

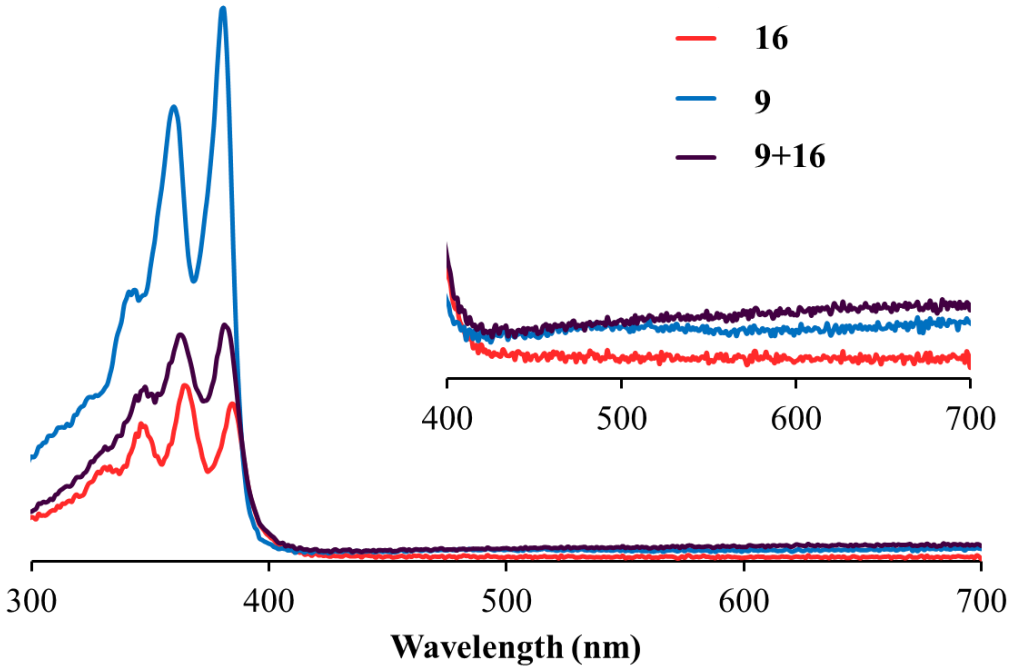

Figure 15- UV-vis spectroscopic analysis of solutions (3×10^{-3} M) of π-electron deficient polymer **9**, π-electron rich polymer **16** and the subsequent blend (**9**+**16**), which does not reveal a charge-transfer absorption band.

The lack of charge-transfer absorption was not surprising, as the model compound studies exhibited a similar trend with no obvious charge transfer colour (see Figure 7) and a low binding constant of $K_a = 4\ M^{-1}$ calculated using Bindfit. The low binding constant was predicted, to some extent, by the computational modelling, which indicated the presence of only two of three aromatic rings of anthracene situated between the NDI units of the tweezer.

Upon including the π-electron donor and acceptor groups within a polymer structure, further constraints need to be overcome in order for the π-stacking motifs to self-assemble. With the inclusion of polymer chains to a π-stacking system, the enthalpic energy of the π-stacking interactions needs to overcome the entropic energy of the polymer chains to naturally adopt a free (unbound) state in solution.[34] The experimental data obtained for the complexation studies between polymers **9** and **16** indicated that unlike the pyrene and perylene derivatives of **16**, the π-stacking interaction did not provide significant enthalpic energy in order to overcome the entropic effects of the polymer chains in solution. Only minimal interaction between the motifs was evident as observed from ^{1}H NMR spectroscopic analysis and no charge-transfer absorption bands were observed in UV-vis spectroscopy.

2.2.7 Drop-on-Demand Inkjet Deposition of Polymeric Materials

Despite the lack of π-stacking interactions observed between polymers **9** and **16** it was decided to investigate the printability of the novel and soluble bis-anthryl polymer and the NDI polymer. Before the materials were deposited using a drop-on-demand printer, the viscosities of the polymer solutions were investigated to ensure that they fell within the correct range for successful inkjet deposition. The formulation properties required depend on the type of inkjet printhead to which they will be subjected.[35] The viscosity range for the Dimatix™ drop-on demand printhead used at Domino Printing Sciences lies between 2–12 cP.[36] If the formulation viscosity exceeds these parameters it can inhibit the ink from leaving the nozzle, resulting in nozzle blockage. On the other hand, a very low viscosity formulation is likely to drip from the nozzle, resulting in uncontrolled deposition of droplets and spoilage of the substrate. Formulations of polymers **9** and **16** were prepared at a concentration of 100 mg mL^{-1} in a mixture of THF and 1,2-hexanediol (1:1 v/v). The viscosities of both of the polymer formulations fell within a suitable range for inkjet deposition using the Fujifilm Dimatix™ printhead, with the chainfolding naphthalene diimide polymer **9** possessing a much higher viscosity (9.1 cP) than the bis-anthryl polymer **16** (3.6 cP).

Deposition of the polymers was carried out using a Fujifilm Dimatix™ Materials Printer DMP-2800 equipped with a piezoelectric drop-on-demand printhead. Both polymers (**9**+**16**) were prepared as inkjet formulations (100 mg mL^{-1}) using THF:1,2-hexanediol (1:1 v/v) as the carrier solvent to provide a direct comparison with the results from the previous studies by Hart *et al.*, which demonstrated the successful deposition of pyrene- and perylene-appended polymers.[23,32] The formulations were passed

through a PTFE membrane-filter (0.45 µm) before loading into Dimatix™ 11600 series printer cartridges to remove any small particulates which may result in nozzle blockage (Figure 16).

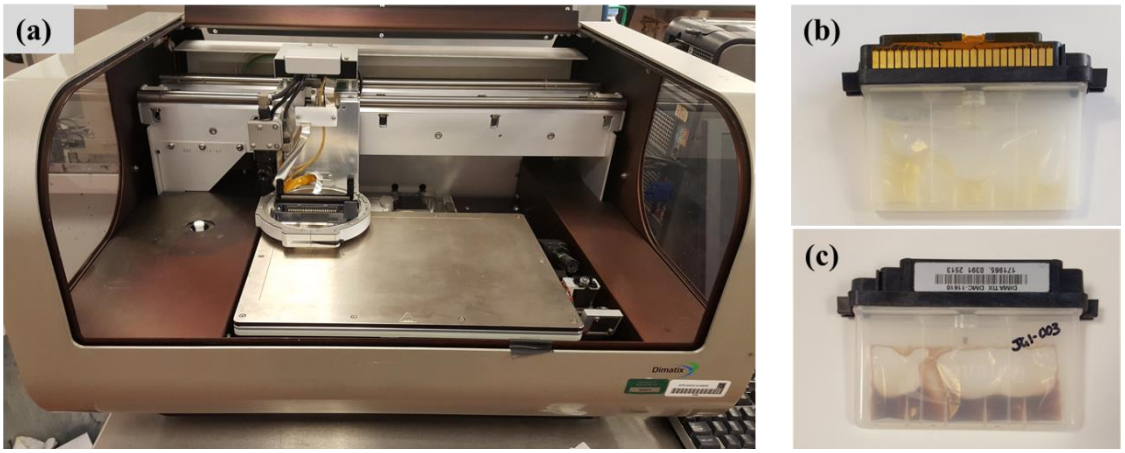

Figure 16- (a) the Fujifilm Dimatix™ DMP 2800 used in these studies, (b) the bis-anthryl polymer **16** and (c) naphthalene diimide polymer **9** formulations in the Dimatix materials cartridges pre-deposition.

The π-electron rich **16** and π-electron deficient **9** polymers were both deposited successfully onto non-optically brightened card. The bis-anthryl polymer **16** was deposited as a colourless printed image, which was barely visible to the naked eye (Figure 17). However, illumination with a standard UV light (254 nm) revealed a sharp fluorescent image, confirming the deposition of the material. The naphthalene diimde polymer **9** was deposited as a pale brown material which did not fluoresce under UV irradiation. The characteristic blue fluorescence of the anthracene moieties in the polymer architecture of **16** was reduced greatly following overprinting of the image with the π-electron deficient polymer **9**, indicating interaction of the aromatic moieties. However, disappointingly, but not unexpectedly, given the data obtained from the solution state blending studies of **9** and **16**, the overprinting of polymeric materials (**16**+**9**) did not produce a coloured image as previously found with the employment of pyrene and perylene as π-electron rich moieties (Figure 17).[15,23,32]

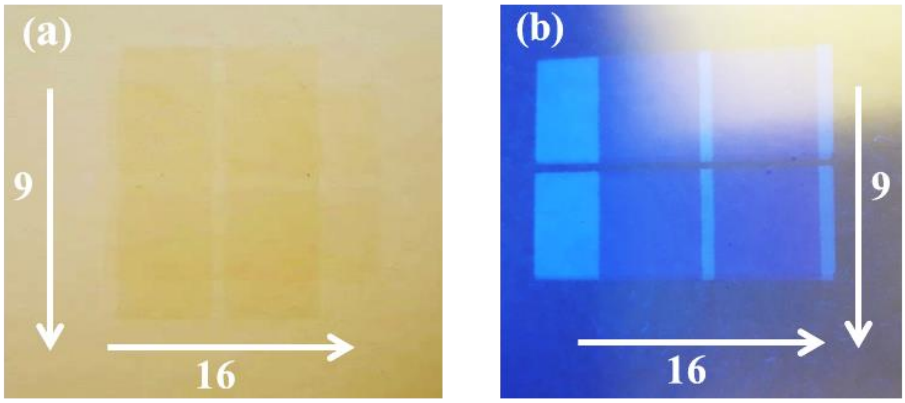

Figure 17- (a) Visible and (b) UV images of overprinting of polymer **16** (horizontal bars) with polymer **9** (vertical bars), resulting in fluorescence quenching under UV light (b) but no charge transfer colour (a).

2.3 Conclusions

A novel anthracene-based π-electron rich polymer has been investigated as a π-electron donor for the formation of supramolecular polymer networks. Initial studies were performed using model compounds to determine the complexation interactions between anthracene and a naphthalene diimide tweezer **3**. ^{1}H NMR spectroscopic analysis of the model compounds revealed that anthracene demonstrated a much smaller complexation shift upon interaction with the naphthalene diiimide moieties in **3** than the analogous pyrene (20 times larger) and perylene (50 times larger) derivatives.[23,26] This observation was further confirmed by the calculation of the association binding constant using Bindfit[29] which demonstrated a weak binding constant of $K_a = 4\ M^{-1}$ (±6%) which was expected as the material failed to show a charge transfer absorption upon interaction of the π-electron rich and deficient materials. The weak binding constant exhibited was attributed to the decrease in surface area of the π-electron density of anthracene that was predicted to be located between the NDI moieties, which resulted in a much weaker interaction than the analogous pyrene and perylene derivatives.

A novel anthracene-terminated polymer **16** was developed by firstly synthesising the anthracene pentanoic acid end-group **11** in order to perform a DCC-mediated coupling with bis (aminopropyl) terminated PEG **10** to produce a soluble, low molecular weight polymer. The binding interactions of the novel anthracene polymer **16** with the naphthalene diimide chainfolding polymer **9** were investigated using ^{1}H NMR spectroscopy, which revealed a small upfield shift of the aromatic resonances for polymer **9** (0.02 ppm) and polymer **16** (0.03 ppm). UV-vis spectroscopy was also carried out on the pale brown blend of polymers **9** and **16** which did not exhibit a charge-transfer absorption band. The lack of charge-transfer between the two polymers was not surprising considering the small binding constant ($4\ M^{-1}$) observed between anthracene and the NDI model compound **3**, but also because of the added complexity of the behaviour of the polymer chains in solution. The small binding constant observed was concluded to be insufficient to overcome the entropic tendency of the polymer chains to remain in the unbound state, resulting in an extremely weak interaction between the two functionalised PEG polymers.

Both of the polymers synthesised in this study were deposited using a piezoelectric drop-on-demand printhead to produce clear, sharp images. The bis-anthryl polymer **16** was deposited to produce a very pale yellow image, which was barely visible to the naked eye, but demonstrated characteristic blue fluorescence of anthracene upon illumination using a UV lamp (245 nm). The chainfolding naphthalene diimide polymer **9** was deposited to produce a pale brown image. The overprinting of polymer **9** onto polymer **16** resulted in fluorescence quenching of the anthracene moieties, but no charge-transfer between the two polymers.

2.4 Experimental

Reagents and solvents were purchased from Sigma Aldrich (Merck) or Alfa Aesar and were used without further purification with the exception of THF, which was dried by distillation from sodium/benzophenone under argon, and dichloromethane and chloroform, which were dried by distillation over calcium hydride under an argon atmosphere. ^{1}H NMR (400 MHz) and ^{13}C NMR (100 MHz) spectra were obtained on a Bruker Nanobay 400 spectrometer using $CDCl_3$ as solvent (unless otherwise stated), with TMS as internal standard. IR spectra of samples were recorded using a Perkin Elmer 100 FT-IR instrument with a diamond-ATR sampling accessory. UV-vis spectrometry was performed on a Varian Cary 300 UV-vis spectrometer in acetonitrile. Gel Permeation chromatography (GPC) was performed using an Agilent Technologies 1260 Infinity series in THF (2 mg mL^{-1}) (HPLC grade) coupled with an RI detector calibrated to PEG. Differential Scanning Calorimetry (DSC) data were recorded using a TA-Q2000 DSC. Mass Spectrometry was performed on a Thermofisher Scientific Orbitrap XL. MALDI-TOF mass spectra of were acquired using a Bruker Micro TOF QII. Samples were prepared by dissolution in acetonitrile (0.5 mg mL^{-1}) and combining with DHB matrix (20 mg mL^{-1}) in a 1:1 ratio v/v. The sample/matrix solution (0.5 μL) was applied to MALDI-TOF plate and solvent evaporated. Dynamic viscosities were measured at 30, 50 and 60 RPM on a Brookfield viscometer LVDV-E230 at 25 °C in MEK. DOD printing was carried out using a Fujifilm Dimatix™ Materials Printer DMP-2800 series using 11600 series Dimatix™ materials cartridges with 16 nozzles in a linear arrangement at 254 μm intervals. Substrates were provided by Domino Printing Sciences Ltd, Bar Hill, Cambridge.

2.4.1 Synthesis of Ethylhexylimide Diacid 6

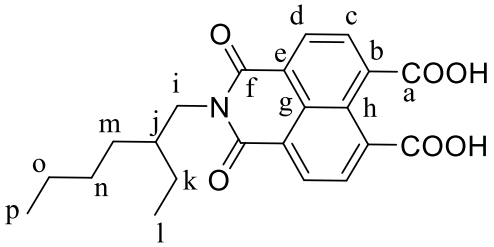

1,4,5,8-Tetracarboxylicdianhydride (2.06 g, 7.70 mmol) was added to a solution of KOH (2.03 g, 36 mmol) in deionised water (350 mL) and stirred for 1 hour. The solution was acidified to pH 6.3 using phosphoric acid, and then stirred for 10 minutes. 2-Ethyl-1-hexylamine (1.45 mL, 8.85 mmol) was then added and the solution re-acidified to pH 6.3 using phosphoric acid. The solution was heated at reflux for 18 hours and then cooled to room temperature. Acetic acid (5 mL) was then added to form a creamy-brown precipitate and the solid was collected by vacuum filtration. The resulting solid was dried at 50 °C *in vacuo* to produce a creamy peach solid (1.90 g, 62%). M.p.= 171–173 °C (lit.[24] 173–174 °C); IR(ATR) ν/cm^{-1}: 3075 (aromatic C–H), 2933 (O–H), 1699 (C=O), 1660 (C=O), 1583 (C=C), 1446 (C=C aromatic), 1295 (C–N), 1215 (C–O), 1095 (C–N), 885 (aromatic C–H); ^{1}H NMR (400

MHz/$CDCl_3$:CF_3CO_2H 9:1) δ ppm: 8.81 (2H, appt. d, appt. J = 7.6 Hz, H_{c+d}), 8.46 (2H, appt. d, appt. J = 7.6 Hz, H_{c+d}), 4.28–4.04 (2H, m, H_i), 1.92 (1H, m, H_j), 1.52–1.15 (8H, m, $H_{k,m,n+o}$), 1.09–0.66 (6H, m, H_{l+p}) (No OH resonance observed); ^{13}C NMR (100 MHz/$CDCl_3$:CF_3CO_2H 9:1) δ ppm: 163.8 (C_f), 159.8 (C_a), 134.0 (C_c), 132.3 (C_d), 129.1 (C_h), 127.8 (C_e), 127.0 (C_g), 123.0 (C_b), 45.7 (C_i), 38.2 (C_j), 30.8 (C_m), 28.7 (C_n), 24.1(C_k), 23.1 (C_o), 14.0 (C_p), 10.5 (C_l); ESI-MS: Calculated $[C_{22}H_{23}NO_6Na]^+$: 420.1423; Found: 420.1418 $[C_{22}H_{23}NO_6Na]^+$

2.4.2 Synthesis of Naphthalene Diimide Tweezer 3

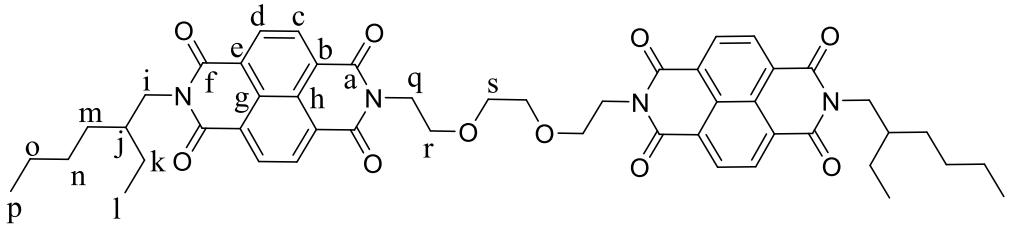

2,2-Ethylenedioxybis(ethylamine) (0.10 mL, 0.70 mmol) was added dropwise to a solution of ethylhexylimidediacid **6** (0.60 g, 1.50 mmol) in dimethylacetamide (20 mL) and toluene (2 mL) and the solution was heated at reflux for 18 hours. The reaction mixture was cooled and the solution was precipitated dropwise into diethyl ether (250 mL). The precipitate was collected by vacuum filtration and the resulting solid dried *in vacuo* overnight to yield a brown powder (0.45 g, 75%). M.p.= 222–226 °C (lit.[24] 223–224 °C); IR (ATR) ν/cm^{-1}: 2931 (C–H alkane), 1704 (C=O imide), 1580 (C=C aromatic), 1450 (C–H bend), 1332 (C–N aromatic), 1240 (C–N aliphatic), 1119 (C–O ether), 1092 (C–O ether), 764 (C–H aromatic); ^{1}H NMR (400 MHz./$CDCl_3$) δ ppm: 8.71 (8H, s, H_{d+c}), 4.36 (4H, t, J = 5.9 Hz, H_q), 4.18–4.08 (4H, m, H_i), 3.76 (4H, t, J = 5.9 Hz, H_r), 3.65 (4H, s, H_s), 1.96–1.90 (2H, m, H_j), 1.41–1.30 (16H, m, $H_{k,m,n+o}$), 0.95–0.86 (12H, m, H_{l+p}); ^{13}C NMR (100 MHz/$CDCl_3$) δ ppm: 163.1 (C_f), 162.8 (C_a), 130.6 (C_{c+d}), 126.9 ($C_{b,e,g+h}$), 70.5 (C_s), 67.6 (C_r), 45.0 (C_i), 39.8 (C_q), 38.0 (C_j), 29.8 (C_m), 29.5 (C_n), 24.0 (C_k) 23.5 (C_o), 14.3 (C_p), 10.5 (C_l); ESI-MS: Calculated $[C_{50}H_{54}N_4O_{10}Na]^+$: 893.3738; Found: 893.3716 $[C_{50}H_{54}N_4O_{10}Na]^+$

2.4.3 Synthesis of chain folding polynapthalenediimide 9

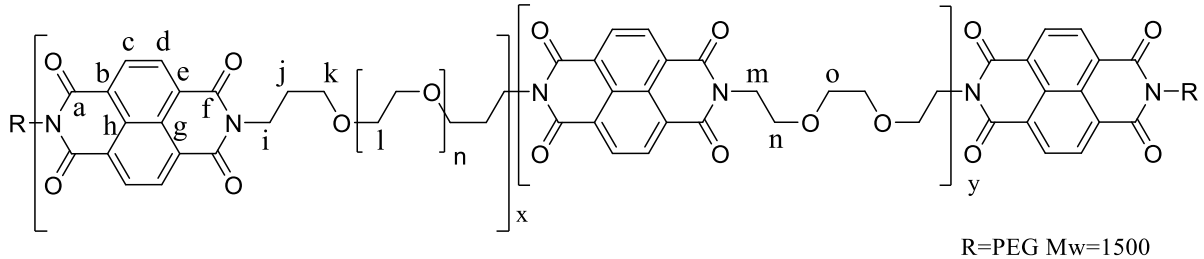

To a suspension of 1,4,5,8-naphthalenetetracarboxylic dianhydride (0.70 g, 2.6 mmol) in dry dimethylacetamide (30 mL) and toluene (2.5 mL) was added, dropwise, a solution of bis-3-

(aminopropyl) poly(ethylene glycol) (3.00 g, 2.0 mmol) and 2,2'-(ethylenedioxy)bis-ethylamine (0.19 g, 1.28 mmol) in dry dimethylacetamide (10 mL). The solution was heated to 135 °C for 18 hours and then the reaction mixture was cooled to room temperature and precipitated into diethyl ether (250 mL). The solid was collected by filtration and the crude material subjected to Soxhlet extraction in diethyl ether. The purified product was dissolved in warm THF and the solvent removed *in vacuo* to form a dark brown solid. (2.64 g, 69%); IR (ATR) ν/cm^{-1}: 2880 (C–H alkane), 1706 (C=O imide), 1663 (C=C aromatic), 1580 (C=C aromatic), 1454 (C–H bend), 1341 (C–N aromatic), 1280 (C–N aliphatic), 1244 (C–N aliphatic), 1104 (C–O ether) 767 (C–H aromatic); ^{1}H NMR (400 MHz/$CDCl_3$) δ ppm: 8.85–8.60 (12H, m, H_{c+d}), 4.40–4.35 (4H, m, H_m), 4.33–4.27 (12H, m, H_i), 4.00–3.39 (327H, m, H_{l+o}), 2.05 (12H, m, H_j). ^{13}C NMR(100 MHz/$CDCl_3$) δ ppm: 162.9 (C_{a+f}), 131.0 ($C_{c,\ d,\ h+g}$), 126.7 (C_{b+e}), 70.6 ($C_{,l+o}$), 69.2 (C_k), 67.7 (C_n), 39.6 (C_m), 38.6 (C_i), 28.3 (C_j); GPC (THF, 2 mg mL^{-1}) M_n = 6700 g mol^{-1}, M_w = 12,500 g mol^{-1}, $Đ$ = 1.87; DSC: T_g = 145 °C, T_m = 36 °C.

2.4.4 Synthesis of methylpent-4-enoate 12

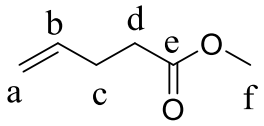

Potassium carbonate (6.40 g, 46 mmol) and 4-pentenoic acid (3.80 mL, 37 mmol) were stirred in acetone (60 mL) for 10 minutes. The solution was cooled to 0 °C for 5 minutes and iodomethane (2.32 mL, 37 mmol) was added. The solution was warmed to room temperature and stirred for 30 minutes. The reaction mixture was refluxed for 18 hours, then cooled and filtered *in vacuo* over a short path of celite. The filtrate was concentrated and purified by distillation to yield a colourless liquid (3.20 g, 76%); IR (ATR) ν/cm^{-1}: 2954 (C–H), 1736 (C=O), 1642 (C=C), 1167 (C–O), 916 (C=C–H); ^{1}H NMR (400 MHz/$CDCl_3$) δ ppm: 5.83 (1H, m, H_b), 4.98 (1H, dd, J = 17.2 Hz, H_a), 4.93 (1H, J = 10.3 Hz, H_a), 3.67 (3H, s, H_f), 2.39 (4H, m, H_{c+d}); ^{13}C NMR (100 MHz/$CDCl_3$) δ ppm: 173.4 (C_e), 136.6 (C_b), 115.4 (C_a), 51.5 (C_f), 33.3 (C_d), 28.8 (C_c); ESI-MS: Calculated $[C_6H_{10}O_2H]^+$ ($[MH]^+$):115.0759; Found: 115.0752 $[C_6H_{10}O_2H]^+$

2.4.5 Synthesis of 9-anthracenylpentanoate ester 15

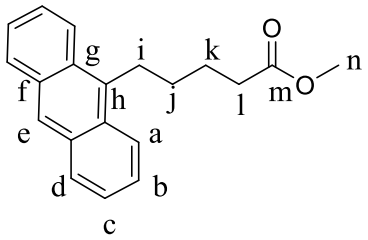

A solution of 9-BBN (0.5 M in THF) (11.0 mL, 5.50 mmol) and methylpent-4-enoate **12** (0.55 g, 5.50 mmol) was degassed and stirred under argon for 3 hours at room temperature.

9-Bromoanthracene (0.97 g, 3.76 mmol), sodium methoxide (0.89 g, 16.5 mmol) and [1,1'-bis(diphenylphosphino)ferrocene] dichloropalladium(II) (0.11 g, 0.15 mmol) were then stirred under argon in dry, degassed THF (15 mL). The solution of 9-BBN and methylpent-4-enoate **12** was added dropwise over 10 minutes to the solution of 9-bromoanthracene and the reaction mixture heated under reflux for 18 hours. The reaction mixture was then cooled and distilled water (10 mL) was added. The crude product was extracted using chloroform (2 × 15 mL) and the organic layers were washed with brine (20 mL), dried over $MgSO_4$ and filtered before being concentrated *in vacuo* to produce a yellow-brown solid, which was purified by column chromatography ($CHCl_3$) to produce an orange-yellow solid (0.75 g, 68%) M.p.= 72–75 °C (lit.[33]73–75 °C); IR (ATR) ν/cm^{-1}: 2953 (C–H alkane), 1737 (C=O), 1437 (C=C), 1193 (C–O ester), 1166 (C–O); ^{1}H NMR (400 MHz/$CDCl_3$) δ 8.34 (1H, s, H_e), 8.24 (2H, d, J = 8.8 Hz, H_a), 8.00 (2H, d, J = 8.3 Hz, H_d), 7.56–7.41 (4H, m, H_{b+c}), 3.68 (3H, s, H_n), 3.66–3.59 (2H, m, H_i), 2.43 (2H, t, J = 7.2 Hz, H_l), 2.01–1.77 (4H, m, H_{j+k}); ^{13}C NMR (100 MHz/$CDCl_3$) δ ppm: 174.1 (C_m), 134.7 (C_h), 131.8 (C_f), 129.7 (C_g), 129.4 (C_d), 125.9 (C_e), 125.7 (C_c), 125.0 (C_b), 124.4 (C_a), 51.7 (C_n), 34.2 (C_l), 30.9 (C_k), 27.8 (C_i), 25.7 (C_j); ESI-MS: Calculated [$C_{20}H_{21}O_2$] = 293.1463; Found: 293.1532 [$C_{20}H_{21}O_2$].

2.4.6 Synthesis of 9-anthracenylpentanoic acid 11

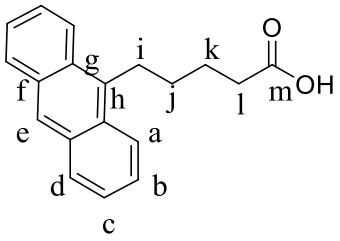

To a solution of KOH (0.14 g, 2.4 mmol) in ethanol (5 mL) was added 9-anthracenyl-5-pentenoate **15** (0.37 g, 1.2 mmol). The solution was stirred for 18 hours and then the solvent was removed *in vacuo* to produce an orange-brown solid. The solid was dissolved in deionised water (10 mL) and acidified (glacial acetic acid) to form a solid. The resulting solid was collected by filtration, washed with deionised water and dried to yield a yellow solid (0.35 g, 98%). M.p.= 154–156 °C (lit.[33] 154–156 °C); IR (ATR) ν/cm^{-1}: 3080 (O–H), 2970–2855 (C–H alkane), 1715 (C=O), 1260 (C–O), 930 (O–H), 840 (C–H aromatic); ^{1}H NMR (400 MHz/$CDCl_3$) δ 8.32 (1H, s, H_e), 8.22 (2H, d, J = 8.7 Hz, H_a), 7.98 (2H, d, J = 8.2 Hz, H_d), 7.55–7.35 (4H, m, H_{b+c}), 3.75–3.45 (2H, m, H_i), 2.52–2.30 (2H, m, H_l), 1.92 (4H, s, H_{j+k}) (No OH resonance observed); ^{13}C NMR (100 MHz/$CDCl_3$) δ ppm: 180.0 (C_m), 134.6 (C_h), 131.7 (C_f), 129.6 (C_g), 129.4 (C_d), 125.9 (C_e), 125.6 (C_c), 124.9 (C_b), 124.4 (C_a), 34.2 (C_l), 30.8 (C_j), 27.7 (C_i), 25.4 (C_k); ESI-MS: Calculated [MH^+] [$C_{19}H_{19}O_2$] = 279.1385; Found: 279.1381 [MH^+] = [$C_{19}H_{19}O_2$].

2.4.7 Synthesis of 9-anthracenpentyl terminated PEG 16

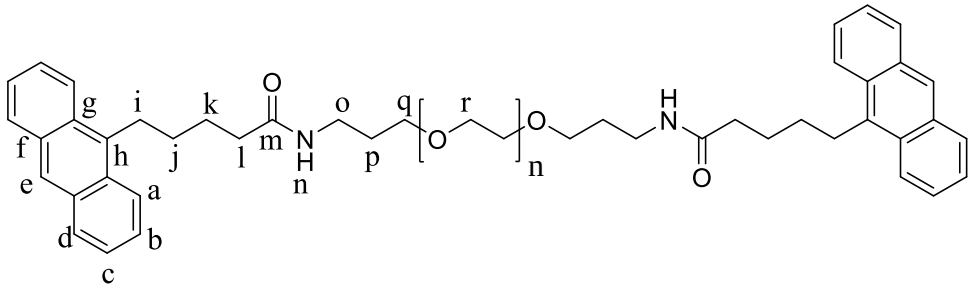

Under an inert argon atmosphere, bis(3-aminopropyl) terminated PEG (1.80 g, 1.20 mmol) and DMAP (0.06 g, 0.45 mmol) were added to dry dichloromethane (15 mL) and stirred for 10 minutes until the materials had fully dissolved. 9-Anthracenyl pentanoic acid **11** (0.75 g, 2.69 mmol) was then dissolved in dichloromethane and added to the reaction mixture. The reaction was cooled to 0 °C and stirred for 20 minutes. DCC (0.58 g, 2.80 mmol) was then added and the reaction mixture was warmed to room temperature and stirred for 72 hours. The solution was then cooled in an ice bath and filtered. The filtrate was concentrated and precipitated dropwise into diethyl ether (300 mL) in an acetone/dry ice bath. The product was collected by vacuum filtration whilst cold to afford a waxy pale brown solid (1.26 g, 52%); IR (ATR) ν/cm^{-1}: 3325 (N–H amide), 2882 (C–H alkane), 1677 (C=O amide), 1467 (C=C aromatic), 1279 (C–O ether), 841 (C–H aromatic); ^{1}H NMR (400 MHz/$CDCl_3$) δ 8.32 (2H, s, H_e), 8.25 (4H, appt. d, appt. J = 8.8 Hz, H_a), 7.99 (4H, appt. d, appt. J = 8.2 Hz, H_d), 7.48 (8H, m, H_{b+c}), 6.25 (2H, s, H_n), 3.64 (184H, s, $H_{i,\ q+r}$), 3.38–3.30 (4H, m, H_o), 2.23 (2H, t, J = 7.2 Hz, H_l), 1.96–1.80 (8H, m, H_{j+k}), 1.75–1.70 (2H, m, H_p); ^{13}C NMR (100 MHz/$CDCl_3$) δ ppm: 172.8 (C_m), 134.8 (C_h), 131.6 (C_f), 129.5 (C_g), 129.2 (C_d), 125.6 (C_e), 125.5 (C_c), 124.8 (C_b), 124.4 (C_a), 70.6 (C_{q+r}), 37.9 (C_o), 36.7 (C_l), 31.0 (C_j), 28.9 (C_p), 27.8 (C_i), 26.4 (C_k); GPC (THF, 2 mg mL^{-1}) M_n = 2400, M_w = 2600, $Đ$ = 1.08; DSC: T_g = 32 °C, T_m = 48 °C; MALDI TOF-MS: m/z calculated for $[C_{104}H_{168}N_2O_{33}Na]^+$ = 1996.1422 Da ± 44 Da; Found = 1995.9314 Da ± 44 Da.

2.5 References

1 H. M. Colquhoun and B. Klumperman, *Polym. Chem.*, 2013, **4**, 4832–4833.

2 L. Yang, X. Tan, Z. Wang and X. Zhang, *Chem. Rev.*, 2015, **115**, 7196–7239.

3 L. M. De Espinosa, G. L. Fiore, C. Weder, E. J. Foster and Y. C. Simon, *Prog. Polym. Sci.*, 2015, **49**–**50**, 60–78.

4 L. R. Hart, J. L. Harries, B. W. Greenland, H. M. Colquhoun and W. Hayes, *Polym. Chem.*, 2013, **4**, 4860–4870.

5 S. Burattini, B. W. Greenland, D. Chappell, H. M. Colquhoun and W. Hayes, *Chem. Soc. Rev.*, 2010, **39**, 1973–1985.

6 D. G. Bekas, K. Tsirka, D. Baltzis and A. S. Paipetis, *Composites Part B.*, 2016, **87**, 92–119.

7 P. Zhang and G. Li, *Prog. Polym. Sci.*, 2016, **57**, 32–63.

8 E. B. Murphy and F. Wudl, *Prog. Polym. Sci.*, 2010, **35**, 223–251.

9 T. R. Hebner, C. C. Wu, D. Marcy, M. H. Lu and J. C. Sturm, *Appl. Phys. Lett.*, 1998, **72**, 519–521.

10 D. Pede, G. Serra and D. de Rossi, *Mater. Sci. Eng. C*, 1998, **5**, 289–291.

11 J. Moon, V. Knezevic, E. M. Sachs, J. E. Grau and M. J. Cima, *J. Am. Ceram. Soc.*, 2002, **85**, 755–762.

12 S. Magdassi, *The Chemistry of Inkjet Inks*, World Scientific Publishing, Singapore, 2010.

13 L. R. Hart, J. L. Harries, B. W. Greenland, H. M. Colquhoun and W. Hayes, *ACS Appl. Mater. Interfaces*, 2015, **7**, 8906–8914.

14 L. R. Hart, S. Li, C. Sturgess, R. Wildman, J. R. Jones and W. Hayes, *ACS Appl. Mater. Interfaces*, 2016, 3115–3122.

15 L. R. Hart, J. L. Harries, A. Clifton, H. M. Colquhoun, and W. Hayes, Inkjet Composition, Patent No: WO 2014111722 A1, 24th July 2014.

16 K. Pataky, T. Braschler, A. Negro, P. Renaud, M. P. Lutolf and J. Brugger, *Adv. Mater.*, 2012, **24**, 391–396.

17 C. B. Highley, C. B. Rodell and J. A. Burdick, *Adv. Mater.*, 2015, **27**, 5075–5079.

18 A. Wild, A. Teichler, C. L. Ho, X. Z. Wang, H. Zhan, F. Schlütter, A. Winter, M. D. Hager, W. Y. Wong and U. S. Schubert, *J. Mater. Chem. C*, 2013, **1**, 1812–1822.

19 C. Friebe, A. Wild, J. Perelaer and U. S. Schubert, *Macromol. Rapid Commun.*, 2012, **33**, 503–509.

20 F. Gao, Z. Xu, Q. Liang, H. Li, L. Peng, M. Wu, X. Zhao, X. Cui, C. Ruan and W. Liu, *Adv. Sci.*, 2019.

21 A. M. Pekkanen, R. J. Mondschein, C. B. Williams and T. E. Long, *Biomacromolecules*, 2017, **18**, 2669–2687.

22 R. P. Sijbesma, E. W. Meijer and A. W. Bosman, *Mater. Today*, 2004, 34–39.

23 L. R. Hart, N. A. Nguyen, J. L. Harries, M. E. Mackay, H. M. Colquhoun and W. Hayes, *Polymer.*, 2015, **69**, 293–300.

24 B. W. Greenland, S. Burattini, W. Hayes and H. M. Colquhoun, *Tetrahedron*, 2008, **64**, 8346–8354.

25 B. W. Greenland, M. B. Bird, S. Burattini, R. Cramer, R. K. O'Reilly, J. P. Patterson, W. Hayes, C. J. Cardin and H. M. Colquhoun, *Chem. Commun.*, 2013, **49**, 454–456.

26 L. R. Hart, Supramolecular Polymer Networks: Novel Healable and Printable Materials,PhD Thesis, University of Reading, 2014.

27 P. Thordarson, *Chem. Soc. Rev.*, 2011, **40**, 1305–1323.

28 C. Bohne, *Chem. Soc. Rev.*, 2014, **43**, 4037–4050.

29 Bindfit binding constant calculator, supramolecular.org, accessed: [29/07/19].

30 P. Job, *Ann. Chim.*, 1928, **9**, 113–203.

31 Bindfit calculation for NDI tweezer **3** and anthracene **8**, http://app.supramolecular.org/bindfit/view/8c8af898-d383-41fe-9766-befc386144dc Accessed: [29/07/19].

32 L. R. Hart, J. L. Harries, B. W. Greenland, H. M. Colquhoun and W. Hayes, *ACS Appl. Mater. Interfaces*, 2015, **7**, 8906–8914.

33 G. Esteban, M. A. López-Sánchez, M. E. Martínez and J. Plumet, *Tetrahedron*, 1998, **54**, 197–212.

34 P. J. Flory, *J. Chem. Phys.*, 1942, **10**, 51–61.

35 P. Calvert, *Chem. Mater.*, 2001, **13**, 3299–3305.

36 FUJIFILM, *Dimatix Materials Printer DMP-2800 Series*, 2010, Revision 4.

Chapter 3

Novel UV-curable Materials for Inkjet Formulations: Polymers Featuring Photo-dimerisable Anthracene End Groups

Abstract

In this chapter the synthesis and characterisation of two novel, low molecular weight poly(ethylene glycol) polymers with UV-dimerisable anthracene end groups are described. These novel polymers exhibited good solubility (100 g/L) in common organic solvents and were deposited successfully using a drop-on-demand (DOD) inkjet printhead to produce clear prints. UV irradiation (>365 nm) studies of the bis-anthracene terminated PEG material demonstrated polymerisation via the formation of anthracene dimers, whilst also maintaining solubility in common organic solvents, to allow for solution state analysis of the dimerisation process using UV-vis and ^{1}H NMR spectroscopies.

In contrast, UV irradiation of a branched tris-anthracene PEG material resulted in the formation of an insoluble, cross-linked network, which was characterised using rheometry, differential scanning calorimetry and lap shear tensiometry. The polymer showed improved physical properties following UV irradiation, transitioning from a viscous oil to an elastomeric material. It was found that the inclusion of solvent-soluble, transition metal complex dyes into tris-anthracene PEG formulations resulted in an increase in UV-cure time, although curing still occurred, highlighting the suitability of the tris-anthracene PEG material as a UV-curable polymer for inclusion in inkjet formulations.

3.1 Introduction

The field of UV-curable inks is the fastest growing sector in the global digital print market, valued at £955 million in 2018 and estimated to reach £1632 million by 2025.[1] The market already employs UV inks for product decoration, packaging and coding and marking.[2] These materials pose several advantages when compared to solvent-based and aqueous inks. The benefits of employing UV-curable inks include: (i) rapid curing of the deposited material, allowing high speed printing, (ii) UV-curing lamps occupy less space and consume less energy than conventional dryers, (iii) strong substrate adhesion and (iv) enhanced solvent, scratch and physical resistance as a result of their cross-linked nature.[2–6] Furthermore, several UV-curable inks are suitable for deposition onto a large variety of substrates without the requirement for pre-treatment of the surface with an ink-receiving layer.[2,7]

Common UV-curing inks consist of monomers with vinyl, methacrylate and acrylate functionalities. Mixtures of these monomers are often used in formulations to achieve the desired properties of the final product.[3,6] As well as reactive monomers or oligomers, UV ink formulations also commonly

contain: photoinitiators, synergists, surfactants, colourants and adhesion promoters. However, the photo-initiators and monomer reactivity can be considered the most important factors in determining the efficiency of polymerisation.[2]

Despite the effective curing of acrylate monomers, the use of small compounds in UV-curable formulations, such as photoinitiators, monomers and oligomers, poses some practical disadvantages; particularly for their use in the food packaging sector. Unreacted small compound can, for example, migrate through packaging from the print, resulting in failure to attain European Food Safety Authorisation (EFSA) approval for their use in non-contact food packaging.[4]

The functionalisation of soluble, low molecular weight polymer backbones with photo-active end groups can provide an alternative approach to monomer and photoinitiator based UV inks. Polymeric materials that form extended covalently bonded networks following UV irradiation have been previously reported[8–10] and include the use of coumarin,[10–21]cinnamate ester[22–26] and anthracene[19,27–42] as UV-crosslinking moieties.

Coumarins have been employed as reversible, photodimerisable groups since 1990 when Chujo *et al*. reported the synthesis of a polyoxazoline hydrogel with pendant coumarin groups (M_n = 22,300 g mol^{-1}).[16] The study employed UV-vis spectroscopic analysis to demonstrate the formation of a cross-linked hydrogel from the soluble polyoxazoline polymer via irradiation with UV light (>300 nm) and the subsequent photocleavage of the cross-links with short wavelength UV light (~254 nm) to recover the soluble polyoxazoline.[16] Chen *et al*. later expanded the application of coumarins as reversible UV-cross-linkers for polymeric systems by appending coumarins to a variety of polymer backbones including poly(vinyl acetate),[17] polyacrylates,[20] polyethers[12] and polyurethanes.[18] The initial reports by that group described the UV-dimerising properties of a poly(vinyl acetate) with a singular coumarin end-group, utilising UV-vis spectroscopy to monitor the dimerisation process.[17] The group also investigated a series of comb-type copolyacrylates[13,20] as well as linear bis-coumarin polyethers[12] and polyurethanes,[18] all of which dimerised successfully using UV-irradiation.

The photo-dimerisation of cinnamate ester functionalised polymers has also been investigated. In 2004, Gupta *et al*. produced a poly(methyl methacrylate-*co*-2-hydroxyethyl acrylate) (M_n = 333,000 g mol^{-1}) that was functionalised with pendant cinnamate groups to produce a UV-cross-linkable, comb-type polymer, which was irradiated *in situ* during electrospinning to form an insoluble gel.[23] More recently Rochette *et al*. investigated the light-induced shape memory of a series of poly(ester urethane)s with pendant cinnamate and cinnamide groups.[24] The polymers ranged in molecular weight (M_n = 2,000–8,000 g mol^{-1}) and all exhibited the ability to achieve light-induced shape memory by first irradiating the materials with UV light (>300 nm) whilst applying stress to form an elongated material,

and then subsequently irradiating with short wavelength UV light (~260 nm) to reverse the crosslinking and return the materials to their original shape.

Anthracene also reacts under long-wave UV-irradiation (>365 nm) via a [4+4] photocycloaddition to form a dimeric species without the requirement for photoinitiators or synergists[43–46] and has been appended to a variety of different polymeric backbones including linear,[27,28,35–38,42] comb[32,39–41] and branched or dendritic[19,29–31] systems. The photoreactivity of anthracene groups has been exploited to produce larger polymer networks from relatively low molecular weight anthracene appended polymers.

In 2011, Froimowicz *et al*. developed a dendritic polyglycerol (M_n = 10,000 g mol^{-1}) with anthracene functionalities that behaved as a reversible photo-induced dendritic macromonomer.[30] The photo-crosslinking of the material was investigated both in the solid state (cast film) and in solution, and the photo-crosslinking of the materials was confirmed by UV-vis spectroscopy, GPC and DSC analyses. The reversibility of the dimer formation was also investigated and dimer scission was achieved by irradiation of cross-linked material produced with low wavelength UV light (254 nm). The reversibility of the photodimerisation indicated the suitability of the anthracene dendrons as healable materials.[30]

In a similar study, Han *et al*. produced polysiloxanes (M_n > 5,100 g mol^{-1}) with pendant anthracene groups and subjected them to UV-irradiation (365 nm) to form a cross-linked network.[32] The formation of dimers between anthracene moieties was monitored using ^{1}H NMR and UV-vis spectroscopies. The reversal of cross-linking was achieved using heat-triggered cleavage of the dimers at 120 °C for 3 hours in place of irradiation with short wavelength UV light, which was said by the group to pose more risk of side reactions. The polysiloxanes produced were also applied as coatings on UV-LED bulbs and cross-linked *in situ* to form a film that exhibited a strong green luminescence under UV light. Adjustment of the luminescent groups on the polymers could therefore provide a route to the production of a wide range of coloured luminescent coatings for UV-LED bulbs.

More recently, Kan *et al*. produced[19] a branched polyurethane with anthracene end groups as a viscous yellow solid, which was successfully cross-linked using UV-irradiation to form an elastomeric polymer film with enhanced mechanical properties. It was found that scratching or compression of the film resulted in characteristic blue fluorescence under UV light as a result of formation of anthracene monomers in the affected regions.

The solubility of the previously discussed anthracene-appended polymers enabled facile spectroscopic characterisation of the materials, and the enhanced physical properties of the polymers following UV-irradiation, highlighting their suitability as UV-curable polymer inks for inkjet printing. Selection of a polymer backbone that demonstrates good solubility, low viscosity and a low molecular weight will

produce a material that is suitable for inkjet deposition. Furthermore, ample functionalisation of the material with UV-dimerisable anthracene groups can produce a highly crosslinked network following UV irradiation to produce an insoluble, durable print.

In the studies presented in this chapter, two anthracene appended polymers; one linear and one branched, have been synthesised and characterised, and their suitability as UV-curing polymers for inkjet formulations investigated.

3.2 Results and Discussion

3.2.1 Polymer Synthesis and Characterisation

To achieve polymer networks with varying degrees of UV-initiated crosslink densities, both linear **1** (Scheme 1) and branched **2** (Scheme 2) PEGs with UV-dimerising anthracene end-groups were synthesised. Linear PEG **1** with anthracene end-capping groups was obtained by using two different synthetic pathways.

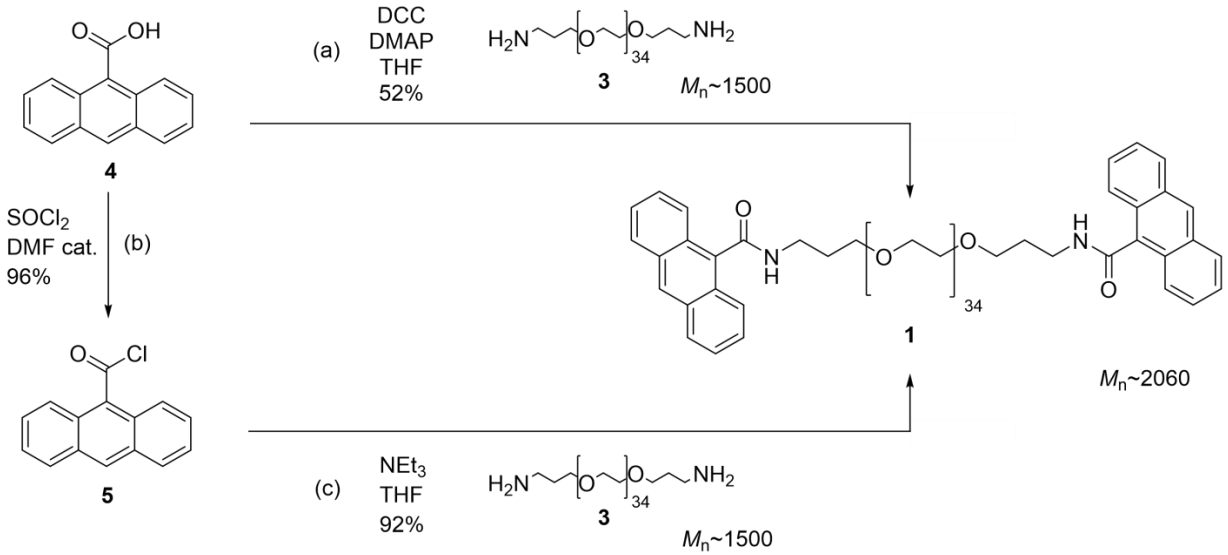

Scheme 1- Synthesis of bis-anthracene terminated poly(ethylene glycol) **1**. The schematic shows two synthetic pathways to obtain **1**; a) DCC-mediated coupling of 9-anthracene carboxylic acid **4** with bis(aminopropyl) terminated poly(ethylene glycol) **3**, and b) The activation of **4** by forming the corresponding acyl chloride and then c) the subsequent reaction of anthracene acyl chloride **5** with bis(aminopropyl) terminated poly(ethylene glycol) **3**.

Initially, bis-anthracene terminated PEG **1** was synthesised via a DCC-mediated coupling employing an adaptation of the protocol reported by Hart *et al.*[47–49] Bis (3-aminopropyl) terminated PEG (M_n = 1,500 g mol^{-1}, $Đ$ = 1.07) **3** and 9-anthracene carboxylic acid **4** were reacted in the presence of DCC and DMAP over 72 hours to produce bis-anthracene capped PEG **1** in a moderate yield of 52% (Scheme 1). The DCC-mediated synthetic approach proceeded slowly and even following extended reaction times, and an increase in molar equivalents of **4**, the reaction did not go to completion.

An alternative synthetic approach was therefore investigated to increase both the reaction rate and yield of bis-anthracene PEG **1**. In the second synthetic approach, 9-anthracene carboxylic acid **4** was converted to the more reactive 9-anthracene carbonyl chloride **5** by reaction with an excess of thionyl chloride. 9-Anthracene acyl chloride **5** was then reacted with bis-amino terminated PEG **3** in the presence of triethylamine to produce the desired bis-anthracene terminated PEG **1** in excellent yield (92%), following a shorter reaction time of 18 hours when compared to the DCC-mediated approach (Scheme 1). This synthetic approach utilising 9-anthracene acyl chloride **5** as an end-capping group was therefore employed for the duration of these studies.

The synthesis of polymer **1** from compound **5** produced solely bis-anthracene PEG **1** confirmed by ^{1}H NMR spectroscopic analysis, which revealed the absence of the triplet resonance at 2.80 ppm correlating to the methylene protons adjacent to the terminating amine of **3**, as well as formation of an amide NH resonance at 7.06 ppm (Figure 1).

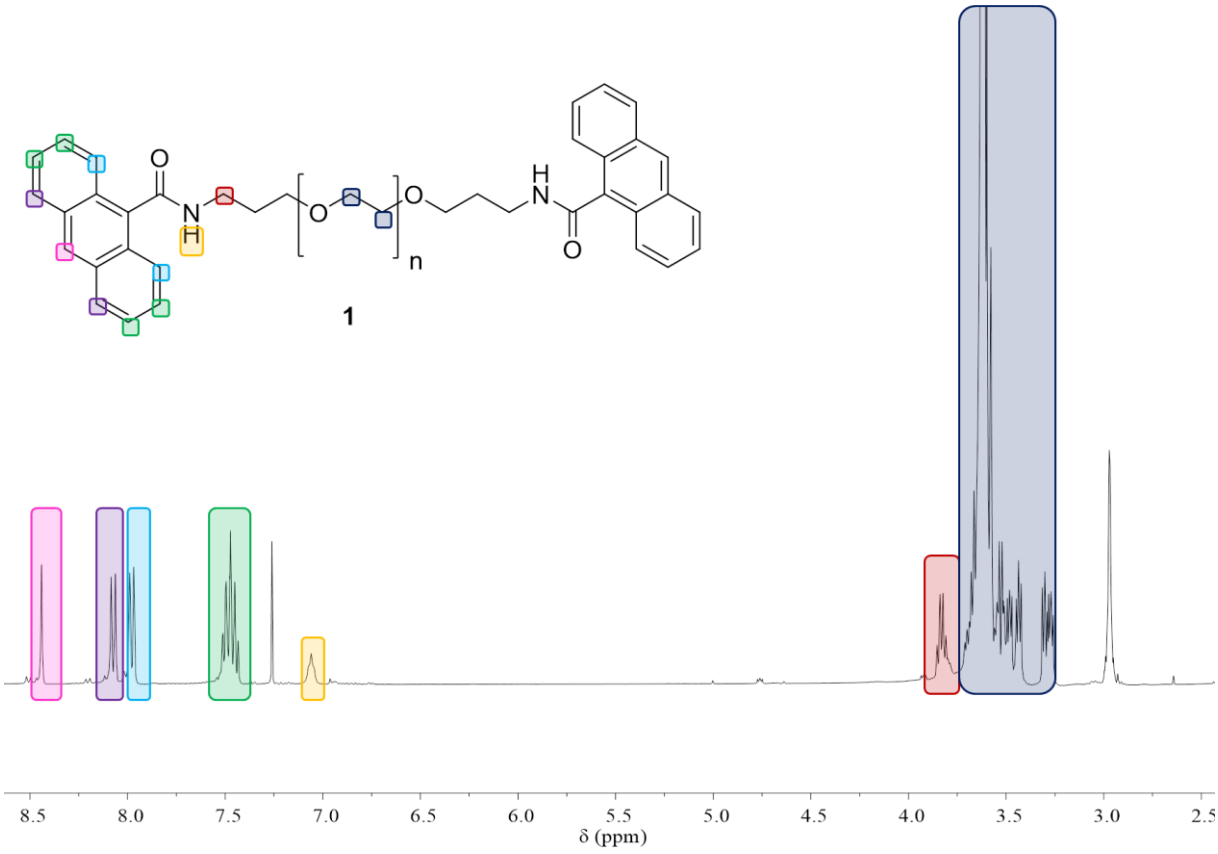

Figure 1- ^{1}H NMR spectrum of polymer **1** indicating the absence of methylene group resonances observed in the ^{1}H NMR spectrum of bis(3-aminopropyl) terminated PEG (2.80 ppm) as well as the formation of a novel amide bond shown by the resonance at 7.06 ppm (yellow).

MALDI-TOF mass spectroscopic analysis was conducted to determine the average molecular weight of polymer **1** and therefore calculate the number of ethylene glycol repeat units present. The strongest peak was at m/z 2060.9 Da and corresponds to the sodiated species of polymer **1** $[C_{104}H_{168}N_2NaO_{37}]^+$ with a calculated mass of 2060.1 Da and an average of 34 ethylene glycol repeat units. The spacing between this series is 44 Da; equal to one ethylene glycol repeat unit (Figure 2). Two further species were also observed in the mass spectrum, both of which demonstrated the same spacing between peaks of 44 Da. The second most prominent species displayed an increase in mass ions of 16 Da when compared to the most abundant (sodiated) series, and therefore correlated to the potassiated series of bis-anthracene PEG **1**. The lower intensity species observed was attributed to partial laser-fragmentation[50] of anthracene end-groups from the polymer backbone of PEG **1** and demonstrated a most abundant mass ion of 1871.79 Da, corresponding to the potassiated mono-anthracene species $[C_{89}H_{160}N_2KO_{36}]^+$ with a calculated mass of 1872.04 Da.

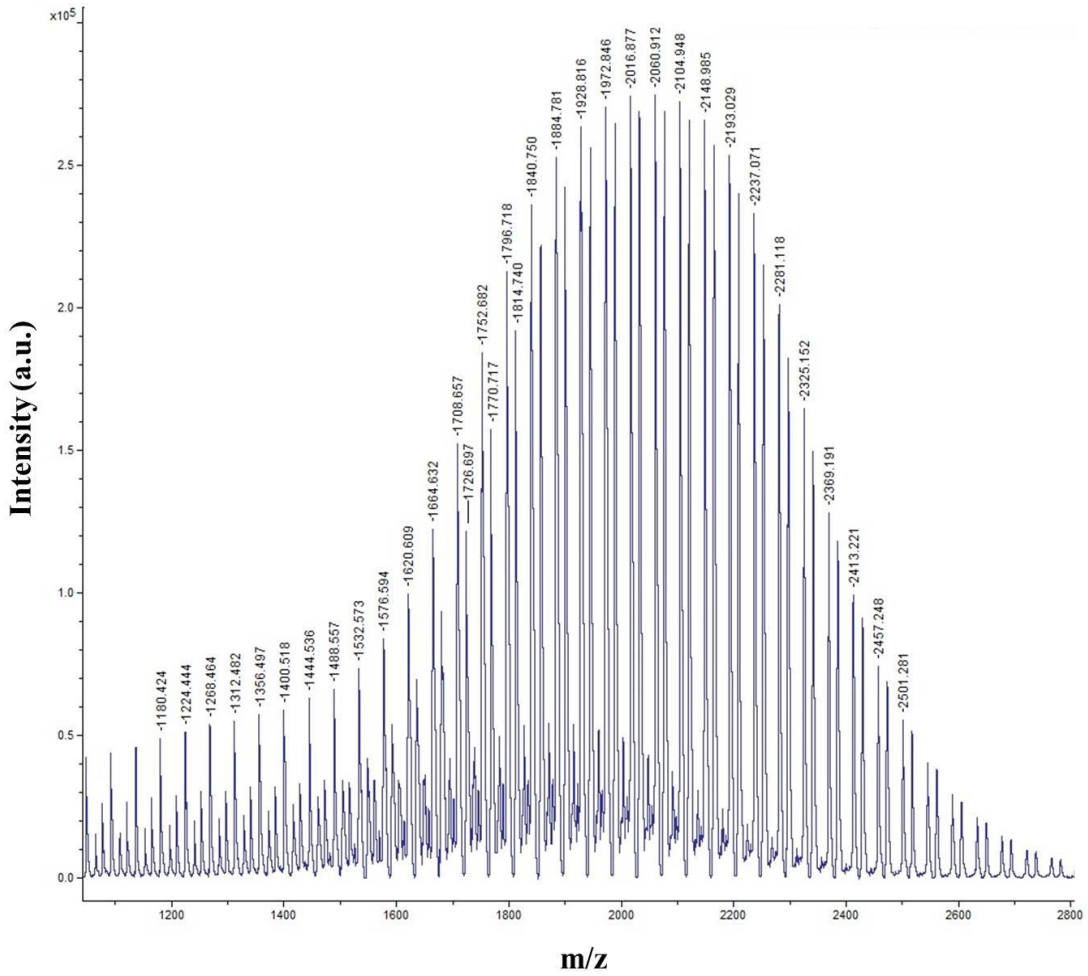

Figure 2-MALDI-TOF mass spectrum of bis-anthracene polymer **1** revealing the mass ion at 2060.9 Da (±44n Da) corresponding to a polymer with 34 repeat units. MALDI-TOF samples were prepared in a DHB matrix at a concentration of 0.25 mg mL^{-1}.

A similar synthetic approach was used to obtain the branched polymer **2**. Anthracene acyl chloride **5** was reacted in the presence of triethylamine with glycerol ethoxylate **6** (M_n = 1000 g mol^{-1}) to obtain the desired branched polymer **2**, end-capped with anthracene units, in good yield (84%) (Scheme 2).

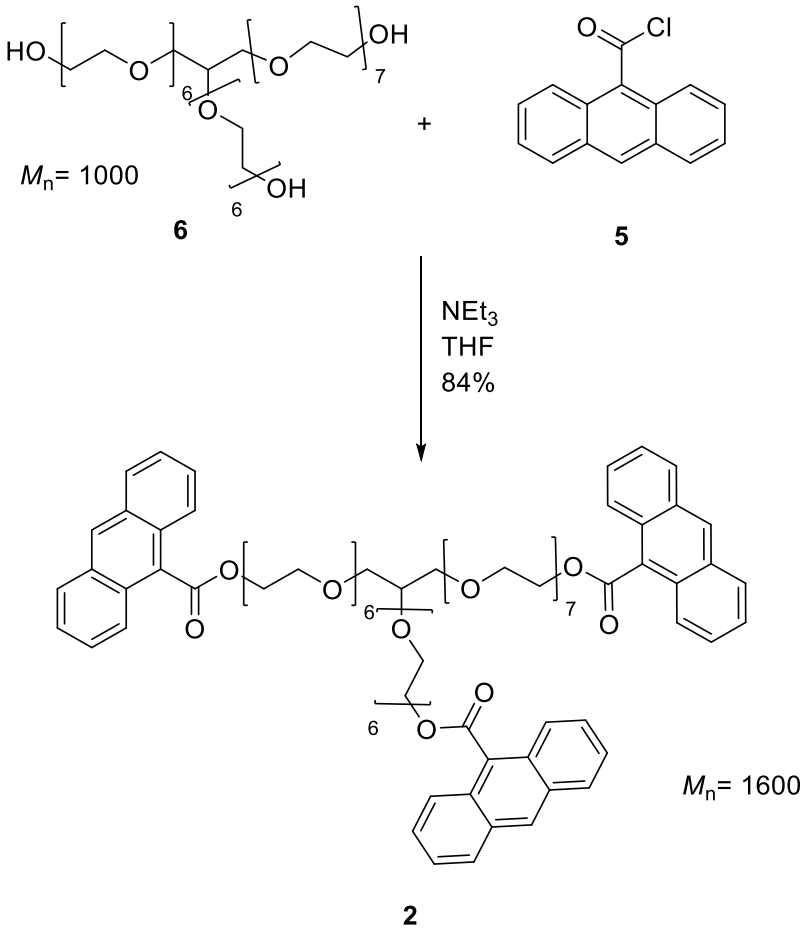

Scheme 2- Synthesis of tris-anthracene poly(ethylene glycol) **2** by coupling of 9-anthracene acyl chloride **5** and glycerol ethoxylate **6** in the presence of trimethylamine.

The formation of ester linkages to produce polymer **2** was confirmed by ^{1}H NMR spectroscopic analysis. Two novel methylene resonances were observed at 4.75 and 3.89 ppm, which were attributed to the two methylene groups adjacent to each ester linkage. The more downfield resonance (4.75 ppm) is assigned to the methylene group directly adjacent to the ester functionality, which is subjected to a greater de-shielding effect by the ester oxygen and is indicated in orange in Figure 3.

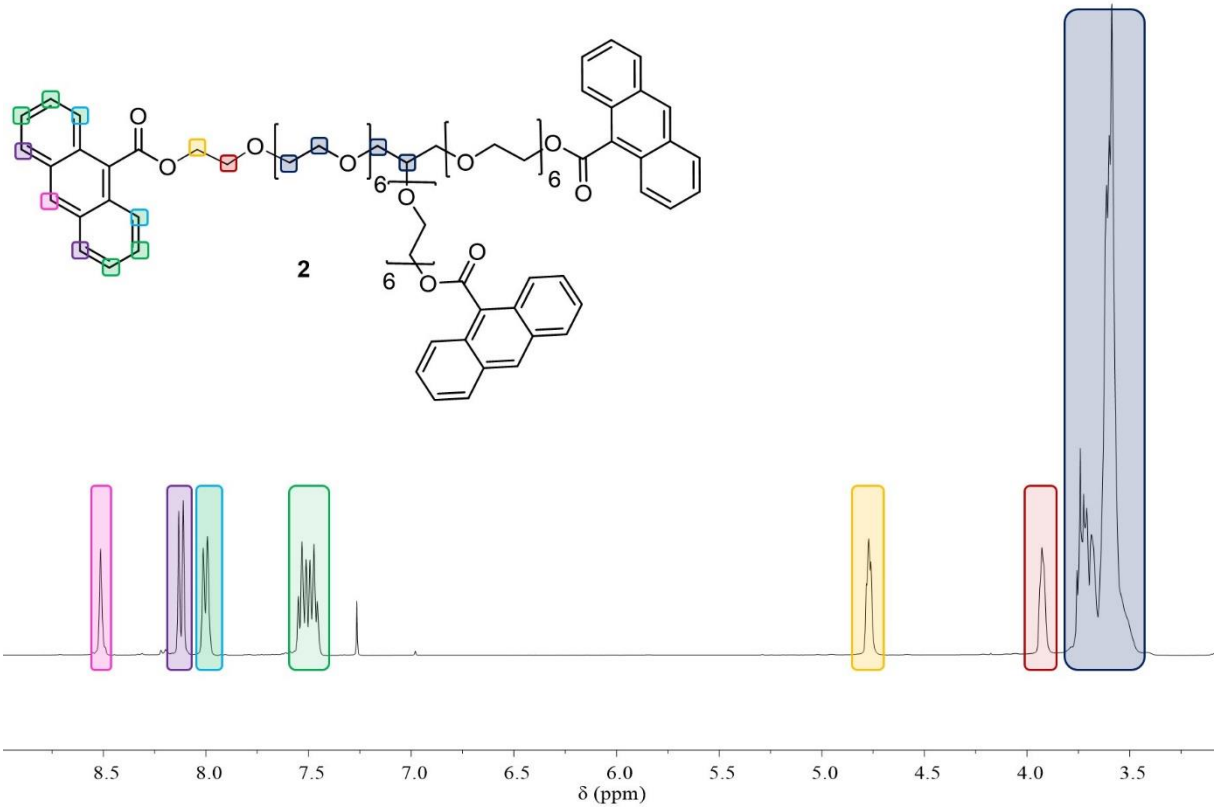

Figure 3- ^{1}H NMR spectrum of polymer **2**, indicating the assigned proton resonances of the polymer. Analysis performed at 400 MHz in $CDCl_3$ at a concentration of 10 mg mL^{-1}.

Polymer **2** was obtained as a viscous yellow oil with a glass transition temperature (T_g) of –24 °C, 55 °C lower than the T_g value for the waxy solid bis-anthracene terminated PEG **1** (31 °C). The lower T_g value observed for polymer **2** was attributed the lower molecular weight of the starting poly(ethylene glycol) (i.e. **6** = 1,000 *cf.* **3** = 1,500 g mol^{-1}), the presence of two amide linkages that permit hydrogen bonding plus the branched structure of polymer **2** which prevent the polymer chains packing less densely when compared to the linear polymer **1**.

MALDI-TOF mass spectroscopic analysis was conducted to determine the average molecular weight and the number of repeat units in the polymer backbone. The most abundant mass ion for polymer **2** was observed at m/z 1624.92 Da ± 44 Da, which corresponds to the potassiated series $[C_{88}H_{112}KO_{26}]^{+}$ with a calculated mass of 1624.94 Da and a total of 19 ethylene glycol repeat units. The sodiated series is also evident in the mass spectrum obtained with a difference in mass ion peaks of 16 Da when compared to the potassiated series. A third series was also observed in the spectrum and is attributed to the partial fragmentation[50] of polymer **2** to produce a bis-anthracene PEG series with a peak mass ion of m/z 1419.84 Da corresponding to the formula $[C_{73}H_{104}KO_{25}]^{+}$ with a calculated mass of 1419.65 Da (Figure 4).

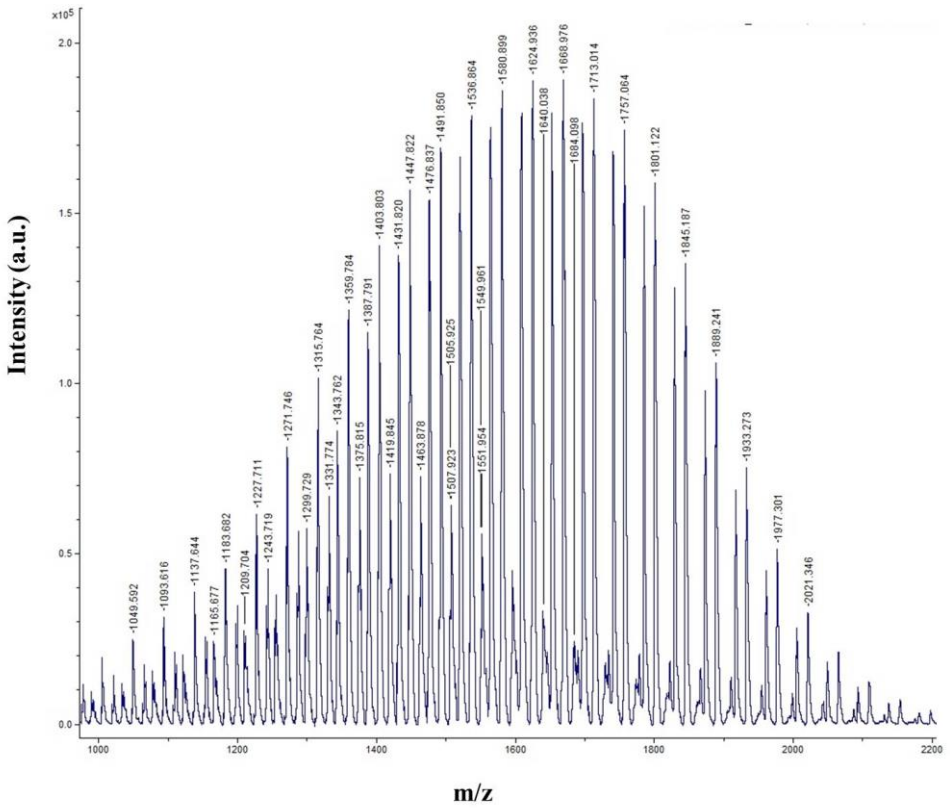

Figure 4- MALDI-TOF mass spectrum of polymer **2** showing a mass ion peak at m/z = 1624.92 Da with a spacing of 44 Da equal to that of one ethylene glycol unit. MALDI-TOF samples were prepared in a DHB matrix at a concentration of 0.25 mg mL^{-1}.

3.2.2 Spectroscopic Characterisation of UV-photodimerisation of Linear Polymer 1

Linear polymer **1** was employed as a soluble model compound for investigation into the UV irradiation of anthracene-appended polymers in solution. Bis-anthracene terminated PEG **1** was irradiated under oxygen-free conditions in order to prevent the known competitive photo-oxidation reaction of anthracene units to the corresponding anthraquinone derivatives[51] (Scheme 3).

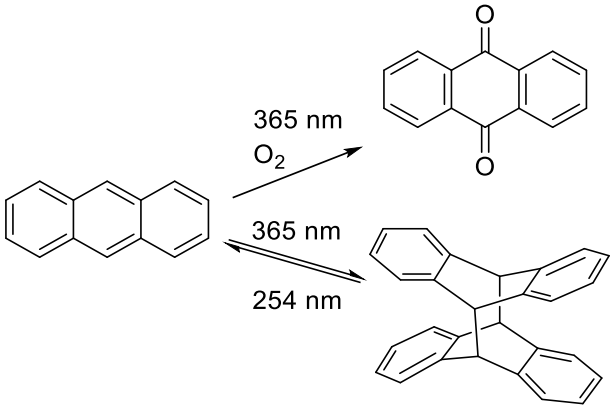

Scheme 3- Schematic representation of the formation of anthracene dimer (bottom right) under UV light (365 nm) and the competitive photo-oxidation of anthracene to anthraquinone (top right) upon irradiation with UV light in the presence of oxygen.[51]

UV-vis spectroscopy was conducted to monitor the dimerisation of anthracene moieties throughout the irradiation with UV light. Bis-anthracene PEG **1** was dissolved in acetonitrile (100 mg mL^{-1}) and irradiated in a quartz test tube with UV-vis light (350–500 nm) using a 36 W LED-UV lamp. Aliquots from the solution were taken across a time course of 24 hours and the intensity of characteristic anthracene absorptions monitored.

The intensities of the characteristic absorptions of anthracene in polymer **1** decrease as the length of time under UV increases. These changes can be attributed to the loss of aromaticity in the central anthracene ring following dimerisation of anthracene units via a [4+4] photocycloaddition process[29,30,36] (Scheme 3). The UV-vis spectrum of the aliquot of **1** recorded at 24 hours (dark green) demonstrates a large reduction in the absorption at 253 nm and also dramatic reduction in the intensity of the absorptions at 345, 363 and 383 nm, respectively, that were present at the start of this experiment (Figure 5).

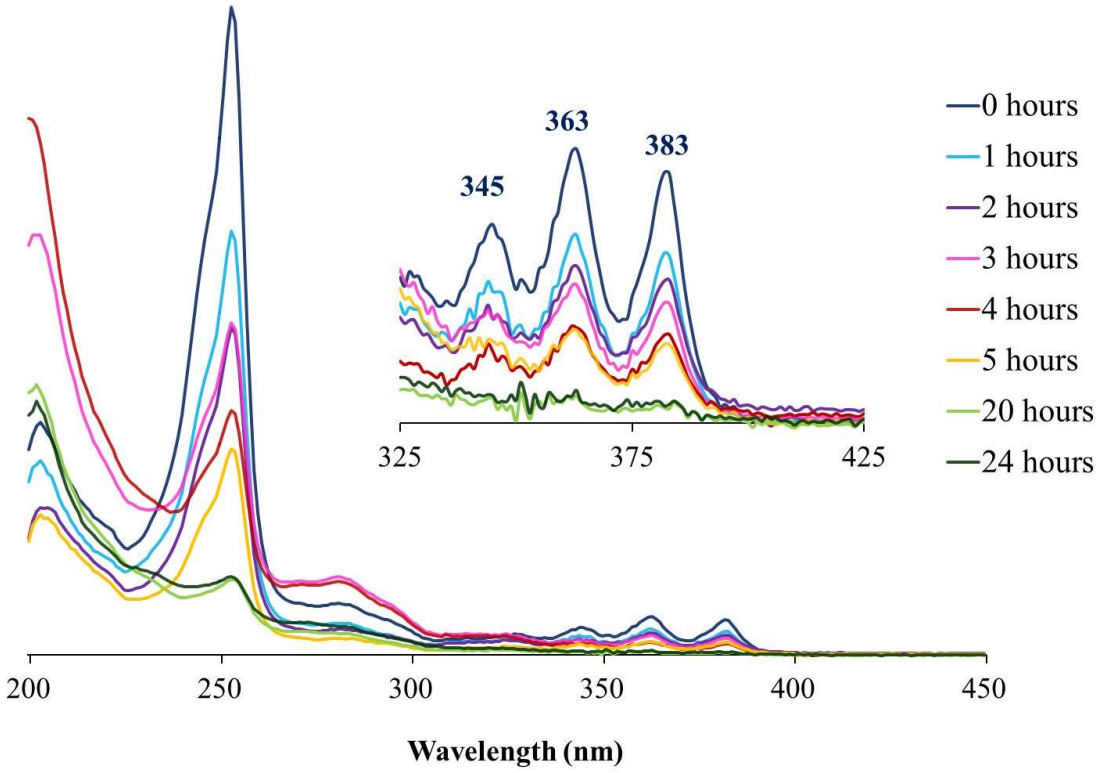

Figure 5- Stacked UV-absorption spectra of a solution of **1** (100 mg mL^{-1}, acetonitrile) irradiated for different periods of time (0–24 hours) in 100 mg mL^{-1} acetonitrile solution under argon. The spectra show the decrease in characteristic absorptions of anthracene following extended UV-irradiation (spectra recorded in acetonitrile at 1 μg mL^{-1}).

The photodimerisation of **1** was also monitored using fluorescence spectroscopy, which revealed a similar spectroscopic trend to that of the UV-vis analysis. Polymer **1** exhibits fluorescence emissions at 409 and 433 nm, but, irradiation of the polymer with long-wavelength UV light showed a sharp decrease in these fluorescence emissions.

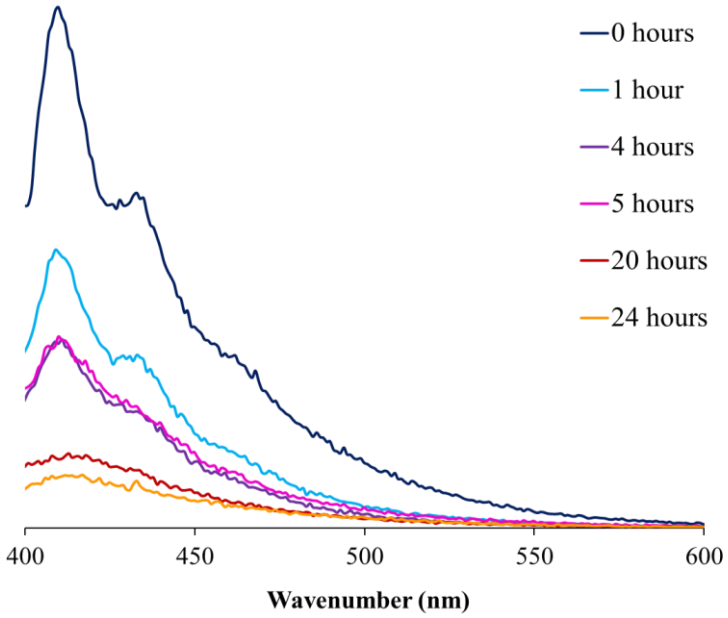

Figure 6- Fluorescence spectra of aliquots of bis-anthracene polymer **1** irradiated for different periods of time (0–24 hours) showing a decrease in the fluorescence emission of anthracene units as irradiation time increases.

Although UV and fluorescence spectroscopy demonstrate the loss of aromaticity upon UV-irradiation of anthracene moieties in polymer **1**, the data are non-conclusive as a similar spectroscopic trend would be observed upon formation of anthraquinone from anthracene (see Scheme 3). It is important to determine that the anthracene end-groups in polymer **1** were forming dimers upon UV-irradiation and not photo-oxidation products. As the anthracene-based materials are intended for application in the field of UV-curable inks and therefore are required to form an extended polymer network upon UV-irradiation to produce a material with enhanced mechanical properties and decreased solubility. If the materials are prone to forming photo-oxidation products, then a higher molecular weight material will not be produced following UV-curing and the desired properties will not be achieved.

^{1}H NMR spectroscopy was therefore used to confirm the formation of anthracene dimers during irradiation. Anthraquinone and anthracene dimers are easily distinguishable using ^{1}H NMR spectroscopy as the aromatic proton resonances of anthraquinone (8.33 and 7.81 ppm) are located downfield when compared to those of dimerised anthracene (7.01 and 6.77 ppm) as a result of the de-shielding effect of the carbonyl functionalities on the central ring of anthraquinone. The irradiation of polymer **1** resulted in significant changes in the aromatic region of the spectrum with the reduction of the intensity of the proton resonances of 9-substituted anthracene (8.44, 8.07, 7.98 and 7.47 ppm) and the appearance of novel resonances attributed to the corresponding 9-substituted anthracene dimers. However, after 5 hours, further lower intensity resonances attributed to anthraquinone were also observed as a result of failure to completely eliminate oxygen from the irradiated solution (Figure 7).

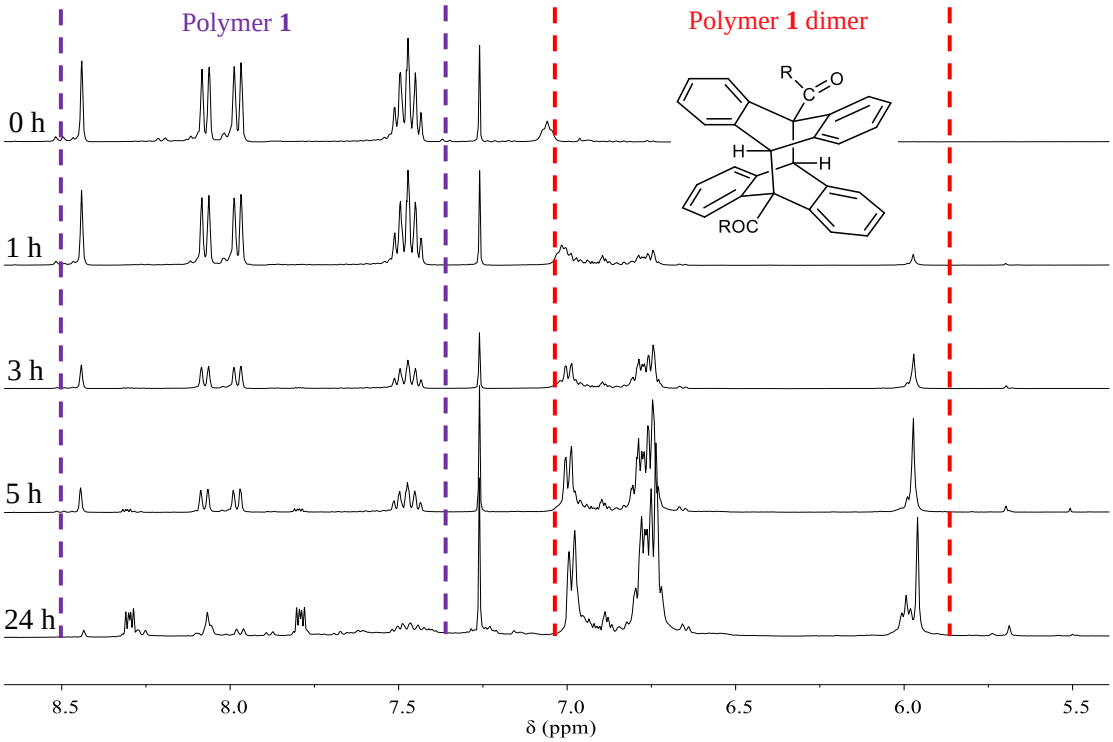

Figure 7- Stacked partial ^{1}H NMR spectra of polymer **1** before (0 h) and throughout irradiation process, showing the depletion of singular anthracene moiety resonances between 8.50–7.4 ppm (purple region) and the appearance of novel anthracene moiety dimer resonances 7.05–6.65 ppm (red region) as length of irradiation time increases.

The spectrum of the sample recorded at 1 hour revealed minor changes in the spectrum with new, but weak, resonances observed between 7.05 and 5.85 ppm. Following 3 hours of UV-irradiation of polymer **1**, a ratio of approximately 1:1 ratio of anthracene monomer resonances to anthracene dimer resonances can be observed. The novel singlet resonance at 5.96 ppm is assigned to the bridgehead protons of dimerised anthracene units and the proton resonances at 7.05–6.70 ppm are attributed to the aromatic protons, with resonance values shifted upfield *cf.* the undimerised anthracene end group following loss of aromaticity in the central anthracene ring. The dimer resonances observed in this study correlate well with the ^{1}H NMR spectra reported by Han *et al*. which indicate the spectroscopic changes pre and post-irradiation for 9-anthracene carboxylic acid **4**.[32]

Closer analysis of the ^{1}H NMR spectra of the irradiated samples of **1** suggests the formation of more than one steric arrangement of the anthracene derived substituents. Substituted anthracenes are known to form dimer units, with substituents stacked either *cis* (head-to-head) or *trans* (head-to-tail) to one another.[45,52–54] The additional resonances observed at 6.89–6.87, 6.65 and 5.69 ppm (indicated in pink) following UV irradiation of **1** have the same integral ratio as the more prominent species, but are much lower in intensity (14:1 a:b), as seen in Figure 8.

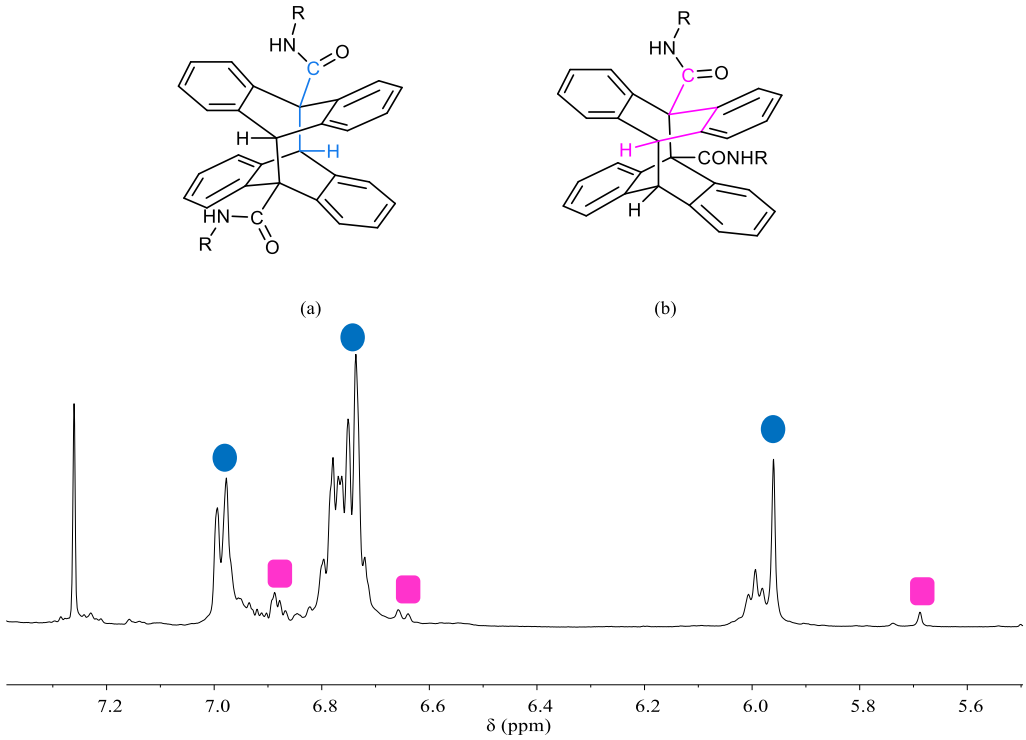

Figure 8- Partial ^{1}H NMR spectrum of polymer **1** after 24 hours of UV-irradiation, showing the formation of (a) head-to-tail arrangement with substituents *trans* to each other and (b) head-to-head arrangement with substituents *cis* to each other. The respective pink and blue bonds demonstrate the number of bonds between the carbonyl group and the bridgehead protons in both cases (R = PEG).

Although ^{1}H NMR spectroscopic analysis suggested the formation of both steric arrangements of anthracene dimer units from polymer **1**, the predominant dimer form could not be determined using solely ^{1}H NMR spectroscopy. Heteronuclear multiple bond correlation (HMBC) spectroscopy was thus conducted to determine the arrangement of substituents in polymer **1** following irradiation for 24 hours. Multiple bond correlation was not observed between the amide carbon and bridgehead proton for the head-to-head stacking, as the two nuclei were separated by 5 bonds (indicated in pink in Figure 8), which is too large a distance for heteronuclear ^{1}H–^{13}C correlation to occur. However, in the head-to-tail arrangement the two atoms are separated by 3 bonds (indicated in blue in Figure 8) and therefore heteronuclear correlation can be observed. The HMBC spectrum confirmed the presence of predominately head to tail stacking of polymer **1**, as a correlation between the C–H bridgehead proton resonance at 5.96 ppm and the amide carbon resonance at 172.9 ppm is observed (Figure 9).

The formation of predominately head-to-tail stacking of anthracene units in polymer **1** can be attributed to electrostatic and steric effects, which in some cases have yielded solely head-to-tail dimers of 9-substituted anthracenes.[54]

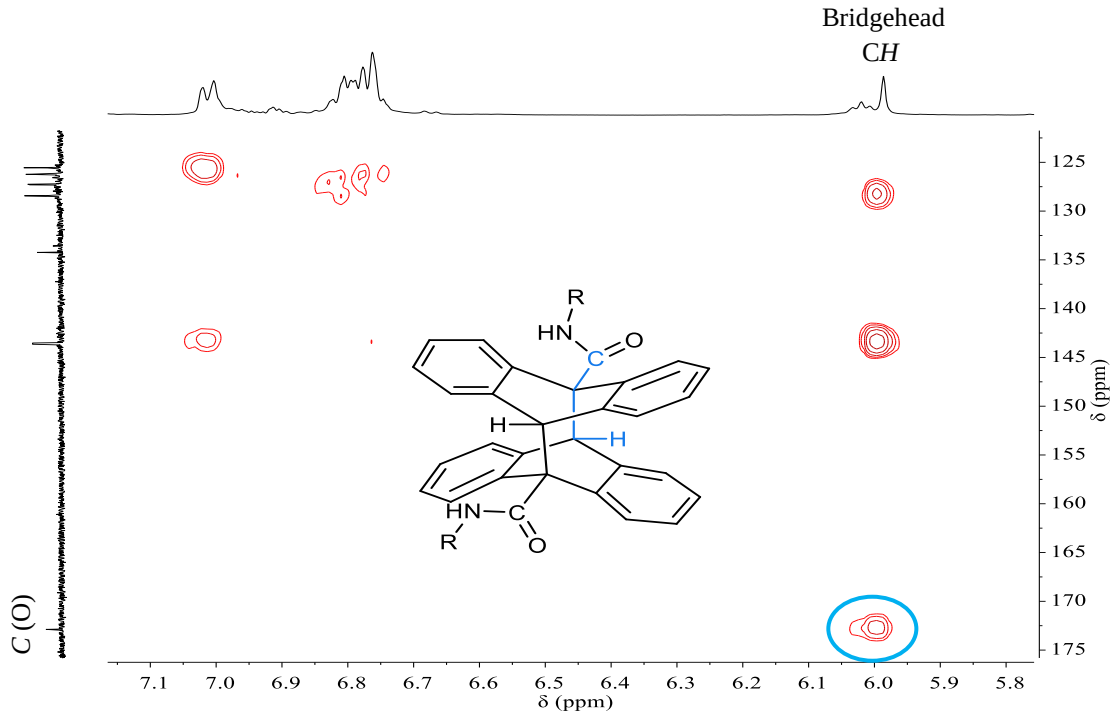

Figure 9- ^{1}H-^{13}C HMBC spectrum showing the multiple bond correlation between the bridgehead C*H* proton and amide carbonyl carbon (indicated in blue) of the head-to-tail arrangement of dimerised polymer **1** with three bonds between the respective ^{13}C and ^{1}H nuclei.

Although bis-anthracene polymer **1** provided useful spectroscopic analysis of the UV-dimerisation of anthracene units within a polymer structure, its application as a UV-curing component for inkjet formulations is limited as the linear polymer cannot form a cross-linked, insoluble network, and therefore remains soluble, even following 24 hours of UV-irradiation. UV-curing formulations are required to transition from a soluble formulation to an insoluble network upon UV irradiation, and this is not demonstrated using the linear system **1**. The formation of an insoluble polymer network is more achievable using a material that is able to cross-link, such as a branched system, rather than one which forms predominately cyclic or chain-extended materials.

3.2.3 Tris-anthracene capped PEG as a UV-crosslinking polymer for inkjet formulations

Formation of insoluble, cross-linked networks was achieved by designing a branched anthracene terminated polymer with a PEG backbone. Glycerol ethoxylate **6** (M_n = 1000 g mol^{-1}) was functionalised with anthracene moieties by reaction with 9-anthracene acyl chloride **5** as described previously (see Scheme 2). Tris-anthracene polymer **2**, unlike linear polymer **1**, formed a cross-linked network with UV-irradiation as depicted in Scheme 4.

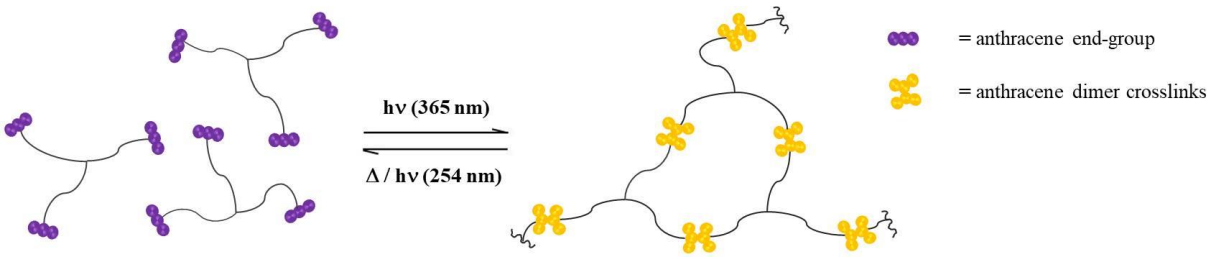

Scheme 4- Schematic depicting the reversible formation of a cross-linked polymer network (yellow) following irradiation of the branched polymer **2** (purple) with UV light >365 nm.

Tris-anthracene polymer **2** was obtained as a viscous, yellow-brown oil, which was irradiated both neat and in solution (acetonitrile, 100 mg mL^{-1}) to monitor the dimerisation of anthracene units. Solution state studies were attempted using UV-vis spectroscopy. A solution of polymer **2** in acetonitrile (100 mg mL^{-1}) was irradiated under a 36 W LED-UV lamp with a UV wavelength range of 350–500 nm. Aliquots were taken at 0, 1 and 2 hours of UV-irradiation and a decrease in anthracene absorption peaks was observed (Figure 10). However, following 2 hours of irradiation an insoluble network, which precipitated out of solution had been formed and further spectroscopic analysis could not be achieved.

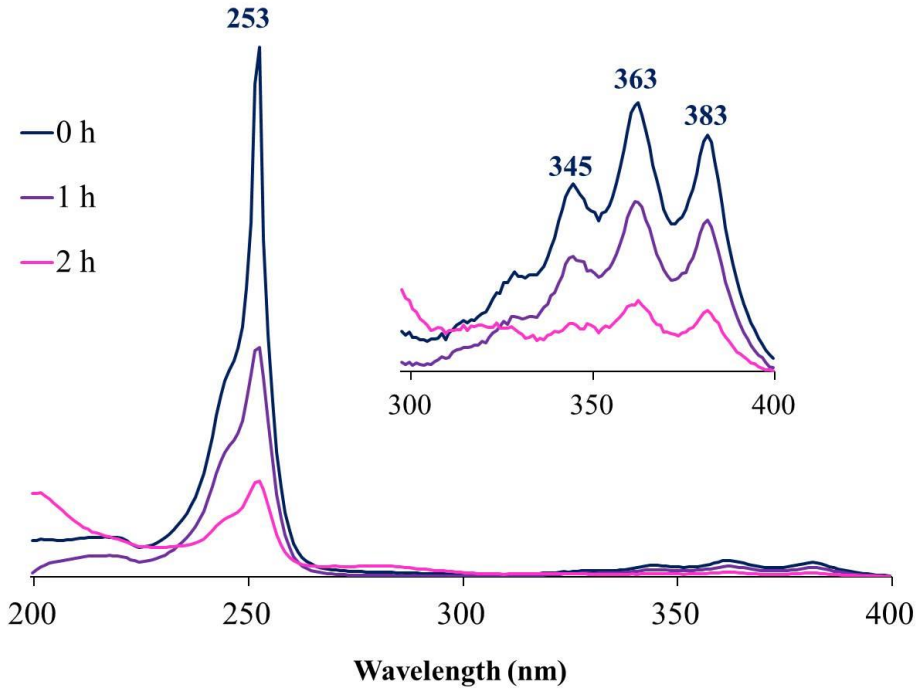

Figure 10- UV-vis spectroscopic analysis of aliquots of polymer **2** following irradiation for 0, 1 and 2 hours. After 2 hours an insoluble material had precipitated from solution and further analysis could not be performed.

In the light of this preliminary data, physical characteristics of polymer **2** throughout UV-irradiation were investigated using solid state techniques. The oil-like nature of tris-anthracene polymer **2** provided sufficient flow in its neat form to permit UV-dimerisation of anthracene units without the requirement for dissolution.

Lap shear tensiometry of UV-cured samples of polymer **2** was conducted to determine the change in lap shear modulus of polymer **2** following different periods of exposure to UV-irradiation. The lap shear modulus is determined by the relationship between the force at break (N) and the area of the lap shear sample (mm^2). Higher values of lap shear modulus indicate a higher shear strength of the material in question (Equation 1).

$$\text{Lap shear modulus} = \frac{\text{Force at break (N)}}{\text{Area of sample (mm}^2\text{)}} \qquad \text{(Equation 1)}$$

A sample of polymer **2** (10 mg) was applied to one end of a glass microscope slide and a second glass slide placed on top with an overlap of 10 mm, ensuring that the polymer was spread evenly as shown in Figure 11. Four sets of three identical samples were prepared and irradiated under UV (350–500 nm) for periods of 0, 2, 5 and 18 hours.

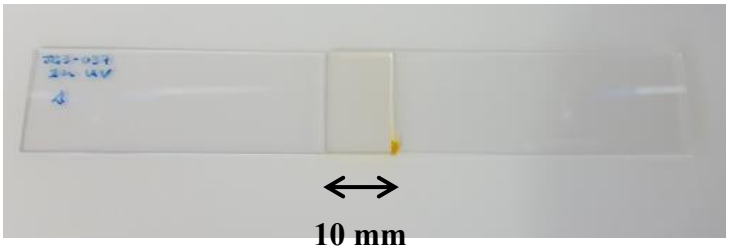

Figure 11- Preparation of an example lap shear sample with a thin layer of tris-anthracene PEG **2** spread evenly within the 10 mm overlap between two glass microscope slides.

Lap shear testing was performed according to a standardised procedure.[55] The initial samples demonstrated an average lap shear modulus of 0, which is related to the shear strain of the viscous polymer **2** without any cross-linking. Irradiation of polymer **2** resulted in an increase in lap shear modulus over extended periods of irradiation (Figure 12). This change was attributed to the dimerisation of anthracene units in polymer **2** and formation of a cross-linked network. Despite the minimal increase in lap shear modulus from 0 to 2 hours of irradiation, a polymeric film was observed, indicating formation of a weakly cross-linked network when compared to that of 18 hours, which shows a much larger lap shear modulus and therefore a stronger cross-linked network.

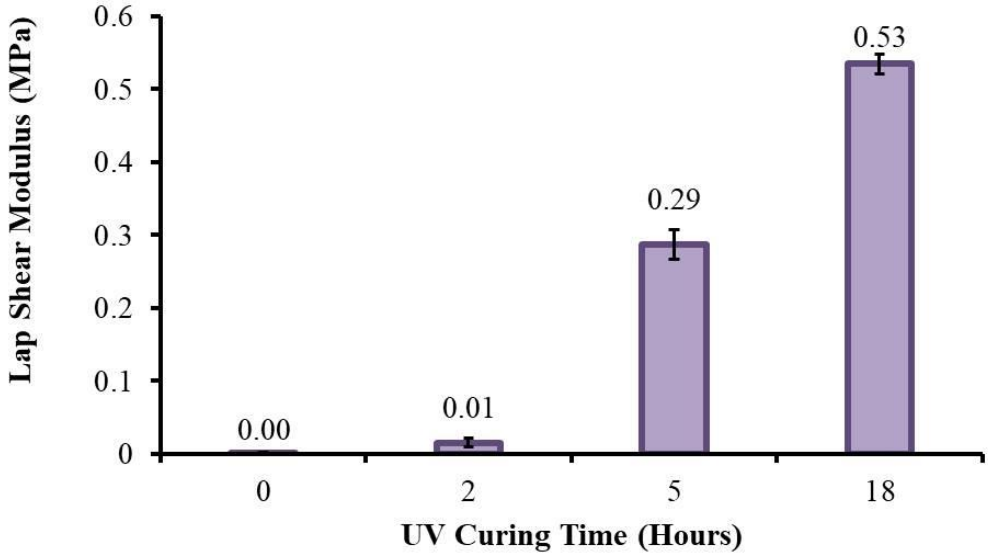

Figure 12- Plot of the respective lap shear moduli for samples of polymer **2** irradiated for 0, 2, 5 and 18 hours showing an overall increase in lap shear modulus of 0.53 MPa following 18 hours of UV irradiation with a 36 W lamp (200 W cm^{-1}). Error bars were acquired by calculation of the standard deviation of the 3 sample repeats.

Rheometric analysis of polymer **2** was also conducted during UV irradiation to determine the visco-elastic point of the material as it transitions from a viscous polymer to a viscoelastic polymeric network. An oscillatory rheometer fitted with a quartz plate was used in conjunction with a 200 W cm^{-1} UV light (350–500 nm). The UV-lamp fitted to the rheometer was much more powerful than the 36 W lamp used for previous studies and the quartz lamp permitted complete passage of UV light, and therefore a more rapid photodimerisation process was expected. Both the storage and loss modulus of polymer **2** were recorded as a function of the irradiation time.

Tris-anthracene PEG **2** shows viscous properties with a greater value for loss modulus (G″) than storage modulus (G′). After 660 seconds of UV-irradiation, the storage and loss modulus of polymer **2** cross-over and the polymer reached its viscoelastic point. From 660 seconds until the full length of irradiation (1000 seconds) polymer **2** acts as a viscoelastic material with a storage modulus greater than its loss modulus. The formation of a viscoelastic material was further confirmed visually by the flexible, elastomeric, insoluble film produced (see (b) in Figure 13).

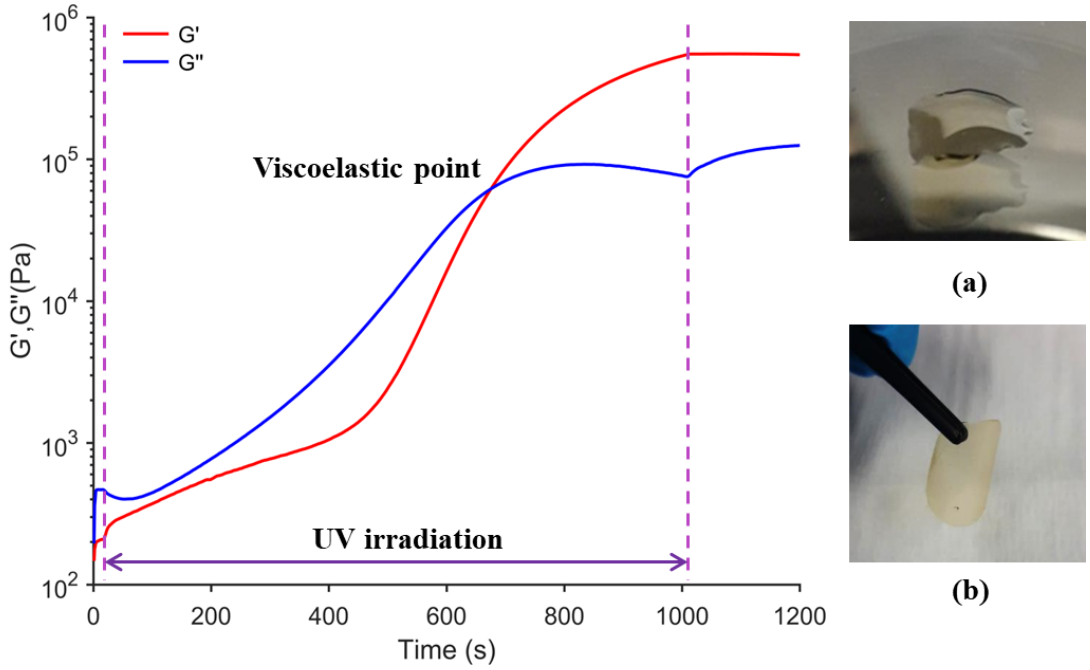

Figure 13- Rheometric analysis of *in situ* UV irradiation of tris-anthracene polymer showing changes in storage (G') and loss (G") modulus and: a) appearance of uncrosslinked oil **2** and b) crosslinked film following 1000 seconds of irradiation. Oscillatory rheometry was performed with strain set to 0.1% using a 200 W UV lamp with 350-500 nm filter as an irradiation source.

3.2.4 Dielectric cure monitoring of tris-anthracene polymer 2

The curing of UV-formulations can be monitored using a technique known as dielectric cure monitoring. This technique is more commonly used for the cure-monitoring of thermosets such as polyurethanes, epoxy resins and acrylics, which are cured by heating to elevated temperatures to form cross-linked networks.[56] Throughout the curing process, the dielectric properties of the material namely; the permittivity (ε') and log ion viscosity (ρ_{DC}) are measured using an electrode. The cure of the material is monitored using the log ion viscosity, also known as frequency dependant resistivity, which is determined by the ionic mobility through the material.[56] As the material forms a cross-linked network, the mobility of ions is hindered and the resistivity, and therefore the log ion viscosity increases.

This technique was conducted using a comb-type electrode attached to a scaled down version of Domino Printing Sciences UV production line, known as a slider, to monitor the UV-curing of tris-anthracene polymer **2**. The UV slider at Domino Printing Sciences utilises two lamps; an LED lamp followed by a second mercury arc UV lamp (Figure 14).

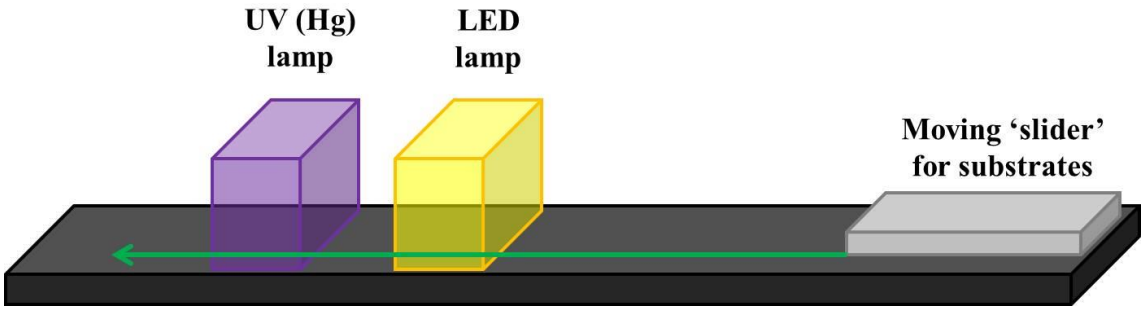

Figure 14- Schematic representation of the UV 'slider' at Domino Printing Sciences at Bar Hill. The substrates with UV-curable material were attached to the moving slider with magnets and passed under the two successive UV and LED lamps at a constant speed. The lamps are only initiated by the approach of the moving slider and turn off once the slider has passed.

The dielectric properties of polymer **2** were recorded following each pass under the UV slider, with both lamps on maximum illumination and a slider speed of 10 m min^{-1}. The log ion viscosity of polymer **2** increased with each pass under the LED and mercury arc lamps, revealing a decrease in the ionic mobility within the structure as the extent of cross-linking increases via photodimerisation of anthracene moieties (Figure 15).

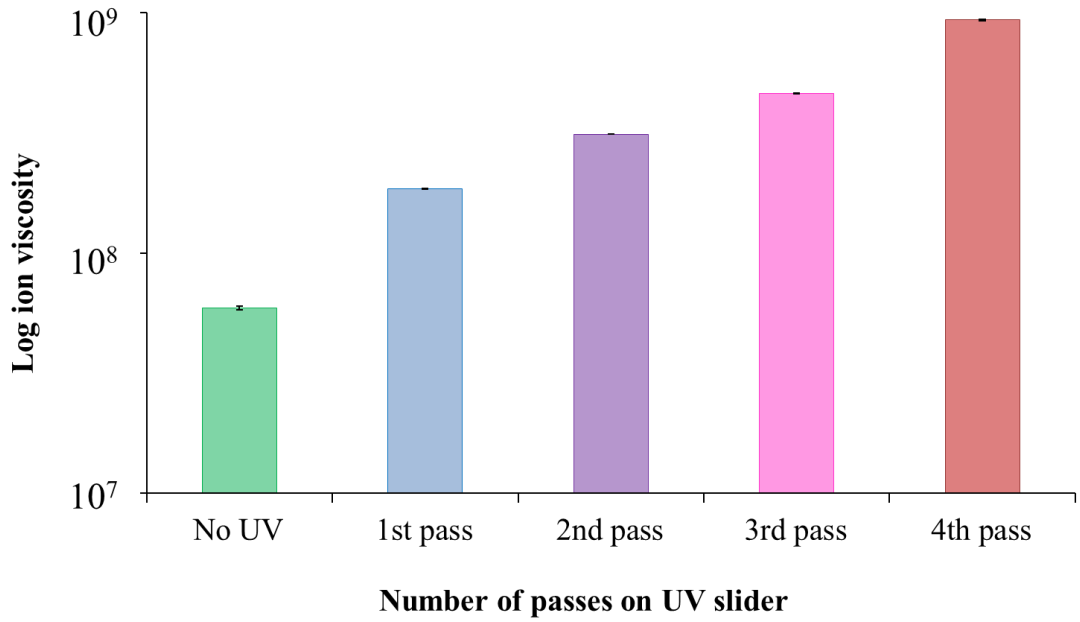

Figure 15- Graph showing the increase in log ion viscosity of polymer **2** following each pass along a scaled down UV-curing production line. The increase in log ion viscosity is recorded indicating an increase in mechanical properties of the polymer as a result of UV-photodimerisation of anthracene moieties. The values displayed show the average log ion viscosity value recorded over a 12 second period following UV-irradiation. Error bars were calculated using standard deviation from 2000 data points recorded over a 12 second period.

The increase in log ion viscosity relates to an increase in the mechanical viscosity of polymer **2**. The data are in agreement with the rheometric analysis and lap shear tensiometry, which also demonstrated an increase in the mechanical properties of **2** following UV-irradiation.

As well as improved mechanical properties when compared to polymer **2**, the films produced proved to be insoluble (at 2–10 mg mL^{-1}) in MEK, acetone, THF, CH_2Cl_2 and $CHCl_3$ which is beneficial for their application in formulations to produce printed images that require a degree of solvent resistance.

3.2.5 Inkjet Deposition of Anthracene-Capped Polymers

The ability to deposit both polymers **1** and **2** via inkjet printing was tested to determine their suitability as inkjet inks. The polymers were formulated as 100 mg mL^{-1} solutions in THF/1,2-hexanediol (1:1 v/v) as utilised in previous studies.[47–49] Both of the anthracene-capped polymers were deposited successfully onto non-optically brightened card as inkjet inks using a Fujifilm Dimatix™ Materials Printer DMP-2800 DOD printhead to produce clear, pale yellow images, which were barely visible to the naked eye (see Figure 16). Illumination under a 254 nm UV lamp revealed characteristic blue emission from the anthracene moieties within the polymer network, which permitted visualisation of the printed image, thus confirming the deposition of the material onto the substrate (Figure 16(b)).

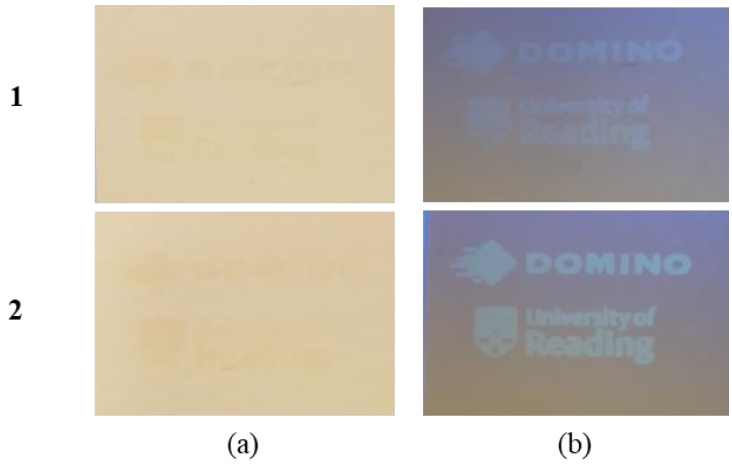

Figure 16- Polymers **1** and **2** deposited onto non-optically brightened card using a Dimatix™ drop-on-demand inkjet printhead showing the images under (a) visible light and (b) UV light (254 nm) for clarity, with fluorescence arising from excitation of anthracene moieties.

Although deposition in these solvent conditions was effective, the low volatility and large percentage of 1,2-hexanediol used in the formulation of polymers **1** and **2** resulted in slow evaporation of carrier solvent from the print. In a high throughput printing environment fast drying prints are desired, therefore a more volatile humectant was required to permit rapid UV-curing. Although polymer **1** was printable, it did not form an insoluble, UV-cross-linked network and therefore did not exhibit the

desired durability required for a UV-cured print. However, polymer **2** did demonstrate insolubility in common organic solvents post-UV-irradiation and therefore was investigated further as a potential UV-curable ink.

An alternative solvent, 1,2-propanediol (b.p. 188 °C) was used *in lieu* of 1,2-hexanediol (b.p. 223 °C) as a more volatile humectant to decrease drying time of prints containing polymer **2**. Two novel formulations of polymer **2** (100 mg mL^{-1}) were produced employing different solvent ratios of THF and 1,2-propanediol. The viscosities of the solutions were measured and compared to the previous formulation containing 1,2-hexanediol (Table 1).

Table 1- Viscosities of formulations of polymer **2,** using formulations of THF with [a]1,2-hexanediol or [b] 1,2-propanediol. Viscosity values were recorded using an Anton Paar Stabinger viscometer, with a polymer concentration of 100 mg mL^{-1}.

	Formulation ratio (THF:humectant)		
Viscosity (cP)	**1:1[a]**	**9:1[b]**	**8:2[b]**
	2.9	0.68	0.86

The minimum viscosity required for successful drop-on-demand printing using the Dimatix™ is 2 cP, therefore a viscosity modifier, cellulose acetate butyrate (CAB), was added in increments to the formulations based upon 1,2-propanediol to increase the overall viscosity of the formulations (Table 2).

Table 2- Viscosity modification of formulations of polymer **2** in [a]1,2-propanediol and [b]THF (10:90 and 20:80 v/v with polymer **2** at a concentration of 100 mg mL^{-1}) using cellulose acetate butyrate (CAB) as a viscosity modifier.

Solvent ratio[(a:b)]	**Amount of CAB in formulation (wt%)**							
	0	**0.1**	**0.2**	**0.5**	**1.0**	**1.5**	**2.0**	**2.5**
10:90	0.68	0.72	0.77	0.91	1.21	1.55	1.89	2.35
20:80	0.86	0.91	0.96	1.14	1.45	1.91	2.42	-

Formulation viscosities of above 2 cP were achieved by the addition of 2 and 2.5 weight percent of CAB to the 1:9 v/v and 1:4 v/v 1,2-propanediol:THF formulations, respectively. Solvent blue 44, a copper phthalocyanine dye was included in these formulations, as a solvent soluble dye, to aid visualisation of the printed image and the formulations were deposited using a drop-on-demand print

head to determine their printability and quality of print. The differences between each carrier solvent can be seen in Figure 17.

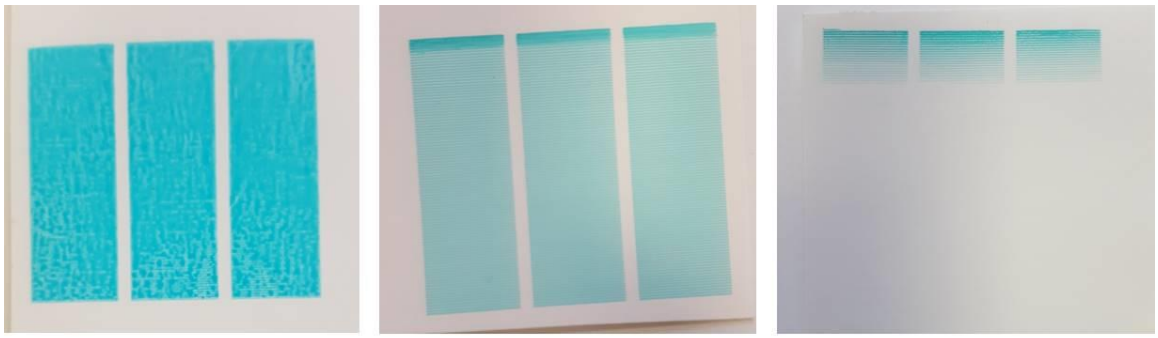

Figure 17- Deposition of formulations of polymer **2** with Solvent blue 44 dye added as a visual aid using different carrier solvents (a) 1:1 v/v 1,2-hexanediol: THF (b) 2:8 v/v 1,2,-propanediol: THF (2 wt% CAB) and (c) 1:9 v/v 1,2,-propanediol: THF (2.5 wt% CAB).

As previously discussed, the use of 1,2-hexanediol as a carrier solvent (see Figure 17 (a)) produced slow drying prints, resulting in a high risk of smudging or transfer of the printed image, even after UV-curing. The substitution of 1,2-hexanediol (1:1 v/v) with 1,2-propanediol (1:9 v/v) in THF resulted in failure of print. The amount of humectant in the formulation was concluded to be insufficient to prevent evaporation of the carrier solvent at the nozzle of the DOD printhead, resulting in nozzle blockage. Increasing the ratio of 1,2-propanediol:THF to 1:4 v/v provided a sufficient increase in humectant to prevent nozzle blockage and produced an image within a faster drying time (Figure 17 (b)).

A formulation of polymer **2** in 1,2-propanediol:THF (1:4 v/v 100 mg mL^{-1}) with CAB (2 wt%) was therefore utilised with the inclusion of three dye compounds to produce UV-curable coloured images. Solvent blue 44 (Cu phthalocyanine), red 8 (Cr azo) and yellow 151 (Co azo) dyes (5 mg mL^{-1}) were used to produce a basic colour palette for inkjet deposition. The solvent soluble transition metal dyes were selected as they show good solubility in a range of organic solvents and exhibit strong resistance to light and heat, indicating that they would not degrade under UV-light. The coloured inks were deposited successfully using a Dimatix™ drop-on-demand printhead to produce clear, sharp prints. The colour palette produced can be extended by overprinting of the inks to produce red, yellow, blue, orange, green and purple prints (Figure 18 (a-f)).

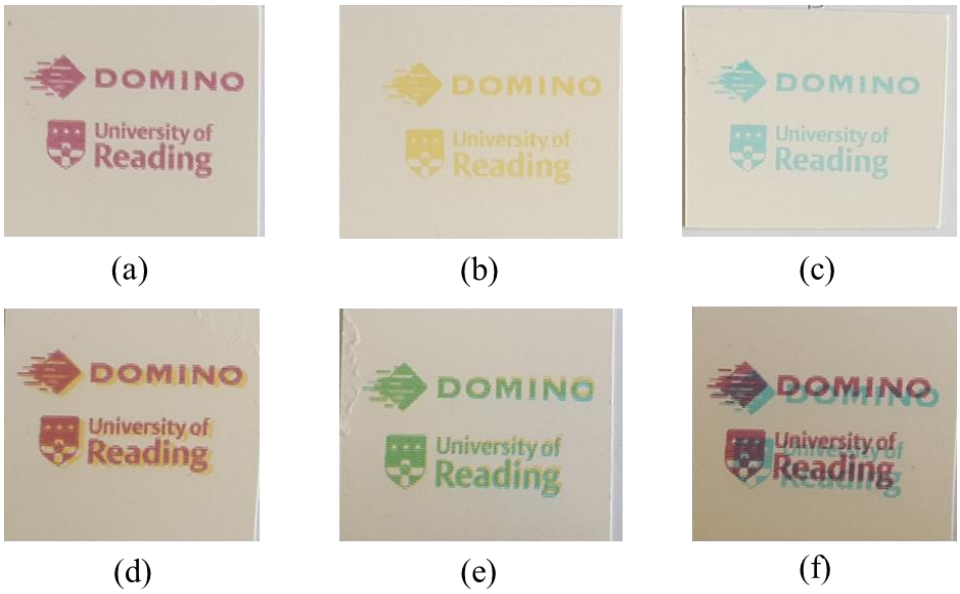

Figure 18- Deposition of formulations of polymer **2** with inclusion of Valifast ® dyes to produce red, yellow and blue prints (a-c) as well as orange, green and purple (d-f) images produced by overprinting of a-c.

3.2.6 UV-curing of Dye-Containing Formulations of Tris-anthracene Polymer 2

The tris-anthracene PEG **2** and dye formulations were deposited onto sheen card from a solution of THF, using a draw-down bar to produce a 24 μm film. The coloured inkjet formulations were then irradiated using a 200 W cm^{-2} UV lamp with a 350–500 nm waverange for 0, 1, 2, 3 and 4 seconds. After each of these passes, peel tests were performed to determine the extent of curing of the different formulations. Tape was placed on top of the film of polymer **2** and pressure applied. The tape was then peeled away and the amount of material removed with the tape analysed (see Figure 19).

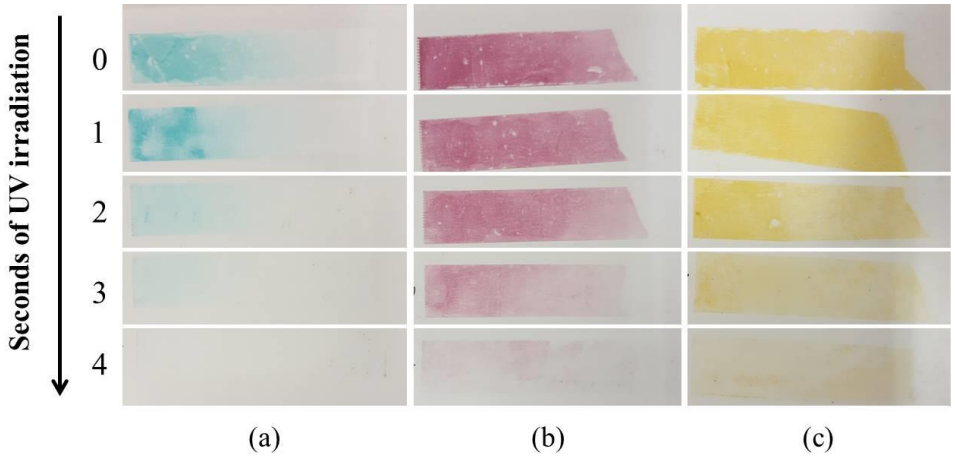

Figure 19- Peel tests showing the extent of UV cure of polymer **2** in the presence of (a) Solvent blue 44, (b) Solvent red 8 and (c) Solvent yellow 151 following 0–4 seconds of irradiation with a 200 W cm^{-2} UV lamp (350–500 nm).

The Solvent blue 44 dye demonstrated the least interference with the UV photodimerisation of anthracene units in polymer **2**, showing the least material removed by peel test, with complete cure, (no material being removed) following irradiation for 4 seconds. The Solvent red 8 and yellow 151 dyes, on the other hand, showed greater interference in the curing process of polymer **2**. Following two seconds of irradiation the difference in amount of material removed by the peel test for the red (b) and yellow (c) formulations was much larger than for the blue dye (a) (see Figure 19). However, all three dye formulations exhibited curing following 4 seconds of irradiation with the 200 W cm^{-2} UV lamp, indicating that polymer **2** is a suitable UV curable material for inclusion in UV inkjet formulations.

3.3 Conclusions

A series of novel UV-curable polymers containing anthracene moieties has been developed. The linear system (polymer **1**) was fully characterised by spectroscopic analysis throughout the UV-dimerisation process, allowing definitive confirmation of dimer formation using 2-dimensional ^{1}H NMR spectroscopy. The branched system (polymer **2**) formed a crosslinked network upon UV-irradiation to produce an elastic material with improved physical properties as well as insolubility in organic solvents such as MEK, acetone, $CHCl_3$, CH_2Cl_2 and THF.

Both the linear and branched polymers were relatively low molecular weight and demonstrated good solubility in MEK, acetone, $CHCl_3$, CH_2Cl_2 and THF, allowing for facile formulation and deposition of the materials using a drop-on-demand printhead. The branched system (polymer **2**) was investigated further as a UV-curable inkjet component and cured within 4 seconds under UV lamps (LED then mercury arc 200 W cm^{-2}) on a slow moving (5 m min^{-1}) model for a production line belt.

Polymer **2** has also shown UV curing with the inclusion of dye compounds in the formulation. The Valifast® range of dyes was investigated and it was found that the blue dye showed little to no interference in the UV curing of polymer **2**. The red and yellow dyes indicated slight interference in the cure times of polymer **2**, with small amounts of the print being removed by peel test after 4 seconds of UV irradiation. The dyes did not completely disrupt the curing process as each second of UV-irradiation resulted in less material being removed by peel test. Polymer **2** is therefore a material that has potential as a UV-curable polymer for future use in UV-inkjet formulations.

3.4 Experimental

Reagents, spectral data and printing of formulations were carried out as in Section 2.4. Fluorescence spectroscopy was performed using a Cary Eclipse Fluorimeter at a waverange of 400–600 nm. Viscometry data was recorded using an Anton Paar Stabinger viscometer. Rheometric data were recorded on an Anton Paar Modular Compact Rheometer (MCR) 302 equipped with a 200 W cm^{-2} Omnicure series 2000 mercury arc UV lamp with a waverange of 350–500 nm. UV-curing, manufacturing line tests were carried out using a UV slider moving at 10 m min^{-1} at Domino Printing Sciences that was equipped with an LED lamp and a 200 W cm^{-2} mercury arc UV lamp with a waverange of 350–500 nm.

3.4.1 Synthesis of 9-anthracene acyl chloride 5 [57]

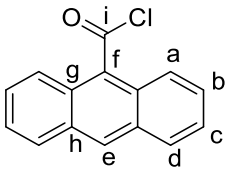

To 9-anthracene carboxylic acid (3.00 g, 13.5 mmol) was added thionyl chloride (15.0 mL) and *N*-dimethylformamide (0.10 mL). The solution was stirred for 18 hours and the volatiles removed *in vacuo.* The remaining solid was re-dissolved in dry chloroform and solvent removed *in vacuo* to yield a dark yellow compound (3.12 g, 96%), m.p: 88–91 °C, (lit. 89–91 °C)[57]; IR (ATR) ν/cm^{-1}: 3056 (aromatic C–H), 1762 (C=O), 1557 (aromatic C=C), 1524 (aromatic C=C), 735 (C–Cl) ; ^{1}H NMR (400 MHz/$CDCl_3$) δ ppm: δ 8.60 (1H, s, H_e), 8.13 (2H, d, J = 8.8 Hz, H_d), 8.07 (2H, d, J = 8.5 Hz, H_a), 7.68 – 7.60 (2H, m, H_b), 7.55 (2H, t, J = 7.5 Hz, H_c);^{13}C NMR (100 MHz/$CDCl_3$) δ ppm: 170.8 (C_i), 130.9 (C_e), 128.9 (C_a), 128.1 (C_b), 126.3 (C_{g+h}), 126.1 (C_c), 124.1 (C_d).

3.4.2 Synthesis of bis-anthracene terminated PEG 1

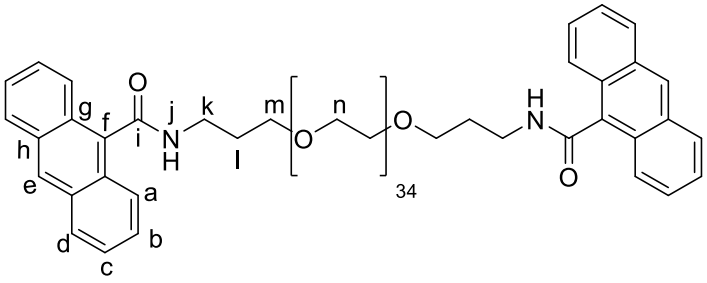

Bis-(3-aminopropyl) terminated polyethylene glycol (M_n ~1500 g mol^{-1}, $Đ$ = 1.08) (3.00 g, 2.00 mmol) was dissolved in dry THF (50 mL) with gentle heating and stirring under nitrogen. 9-Anthracene acyl chloride (1.30 g, 5.00 mmol) was added and the solution was stirred for 5 minutes. Triethylamine (1.00 mL, 7.00 mmol) was then added and the solution was stirred for a period of 48 hours. The solution was then concentrated *in vacuo* and resultant solid re-dissolved in the minimum volume of THF. Any undissolved material was removed by filtration and the filtrate concentrated *in vacuo* before

precipitating the product into diethyl ether held in an acetone/dry ice bath. The solid was collected by filtration whilst cold. The solid obtained was dissolved in chloroform and solvent removed to yield a waxy brown solid (2.97 g, 78%). IR (ATR) ν/cm^{-1}: 3425 (N–H), 2915, 2870 (aromatic C–H), 1720 (C=O amide), 1095 (C–O ether); ^{1}H NMR (400 MHz/$CDCl_3$) δ ppm: δ 8.44 (2H, s, H_e), 8.07 (4H, d, *J* = 8.5 Hz, H_d), 7.98 (4H, d, *J* = 8.1 Hz, H_a), 7.47 (8H, m, H_{b+c}), 7.06 (2H, s, H_j), 3.83 (4H, m, H_k), 3.72–3.24 (152H, m, H_{n+m}), 2.11–1.90 (4H, m, H_l); ^{13}C NMR (100 MHz/$CDCl_3$) δ ppm: 169.4 (C_i), 132.6 (C_h), 131.2(C_g), 128.5 (C_a), 128.1 (C_f), 128.0 (C_e), 126.6 (C_b), 125.6 (C_c), 125.4 (C_d), 70.6 (C_n), 61.8 (C_m), 38.9 (C_k), 29.3 (C_l); GPC (THF) M_n = 2200 M_w = 2500 *Đ* =1.13; DSC: T_g = 30.9 °C T_m = 47.1 °C; MALDI-TOF MS: m/z calculated for $[C_{104}H_{168}N_2NaO_{37}]^+$ = 2060.1224 Da ± 44n Da; Found = 2060.9120 ± 44n Da.

3.4.3 Synthesis of tris-anthracene terminated PEG 2

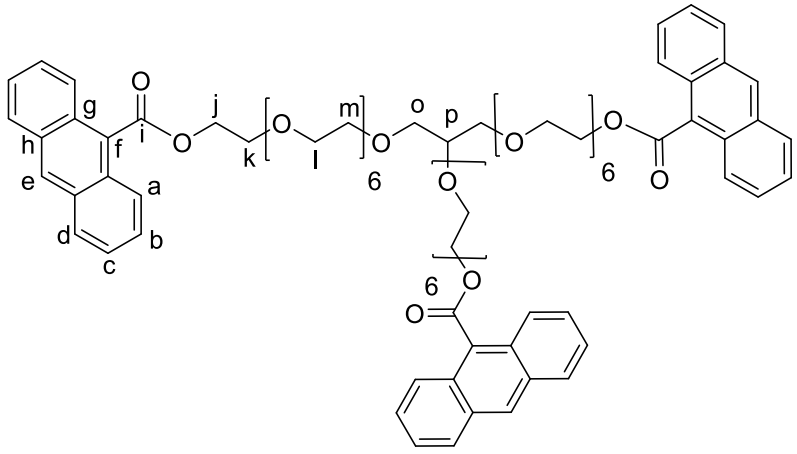

To a stirred solution of glycerol ethoxylate (M_n ~ 1000 g mol^{-1}) (3.00 g, 3.00 mmol) in dry THF (50 mL) under nitrogen was added 9-anthracene acyl chloride (3.00g, 12.5 mmol). Following dissolution, triethylamine (3.00 mL, 21.5 mmol) was added and solution stirred for 48 hours. The solution was concentrated *in vacuo* and the resultant solid re-dissolved in the minimum volume of THF. Any undissolved material was removed by filtration and the filtrate concentrated *in vacuo* and then precipitated into diethyl ether held in an acetone/dry ice bath. The solid thus produced was collected via filtration whilst cold. The solid was then dissolved in chloroform and the solvent removed to yield a yellow-brown oil (3.5 g, 72%). IR (ATR) ν/cm^{-1}: 2855 (aromatic C–H), 1714 (C=O ester), 1346, 1288, (C–O ester), 1095 (C–O ether); ^{1}H NMR (400 MHz/$CDCl_3$) δ ppm: 8.42 (3H, s, H_e), 8.07 (6H, d, *J* = 8.7 Hz, H_d), 7.92 (6H, d, *J* = 8.1 Hz, H_a), 7.52–7.35 (12H, m, H_{b+c}), 4.75 (6H, apparent t, H_j), 3.89 (6H, m, H_k), 3.58 (81H, m, $H_{l+m+o+p}$); ^{13}C NMR (100 MHz/$CDCl_3$) δ ppm: 169.5 (C_i), 131.0 (C_g), 129.5 (C_e), 128.6 (C_a), 127.7 (C_h), 127.0 (C_c), 125.5 (C_b), 125.3 (C_d), 70.7 (C_{l+m+o}), 69.2 (C_k), 64.6 (C_j), 61.8 (C_p); GPC (THF) M_n = 1600, M_w =1800, *Đ* =1.14; DSC: T_g = –24.0 °C; MALDI-TOF MS: m/z calculated for $[C_{88}H_{112}KO_{26}]^+$ = 1624.9132 Da ± 44n Da; Found = 1624.9361 ± 44n Da.

3.5 References

1. The Market Reports, *Global UV Offset Inks Market Research Report*, 2019, pp. 1-109.

2 M. Graindourze, *UV-Curable Inkjet Inks and Their Applications in Industrial Inkjet Printing, Including Low-Migration Inks for Food Packaging*, In: Industrial Inks For Inkjet Printing, John Wiley and Sons Ltd, Weinheim, Germany, 2017, pp. 129–150.

3 S. Magdassi, *The Chemistry of Inkjet Inks*, World Scientific Publishing, Singapore, 2010.

4 S. E. Edison, *UV-Curable Inkjet Inks Revolutionize Industrial Printing*, Radtech, 2006, pp. 28-33.

5 Z. W. Wicks Jr, F. N. Jones, S. Peter Pappas, *Organic Coatings*, in: *Organic Polymers and Coatings*, John Wiley and Sons Ltd, New Jersey, USA, 2007, pp. 574-593.

6 I. M. Hutchings and G. D. Martin, *Inkjet Technology for Digital Fabrication*, John Wiley and Sons Ltd, Chichester, UK, 2013.

7 S. Yuan, S. Sargeant, J. Rundus, N. Jones, K. Nguyen and M. Street, *Recent Prog. Inkjet Technol. II*, 1999, 378–382.

8 R. J. Wojtecki, M. A. Meador and S. J. Rowan, *Nat. Mater.*, 2011, **10**, 14–27.

9 D. Habault, H. Zhang and Y. Zhao, *Chem. Soc. Rev.*, 2013, **42**, 7244–7256.

10 S. R. Trenor, A. R. Shultz, B. J. Love and T. E. Long, *Chem. Rev.*, 2004, **104**, 3059–3077.

11 E. Sato, S. Nagai and A. Matsumoto, *Prog. Org. Coatings*, 2013, **76**, 1747–1751.

12 Y. Chen and C. Jean, *J. Appl. Polym. Sci.*, 1996, **64**, 1759–1768.

13 Y. Chen and J. L. Geh, *Polymer*, 1996, **37**, 4473–4480.

14 P. O. Jackson, M. O'Neill, L. W. Duffy, P. Hindmarsh, S. M. Kelly and G. J. Owen, *Chem. Mater.*, 2001, **13**, 694–703.

15 R. H. Huyck, S. R. Trenor, B. J. Love and T. E. Long, *J. Macromol. Sci. Part A Pure Appl. Chem.*, 2008, **45**, 9–15.

16 Y. Chujo, K. Sada and T. Saegusa, *Macromolecules*, 1990, **23**, 2693–2697.

17 Y. Chen and C. Chou, *J. Polym. Sci. Part A Polym. Chem.*, 1995, **33**, 2705–2714.

18 Y. Chen and K. H. Chen, *J. Polym. Sci. Part A Polym. Chem.*, 1997, **35**, 613–624.

19 L. Kan, H. Cheng, B. Li, X. Zhang, Q. Wang, H. Wei and N. Ma, *New J. Chem.*, 2019, **43**, 2658–2664.

20 Y. Chen and J. L. Geh, *Polymer*, 1996, **37**, 4481–4486.

21 D. Gindre, K. Iliopoulos, O. Krupka, M. Evrard, E. Champigny and M. Sallé, *Molecules*, 2016, **21**, 1–13.

22 L. M. Minsk, J. G. Smith, W. P. van Deusen and J. F. Wright, *J. Appl. Polym. Sci.*, 1959, **11**, 302–307.

23 P. Gupta, S. R. Trenor, T. E. Long and G. L. Wilkes, *Macromolecules*, 2004, **37**, 9211–9218.

24 J. M. Rochette and V. S. Ashby, *Macromolecules*, 2013, **46**, 2134–2140.

25 A. C. Fonseca, M. S. Lima, A. F. Sousa, A. J. Silvestre, J. F. J. Coelho and A. C. Serra, *Polym. Chem.*, 2019, **10**, 1696–1723.

26 X. Hu, X. Chen, H. Cheng and X. Jing, *J. Polym. Sci. Part A - Polym. Chem.*, 2009, **47**, 161–169.

27 J. van Damme, O. van den Berg, J. Brancart, L. Vlaminck, C. Huyck, G. van Assche, B. van Mele and F. Du Prez, *Macromolecules*, 2017, **50**, 1930–1938.

28 M. Coursan, J. P. Desvergne and A. Deffieux, *Macromol. Chem. Phys.*, 1996, **197**, 1599–1608.

29 Y. Zheng, M. Micic, S. V. Mello, M. Mabrouki, F. M. Andreopoulos, V. Konka, S. M. Pham and R. M. Leblanc, *Macromolecules*, 2002, **35**, 5228–5234.

30 P. Froimowicz, H. Frey and K. Landfester, *Macromol. Rapid Commun.*, 2011, **32**, 468–473.

31 L. A. Connal, R. Vestberg, C. J. Hawker and G. G. Qiao, *Adv. Funct. Mater.*, 2008, **18**, 3315–3322.

32 D. Han, H. Lu, W. Li, Y. Li and S. Feng, *RSC Adv.*, 2017, **7**, 56489–56495.

33 K. Rameshbabu, Y. Kim, T. Kwon, J. Yoo and E. Kim, *Tetrahedron Lett.*, 2007, **48**, 4755–4760.

34 S. Tazuke and N. Hayashi, *J. Polym. Sci. Polym. Chem. Ed.*, 1978, **16**, 2729–2739.

35 Y. K. Song, K. H. Lee, W. S. Hong, S. Y. Cho, H. C. Yu and C. M. Chung, *J. Mater. Chem.*, 2012, **22**, 1380–1386.

36 X. Zhang, Y. Gao, Y. Lin, J. Hu and Y. Ju, *Polym. Chem.*, 2015, **6**, 4162–4166.

37 J. T. Goldbach, T. P. Russell and J. Penelle, *Macromolecules*, 2002, **35**, 4271–4276.

38 S. Paul, W. Knoll and K. Müllen, *Acta Polym.*, 1994, **45**, 235–243.

39 L. López-Vilanova, I. Martínez, T. Corrales and F. Catalina, 2014, **56**, 69–76.

40 X. A. Trinh, J. Fukuda, Y. Adachi, H. Nakanishi, T. Norisuye and Q. Tran-Cong-Miyata, *Macromolecules*, 2007, **40**, 5566–5574.

41 H. Xie, M. J. He, X. Y. Deng, L. Du, C. J. Fan, K. K. Yang and Y. Z. Wang, *ACS Appl. Mater. Interfaces*, 2016, **8**, 9431–9439.

42 J. F. Xu, Y. Z. Chen, L. Z. Wu, C. H. Tung and Q. Z. Yang, *Org. Lett.*, 2013, **15**, 6148–6151.

43 G. W. Breton and X. Vang, *J. Chem. Educ.*, 1998, **75**, 81–82.

44 R. Morě, G. Busse, J. Hallmann, C. Paulmann, M. Scholz and S. Techert, *J. Phys. Chem. C*, 2010, **114**, 4142–4148.

45 H. Bouas-Laurent, A. Castellan, J. P. Desvergne and R. Lapouyade, *Chem. Soc. Rev.*, 2001, **30**, 248–263.

46 H.-D. Becker, *Chem. Rev*, 1993, **93**, 145–172.

47 L. R. Hart, J. L. Harries, B. W. Greenland, H. M. Colquhoun and W. Hayes, *ACS Appl. Mater. Interfaces*, 2015, **7**, 8906–8914.

48 L. R. Hart, J. L. Harries, A. Clifton, H. M. Colquhoun, and W. Hayes, Inkjet Composition, Patent No: WO 2014111722 A1, 24th July 2014.

49 L. R. Hart, N. A. Nguyen, J. L. Harries, M. E. Mackay, H. M. Colquhoun and W. Hayes, *Polymer*, 2015, **69**, 293–300.

50 L. R. Hart, University of Reading, 2014.

51 N. Sugiyama, M. Iwata, M. Yoshioka, K. Yamada and H. Aoyama, *Bull. Chem. Soc. Jpn.*, 1969, **42**, 1377–1379.

52 H.-D. Becker, H.-C. Becker and L. Vratislav, *J. Photochem. Photobiol. A Chem.*, 1996, **97**, 25–32.

53 T. Salzillo, E. Venuti, C. Femoni, R. G. Della Valle, R. Tarroni and A. Brillante, *Cryst. Growth Des.*, 2017, **17**, 3361–3370.

54 H. Bouas-Laurent, A. Castellan and J.-P. Desvergne, *Pure Appl. Chem.*, 2007, **52**, 2633–2648.

55 ASTM, *Standard test method for Apparent Shear Strength of Single-Lap-Joint Adhesively Bonded Metal Specimens by Tension Loading (Metal-to-Metal)*, West Conshohocken. PA, 2019.

56 H. L. Lee, *The handbook of dielectric analysis and cure monitoring*, Lambient Technologies, Boston, USA, 2014, pp 1-145.

57 SynQuest Laboratories, *Anthracene-9-carbonyl chloride*, 2010, http://synquestlabs.com/product/id/67104.html. [Accessed: 30/07/19].

Chapter 4

Poly(fluorocarbinol)s as Soluble, Hydrophobic Polymer Binders for Inkjet Formulations

Abstract

In this chapter the synthesis of a series of poly(fluorocarbinol)s with varying molecular weights (M_n = 11,500–114,500 g mol^{-1}) is described and the application of these materials as colourless polymer binders for inkjet formulations is investigated. Initial inkjet deposition studies were performed using a Dimatix™ DOD printhead and revealed that the three lowest molecular weight polymers (M_n = 11,500–25,200 g mol^{-1}) exhibited the greatest potential as polymers for inkjet deposition. From these candidates, two of the poly(fluorocarbinol)s (M_n = 11,500 and 25,200 g mol^{-1}) were scaled up and their formulations (MEK as the solvent) were analysed pre-deposition using shear flow rheology and determined to act as either Newtonian (M_n = 11,500 g mol^{-1}) or near-Newtonian (M_n = 25,200 g mol^{-1}) fluids, highlighting their suitability as polymer additives for inkjet formulations.

Both polymers were prepared as inkjet formulations in MEK with Orasol Orange®, a cobalt dye-complex, to visualise the prints. The formulations were deposited successfully onto a variety of different packaging substrates using the Ax-series CIJ printhead producing high resolution prints without any evident satellite droplets. The polymers both showed excellent adhesion to glass, poly(ethylene terephthalate) (PET) and nylon, moderate adhesion to steel and poor adhesion to low density poly(ethylene) (LDPE) and polypropylene (PP). Magnified images of the jetstream exhibited good droplet formation, which was further demonstrated by the jet profiles of the poly(fluorocarbinol)s recorded during the printer run time. The potential of the polymeric materials to generate aerosols and cause subsequent build-up of residue material around the printhead during extended periods of printing was analysed using a DustTrak™ aerosol count. The lowest molecular weight poly(fluorocarbinol) (11,500 g mol^{-1}) was determined to pose minimal risk of polymer residue build-up in the printer, with an aerosol count of below 38 µg cm^{-3}. However, the higher molecular weight polymer (25,200 g mol^{-1}) exhibited some potential to cause build-up with a moderate aerosol count of 89 µg cm^{-3}. Both of the poly(fluorocarbinol)s demonstrated potential as polymeric binders for inkjet formulations, although the lower molecular weight polymer exhibited more desirable properties for a polymer additive for use on a commercial scale as a result of decreased aerosol generation and better droplet break-up in the jetstream.

4.1 Introduction

In inkjet printing, the field of coding and marking is one of the more established areas. Coding and marking is an important procedure and involves the printing of information such as batch numbers, location of manufacture and expiration dates that, in turn, allow for facile identification of the products

and their production path. Once deposited, this information needs to remain on the substrate, a task that is often not achievable using formulations containing solely carrier solvents and a pigment/dye, particularly for the wide variety of materials used in the packaging of materials. Polymeric materials have thus been included in a variety of inkjet formulations and can provide beneficial properties both during and after deposition.[1] The presence of a low concentration of polymeric materials in inkjet formulations can aid efficient droplet formation and reduce the generation of satellite droplets,[1–4] which, in turn, improves the resolution of the printed image. Polymers have also been used to modify the formulation viscosity,[5] improve pigment dispersion[1,2,6] and increase the permanence of the printed image.[2,7]

In the coding and marking industry, permanence of the print is extremely important as it ensures that the product information is legible throughout the required lifetime of the packaged product. However, despite the enhanced properties gained by the addition of polymer to an inkjet formulation, higher concentrations of polymers or the implementation of high molecular weight materials can have an adverse effect on drop generation and ejection from the nozzle.[3,4,8] Therefore, careful selection of polymer is required to produce an inkjet formulation that demonstrates useful post-deposition properties, but also demonstrates good droplet formation and minimal satellite drop generation. The polymeric materials selected need to demonstrate good solubility in the polar solvents used in the inkjet formulation, but also demonstrate a degree of hydrophobicity post-deposition to improve the permanence of the print.

It is known that polymers containing trifluoromethyl groups exhibit segregation of trifluoromethyl groups at the polymer-air interface[9] resulting in films with hydrophobic properties, low surface energies and chemical inertness to water.[10] The application of trifluoromethyl containing polymers as hydrophobic materials has been extensively investigated.[9–14] Banerjee *et al*. produced a series of trifluoromethyl containing polymers via radical copolymerization of 2,2,2-trifluoroethyl α-fluoroacrylate (FATRIFE) with different molar equivalents of 2-(trifluoromethyl)acrylic acid (MAF) to produce a series of poly(FATRIFE-*co*-MAF) materials (Figure 1).

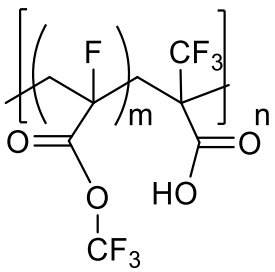

Figure 1- The structure of poly(FATRIFE-*co*-MAF) synthesised in the work of Banerjee *et al*.[10]

The hydrophobicity of the poly(FATRIFE-*co*-MAF) films varied according to the co-monomer ratio. Polymers with increasing MAF content (42 mol%) showed a decrease in hydrophobicity (water contact angle 81°) as a result of increased abundance of polar groups (COOH) when compared to those materials possessing only FATRIFE units (water contact angle 107°).[10]

In some cases the addition of trifluoromethyl groups to polymeric systems can aid solubility, as described in the studies reported by Liu *et al.*[14] Poly(ether ketone) (PEK) materials were produced both without and with trifluoromethylphenyl side groups (Figure 2) and it was found that the inclusion of trifluoromethylphenyl groups enhanced the solubility of the polymers. The materials produced showed enhanced solubility in organic solvents including tetrahydrofuran (THF), dimethylformamide (DMF), dimethylacetamide (DMAc) and *N*-methyl-2-pyrrolidone (NMP) when compared to the non-fluorinated PEK derivatives.[14]

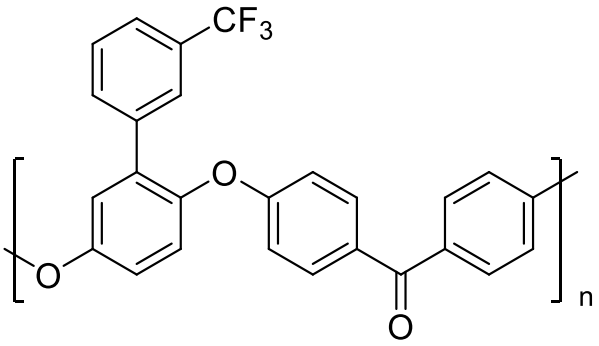

Figure 2- The PEK with trifluoromethylphenyl synthesised by Liu *et al.*[14] The novel material showed enhanced solubility over the corresponding unsubstituted PEK derivative.

Although the trifluoromethylated polymers discussed exhibited hydrophobicity when deposited as films, the solubility of the materials in polar solvents proved to be either very poor or non-existent, which renders the materials inutile for inkjet deposition purposes. However, the solubility of fluoropolymers in polar solvents could be improved by the incorporation of polar groups into the polymer architecture alongside the trifluoromethyl groups to produce materials that contain both hydrophilic and hydrophobic functionalities. This type of chemistry has been investigated thoroughly[15–20] in the synthesis of small compounds with both strongly hydrophobic trifluoromethyl groups and strongly hydrophilic hydroxyl groups on a single carbon. These types of compounds are known as fluorocarbinols (Figure 3).

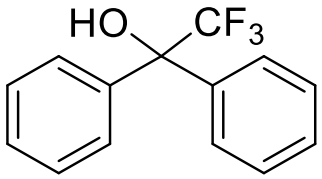

Figure 3- Example of a fluorocarbinol compound that contains both a trifluoromethyl group and a hydroxyl group adjoined to a single carbon.

The synthesis of fluorocarbinols can be achieved using trifluoromethyltrimethyl silane (Ruppert's reagent). Following the successful synthesis of trifluoromethlyated organo(chloro)silanes by Ruppert *et al*. in 1984,[15] this reagent has been widely employed. The reagent has been used successfully, in the presence of tetra-*n*-butyl ammonium fluoride (TBAF), to convert carbonyl containing compounds into their fluorocarbinol derivatives via the trifluoromethylsilyl ether derivative.[16–20] Prakash *et al*. first exploited the use of Ruppert's reagent in 1989 for the conversion of small compounds with ketone functionalities into the trifluoromethylated siloxy adduct. The resulting compounds were then subjected to hydrolysis using hydrochloric acid to form the fluorocarbinol derivatives.[17] Singh *et al*. also investigated the use of Ruppert's reagent as a trifluoromethylating agent for the conversion of esters, aldehydes and ketones[18] as well as a variety of α-keto amides,[19] all of which reacted successfully with Ruppert's reagent to produce a wide range of organic compounds that contained the fluorocarbinol functionality.

Despite the extensive investigations on the trifluoromethylation of small compounds, only recently has this chemistry been applied to polymeric systems. In 2018 Leroux *et al*. demonstrated[21] the trifluoromethylation of a series of poly(ether ketone)s produced via step-growth polymerisation using a variety of monomers. The solubility of the starting poly(ether ketone)s was very poor in polar solvents, but the fluorocarbinol-containing polymers demonstrated good solubility in polar solvents such as acetone, methanol (MeOH), ethanol (EtOH) and *iso*-propyl alcohol (*i*-PrOH). Despite the high polarity of the poly(fluorocarbinol) materials, the surfaces of cast films exhibited hydrophobic properties with water contact angles of ~90°. The hydrophobicity of the films was attributed to the enrichment of the polymer-air interface with trifluoromethyl groups and this was confirmed by X-ray photoelectron spectroscopy analyses of the surfaces of the films.[21]

The poly(fluorocarbinol) materials first reported by Leroux *et al*.[21] are potentially suitable for application in inkjet formulations. The polymeric materials demonstrated good solubility in polar solvents, highlighting their suitability for formulation in MEK-based inks, as used in the Ax-series CIJ printer at Domino. The poly(fluorocarbinol) films produced are colourless and exhibit hydrophobic properties, which indicates their suitability towards polymer binders or coatings for inkjet printing.

4.2 Results and Discussion

4.2.1 Synthesis of Poly(fluorocarbinol)s

The synthesis of a high molecular weight poly(fluorocarbinol) (PFO) **1** (Figure 4) was achieved using the three-step synthetic route developed by Leroux *et al.*[21]

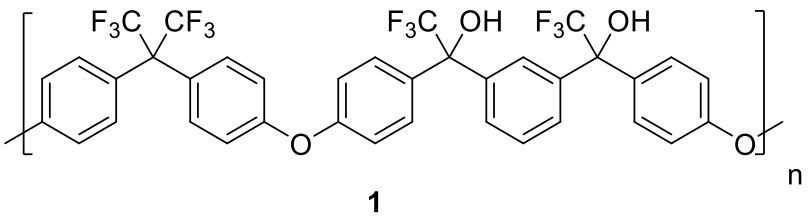

1

Figure 4- Structure of the poly(fluorocarbinol) targeted in this study.

The synthetic route first entails a step growth polymerisation reaction between equimolar quantities of 4,4'-hexafluoro(*iso*propylidene) diphenol **2** and 1,3'-bis(fluorobenzoyl) benzene monomer **3** to produce a high molecular weight poly(ether diketone) (PEKK) **4** (M_n = 114,000 g mol^{-1}), with a polydispersity of $Đ$ = 2.29 and a glass transition temperature of T_g = 162 °C (Scheme 1).

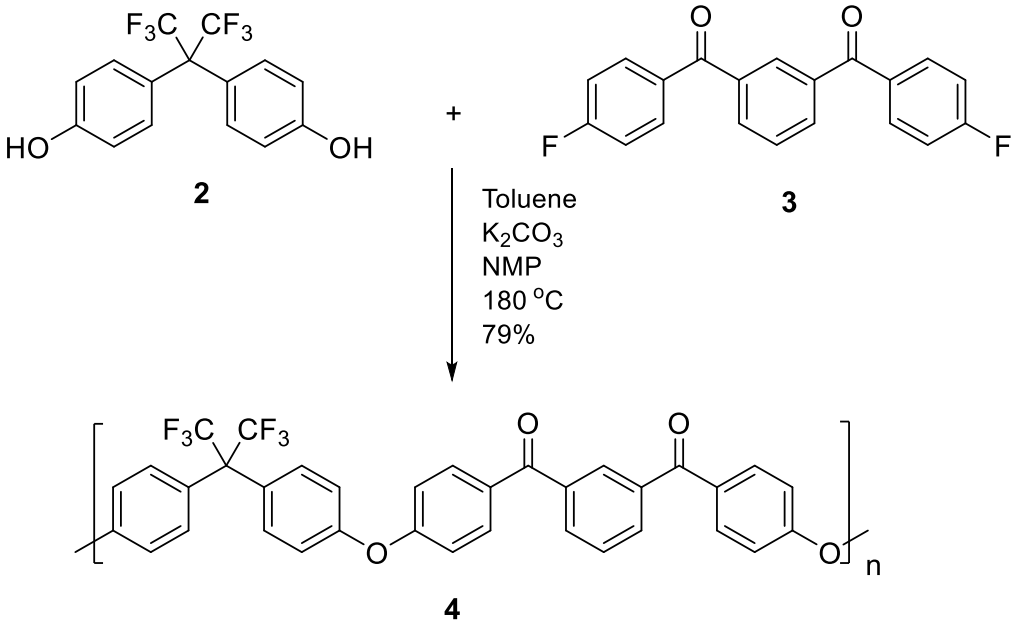

Scheme 1- Synthetic route used to obtain PEKK **4**. The polymer was synthesised via a step-growth polymerisation using an equimolar ratio of monomers **2** and **3** to produce a high molecular weight polymer (M_n = 114,000 g mol^{-1}). The molecular weight of the polymer was obtained using GPC (2mgmL^{-1} in THF).

The diketone 1,3'-bis(fluorobenzoyl)benzene monomer **3**, was chosen *in lieu* of a monomer that possessed a single ketone functionality to afford PEKK **4** with two ketone functionalities per repeat unit. The presence of two ketone functionalities meant that, upon the subsequent 2-step process to

convert PEKK **4** to the fluorocarbinol derivative **1**, a material with two hydroxyl groups per repeat unit would be obtained. The presence of two hydroxyl groups, rather than one, was predicted to increase the solubility of the polymer in polar solvents, such as methyl ethyl ketone (MEK), to allow for facile formulation of the resultant PFO materials for inkjet deposition purposes.

The second synthetic step towards the production of PFO **1**, was the conversion of PEKK **4** to form the poly(trifluoromethyl silyl ether) (PSE) derivative **5**. PEKK **4** and trifluoromethyltrimethyl silane (Ruppert's reagent) were combined in the presence of a catalytic amount of TBAF to afford PSE **5** with an increased molecular weight of M_n = 195,300 g mol^{-1} (determined by GPC (THF)) as a result of the presence of two trifluoromethyl and trimethyl silyl ether functionalities per repeat unit, which increase the radius of gyration of the polymer (Scheme 2).

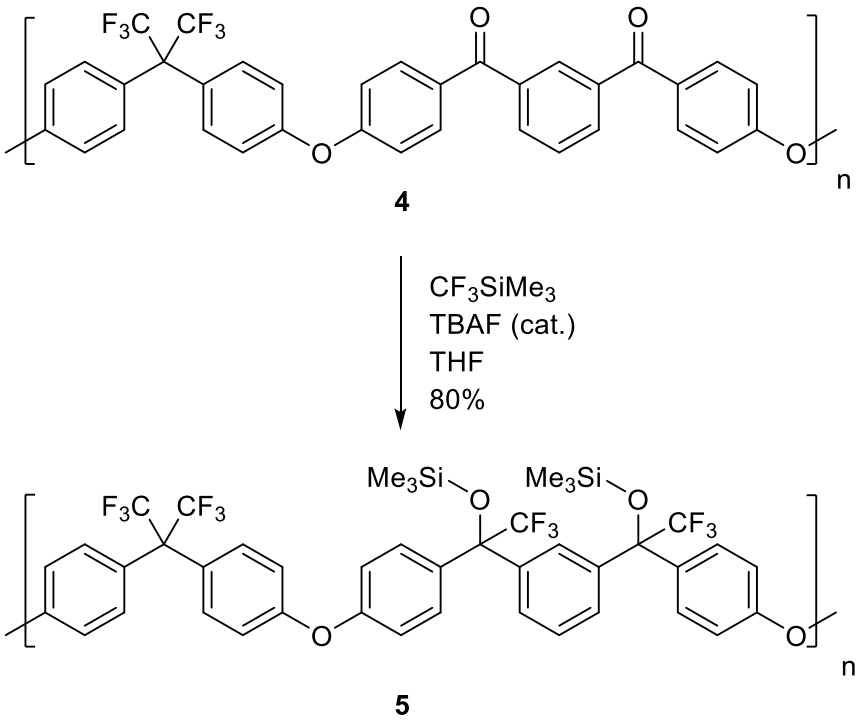

Scheme 2- Synthesis of PSE **5** via the reaction of PEKK **4** with Ruppert's reagent in the presence of a catalytic amount of TBAF.

The conversion of PEKK **4** to the PSE **5** was indicated by IR spectroscopy which showed the absence of a carbonyl absorption at 1663 cm^{-1} in the spectrum of PSE **5**, which was observed for PEKK **4**. Significant changes in the DSC thermogram of PSE **5** *cf*. PEKK **4** were also noted with a large decrease (31 °C) in glass transition temperature from T_g = 162 °C (**4**) to T_g = 131 °C (**5**) (Figure 5).

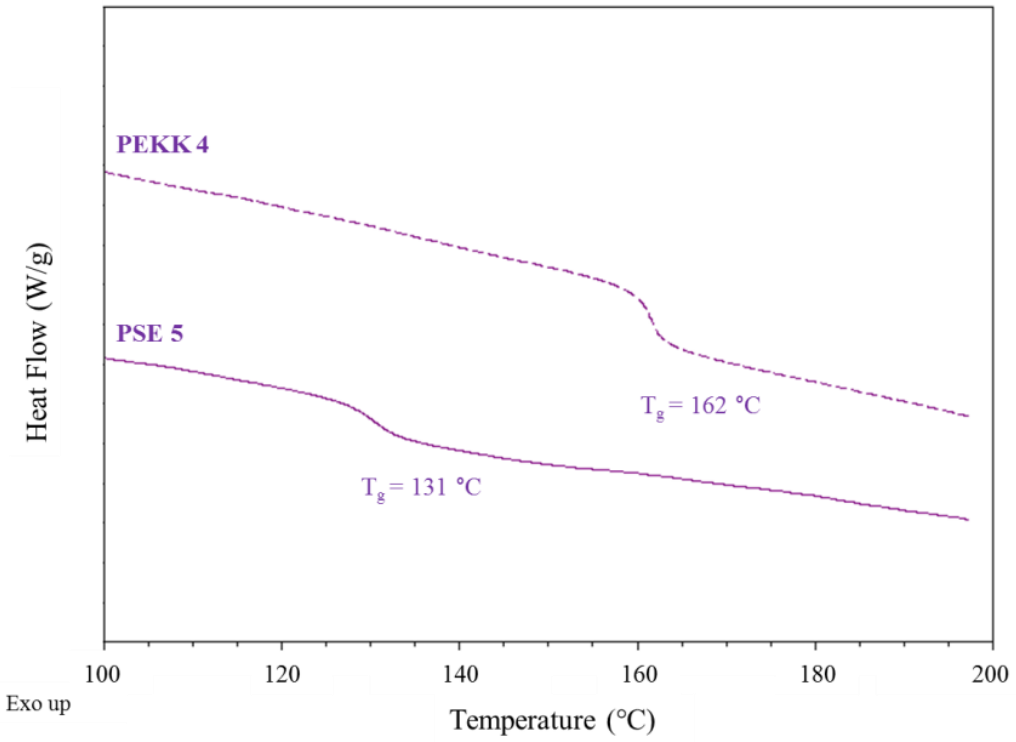

Figure 5- Stacked DSC thermograms of PEKK **4** and PSE **5** revealing a decrease of 31 °C in T_g (midpoint) following the addition of bulky silyl ether and trifluoromethyl groups to the polymer backbone.

PSE **5** exhibited a decrease in rigidity of the polymer backbone, upon conversion of the carbonyl functionalities in PEKK **4** to trifluoromethyl silyl ether groups. This decrease in rigidity along the polymer backbone was accompanied by an increase in the internal rotational freedom along the main chain, resulting in an overall decrease in the glass transition temperature of PSE **5**.[22]

The formation of PSE **5** was also clearly identifiable using ^{1}H NMR spectroscopy, with significant changes observed in the aromatic region, as well as the appearance of a methyl resonance at –0.1 ppm that was attributed to the methyl protons of the trimethyl silyl ether groups.

The introduction of trifluoromethyl and silyl ether groups (PSE **5**) in place of ketone functionalities (PEKK **4**) resulted in an upfield shift of the aromatic proton resonances, as a result of the shielding effect of the silyl ether groups in PSE **5**, when compared to the deshielding effect of the electron withdrawing ketone functionalities of PEKK **4** (Figure 6).

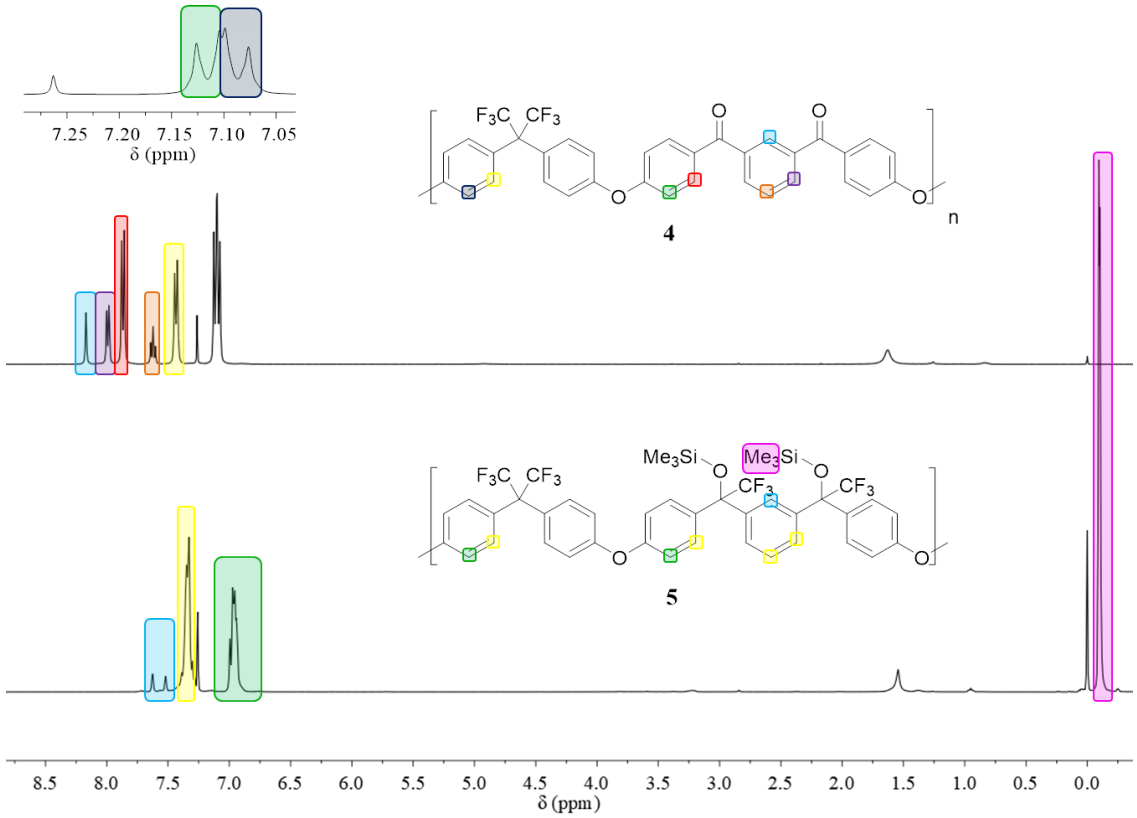

Figure 6- Stacked ^{1}H NMR spectra of PEKK **4** and PSE **5**, showing the formation of a novel methyl resonance at –0.1 ppm (shown in pink). The spectra were recorded in $CDCl_3$ at 400 MHz.

Another interesting feature in the ^{1}H NMR spectrum was noted when examining the resonance for the ortho aromatic positioned between the trifluoromethylsilyl ether groups (indicated in light blue Figure 6), which exhibited two resonances for a single proton. The splitting of the aromatic resonance was attributed to the formation of a chiral centre following trifluoromethyl silylation of the carbonyl functionalities. The two resonances were attributed to the *RR*/*SS* and *RS*/*SR* arrangement of atoms at the chiral centre, which exhibited similar, but not equal (0.53:0.47), intensities.[21]

The successful addition of the novel trifluoromethyltrimethyl silyl groups was also evident from ^{19}F NMR spectroscopic analysis which revealed two ^{19}F-nuclei resonances at –72.7 and –72.8 ppm, as well as the bis(trifluoromethyl) group resonance at –64.1 ppm, which was also observed in the ^{19}F NMR spectrum for PEKK **4** (Figure 7). The novel resonances were attributed to the trifluoromethyl groups adjoined to the silyl ether carbon in PSE **5**. The appearance of two resonances was again as a result of the formation of chiral centres at the carbons to which the trifluoromethyl groups were adjoined and once again showed similar, but not equal intensities (0.57:0.43). The ratio of intensities observed was slightly different to those recorded in ^{1}H NMR spectroscopy, however, this minor difference was attributed to the lack of resolution between the two resonances in the ^{19}F NMR spectrum, making accurate integration more difficult.

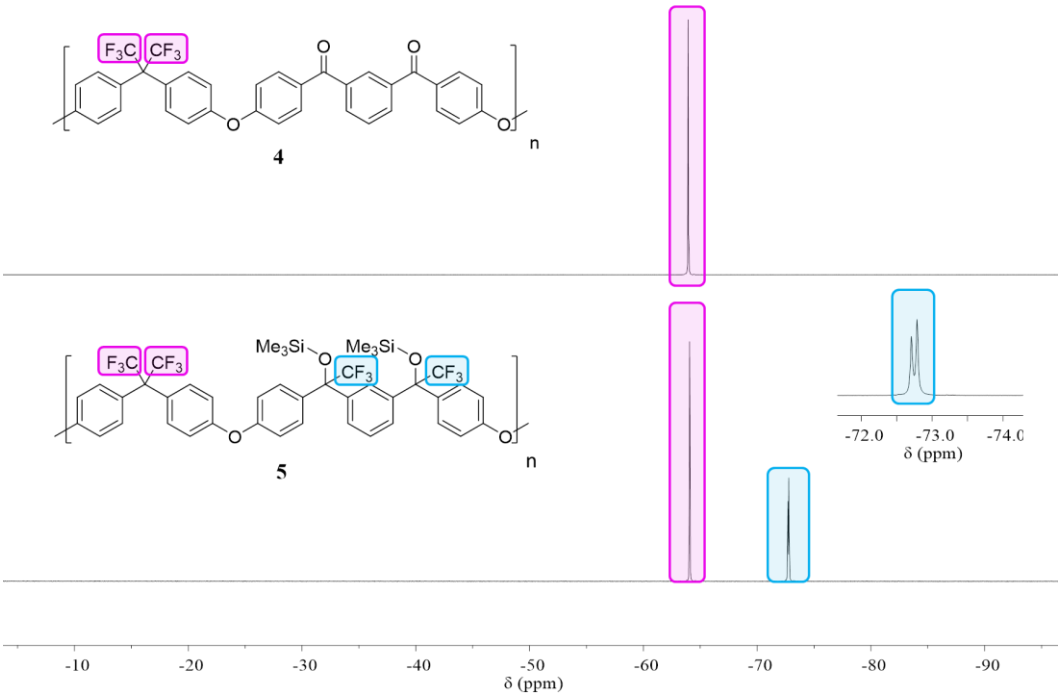

Figure 7- Stacked ^{19}F NMR spectra of PEKK **4** and PSE **5** showing the appearance of two novel ^{19}F resonances (indicated in blue), as a result of the formation of chiral centres at the carbons to which the novel trifluoromethyl groups were bonded. The spectra were recorded in $CDCl_3$ at 376 MHz.

The targeted PFO **1** was obtained by desilylation of PSE **5** using an excess of TBAF, followed by precipitation into deionised water to produce a polymer with a molecular weight of M_n = 114,500 g mol^{-1} (determined by GPC(THF)) and a glass transition temperature of 141 °C (Scheme 3).

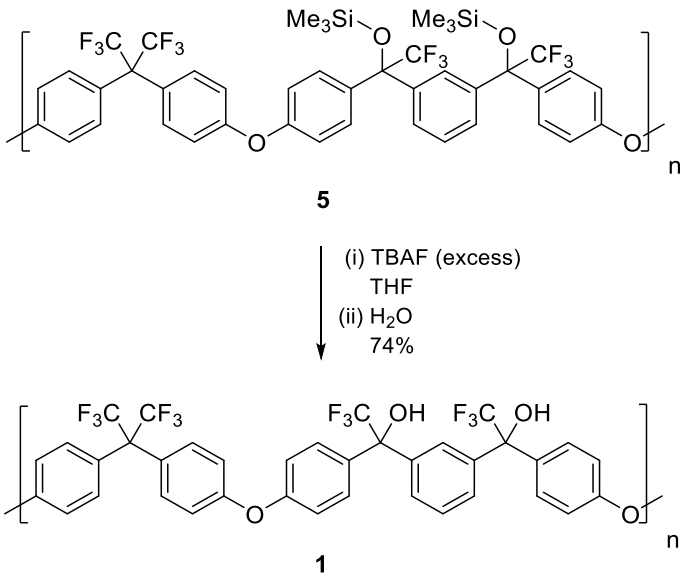

Scheme 3- The synthetic route used to obtain the desired PFO **1** via the desilylation and subsequent protonation of PSE **5**.

The desilylation of PSE **5** was evident from ^{1}H NMR spectroscopic analysis, which indicated the absence of trimethyl silyl resonances (–0.1 ppm) in the spectrum of PFO **1**. In addition, a novel hydroxyl resonance was also observed at 3.05 ppm in the ^{1}H NMR spectrum which was attributed to the two hydroxyl functionalities present in PFO **1** (Figure 8).

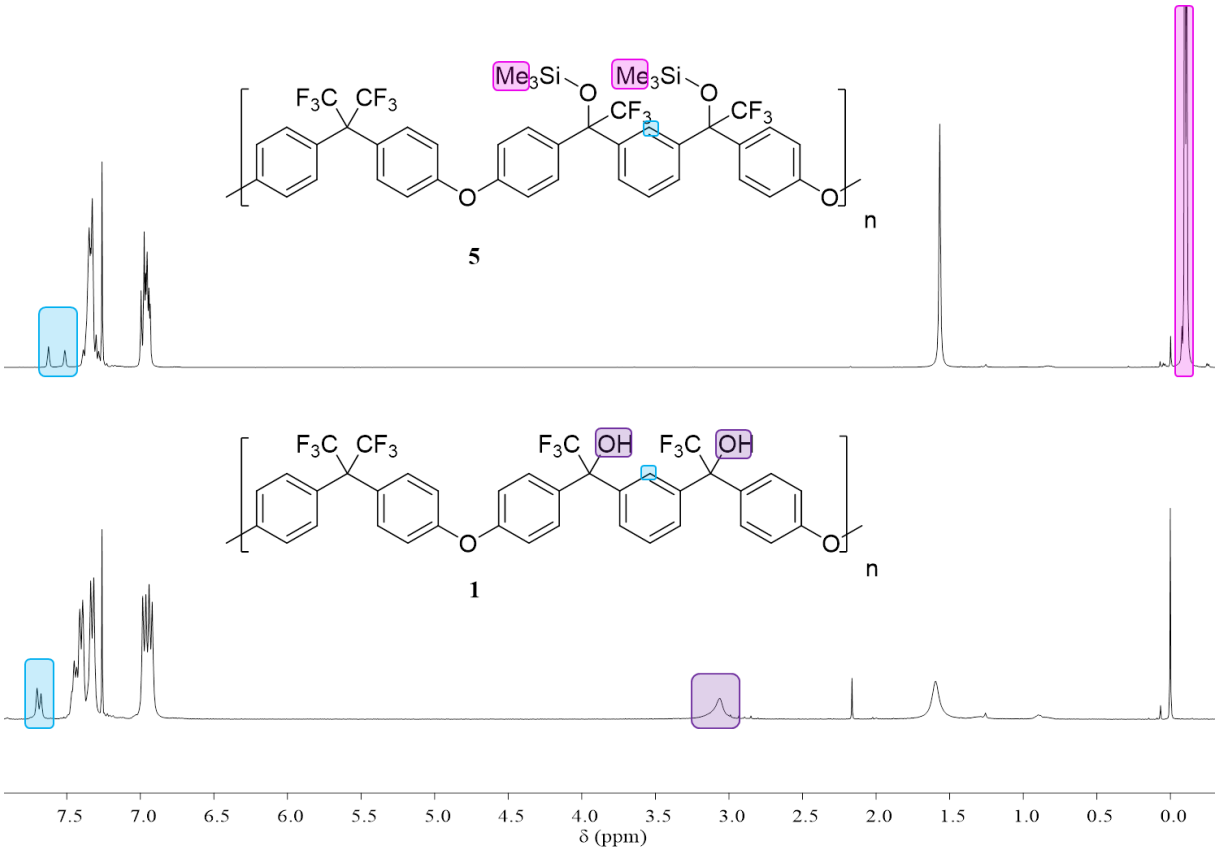

Figure 8- Stacked ^{1}H NMR spectra of PSE **5** (top) and PFO **1** (bottom) showing the absence of a methyl resonance at –0.1 ppm and the appearance of a novel resonance at 3.05 ppm attributed to the hydroxyl proton in PFO **1**. Spectra recorded in $CDCl_3$ at 400 MHz.

The ^{1}H NMR spectrum of PFO **1**, as in the case of PSE **5**, revealed two resonances for the aromatic ortho proton located between the trifluorocarbinol functionalities (see Figure 8). Once again this pattern occurred as a result of the different configurations of atoms around the chiral centres in PFO **1**. However, unlike the ^{19}F NMR spectrum for PSE **5** (see Figure 7), the resonance for the trifluorocarbinol ^{19}F nuclei in PFO **1** exhibits only one resonance, which shows a small upfield shift to -74.5 ppm when compared to PSE **5** (–72.7 and –72.8 ppm) (Figure 9).

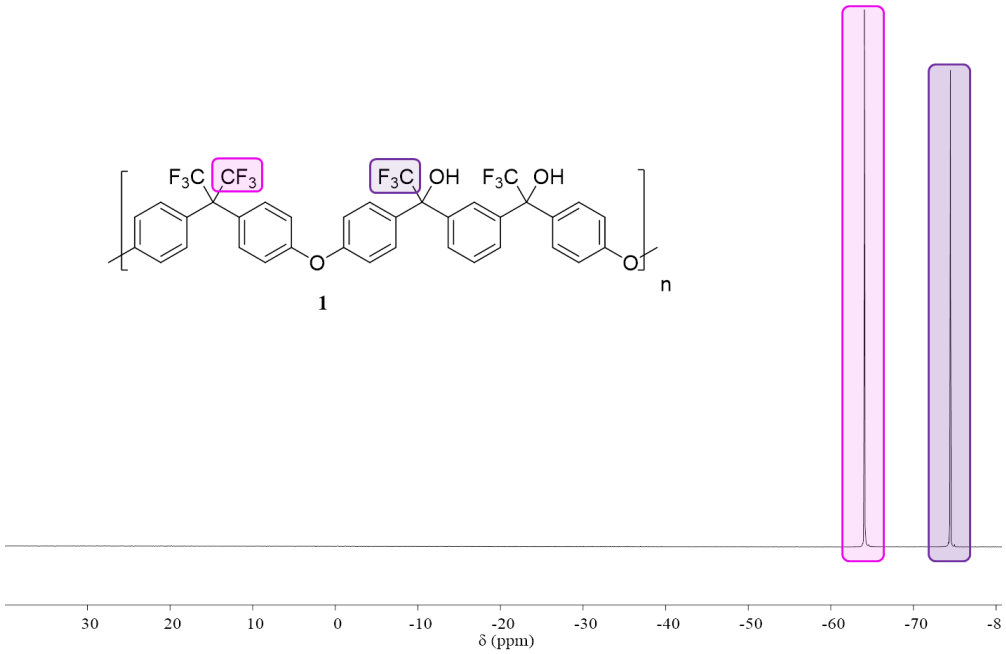

Figure 9- ^{19}F NMR spectrum of PFO **1** showing the two ^{19}F resonances of the trifluoromethyl groups. The resonance for the trifluoromethyl group adjacent to the hydroxyl functionality exhibits an upfield shift (–74.5 ppm) compared to the corresponding resonance for PSE **5** (–72.7 and –72.8 ppm).

Despite the high molecular weight of polymer **1** (M_n = 114,500 g mol^{-1}), it proved to be soluble in a variety of organic solvents of varying polarity, including: MEK, acetone, THF, $CHCl_3$, CH_2Cl_2, MeOH, EtOH, i-PrOH. The solubility of polymer **1** was attributed to the presence of the two hydroxyl functionalities per repeat unit, which aid solvation in the more polar solvents when compared to the PEKK precursor **4**, which was only soluble in THF, $CHCl_3$ and CH_2Cl_2.

4.2.2 Contact Angle Measurements of Films of PFO 1

Despite the solubility in high polarity solvents of PFO **1** previously discussed, the polymeric films cast from solution demonstrated hydrophobic properties. These intriguing properties are of great interest in the inkjet industry in providing a soluble material which can be deposited from an inkjet printhead, and then dries to produce a hydrophobic printed image. In order to investigate the hydrophobic properties, films of PFO **1** were cast from MEK (5 mg mL^{-1}), using a draw down kit to produce an even, thin film (film thickness = 24 µm). The films of PFO **1** were deposited onto glass, steel, PET, nylon, LDPE and PP.

The hydrophobicity of the polymer films was determined by investigating the wettability of the film surface with water droplets. The wettability of a surface by liquids on a macroscopic scale can be determined using Young's equation[23] (Equation 1).

$$\gamma_{LV}\cos\theta = \gamma_{SV} - \gamma_{SL} \qquad \text{(Equation 1)}$$

Where γ_{SL} is the solid-liquid interfacial free energy, γ_{LV} is the liquid vapour interfacial tension and γ_{SV} is the solid surface free energy. The contact angle, θ, was calculated, using the OneAttension® software, by measuring the angle between the tangent lines of the solid-liquid and liquid-vapour interfaces (Figure 10).

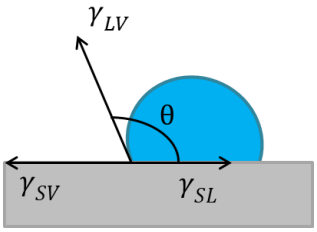

Figure 10- Schematic representation depicting the measurements used to calculate the contact angle of a liquid with a substrate using Young's equation.

The water contact angle on the uncoated substrates and those coated with a 24 µm film of PFO **1** were measured using a KSV CAM 200 optical tensiometer in sessile drop mode. The sessile drop method suspended 5 µL water droplets from the solvent nozzle, before manual agitation forced the droplet from the nozzle and onto the substrate. The angles of the droplet were recorded by the software every 0.1 seconds for 20 seconds, in which time the surface droplet had ceased spreading (Figure 11).

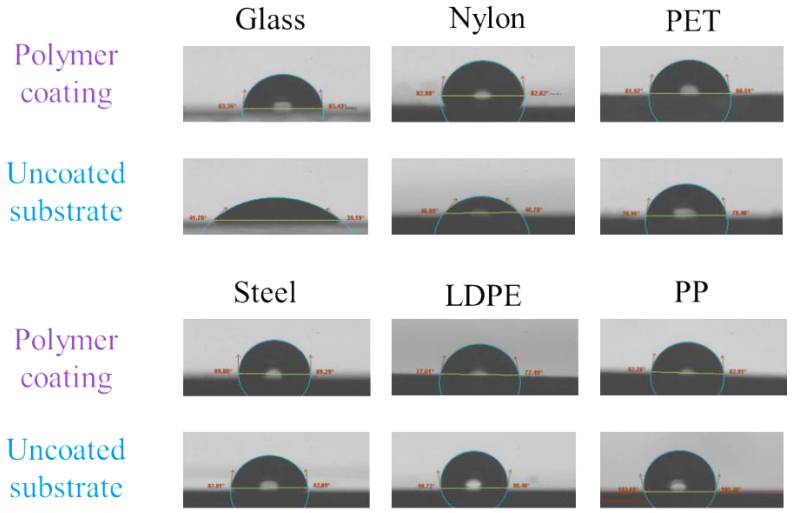

Figure 11- Images of water droplets on uncoated and PFO **1** coated glass, nylon, PET, nylon, LDPE and PP, showing the change in the contact angles of water droplets on the poly(fluorocarbinol) **1** coated substrates *cf.* the uncoated substrates.

The images obtained using the KSV CAM 200 optical tensiometer showed significant changes in the contact angle of water droplets on the polymer coated substrates when compared to the uncoated substrates. The KSV CAM software used these images to calculate the contact angle between the droplet and the substrate and each measurement was repeated six times to establish an average contact angle measurement. Uncoated glass and nylon exhibited very low contact angles of 41° and 49°,

respectively, indicating very hydrophilic surfaces. However, the water contact angles of the substrates increased to 83° and 84°, respectively, following coating with PFO **1** to produce slightly hydrophobic surfaces. Uncoated steel, LDPE and PP exhibited non-polar surfaces that revealed substrate-water contact angles of 90°, 99° and 104°, respectively.

The PFO **1** coated substrates exhibited a decrease in the water contact angle to 84°, 76° and 80° for coated steel, LDPE and PP respectively, indicating the formation of more hydrophilic surfaces. Uncoated PET and the PFO coated PET demonstrated very similar contact angles of 78° and 82°, respectively. The similarity in contact angle could be because of a similar surface polarity of PET and PFO **1**, as they are both linear polymers with aryl groups in the polymer backbone. Nonetheless, the PFO **1** coated substrates showed a small variation in contact angle; with a range from 76–84° which could be attributed to variations in the homogeneity across the polymer surface (Figure 12).

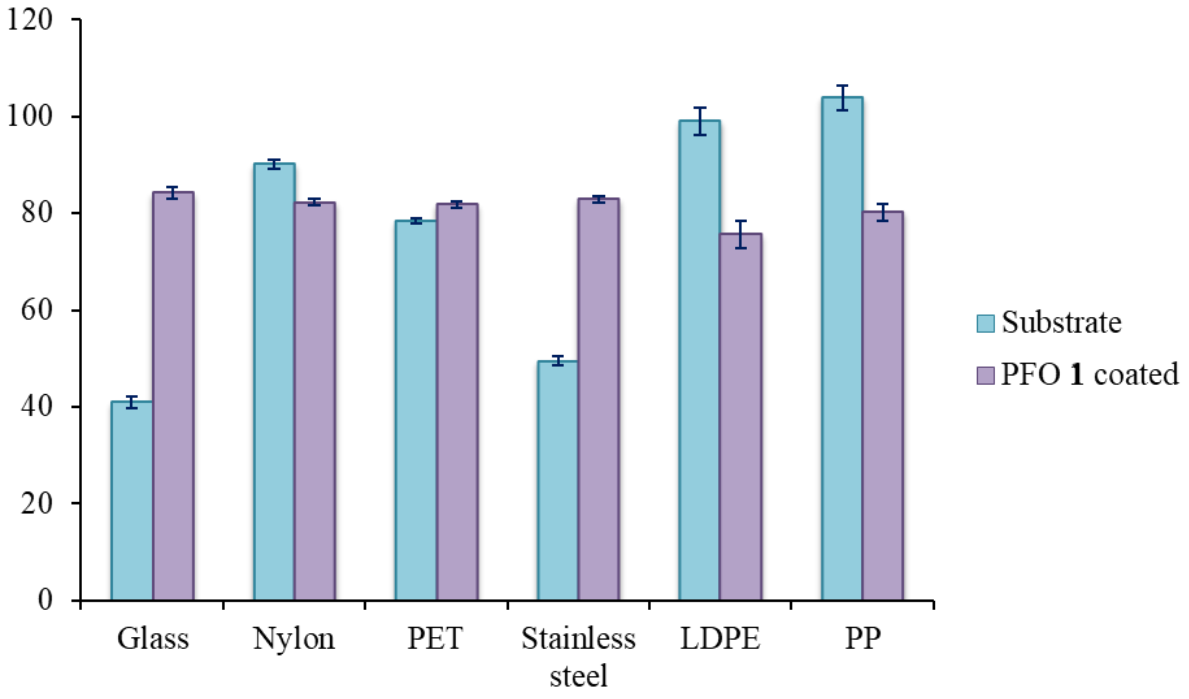

Figure 12- Contact angle measurements for uncoated glass, nylon, PET, stainless steel, LDPE and PP (blue) and PFO **1** coated substrates (purple), showing the change in the hydrophobicity of the substrate following the application of a thin coating (24 µm) of the PFO **1**. Error bars were calculated from 6 repeat measurements using standard deviation.

4.2.3 Surface Free Energy Calculations of PFO 1 Films

The surface free energy of substrates was also calculated using the contact angle measurements obtained using the KSV CAM 200 instrument. Although Young's equation does not extend far enough to enable calculation of the surface free energy of substrates, later studies by Fowkes,[24,25] and then Owens and Wendt,[26] Rabel[27] and Kaelble[28] (OWRK) provided a suitable solution. The OWRK (or extended Fowkes) method of surface free energy calculation requires the measurement of contact angles of at least two liquids; one that is polar and the other dispersive in nature to determine the surface energy of the substrate. The most suitable liquids include: water, glycerol and formamide as polar components (P) and 1-bromonaphthalene or diiodomethane as the dispersive components (D) (Equation 2).

$$\sqrt{\gamma_{SV}^{D}\,\gamma_{LV}^{D}} + \sqrt{\gamma_{SV}^{P}\,\gamma_{LV}^{P}} = \frac{1}{2}\gamma_{LV}\,(1+\cos\theta) \qquad \text{(Equation 2)}$$

The polar interactions in Equation 2 arise as a result of permanent dipole–dipole forces and are stronger than the dispersive component interactions, which are resultant of London forces, also known as induced–dipole interactions.

The OWRK method was employed for the calculation of surface energies of thin films of PFO **1** and therefore further contact angle measurements were recorded using ethylene glycol and 1-bromonaphthalene to provide contact angle measurements for two polar solvents and one dispersive solvent with known surface energies. The surface energies of the solvents and the contact angles of the solvent on the substrate are used to calculate the surface energy of the substrate in question. The surface energies (γ^{tot}) for the PFO **1** films were calculated on the OneAttension® software of the KSV CAM 200 using the OWRK (extended Fowkes) method. High surface energy values indicate higher polarity of the surface, which is often favourable for the adhesion of materials to the substrate. Lower surface energies indicate lower polarity and therefore wetting and adhesion of materials to the substrate proves much less likely. The surface free energy values calculated for the films of PFO **1** coated onto different substrates were relatively consistent for all of the substrates (37.8–39.4 mN m^{-1}), except LDPE which exhibited a higher surface energy of 44.5 mN m^{-1}. Although the PFO films exhibited consistent surface energies (excluding LDPE), the percentage change of the surface energy values, when compared to the uncoated substrates varied greatly (Table 1).

Table 1- Calculated surface energies and average contact angles for glass, nylon, PET, steel, LDPE and PP uncoated substrates and substrates coated with films of PFO **1**.

	Substrate					
	Glass	**Nylon**	**PET**	**Steel**	**LDPE**	**PP**
Substrate γ^{tot} (mNm^{-1})	53.3	42.8	43.8	34.6	32.4	25.7
PFO coating γ^{tot} (mNm^{-1})	38.5	38.7	37.8	39.0	44.5	39.4
Percentage change γ^{tot} (%)	–27.8	–9.5	–13.7	+12.7	+37.3	+53.3
Substrate water contact angle (°)	41	49	78	90	99	104
PFO coating water contact angle (°)	84	83	82	82	76	80
Percentage change in contact angle (%)	+104.9	+69.4	+5.1	–8.9	–23.2	–23.1

The uncoated glass substrate exhibited the highest surface energy (53.3 mN m^{-1}) as a result of the large amount of reactive polar groups present on the surface of the substrate. The addition of the PFO **1** film to the glass substrate lowered the surface energy by –27.8%, to produce a much more hydrophobic surface, with a water contact angle over double (84°) that observed for the uncoated glass (41°). Materials containing fluorocarbinol functionalities are known to effectively minimise the surface energy of the films by enrichment of the polymer-air interface with the trifluoromethyl groups.[9,21] The increase in the hydrophobicity of the PFO **1** films on the glass substrate was therefore attributed to the surface active properties of the fluorocarbinol functionalities within the polymer architecture. The surface energies obtained for the uncoated nylon and PET substrates (42.8 and 43.8 mN m^{-1}, respectively) also exhibited a percentage decrease upon coating with PFO **1** (–9.5 and –13.7%, respectively) which was similarly attributed to the enrichment of the polymer-air interface with trifluoromethyl groups.

The surface energy values observed for the uncoated steel and LDPE (34.6 and 32.4 mN m^{-1}, respectively) were similar, but the values recorded for the PFO **1** coated substrates were quite different. The surface energy value obtained for PFO coated steel was more consistent with the rest of the PFO coated substrates (37.8–39.4 mN m^{-1}) with an increase in surface energy to 39.0 mN m^{-1}

(+12.7%). However, PFO **1** coated LDPE exhibited a higher surface energy value of 44.4 mN m^{-1}, which indicated a more polar surface than for the other PFO coated substrates. LDPE is a non-polar substrate, but its surface energy value was not so low as to prevent wetting of the substrate with the solution of PFO **1**. The increase in surface energy of the polymer film on LDPE *cf*. the other substrates could be a result of the preferential interaction of trifluoromethyl groups with the non-polar LDPE surface and not the air-interface, resulting in a polymer film with more hydroxyl functionalities at the air-interface. This arrangement of functional groups may also have contributed to the reduced hydrophibicity and a slightly lower contact angle (76° *cf*. ~84° for the other PFO **1** coated substrates) of the PFO **1** film on LDPE.

Interestingly, although PFO **1** coated PP exhibited an increase in surface free energy value (39.4 mNm^{-1}, +53.3%), when compared to the uncoated substrate (25.7 mNm^{-1}), it fell within the same surface energy value range as the other PFO coated substrates (except LDPE). It was expected that PP would have exhibited a similar trend to that observed for the PFO coated LDPE, in that the trifluoromethyl groups would interact with the non-polar surface, forcing more hydroxyl functionalities to the air-interface, thus increasing the total surface energy of the polymer film. However, as uncoated PP has a very low surface energy itself (25.7 mNm^{-1}), wetting of its surface is minimal and adhesion of polymers is extremely poor.[29,30] The poor wetting characteristic of PP indicates that minimal interaction between PP and the PFO **1** would have occurred upon casting the polymer film and therefore the arrangement of trifluoromethyl groups as with the other substrates exhibited a preference towards the air-interface to minimise the surface energy of the polymer film.

4.2.4 Drop-on-demand Inkjet Deposition of PFO 1

Before PFO **1** could be deposited using the Dimatix™ drop-on-demand (DOD) printhead it was important to determine the viscosity of the formulation to ensure that it fell within a suitable range for DOD deposition (2–12 cP) using the Dimatix™ printhead. The viscosities of various loadings (100, 75 and 50 mg mL^{-1}) of PFO **1** in MEK were recorded using an Anton Paar Stabinger Dynamic Viscometer. The 100 mg mL^{-1} solution (17.5 cP) was above the upper limit of viscosity for inkjet deposition using the Dimatix™ DOD printhead. Reducing the polymer loading to 75 mg mL^{-1} decreased the viscosity of the solution to 8.1 cP and an even lower viscosity (3.5 cP) was observed for the formulation containing 50 mg mL^{-1} of PFO **1** (Figure 13).

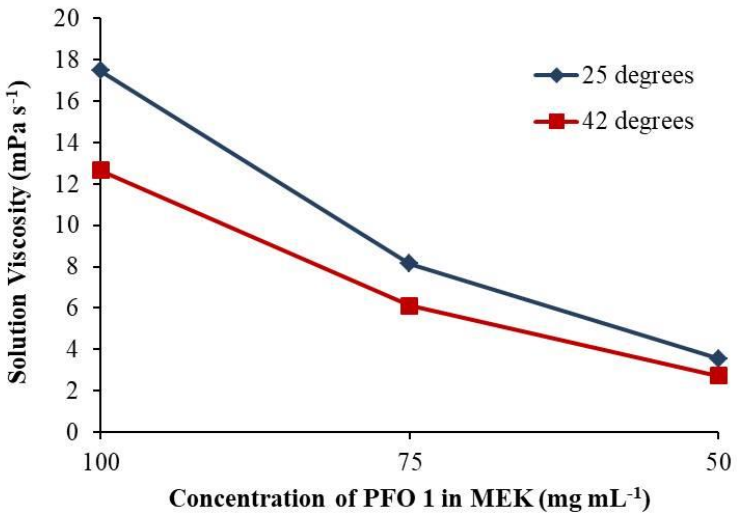

Figure 13- Viscosity measurements of poly(fluorocarbinol) **1** in MEK at concentrations of 100, 75 and 50 mg mL^{-1} at 25 °C and at CIJ jetting temperature (42 °C).

The formulation of PFO **1** at 50 mg mL^{-1} was selected as the optimum formulation for drop-on-demand printing as a viscosity of 3.5 cP allows a large enough margin for the addition of a humectant, without surpassing the optimum jetting viscosity boundary. Drop-on-demand printing cannot be performed in solely MEK because it is highly volatile and therefore solvent will evaporate at the nozzle, resulting in nozzle blockage. Consequently, carrier solvents with boiling points above 100 °C are preferred.[31] Di(propylene glycol) dimethyl ether (b.p. 190 °C) was thus used as a humectant alongside MEK (1:1 v/v) and the printability of the polymer **1** tested using the Dimatix™ DOD printhead.

Different cartridge temperatures and voltages were employed to find the optimum print settings, however, the material did not print at all below 40 V (maximum voltage) and even at maximum voltage only a minor amount of material was deposited before the printing failed and no further material was deposited (Table 2).

Table 2- Different printer settings used for attempted deposition of poly(fluorocarbinol) **1**, indicating the settings which resulted in failure to print (×) and those which resulted in a partial print, before nozzle blockage (×).

	Cartridge Temperature (°C)				
Voltage	**25**	**30**	**35**	**40**	**50**
30	×	×	×	×	×
35	×	×	×	×	×
40	×	×	×	×	×

The PFO **1** was therefore not suitable for inkjet deposition, despite its solubility and relatively low viscosity. It was concluded that the high molecular weight (M_n = 114,500 g mol^{-1}) of the material prohibited successful jetting as a result of elastic stresses originating from elongational flow in the nozzle.[1,32,33] Elongational flow occurs locally in all flows that possess a stream-wise velocity gradient e.g. flow through intersects, contractions or expansions. Viscoelastic polymeric fluids under this deformation exhibit a complex rheological response.[34,35] The maximum flow rate of the viscoelastic fluids under high elongational flow conditions is determined by the elastic instabilities of the fluid. At high elongational flow, the formation of an elastic strand can occur and elastic stresses dominate, leading to a non-Newtonian increase in viscosity, which in the case of inkjet can result in nozzle blockage and failure of print.

Despite the inability to deposit the high molecular weight PFO **1** using the Dimatix™ DOD system, the high polarity and good solubility of the material warranted further investigation into PFO materials to produce suitable inkjet materials. It was envisaged that decreasing the molecular weight of the PFO materials would improve the printability of the materials as a result of a decrease in viscosity, potentially eliminating the risk of nozzle blockage. Furthermore, reducing the molecular weight of the PFO without altering the structure of the polymeric repeat unit would possibly enable the retention of the hydrophobic film properties of the materials, as a result of the presence of the fluorocarbinol functionalities. An approach to produce lower molecular weight poly(fluorocarbinol)s was therefore investigated in an attempt to produce a printable material.

4.2.5 Molecular Weight Control of Step-Growth Polymerisation

The first synthetic process in the production of PFO **1** was the step-growth polymerisation between monomers **2** and **3** to produce PEKK **4** (see Scheme 1). According to the Carothers equation, developed in 1920, in a two monomer AA/BB step-growth polymerisation, the degree of polymerisation ($\overline{X}_n$) is a function of the stoichiometric ratio (r) of monomers (Equation 3).[36]

$$\overline{X}_n = \frac{1 + r}{1 - r} \qquad \text{(Equation 3)}$$

Therefore by adjusting the stoichiometric ratio (r) of the two monomers **2** and **3**, the molecular weight of the PEKK produced will be controlled and ultimately reduced. The bis(hydroxyl)-terminated monomer, **2**, was selected as the limiting monomer to produce poly(ether ketone)s with fluorine terminating groups. The fluorine terminated polymers were more stable than the analogous hydroxyl terminated polymers to the subsequent synthetic procedures that involved the use of TBAF. Using Equation 3, the degree of polymerisation ($\overline{X}_n$) of polymers produced using different stoichiometric ratios of monomers was calculated. Multiplication of the calculated values by the molecular weight of one repeat unit of the polymer provided a prediction of the number average molecular weights of the poly(ether diketones) that would be produced.

Table 3- Predicted molecular weights (M_n) of PEKKs produced using different monomer feed ratios, calculated using the Carothers equation (Equation 3).

Compound number	Monomer 2 feed	Monomer 3 feed	$\overline{X_n}$	Calculated M_n (g mol^{-1})
6a	0.9	1.0	19	11,800
6b	0.925	1.0	26	16,000
6c	0.95	1.0	39	24,000
6d	0.975	1.0	79	42,500

The molecular weights calculated in Table 3 were predicted to be within a suitable range to provide materials that would be suitable for inkjet deposition, not only using a Dimatix™ DOD printhead, but also for testing in an Ax-series continuous-inkjet system. A series of lower molecular weight poly(ether diketones) (**6a**–**6d**) were synthesised via the same protocol for PEKK **4** (Scheme 1), but using the monomer ratios stated in Table 3 to afford a series of PEKK's with molecular weights within close range of those predicted (Scheme 4).

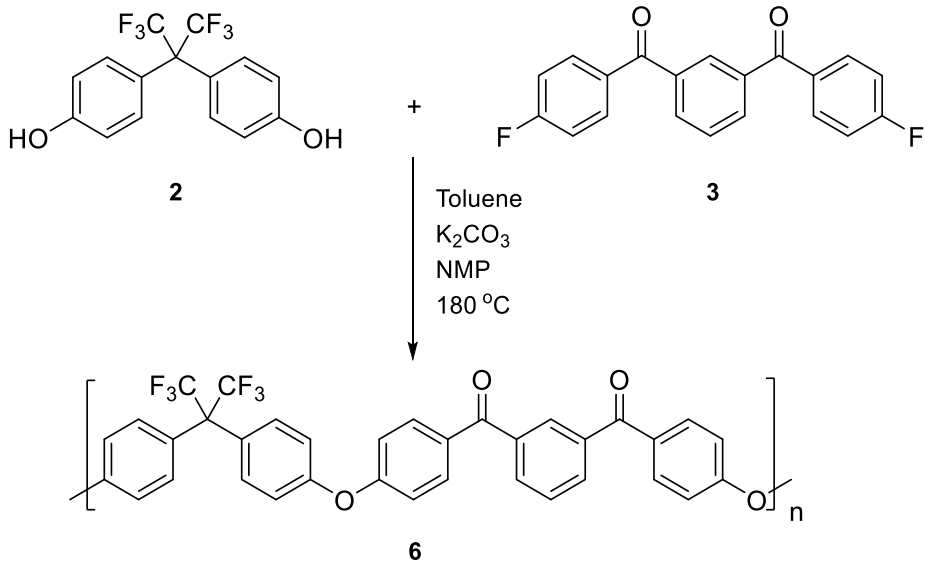

Compound number	Predicted M_n (g mol^{-1})	M_n observed GPC (g mol^{-1})
6a	**11,800**	**10,500**
6b	**16,000**	**15,600**
6c	**24,000**	**22,000**
6d	**42,500**	**42,500**

Scheme 4- The synthesis of PEKKs of different molecular weights by controlling the monomer feed ratio of bis(phenol) monomer **2**, showing the molecular weights predicted and obtained for each monomer ratio (**6a**–**d**). GPC was performed in THF, using PEG as a calibration standard.

Reducing the feed of monomer **2** to 0.9, 0.925, 0.95 and 0.975 equivalents (*cf.* monomer **3**) produced PEKKs of molecular weights (M_n): 10,500 (**6a**), 15,600 (**6b**), 22,000 (**6c**) and 42,500 (**6d**) g mol^{-1}, respectively, as determined by GPC (Figure 14).

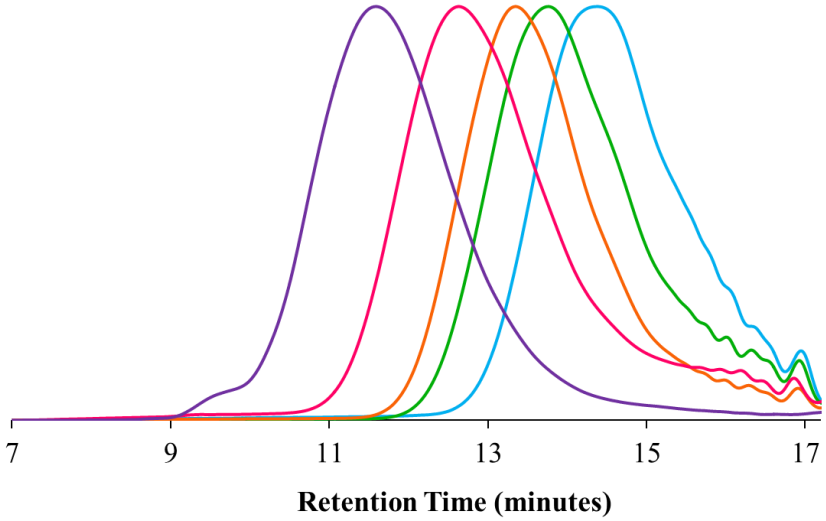

PEKK	M_n	M_w	$Đ$
6a	10,500	18,300	1.74
6b	15,600	30,500	1.95
6c	22,000	43,200	1.91
6d	42,500	87,700	2.06
4	114,000	260,900	2.29

Figure 14- GPC chromatograms (THF as eluent) showing the GPC traces of PEKK **4** and molecular weight controlled PEKKs **6a–d**. The GPC chromatogram showed a clear decrease in molecular weight of the PEKKs by decreasing the monomer feed of 4,4'-hexafluoro(*iso*propylidene) diphenol **2**. GPC analysis was performed in THF at polymer concentrations of 2 mg mL^{-1}with PEG as a calibration standard.

It is noted that the polydispersity values ($Đ$) of the polymers **6a–c** are below the expected minimum value of 2 for a step-growth polymerisation and therefore the weight average molecular weight (M_w) is less than double that of the number average molecular weight (M_n). This result was not anticipated, however, it was noted that the lower molecular weight poly(ether diketones) **6a–c** were more powder-like when compared to PEKK **4** and **6d**, and showed some solubility in methanol as the precipitation solution became cloudy. It is possible that the lower molecular weight fragments of PEKKs **6a–c** may not have precipitated out of solution, even when precipitating into cold methanol and therefore the polydispersity values exhibited a decrease as a result of loss of the lower molecular weight fragments.

Differential scanning calorimetry of the PEKKs was performed to determine the glass transition temperatures of the lower molecular weight materials, which were predicted to decrease with decreasing molecular weight. This relationship is described in the Flory–Fox equation which relates

the glass transition temperature, T_g, to the number average molecular weight of the polymer, M_n (Equation 4).[37,38]

$$T_g = T_{g,\infty} - \frac{K}{M_n} \quad \text{(Equation 4)}$$

Where $T_{g,\infty}$ is the limiting value for the glass transition temperature at a very high molecular weight material and K, a constant that is related to the free space present in the polymer. As seen in Equation 4, decreasing the number average molecular weight of a polymer results in a decrease in T_g. Lower molecular weight polymers also have a larger volume of free space present in the polymer, K, as the polymer chains decrease in length, further decreasing the value obtained for T_g. Therefore the lower the molecular weight of the polymer, the larger the decrease in the glass transition temperature when compared to the maximum glass transition temperature, $T_{g,\infty}$ for a high molecular weight polymer.[37,38]

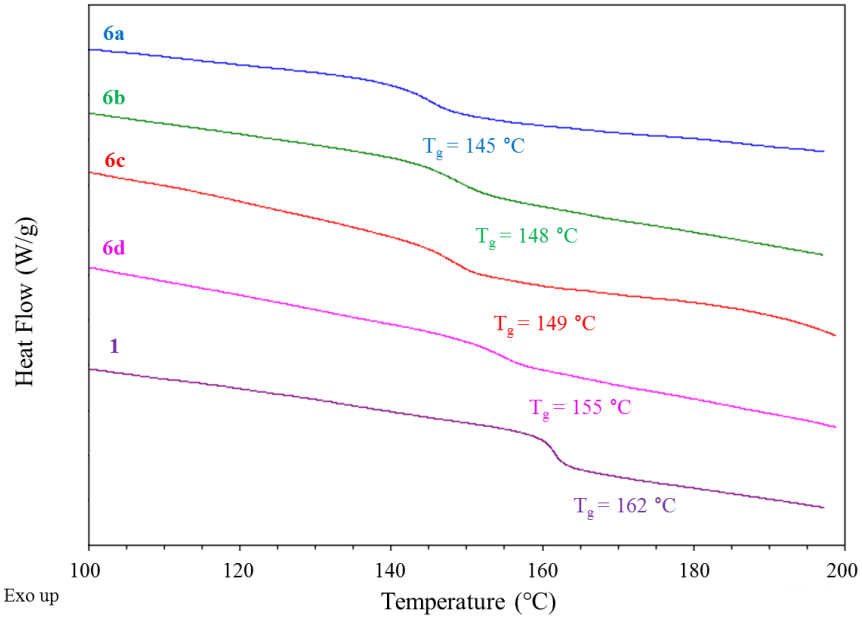

Figure 15- Stacked DSC thermograms of poly(ether diketone)s **6a–6d** and **1** showing the change in glass transition temperature, T_g, as molecular weight increases (from top to bottom).

Following the successful molecular weight control of the step-growth polymerisation of monomers **2** and **3**, the series of PEKKs **6a**–**6d** were converted to the corresponding silyl ether derivatives using Ruppert's reagent as described previously (see Scheme 2) to produce poly(trifluoromethylsilyl ether)s **7a**–**d**. The conversion of the PEKKs to PSEs was monitored using IR, ^{13}C, ^{1}H NMR and ^{19}F NMR spectroscopies, as with the synthesis of PSE **5** (see Scheme 2). The materials were purified by precipitation into cold methanol as the lower molecular weight PSEs **7a**–**d** showed increased solubility in methanol, when compared to the higher molecular weight PSE **4**. The theoretical molecular weight values (M_n) for the PSEs produced were 13,000, 19,000, 27,000 and 52,000 g mol^{-1} for **7a**–**d**,

respectively. However, **7a**–**c** exhibited molecular weight values that were 1.5 (**7a** and **c**) and 1.2 (**7b**) times higher than predicted (Figure 16).

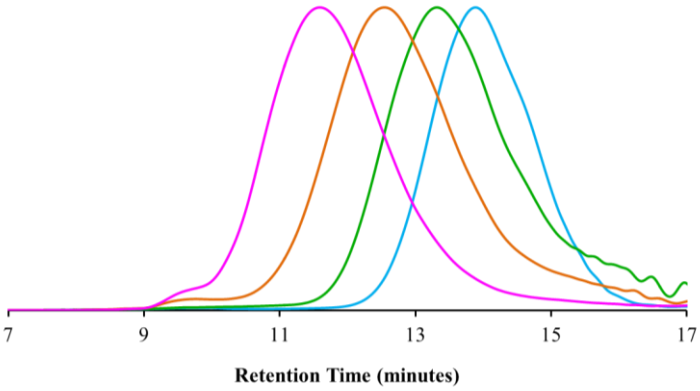

PSE	M_n	M_w	$Đ$
7a	19,500	29,500	1.52
7b	23,300	47,200	2.03
7c	40,200	83,000	2.06
7d	55,100	116,300	2.11

Figure 16- GPC chromatograms (THF as eluent) of poly(trifluoromethylsilyl ether)s **7a–d**, showing an increase in molecular weights when compared to **6a–d** as a result of the addition of two silyl ether and trifluoromethyl groups per repeat unit. GPC analysis was performed in THF with polymer concentrations of 2 mg mL^{-1}.

The silyl ether derivatives (**7a**–**d**) showed a decrease in glass transition when compared to the poly(ether diketones) (**6a**–**d**) as the silyl ether functionalities are less rigid than the corresponding ketone derivative and therefore a greater freedom of internal rotational around the main chain is achieved, decreasing the glass transition temperature. The series of PSEs also showed a small increase in T_g, with increasing molecular weight (Figure 17).

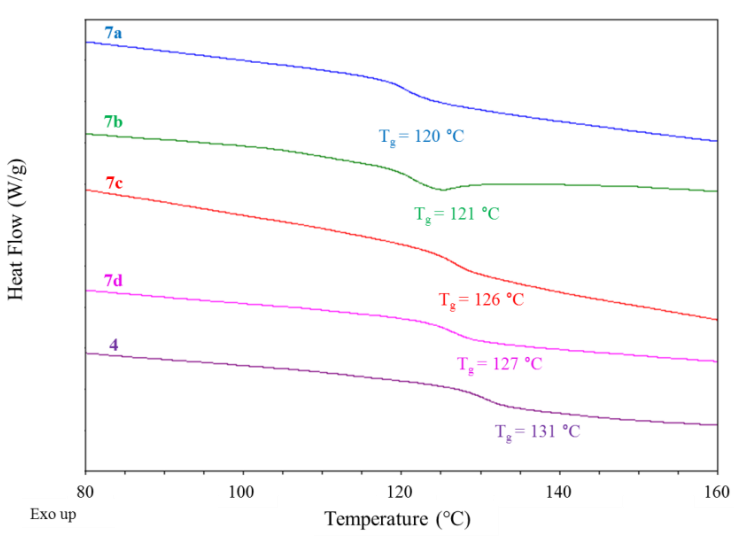

Figure 17- Stacked DSC thermograms of PSEs **7a–7d** and **4**, revealing the small increase in glass transition temperature, T_g with increasing molecular weight (from top to bottom).

The PSEs **7a**–**d** were then desilylated using an excess of TBAF, following the same synthetic procedure seen in Scheme 3, to produce PFOs **8a**–**d** with a molecular weight range (M_n) of 11,500–44,900 g mol^{-1} as determined by GPC analysis (Figure 18).

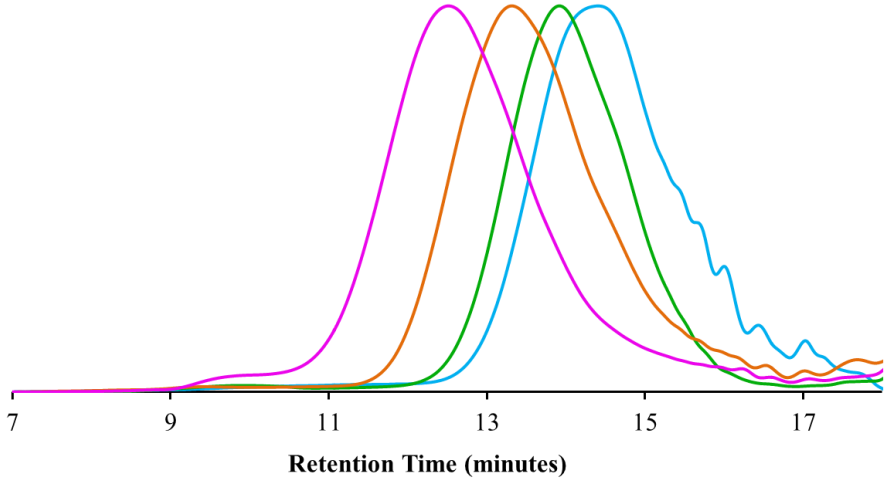

PFO	M_n	M_w	$Đ$
8a	11,500	19,400	1.68
8b	19,100	28,600	1.54
8c	25,200	46,400	1.84
8d	44,900	101,600	2.27

Figure 18- GPC chromatograms for molecular weight controlled PFOs revealing a decrease in molecular weight from **8d–8a** (left to right). GPC analysis was performed in THF with polymer concentrations of 2 mg mL^{-1}.

The molecular weight of the PFOs produced was within close proximity to the theoretical molecular weights following conversion of the PEK derivatives. The theoretical molecular weights of the PFOs were calculated to be 12,400, 18,500, 26,000 and 50,300 g mol^{-1} for **8a**–**d**, respectively.

The molecular weights of the novel PFOs produced were within a more suitable range for inkjet printing when compared to the higher molecular weight PFO **1** (114,500 g mol^{-1}). As described previously, the decrease in the molecular weight of the poly(fluorocarbinol)s also resulted in a decrease in the glass transition temperature. The PFO **1** produced using a 1:1 ratio of monomers **2** and **3** exhibited a glass transition temperature of 141 °C, whereas DSC analysis of the lower molecular weight polymers **8a**–**d** revealed lower glass transition temperatures ranging between 114–134 °C (Figure 19).

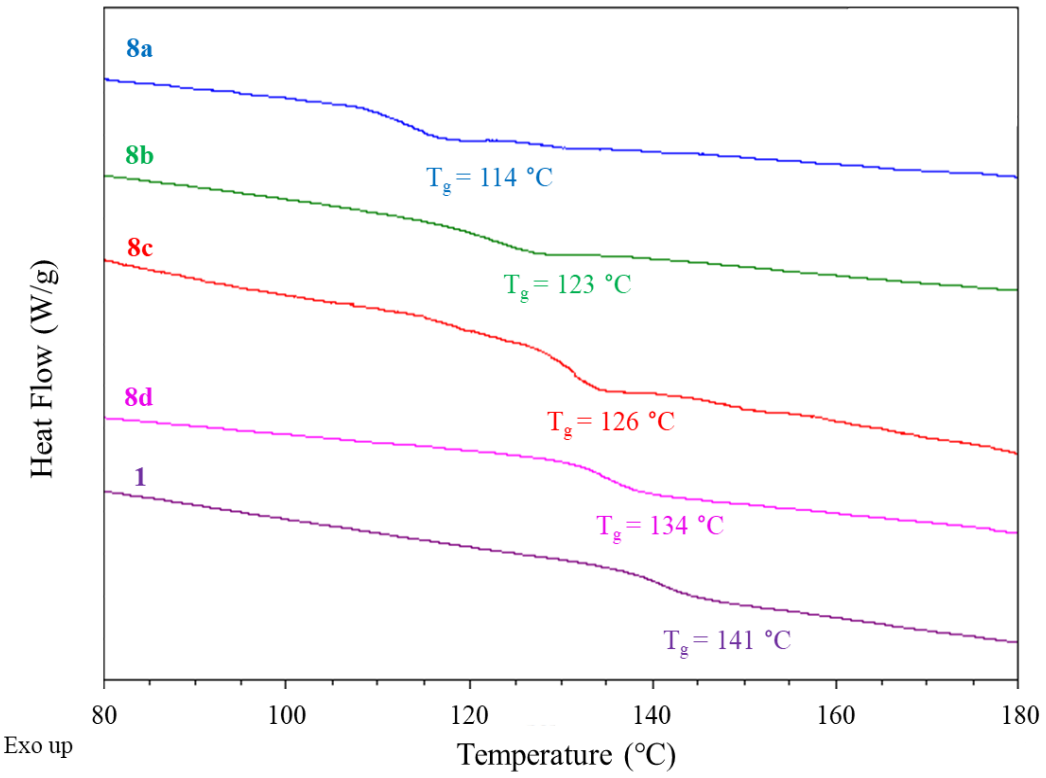

Figure 19- Stacked DSC thermograms showing a decrease in glass transition temperatures of the lower molecular weight PFOs **8a–d** when compared to the higher molecular weight PFO **1** as a result of decreased polymer chain length.

4.2.6 Effect of Polymer Molecular Weight on Hydrophobic Properties of Films

The contact angles of the lower molecular weight polymer films (PEKKs **6a**–**d**, PSEs **7a**–**d** and PFOs **8a**–**d**) with water were investigated and compared to the higher molecular weight materials (**1**, **4** and **5**) to determine whether the molecular weight of the polymer film had an effect on the hydrophobic properties of the material. Thin films of the polymers were prepared on glass substrate as previously described and the water contact angle recorded using a KSV CAM 200 instrument. The studies revealed that the hydrophobic properties of each polymer type were unaffected by the change in molecular weight, with only minor variations in the average contact angles measured. The contact angles for the PEKK family of polymers **6a**–**d** showed a minor trend between the contact angle and molecular weight with a gradual decrease in contact angle from 98° (PEKK **4**) to 94° (PEKK **6a**) as the molecular weight of the PEKK decreases. The PSE films were the most hydrophobic with contact angles between 106° to 103°, however, a clear trend between molecular weight and contact angle was not observed. The PFO films were the least hydrophobic, with all but one of the films exhibiting a water contact angle of 88° and PFO **8c** demonstrating a contact angle of 89° (Figure 20).

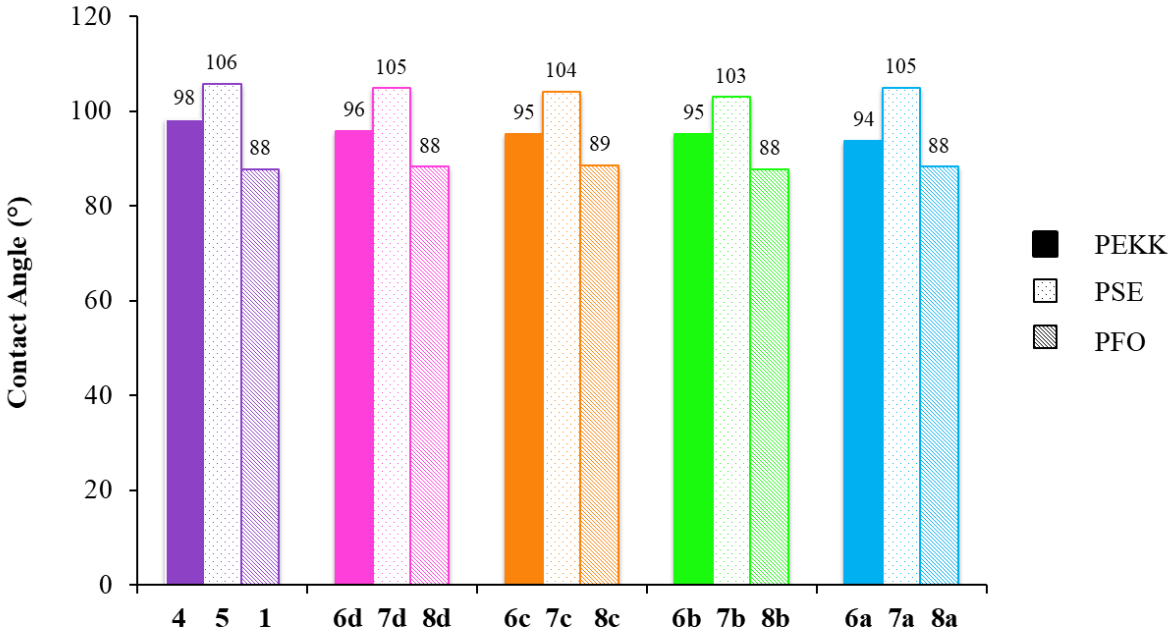

Figure 20- Average contact angle measurements recorded for PEKK, PSE and PFO's of different molecular weights (decreasing from left to right) showing good consistency in hydrophobic properties of the films, regardless of the molecular weight of the polymers. Contact angles shown are the calculated average of 6 repeat measurements.

The results obtained in Figure 20 indicate that the lower molecular weight PFOs (**8a**–**d**) demonstrated comparable hydrophobic properties to that of the high molecular weight PFO **1**. The free surface energies of films of the lower molecular weight PEKKs (**6a**–**d**), PSEs (**7a**–**d**) and PFOs (**8a**–**d**) were calculated using the OneAttension® software, as described in Section 4.2.3, giving comparable surface energies to the analogous high molecular weight polymers **1**,**4** and **5** (Table 4).

Table 4- Calculated surface energies of PEKK (**6a**–**d**), PSE (**7a**–**d**) and PFOs (**8a**–**d**) calculated using the extended Fowkes (OWRK) method on the OneAttension® software of the KSV CAM 200 tensiometer.

	Equivalents of monomer 2				
Surface Energy γ^{tot} (mN m^{-1})	**0.90**	**0.925**	**0.95**	**0.975**	**1.00**
PEKK	41.5 **6a**	41.7 **6b**	40.2 **6c**	40.6 **6d**	41.4 **4**
PSE	39.6 **7a**	37.5 **7b**	39.1 **7c**	38.4 **7d**	37.9 **5**
PFO	38.7 **8a**	39.9 **8b**	39.5 **8c**	38.0 **8d**	38.5 **1**

All three polymer types demonstrated surface free energy values within a similar range, although it is noted that the PEKKs demonstrated slightly higher surface energy values when compared to the PSE and PFO derivatives. The lower surface energy values observed for the PSEs (**7a**–**d**) and PFOs (**8a**–**d**) can be attributed to the introduction of two trifluoromethyl groups per repeat unit, which are known to segregate at the polymer-air interface to minimise surface energy of the polymer.[9,21]

4.2.7 DOD Inkjet Deposition of Lower Molecular Weight PFO materials

Before deposition of the molecular weight controlled PFOs was attempted, the viscosities of the PFO materials (100 mg mL^{-1} in MEK) were measured using an Anton Paar Stabinger viscometer to ensure that they were within the correct range (2–12 cP) for use in the Dimatix™ DOD printhead. The reduction in molecular weight of the PFO materials (**8a**–**d**) resulted in significant decreases in the solution viscosity when compared to PFO **1** (14.5 cP 100 mg mL^{-1} at 25 °C) (Figure 21).

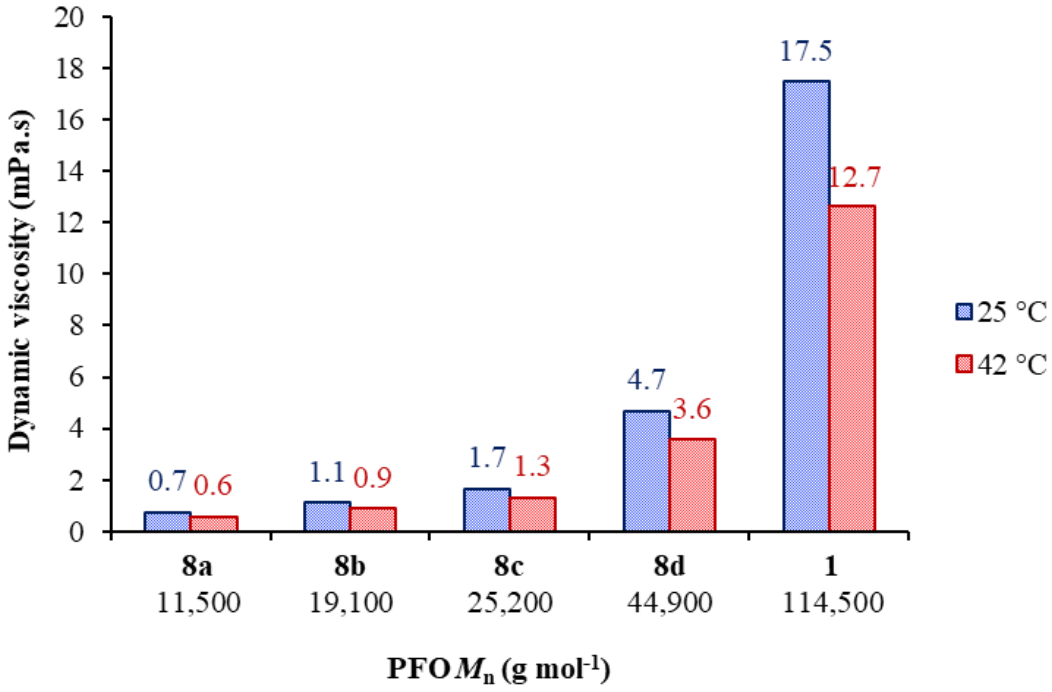

Figure 21- Dynamic viscosities of PFOs **8a–d** and **1** (100 mgmL^{-1} in MEK) showing an increase in viscosity as the molecular weight of the PFO increases (left to right).

Initial inkjet printing studies of the molecular weight controlled PFOs were performed using the Dimatix™ DOD printhead using formulations of PFOs **8a**–**d** (100 mg mL^{-1} MEK: propylene glycol dimethyl ether 1:1 v/v). All four of the PFOs were deposited onto sheen card using the Dimatix™ DOD printhead, with the optimum printing conditions varying for the different molecular weight materials. The highest molecular weight PFO **8d** was printed at a cartridge voltage of 40 V, but was not printable at lower voltages. PFOs **8a** and **8b** displayed optimum jetting at 30 V, whereas although **8c** was printable at 30 V, a more resolved image was observed using a cartridge voltage of 35 V.

Table 5- Details of the various conditions used to print PFOs **8a–d** using the Dimatix™ printhead and whether the material was deposited (✓) or failed to print (×). The optimum conditions for each PFO sample are indicated by the green tick (✓).

		PFO reference			
Temp (°C)	**Volts (V)**	**8a**	**8b**	**8c**	**8d**
40	**40**	✓	✓	✓	✓
30	**35**	✓	✓	✓	×
30	**30**	✓	✓	✓	×
30	**25**	✓	✓	✓	×

4.2.8 Pre-deposition Analysis of PFOs 8a and 8c using Rheology

The Dimatix™ DOD printhead is a useful printer to test the printability of novel materials, but the coding and marking inkjet industry relies on the high throughput printing and coding of materials to meet customer demands. The high throughput coding and marking of materials is achieved using a continuous inkjet printer that can print multi-line messages at high speeds. On the commercial scale continuous inkjet printers will jet a continuous stream of ink droplets that are recycled though the printer system and are only deposited as and when required. However, test rigs for novel inks are not set up to recycle the ink formulations and the material is collected once it has returned to the gutter.

In order to provide ample jetting time a relatively large volume of ink is required (minimum 100 mL) to test in the CIJ printhead. Therefore two of the four PFO samples were selected for scale up and were tested on the Ax-series CIJ printhead at Domino. The lowest molecular weight PFO **8a** (11,500 g mol^{-1}) was selected, as it was likely to pose a lower risk of nozzle blockage resultant of elastic stresses from elongational flow as it possesses the shortest polymer chain length.[1,32,33] The higher molecular weight polymer **8d** was not chosen as it was the most likely to result in nozzle blockage in the Ax-series CIJ printer, as indicated by the initial printing studies on the Dimatix™ DOD printhead (see Table 5) in which a clean print was only observed at the highest cartridge voltage (40 V). PFO **8c** was selected for investigation as an Ax-series CIJ printer formulation as the molecular weight of the material (25,200 g mol^{-1}) is over double that of **8a**, but good printability of **8c** was observed in the initial printing studies of the PFO materials, indicating that the material would be suitable for CIJ deposition.

The viscosity of the formulations tested in the Ax-series CIJ printheads at Domino usually lie within the range of 3–6 cP at 25 °C. The dynamic viscosities of PFOs **8a** and **8c** (100 mg mL^{-1} in MEK) were 0.7 and 1.7 cP, respectively, and therefore the viscosity of the formulations needed to be increased. The concentration of polymers in the formulations of **8a** and **8c** was increased and the viscosities recorded to determine the minimum loading of polymer required to reach the correct jetting viscosity. The higher molecular weight PFO **8c** reached the optimum jetting viscosity range at 200 mg mL^{-1} with a viscosity of 5.3 cP, whereas the lower molecular weight **8a** required a loading of 300 mg mL^{-1} of polymer in MEK to attain the correct viscosity (3.9 cP) for printing (Figure 22).

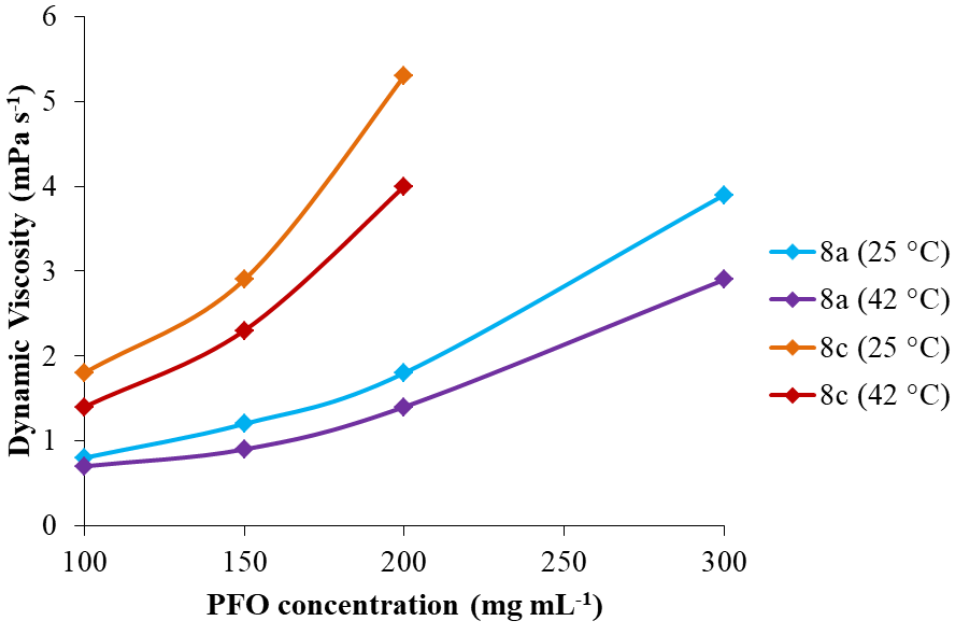

Figure 22- Dynamic viscosities of polymers **8a** and **8c** at different concentrations in MEK showing appropriate viscosity (3–6 cP) for CIJ inkjet deposition at concentrations of 200 mg mL^{-1} and 300 mg mL^{-1} for polymers **8c** (5.3 cP at 25 °C) and **8a** (3.9 cP at 25 °C), respectively.

The addition of polymers to inkjet formulations can alter the Newtonian behaviour of the carrier solvent, as the polymer chains disentangle, align and stretch upon ejection from the narrow nozzle (60 µm diameter in the Ax-series) at high shear rates. Thus, the rheological behaviour of polymers, as they pass through the printhead, is an important factor that defines the suitability of polymers for CIJ printing. The high shear rates observed in CIJ printing can be simulated by performing shear rheology, which allows assessment of polymer chain alignment in a high shear environment.

High shear rheology was performed using a Rheosense VROC® microfluidic device to investigate the shear behaviour of formulations of **8a** and **8c** as they passed through a microchannel at various shear rates. The instrument recorded changes in viscosity by measuring the pressure drop as the liquid passed through the channel. If the viscosity increases at high shear rates, the material is described as

shear thickening; if it decreases, the material is shear thinning and if it is independent of shear rate it is a Newtonian fluid. CIJ printing involves the recirculation of ink through the printer passing the formulation through the nozzle many times. Formulations that exhibit Newtonian behaviour are therefore desirable, as shear thickening or thinning would result in a change in the viscosity, which would affect the consistency of printing over time. The lower molecular weight polymer (**8a**) acted as a Newtonian fluid. However, **8c** exhibited near-Newtonian behaviour with a minor amount of shear thickening, indicated by a maximum increase in viscosity of 0.13 cP, as the shear rate was increased (Figure 23).

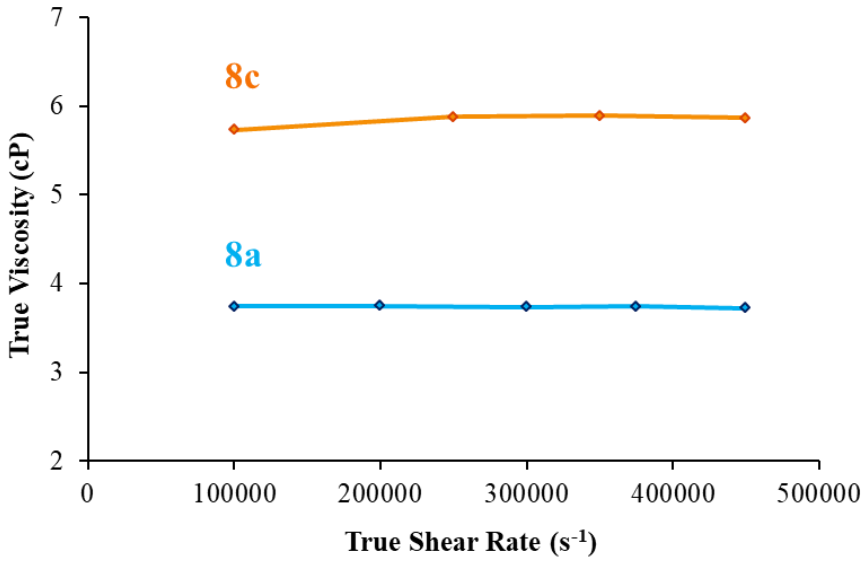

Figure 23- Analysis of the Newtonian behaviour of solutions of PFO samples **8a** and **8c** using the Rheosense VROC® micro fluidic rheometer, showing that viscosity is independent of shear rate for **8a**, but some shear thickening is observed with increasing shear rate for **8c**.

Alongside high-shear performance of the polymers, it is also important to understand the extent of the relaxation of polymer chains at high frequencies. During CIJ printing, the polymer chains need to demonstrate relaxation over a similar timescale to that of the drop formation, or the polymer may demonstrate solid-like behaviour if the polymer relaxation time is too long. The extent of polymer relaxation at high frequencies can be determined using microrheological techniques that monitor the Brownian motion of tracer particles (melamine 615 nm diameter) in the polymeric solution using dynamic light scattering (DLS). A Malvern Zetasizer Nano ZSP was used to determine the viscoelastic responses of polymers **8a** and **8c** at increasing angular frequencies. Both polymers demonstrated a slight decrease in the complex viscosity of solution at higher frequencies, indicating slight viscoelasticity of polymers, with near-Newtonian behaviour. The shear and microrheological exponents were plotted against one another and compared to existing polymer binders used by Domino Printing Sciences to determine the behaviour and suitability of the PFO materials (**8a** and **8c**)

within inkjet formulations. Non-Newtonian fluids would exhibit a low exponent value for both shear rheology and microrheology, whereas purely Newtonian fluids would demonstrate values of 1 for both exponents. Both polymers **8a** and **8c** demonstrated near-Newtonian behaviour as evident by their position in the top right-hand corner of the plot (Figure 24).

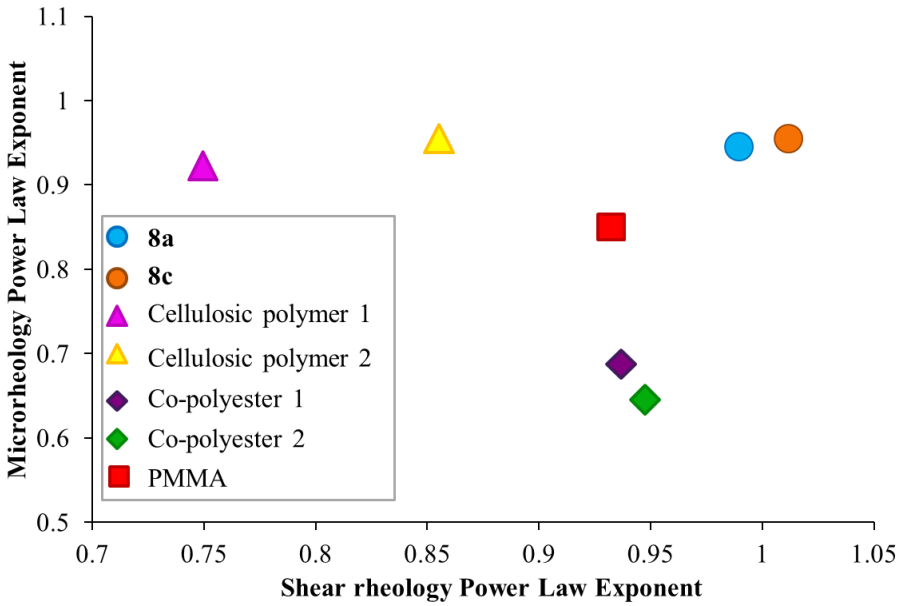

Figure 24- Plot of the power law exponents of the shear rheology and microrheology of solutions of **8a** (300 mg mL^{-1}) and **8c** (200 mg mL^{-1}) with a comparison to other commercial polymer binders currently used at Domino Printing Sciences Ltd.

When compared to the commercial binders used at Domino Printing Sciences, the PFO materials **8a** and **8c** show less shear thinning behaviour when subjected to high shear rates and instead demonstrate a more Newtonian-like behaviour. The viscoelasticity values of the PFOs (y-axis-Figure 24) are comparable to those recorded for the cellulosic-based polymers (pink and yellow-Figure 24) used at Domino Printing Sciences and indicate that the polymers would show sufficient relaxation of polymer chains within the timeframe for drop formation and would not exhibit solid-like behaviour during inkjet deposition. Promisingly, the near-Newtonian behaviour of polymers **8a** and **8c** indicated that the materials were suitable for deposition using the Ax-series CIJ printhead.

4.2.9 CIJ Deposition of Polymers 8a and 8c

Formulations of both PFOs **8a** and **8c** (300 mg mL^{-1} and 200 mg mL^{-1}, respectively) were prepared in MEK (100 mL total solution) and filtered (0.45 µm PTFE membrane) to produce solutions of sufficient viscosity (3.9 and 5.3 cP, respectively) for CIJ deposition. Formulations intended for use in CIJ printers need to exhibit a minimum charge of 400 μScm^{-1} in order to undergo sufficient deflection from the charge electrode onto the substrate; therefore a conductive dye was required, which would aid deflection as well as visualisation of the printed image. Orasol® orange 247 is a cobalt complex

which provides good conductivity at relatively low concentration (4 wt%) and was therefore added to the formulations of **8a** and **8c** to produce formulations with conductivities of 772 and 804 μScm^{-1}, respectively. The materials were then deposited using a Domino Ax-series CIJ printer (Figure 25).

Figure 25- The Domino Ax-series CIJ printer used to deposit formulations of PFO **8a** and **8c**, showing the dis-assembled CIJ printhead to the right-hand side.

The droplet break up of formulations deposited using the Ax-series CIJ printer can be monitored during printing to produce a jet profile, which records the droplet-break up time at increasing nozzle plate modulation amplitudes. The jet profiles recorded for the PFO samples **8a** and **8c** showed a similar trend to the jet profiles of the commercial polymer formulations used at Domino Printing Sciences, which all exhibit two peak maxima, one at a lower voltage and a second at higher voltages. The optimum nozzle plate modulation amplitude for successful droplet break up is determined by the peak maximum at the lowest voltage range on the jet profile curve and is automatically determined during printing. In the case of PFO samples **8a** and **8c** the optimum modulation voltages were 40 and 45 V, respectively, as determined by the peak maxima in the jet profile (Figure 26).

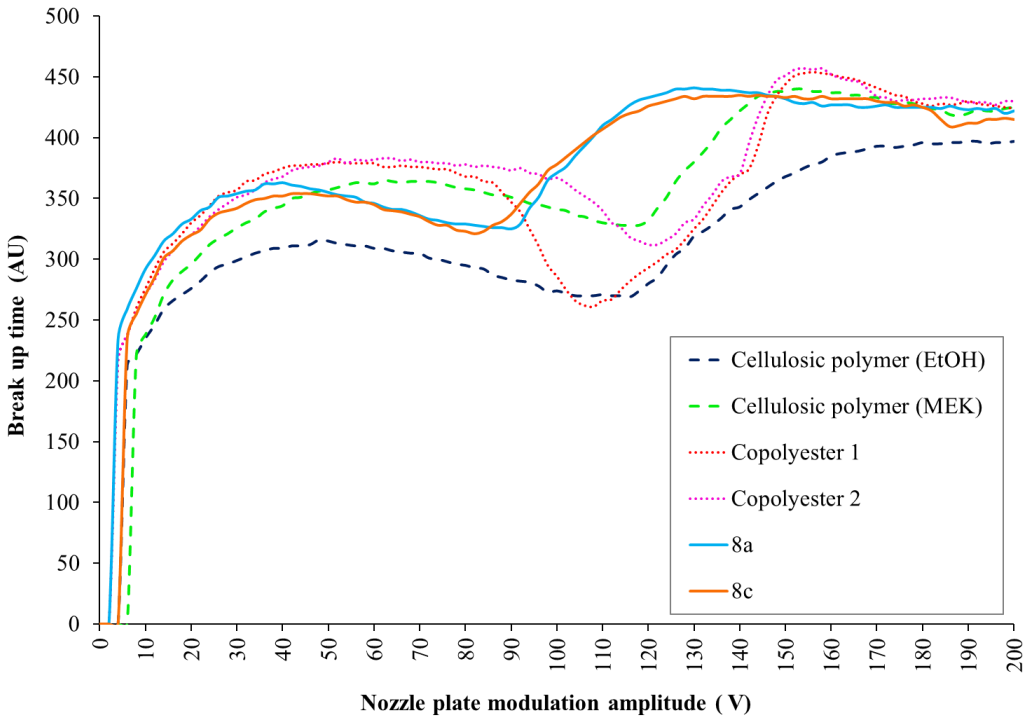

Figure 26- Jet profiles produced using Ax-series printer for formulations of polymers **8a** (300 mg mL^{-1}) and **8c** (200 mg mL^{-1}) demonstrating an optimum modulation voltage of 40 and 45 V, respectively. The jet profiles of a commercial cellulosic polymer (in EtOH and MEK) and two different copolyesters are shown for comparison.

The optimum modulation voltages of **8a** and **8c** are slightly lower than the commercial cellulosic and copolyester polymers used at Domino Printing Sciences (see Figure 26), but are in an acceptable range for CIJ printing. In order for a formulation to show good droplet break up, the optimum modulation voltage needs to coincide with the voltage range of the average good phases, which occur when the charge on the droplet exceeds the minimum charge detection threshold, i.e. the droplet is charged *vs.* uncharged or partially charged. The jet profile software calculates the voltage range at which the droplet is charged and revealed a voltage range of 18–78 V for **8a** and 32–62 V for **8c**, both of which coincided with the respective optimum modulation voltages of 40 and 45 V. This result indicates that both of the formulations will show good droplet breakup and imparting of charge, although, as **8a** has a larger window of good phases, i.e. successful charging of droplets, it exhibits a better jetting profile than **8c**. This could be as a result of the decreased molecular weight or decreased viscosity of **8a** when compared to **8c**, both of which may result in better performance in the printhead.

The break-up of the jetstream of formulations of **8a** and **8c** was also studied using a magnifying eyepiece, which was placed on the printhead to visualise the jet stream, with the aid of a strobe light set to operate at 85 kHz (Figure 27). Both polymers **8a** and **8c** were deposited successfully onto a variety of substrates including glass, nylon, PET, stainless steel, LDPE and PP using the Ax-series CIJ printer and produced clear, neat images with no apparent satellite drops or misfires (Figure 28).

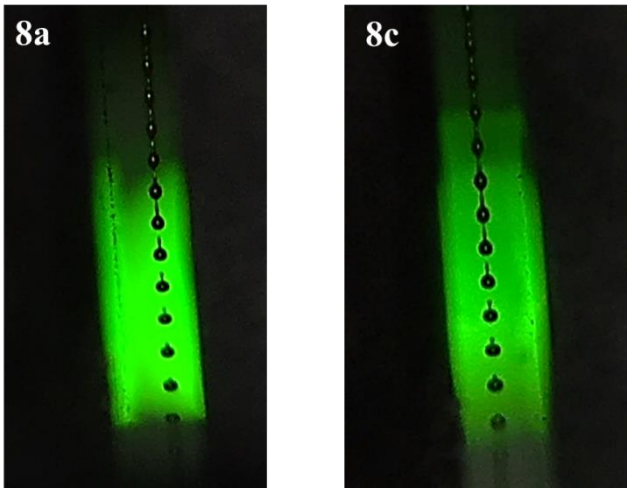

Figure 27- Photographs of the droplet formation during Ax-series CIJ printing of formulations of polymers **8a** and **8c**, obtained using a stroboscopic light set at 85 kHz. Both polymer formulations show good droplet formation without any apparent satellite droplets observed.

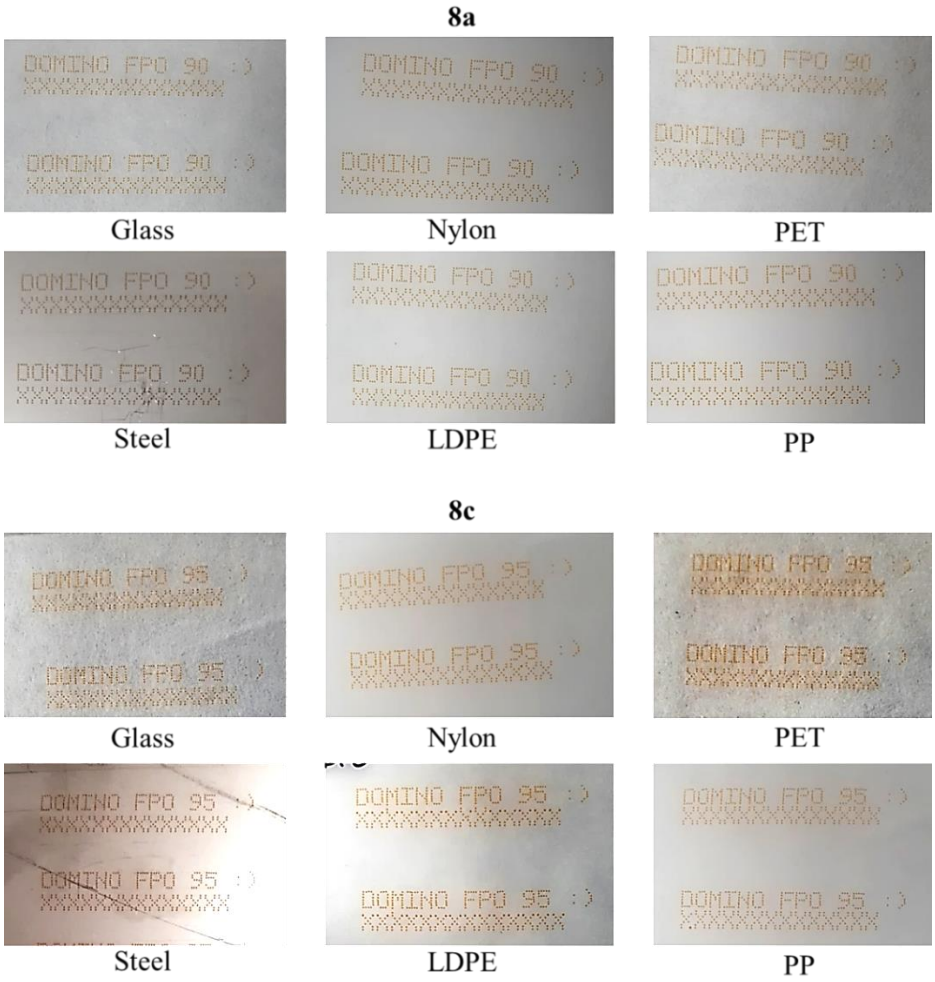

Figure 28- CIJ deposition of formulations of PFO samples **8a** and **8c** onto glass, nylon, PET, stainless steel, LDPE and PP showing clear printed code in all cases.

The adhesion of the polymer and dye to the substrates was then tested using peel tests. Adhesive tape (810 grade) was used and the amount of material removed from the substrate was scored from 1–5, where 1 indicates the complete removal of the print (very poor adhesion) and 5 indicates no removal of print (excellent adhesion). Both PFO samples exhibited very poor adhesion to PP, which was expected since this substrate possesses a very low surface energy (25.7 mNm^{-1} see Table 1). Poor adhesion to the surface of PP occurs as a result of poor wetting of the substrate.[29,30] The PFO polymers exhibited moderate adhesion to steel and excellent adhesion to glass, nylon and PET (Table 6).

Table 6- Grading of adhesion of polymers **8a** and **8c** to different substrates, where 1 (red) = very poor adhesion and 5 (green) = excellent adhesion.

	Substrate					
	Glass	**PET**	**Nylon**	**Steel**	**LDPE**	**PP**
8a	**5**	**5**	**5**	**3**	**1**	**1**
8c	**4**	**5**	**5**	**3**	**1**	**1**

Despite the suitability of polymers **8a** and **8c** to inkjet printing, demonstrated by the good jet profile, good drop-break up, and the clean prints produced, it is important to also analyse the potential of the polymers to cause dusting during CIJ printing. Dusting occurs when minute fragments of polymers or other components of formulations build up on the deflector plates or in the gutter of the CIJ printer over time during normal operation of the printer. It is important that the polymer formulations do not contribute to dusting effects as gradual build-up of material over time can result in the generation of a printer trip fault and shut-down of the production line. Therefore build-up from dusting needs to be detected in the early stages of ink development to prevent loss of time and money.

The potential for materials to cause build-up can be predicted using an aerosol detection device during CIJ printing. The DustTrak™ DRX aerosol monitor was used to measure the quantity of aerosol generation from the jetstream. The detector uses a low vacuum to draw air away from the continuous stream of ink at different distances form the printhead nozzle and the air is passed through collision filters to give an estimation of particle size and the particles counted using laser scattering technology.

Previous studies undertaken at Domino Printing Sciences, have enabled the grading of results (green-red) obtained using the DustTrak™ DRX. Formulations with an aerosol count of below 50 μgm^{-3} (green region) are considered unlikely to cause build-up, those with a count of 50–100 μgm^{-3} (amber region) do not pose a high risk of build-up, but would require further investigation and formulations with an aerosol count over 100 μgm^{-3} (red region) are highly likely to cause build-up.

The aerosol generation of PFO samples **8a** and **8c** was investigated using the DustTrak™ DRX with several aerosol counts recorded at different distances from the printhead nozzle (100–600 µm). The lower molecular weight PFO **8a** (11,000 g mol^{-1}) produced a maximum aerosol count of 38 $µgm^{-3}$ recorded at 200 µm thus falling into the green region, indicating a low chance of build-up. The higher molecular weight PFO **8c** exhibited a larger aerosol count of 89 $µgm^{-3}$ which places it in the amber region; indicating that the formulation would have to be monitored for potential build-up during longer print times (Figure 29).

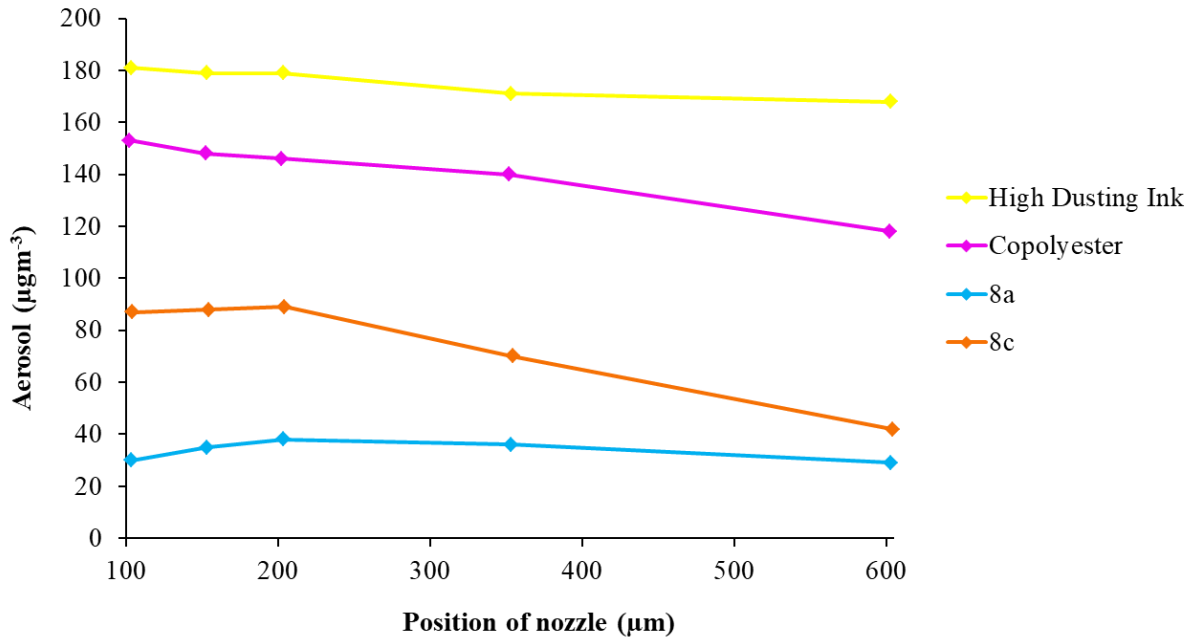

Figure 29- Aerosol generation of polymers **8a** and **8c**, showing the amount of aerosolised particles produced from the jet stream ($µgm^{-3}$) with increasing distance from the printer nozzle (µm). DustTrak™ DRX data for a commercial copolyester used at Domino Printing Sciences and an example of a very high dusting inkjet formulation are also shown for comparison.

The increased aerosol generation for polymer **8c** when compared to **8a** could be a result of the increased molecular weight of the polymer as higher molecular weight polymers tend to undergo messier break up as a result of elongational flow which can result in the production of micro-satellites.[1,32] The increase could also be a result of the higher viscosity of the formulation of **8c** (5.3 cP *cf*. 3.9 cP for **8a**) which in pre-deposition studies demonstrated slight shear thickening, with a deviation from Newtonian behaviour (see Figure 23). The results obtained in this study indicated that polymers **8a** and **8c** were soluble, printable, and demonstrated hydrophobic properties post-deposition. Furthermore, these materials demonstrated Newtonian or near-Newtonian behaviour and little to no risk of causing build-up in the Ax-series CIJ printer, indicating that the materials have potential as soluble, yet hydrophobic polymer binders for inkjet formulations.

4.3 Conclusions

A series of five PEKKs (**4**, **6a**–**d**) have been produced, by effectively controlling the molecular weight of the materials produced, by adjusting the stoichiometric ratio of monomers used in the AA/BB step-growth polymerisation. The PEKKs were then converted successfully to the desired PFOs (**1**, **8a**–**d**) (M_n = 11,500–114,500 g mol^{-1}) via the PSE derivatives (**5**, **7a**–**d**).

The hydrophobicity of the PFO films was investigated using contact angles measurements and revealed consistent hydrophobic properties (water contact angle 88–89°) that were independent of the molecular weight of the poly(fluorocarbinol)s.

Initial printing studies of the PFOs were performed using a Dimatix™ DOD printhead and found that the highest molecular weight polymer **1** (114,500 g mol^{-1}) was not printable as a result of elastic stress from elongational flow, which is often observed in higher molecular weight polymer formulations. The remaining PFOs (**8a**–**d**) were deposited using the DOD printhead described, but the PFO **8d** required maximum voltage of the piezoelectric printhead during deposition, indicating the highest risk of print failure out of the PEKK series.

Polymers **8a** and **8c** were investigated further for potential as inkjet formulations and pre-CIJ deposition screening revealed that both materials were suitable for inkjet printing. Polymer **8a** acted as a Newtonian fluid under high-shear jetting conditions and **8c** exhibited small amounts of shear-thickening (near-Newtonian fluid) indicating minimal risk of viscosity modification during printing. Polymers **8a** and **8c** were both deposited using a Domino Ax-series CIJ printer and demonstrated good drop break-up and jet-profiles, further indicating their suitability as inkjet materials. Both polymers were deposited successfully onto a variety of substrates, including: glass, PET and Nylon, to which the materials demonstrated good adhesion, highlighting their potential as polymer binders. The potential for build-up (dusting) of the formulations in the printhead and gutter was also investigated using the DustTrak™ DRX, which revealed polymer **8a** to show minimal risk of build-up over time in the printhead. Polymer **8c** exhibited a low risk for build-up with a particle count more than double that for **8a**.

Both materials **8a** and **8c** were deemed to be suitable polymer additives for inkjet formulations, with both polymers showing good solubility, jettability, adhesion and hydrophobic properties. However, polymer **8a** was concluded to demonstrate more favourable characteristics for use in an inkjet formulation than **8c** as it acted as a Newtonian fluid in the printhead and exhibited less risk of build-up during extended printing periods.

4.4 Experimental

Reagents, spectral data and printing of formulations were carried out as in Section 2.4. Water contact angles were measured using a KSV CAM 200 optical tensiometer in sessile drop mode with Oneattension. Surface energy measurements were calculated using the (OWRK) extended Fowkes method on the OneAttension® software on the KSV CAM 200. Viscosity measurements were recorded using an Anton Paar Stabinger viscometer with samples dissolved in MEK. Shear rheology experiments were performed using a Rheosense VROC® microfluidic device at shear rates of 100,000–450,000 s^{-1}. Microrheology experiments were performed using a Malvern Zetasizer Nano ZSP with melamine (615 nm diameter) as tracer particles. Continuous inkjet printing was achieved using a Domino Ax-series printer with a 60 μm diameter nozzle. A DustTrak™ DRX aerosol counter was used to determine the aerosol generation during printing with the CIJ printer.

4.4.1 Synthesis of Poly(ether diketone)s

4.4.1.1 Synthesis of PEKK 4

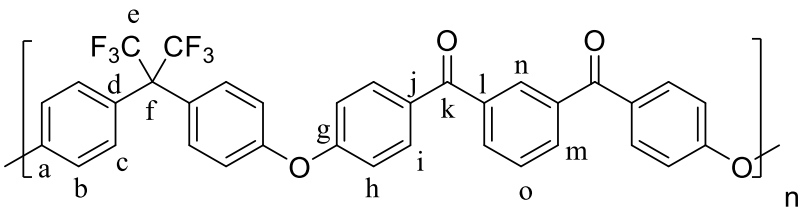

Dried K_2CO_3 (1.17g, 8.50 mmol), 4,4'-(hexafluoro*iso*propylidene) diphenol (2.69 g, 8.00 mmol) and *N*-methyl-2-pyrrolidone (10 mL) were stirred under an N_2 atmosphere for 5 minutes. 1,3-Bis(4-fluorobenzoyl)benzene (2.58 g, 8.0 mmol), *N*-methyl-2-pyrrolidone (10 mL) and toluene (12 mL) were added and the suspension was heated at 180 °C for 8 hours under an N_2 atmosphere, with azeotropic distillation of water using a Dean-Stark trap. The reaction mixture was cooled to room temperature and then poured into methanol (300 mL). The precipitated polymer was collected by filtration, washed with water and dried at 100 °C *in vacuo*. The polymer was re-precipitated twice into methanol (300 mL) following dissolution in the minimum volume of dichloromethane (~30 mL) and dried *in vacuo* to produce **4** as a cream coloured solid (3.67 g, 74%). IR (ATR) ν/cm^{-1}: 3060 (aromatic C–H), 1662 (C=O ketone), 1593 (aromatic C=C), 1499 (aromatic C=C), 1239 (C–O ether), 1173 (C–F), 838 (aromatic C–H); ^{1}H NMR (400 MHz/$CDCl_3$) δ ppm: 8.17 (1H, s, H_n), 7.99 (2H, appt. d, appt. J = 8.8 Hz, H_m), 7.87 (4H, appt. d, appt. J = 8.6 Hz, H_i), 7.62 (1H, appt. t, appt. J = 7.7 Hz, H_o), 7.43 (4H, appt. d, appt. J = 8.5 Hz, H_c), 7.11 (4H, appt. d, appt. J = 8.8 Hz, H_h), 7.08 (4H, appt. d, appt. J = 9.0 Hz, H_b); ^{13}C NMR (100 MHz/$CDCl_3$) δ ppm: 194.5 (C_k), 160.7 (C_g), 156.4 (C_a), 138.0 (C_l), 133.2 (C_m), 132.6 (C_i), 132.2 (C_j), 132.0 (C_c), 130.8 (C_n), 129.0 (C_d), 128.5 (C_o), 119.1 (C_b), 118.3 (C_h); ^{19}F NMR (376 MHz/$CDCl_3$) ppm: –64.1; GPC (THF): M_n = 114,000, M_w = 260,900, $Đ$ = 2.29; DSC: T_g(midpoint) = 162 °C.

4.4.1.2 Synthesis of PEKK 6a

PEKK 6a was synthesised using the procedure described in section 4.4.1.1 employing 0.90 molar equivalents of 1,3-bis(4-fluorobenzoyl)benzene (2.33 g, 7.20 mmol) to yield PEKK **6a** as a cream powder (2.28 g, 51%). IR (ATR) ν/cm^{-1}: 3060 (aromatic C–H), 1662 (C=O ketone), 1593 (aromatic C=C), 1499 (aromatic C=C), 1239 (C–O ether), 1173 (C–F), 838 (aromatic C–H); ^{1}H NMR (400 MHz/$CDCl_3$) δ ppm: 8.17 (1H, s, H_n), 7.99 (2H, appt. d, appt. J = 8.8 Hz, H_m), 7.87 (4H, appt. d, appt. J = 8.6 Hz, H_i), 7.62 (1H, appt. t, appt. J = 7.7 Hz, H_o), 7.43 (4H, appt. d, appt. J = 8.5 Hz, H_c), 7.11 (4H, appt. d, appt. J = 8.8 Hz, H_h), 7.08 (4H, appt. d, appt. J = 9.0 Hz, H_b); ^{13}C NMR (100 MHz/$CDCl_3$) δ ppm: 194.5 (C_k), 160.7 (C_g), 156.4 (C_a), 138.0 (C_l), 133.2 (C_m), 132.6 (C_i), 132.2 (C_j), 132.0 (C_c), 130.8 (C_n), 129.0 (C_d), 128.5 (C_o), 119.1 (C_b), 118.3 (C_h); ^{19}F NMR (376 MHz/$CDCl_3$) ppm: –64.1; GPC (THF): M_n = 10,500, M_w = 18,300, $Đ$ = 1.74; DSC: T_g (midpoint) = 145 °C.

4.4.1.3 Synthesis of PEKK 6b

PEKK 6b was synthesised using the procedure described in section 4.4.1.1 employing 0.925 molar equivalents of 1,3-bis(4-fluorobenzoyl)benzene (2.40 g, 7.40 mmol) to yield PEKK **6b** as a white-cream powder (2.57 g, 56%). IR (ATR) ν/cm^{-1}: 3060 (aromatic C–H), 1662 (C=O ketone), 1593 (aromatic C=C), 1499 (aromatic C=C), 1239 (C–O ether), 1173 (C–F), 838 (aromatic C–H); ^{1}H NMR (400 MHz/$CDCl_3$) δ ppm: 8.17 (1H, s, H_n), 7.99 (2H, appt. d, appt. J = 8.8 Hz, H_m), 7.87 (4H, appt. d, appt. J = 8.6 Hz, H_i), 7.62 (1H, appt. t, appt. J = 7.7 Hz, H_o), 7.43 (4H, appt. d, appt. J = 8.5 Hz, H_c), 7.11 (4H, appt. d, appt. J = 8.8 Hz, H_h), 7.08 (4H, appt. d, appt. J = 9.0 Hz, H_b); ^{13}C NMR (100 MHz/$CDCl_3$) δ ppm: 194.5 (C_k), 160.7 (C_g), 156.4 (C_a), 138.0 (C_l), 133.2 (C_m), 132.6 (C_i), 132.2 (C_j), 132.0 (C_c), 130.8 (C_n), 129.0 (C_d), 128.5 (C_o), 119.1 (C_b), 118.3 (C_h); ^{19}F NMR (376 MHz/$CDCl_3$) ppm: –64.1; GPC (THF): M_n = 15,600, M_w = 30,500, $Đ$ = 1.95; DSC: T_g (midpoint) = 148 °C.

4.4.1.4 Synthesis of PEKK 6c

PEKK 6c was synthesised using the procedure described in section 4.4.1.1 employing 0.95 molar equivalents of 1,3-bis(4-fluorobenzoyl)benzene (2.46 g, 7.60 mmol) to yield PEKK **6c** as a white-cream solid (3.05 g, 65%). IR (ATR) ν/cm^{-1}: 3060 (aromatic C–H), 1662 (C=O ketone), 1593 (aromatic C=C), 1499 (aromatic C=C), 1239 (C–O ether), 1173 (C–F), 838 (aromatic C–H); ^{1}H NMR (400 MHz/ $CDCl_3$) δ ppm: 8.17 (1H, s, H_n), 7.99 (2H, appt. d, appt. J = 8.8 Hz, H_m), 7.87 (4H, appt. d, appt. J = 8.6 Hz, H_i), 7.62 (1H, appt. t, appt. J = 7.7 Hz, H_o), 7.43 (4H, appt. d, appt. J = 8.5 Hz, H_c), 7.11 (4H, appt. d, appt. J = 8.8 Hz, H_h), 7.08 (4H, appt. d, appt. J = 9.0 Hz, H_b); ^{13}C NMR (100 MHz/ $CDCl_3$) δ ppm: 194.5 (C_k), 160.7 (C_g), 156.4 (C_a), 138.0 (C_l), 133.2 (C_m), 132.6 (C_i), 132.2 (C_j), 132.0 (C_c), 130.8 (C_n), 129.0 (C_d), 128.5 (C_o), 119.1 (C_b), 118.3 (C_h); ^{19}F NMR (376 MHz/$CDCl_3$) ppm: –64.1; GPC (THF): M_n = 22,000, M_w = 43,200, $Đ$ = 1.91; DSC: T_g (midpoint) = 149 °C.

4.4.1.5 Synthesis of PEKK 6d

PEKK 6d was synthesised using the procedure described in section 4.4.1.1 employing 0.975 molar equivalents of 1,3-bis(4-fluorobenzoyl)benzene (2.53 g, 7.80 mmol) to yield PEKK **6d** as a white-cream solid (3.48 g, 72%). IR (ATR) ν/cm^{-1}: 3060 (aromatic C–H), 1662 (C=O ketone), 1593 (aromatic C=C), 1499 (aromatic C=C), 1239 (C–O ether), 1173 (C–F), 838 (aromatic C–H); ^{1}H NMR (400 MHz/$CDCl_3$) δ ppm: 8.17 (1H, s, H_n), 7.99 (2H, appt. d, appt. J = 8.8 Hz, H_m), 7.87 (4H, appt. d, appt. J = 8.6 Hz, H_i), 7.62 (1H, appt. t, appt. J = 7.7 Hz, H_o), 7.43 (4H, appt. d, appt. J = 8.5 Hz, H_c), 7.11 (4H, appt. d, appt. J = 8.8 Hz, H_h), 7.08 (4H, appt. d, appt. J = 9.0 Hz, H_b); ^{13}C NMR (100 MHz/ $CDCl_3$) δ ppm: 194.5 (C_k), 160.7 (C_g), 156.4 (C_a), 138.0 (C_l), 133.2 (C_m), 132.6 (C_i), 132.2 (C_j), 132.0 (C_c), 130.8 (C_n), 129.0 (C_d), 128.5 (C_o), 119.1 (C_b), 118.3 (C_h); ^{19}F NMR (376 MHz/$CDCl_3$) ppm: –64.1; GPC (THF): M_n = 42,500, M_w = 87,700, $Đ$ = 2.06; DSC: T_g (midpoint) = 155 °C.

4.4.2 Synthesis of Poly(trifluoromethyltrimethylsilyl ether)s (PSE)

4.4.2.1 Synthesis of PSE 5

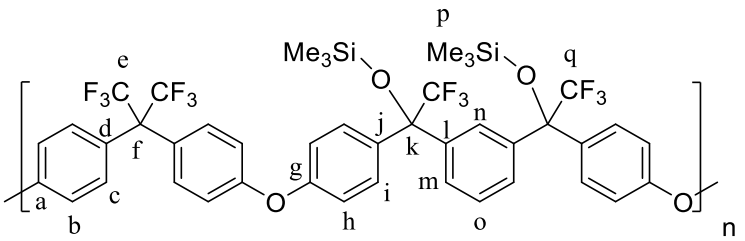

PEKK **4** (2.00 g, 3.20 mmol of repeat units) was dissolved in anhydrous THF (80 mL) under N_2 atmosphere. The solution was cooled to 0 °C for 5 minutes and trifluoromethyltrimethyl silane (Ruppert's reagent) (15 mL, 100 mmol) and tetra-*n*-butylammonium fluoride hydrate (320 mg in 2.0 mL THF, 1.20 mmol) were added dropwise. The reaction mixture was stirred at 0 °C for 3 hours and then for 18 hours at 20 °C. The volatile components were removed *in vacuo* and the resulting polymer was dissolved in the minimum amount of dichloromethane (~ 50 mL) and precipitated into methanol (500 mL). The polymer was collected by filtration and dried at 100 °C *in vacuo* for 2 hours. The polymer was re-precipitated twice into methanol (500 mL) from the minimum volume of dichloromethane. The poly(trifluoromethytrimethylsilyl ether) **5** was obtained as a white solid (2.31 g, 80%). IR (ATR) ν/cm^{-1}: 2980 (aromatic C–H), 1602 (aromatic C=C), 1504 (aromatic C=C), 1251 (C–O ether), 1159 (C–F), 845 (aromatic C–H); ^{1}H NMR (400 MHz/$CDCl_3$) δ ppm: 7.62 and 7.51 (1H, s, H_n), 7.40–7.27 (11H, m, $H_{c,i,m+o}$), 7.01–6.92 (8H, m, H_{b+h}), –0.1 (18H, s, H_p); ^{13}C NMR (100 MHz/ $CDCl_3$) δ ppm: 156.4 (C_a), 155.0 (C_g), 139.5 (C_l), 135.1 (C_j), 130.6 (C_c), 128.7 (C_i), 126.8, 126.6 , 126.3 (C_{m+n+o}), 126.7 (C_d), 117.5 (C_h), 116.6 (C_b), 80.2 (C_k), 0.0 (C_p); ^{19}F NMR (376 MHz/$CDCl_3$) ppm: –64.1, –72.7 and –72.8; GPC (THF): M_n = 195,300, M_w = 537,000, $Đ$ = 2.75; DSC: T_g (midpoint) = 131 °C.

4.4.2.2 Synthesis of PSE 7a

PSE 7a was synthesised using the procedure described in section 4.4.2.1 employing PEK **6a** to yield PSE **7a** as a white powder (1.21 g, 42%). IR (ATR) ν/cm^{-1}: 2980 (aromatic C–H), 1602 (aromatic C=C), 1504 (aromatic C=C), 1251 (C–O ether), 1159 (C–F), 845 (aromatic C–H); ^{1}H NMR (400 MHz/ $CDCl_3$) δ ppm: 7.62 and 7.51 (1H, s, H_n), 7.40–7.27 (11H, m, $H_{c,i,m+o}$), 7.01–6.92 (8H, m, H_{b+h}), –0.1 (18H, s, H_p); ^{13}C NMR (100 MHz/$CDCl_3$) δ ppm: 156.4 (C_a), 155.0 (C_g), 139.5 (C_l), 135.1 (C_j), 130.6 (C_c), 128.7 (C_i), 126.8, 126.6 , 126.3 (C_{m+n+o}), 126.7 (C_d), 117.5 (C_h), 116.6 (C_b), 80.2 (C_k), 0.0 (C_p); ^{19}F NMR (376 MHz/$CDCl_3$) ppm: –64.1, –72.7 and –72.8; GPC (THF): M_n = 19,500, M_w = 29,500, $Đ$ = 1.52; DSC: T_g (midpoint) = 120 °C.

4.4.2.3 Synthesis of PSE 7b

PSE 7b was synthesised using the procedure described in section 4.4.2.1 employing PEK **6b** to yield PSE **7b** as a white powder (1.23 g, 45%). IR (ATR) ν/cm^{-1}: 2980 (aromatic C–H), 1602 (aromatic C=C), 1504 (aromatic C=C), 1251 (C–O ether), 1159 (C–F), 845 (aromatic C–H); ^{1}H NMR (400 MHz/ $CDCl_3$) δ ppm: 7.62 and 7.51 (1H, s, H_n), 7.40–7.27 (11H, m, $H_{c,i,m+o}$), 7.01–6.92 (8H, m, H_{b+h}), –0.1 (18H, s, H_p); ^{13}C NMR (100 MHz/$CDCl_3$) δ ppm: 156.4 (C_a), 155.0 (C_g), 139.5 (C_l), 135.1 (C_j), 130.6 (C_c), 128.7 (C_i), 126.8, 126.6 , 126.3 (C_{m+n+o}), 126.7 (C_d), 117.5 (C_h), 116.6 (C_b), 80.2 (C_k), 0.0 (C_p); ^{19}F NMR (376 MHz/$CDCl_3$) ppm: –64.1, –72.7 and –72.8; GPC (THF): M_n = 23,300, M_w = 47,200, $Đ$ = 2.03; DSC: T_g (midpoint) = 121 °C.

4.4.2.4 Synthesis of PSE 7c

PSE 7c was synthesised using the procedure described in section 4.4.2.1 employing PEK **6c** to yield PSE **7c** as a white solid (1.68 g, 58%). IR (ATR) ν/cm^{-1}: 2980 (aromatic C–H), 1602 (aromatic C=C), 1504 (aromatic C=C), 1251 (C–O ether), 1159 (C–F), 845 (aromatic C–H); ^{1}H NMR (400 MHz/$CDCl_3$) δ ppm: 7.62 and 7.51 (1H, s, H_n), 7.40–7.27 (11H, m, $H_{c,i,m+o}$), 7.01–6.92 (8H, m, H_{b+h}), –0.1 (18H, s, H_p); ^{13}C NMR (100 MHz/$CDCl_3$) δ ppm: 156.4 (C_a), 155.0 (C_g), 139.5 (C_l), 135.1 (C_j), 130.6 (C_c), 128.7 (C_i), 126.8, 126.6 , 126.3 (C_{m+n+o}), 126.7 (C_d), 117.5 (C_h), 116.6 (C_b), 80.2 (C_k), 0.0 (C_p); ^{19}F NMR (376 MHz/$CDCl_3$) ppm: –64.1, –72.7 and –72.8; GPC (THF): M_n = 40,200, M_w = 83,000, $Đ$ = 2.06; DSC: T_g (midpoint) = 126 °C.

4.4.2.5 Synthesis of PSE 7d

PSE 7d was synthesised using the procedure described in section 4.4.2.1 employing PEK **6d** to yield PSE **7d** as a white solid (1.88 g, 65%). IR (ATR) ν/cm^{-1}: 2980 (aromatic C–H), 1602 (aromatic C=C), 1504 (aromatic C=C), 1251 (C–O ether), 1159 (C–F), 845 (aromatic C–H); ^{1}H NMR (400 MHz/$CDCl_3$) δ ppm: 7.62 and 7.51 (1H, s, H_n), 7.40–7.27 (11H, m, $H_{c,i,m+o}$), 7.01–6.92 (8H, m, H_{b+h}), –0.1 (18H, s, H_p); ^{13}C NMR (100 MHz/$CDCl_3$) δ ppm: 156.4 (C_a), 155.0 (C_g), 139.5 (C_l), 135.1 (C_j),

130.6 (C_c), 128.7 (C_i), 126.8, 126.6 , 126.3 (C_{m+n+o}), 126.7 (C_d), 117.5 (C_h), 116.6 (C_b), 80.2 (C_k), 0.0 (C_p); ^{19}F NMR (376 MHz/$CDCl_3$) ppm: –64.1, –72.7 and –72.8; GPC (THF): M_n = 55,100, M_w = 116,300, $Đ$ = 2.11; DSC: T_g (midpoint) = 127 °C.

4.4.3 Synthesis of Poly(trifluoromethyl carbinol)s (PFO)

4.4.3.1 Synthesis of PFO 1

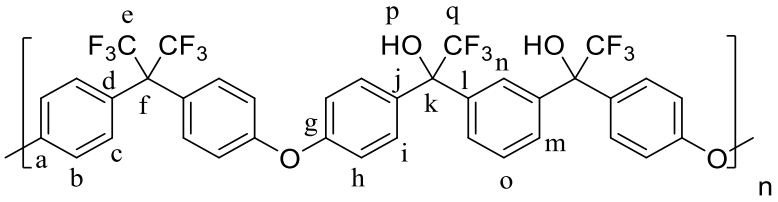

To a stirred solution of PSE **5** (2.00 g, 2.60 mmol of repeat units) in anhydrous THF (110 mL) was added tetra-*n*-butylammonium fluoride hydrate (12.0 g in 20 mL THF, 47.5 mmol) under N_2 atmosphere. The reaction mixture was stirred for 24 hours, before removing the volatile components *in vacuo* and dissolving the residue in the minimum volume of acetone (~ 40 mL) and then precipitating into deionised water (400 mL). The solid was collected by filtration and dried *in vacuo* at 100 °C. The solid was re-precipitated twice from the minimum volume of acetone (~40 mL) into deionised water (400 mL), collected by filtration and dried *in vacuo* to produce **1** as a cream solid (1.46 g, 74%). IR (ATR) ν/cm^{-1}: 3495 (O–H alcohol), 1604 (aromatic C=C), 1504 (aromatic C=C), 1245 (C–O ether), 1152 (C–F), 1062 (C–O alcohol), 830 (aromatic C–H); ^{1}H NMR (400 MHz/$CDCl_3$) δ ppm: 7.70 and 7.69 (1H, s, H_n), 7.46–7.36 (6H, m, H_{i+m}), 7.34–7.27 (5H, m, H_{c+o}), 6.94 (4H, appt. d, appt. J = 8.3 Hz, H_h), 6.91 (4H, appt. d, appt. J = 8.5 Hz, H_b), 3.09 (2H, br, H_p); ^{13}C NMR (100 MHz/$CDCl_3$) δ ppm: 157.3 (C_a), 156.5 (C_g), 139.3 (C_l), 134.5 (C_j), 131.8 (C_c), 129.2 (C_i), 128.3 (C_o), 128.1 (C_d), 127.9 (C_m), 126.5 (C_n), 119.0 (C_h), 118.0 (C_b), 79.1(C_k); ^{19}F NMR (376 MHz/$CDCl_3$) ppm: –64.1 and –74.5; GPC (THF): M_n = 114,500, M_w = 254,800, $Đ$ = 2.22; DSC: T_g (midpoint) = 141 °C.

4.4.3.2 Synthesis of PFO 8a

PFO 8a was synthesised using the same procedure as in section 4.4.3.1 employing PSE **7a** to yield PFO **8a** as a cream powder (1.20 g, 61%). IR (ATR) ν/cm^{-1}: 3495 (O–H alcohol), 1604 (aromatic C=C), 1504 (aromatic C=C), 1245 (C–O ether), 1152 (C–F), 1062 (C–O alcohol), 830 (aromatic C–H); ^{1}H NMR (400 MHz/$CDCl_3$) δ ppm: 7.70 and 7.69 (1H, s, H_n), 7.46–7.36 (6H, m, H_{i+m}), 7.34–7.27 (5H, m, H_{c+o}), 6.94 (4H, appt. d, appt. J = 8.3 Hz, H_h), 6.91 (4H, appt. d, appt. J = 8.5 Hz, H_b), 3.09 (2H, br, H_p); ^{13}C NMR (100 MHz/$CDCl_3$) δ ppm: 157.3 (C_a), 156.5 (C_g), 139.3 (C_l), 134.5 (C_j), 131.8 (C_c), 129.2 (C_i), 128.3 (C_o), 128.1 (C_d), 127.9 (C_m), 126.5 (C_n), 119.0 (C_h), 118.0 (C_b), 79.1(C_k); ^{19}F NMR (376 MHz/$CDCl_3$) ppm: –64.1 and –74.5; GPC (THF): M_n = 11,500, M_w = 19,400, $Đ$ = 1.68; DSC: T_g (midpoint) = 114 °C.

4.4.3.3 Synthesis of PFO 8b

PFO 8b was synthesised using the same procedure as in section 4.4.3.1 employing PSE **7b** to yield PFO **8b** as a cream powder (1.26 g, 64%). IR (ATR) ν/cm^{-1}: 3495 (O–H alcohol), 1604 (aromatic C=C), 1504 (aromatic C=C), 1245 (C–O ether), 1152 (C–F), 1062 (C–O alcohol), 830 (aromatic C–H); ^{1}H NMR (400 MHz/$CDCl_3$) δ ppm: 7.70 and 7.69 (1H, s, H_n), 7.46–7.36 (6H, m, H_{i+m}), 7.34–7.27 (5H, m, H_{c+o}), 6.94 (4H, appt. d, appt. J = 8.3 Hz, H_h), 6.91 (4H, appt. d, appt. J = 8.5 Hz, H_b), 3.09 (2H, br, H_p); ^{13}C NMR (100 MHz/$CDCl_3$) δ ppm: 157.3 (C_a), 156.5 (C_g), 139.3 (C_l), 134.5 (C_j), 131.8 (C_c), 129.2 (C_i), 128.3 (C_o), 128.1 (C_d), 127.9 (C_m), 126.5 (C_n), 119.0 (C_h), 118.0 (C_b), 79.1(C_k); ^{19}F NMR (376 MHz/$CDCl_3$) ppm: –64.1 and –74.5; GPC (THF): M_n = 19,100, M_w = 28,600, $Đ$ = 1.54; DSC: T_g(midpoint) = 123 °C.

4.4.3.4 Synthesis of PFO 8c

PFO 8c was synthesised using the same procedure as in section 4.4.3.1 employing PSE **7c** to yield PFO **8c** as a cream solid (1.42 g, 72%). IR (ATR) ν/cm^{-1}: 3495 (O–H alcohol), 1604 (aromatic C=C), 1504 (aromatic C=C), 1245 (C–O ether), 1152 (C–F), 1062 (C–O alcohol), 830 (aromatic C–H); ^{1}H NMR (400 MHz/$CDCl_3$) δ ppm: 7.70 and 7.69 (1H, s, H_n), 7.46–7.36 (6H, m, H_{i+m}), 7.34–7.27 (5H, m, H_{c+o}), 6.94 (4H, appt. d, appt. J = 8.3 Hz, H_h), 6.91 (4H, appt. d, appt. J = 8.5 Hz, H_b), 3.09 (2H, br, H_p); ^{13}C NMR (100 MHz/$CDCl_3$) δ ppm: 157.3 (C_a), 156.5 (C_g), 139.3 (C_l), 134.5 (C_j), 131.8 (C_c), 129.2 (C_i), 128.3 (C_o), 128.1 (C_d), 127.9 (C_m), 126.5 (C_n), 119.0 (C_h), 118.0 (C_b), 79.1(C_k); ^{19}F NMR (376 MHz/$CDCl_3$) ppm: –64.1 and –74.5; GPC (THF): M_n = 25,200, M_w = 46,400, $Đ$ = 1.84; DSC: T_g (midpoint) = 126 °C.

4.4.3.5 Synthesis of PFO 8d

PFO 8d was synthesised using the same procedure as in section 4.4.3.1 employing PSE **7d** to yield PFO **8d** as a cream solid (1.46 g, 74%). IR (ATR) ν/cm^{-1}: 3495 (O–H alcohol), 1604 (aromatic C=C), 1504 (aromatic C=C), 1245 (C–O ether), 1152 (C–F), 1062 (C–O alcohol), 830 (aromatic C–H); ^{1}H NMR (400 MHz/$CDCl_3$) δ ppm: 7.70 and 7.69 (1H, s, H_n), 7.46–7.36 (6H, m, H_{i+m}), 7.34–7.27 (5H, m, H_{c+o}), 6.94 (4H, appt. d, appt. J = 8.3 Hz, H_h), 6.91 (4H, appt. d, appt. J = 8.5 Hz, H_b), 3.09 (2H, br, H_p); ^{13}C NMR (100 MHz/$CDCl_3$) δ ppm: 157.3 (C_a), 156.5 (C_g), 139.3 (C_l), 134.5 (C_j), 131.8 (C_c), 129.2 (C_i), 128.3 (C_o), 128.1 (C_d), 127.9 (C_m), 126.5 (C_n), 119.0 (C_h), 118.0 (C_b), 79.1(C_k); ^{19}F NMR (376 MHz/$CDCl_3$) ppm: –64.1 and –74.5; GPC (THF): M_n = 44,900, M_w = 101,600, $Đ$ = 2.27; DSC: T_g(midpoint) = 134 °C.

4.5 References

1 A. S. Johns and C. D. Bain, *ACS Appl. Mater. Interfaces*, 2017, **9**, 22918–22926.

2 J. S. R. Wheeler and S. G. Yeates, *Polymers in Inkjet Printing* In: *Fundamentals in Inkjet Printing*, 2015, Wiley, Weinheim, Germany, pp 117–140.

3 D. Xu, V. Sanchez-Romaguera, S. Barbosa, W. Travis, J. De Wit, P. Swan and S. G. Yeates, *J. Mater. Chem.*, 2007, **17**, 4902–4907.

4 Y. Christanti and L. M. Walker, *J. Rheol.*, 2002, **46**, 733–748.

5 O. A. Basaran, H. Gao and P. P. Bhat, *Annu. Rev. Fluid Mech.*, 2013, **45**, 85–113.

6 H. J. Spinelli, *Adv. Mater.*, 1998, **10**, 1215–1218.

7 Z. Zołek-Tryznowska and J. Izdebska, *Dye. Pigment.*, 2013, **96**, 602–608.

8 R. P. Mun, J. A. Byars and D. V. Boger, *J. Non-Newtonian. Fluid Mech.*, 1998, **74**, 285–297.

9 A. Hirao, K. Sugiyama and H. Yokoyama, *Prog. Polym. Sci.*, 2007, **32**, 1393–1438.

10 S. Banerjee, B. V. Tawade, V. Ladmiral, L. X. Dupuy, M. P. MacDonald and B. Améduri, *Polym. Chem.*, 2017, **8**, 1978–1988.

11 Y. Patil and B. Ameduri, *Prog. Polym. Sci.*, 2013, **38**, 703–739.

12 M. Damaceanu, C. Constantin, A. Nicolescu, M. Bruma, N. Belomoina and R. S. Begunov, *Eur. Polym. J.*, 2014, **50**, 200–213.

13 M. Tamura, R. Chaiwattananone and A. Sekiya, *Polym. J.*, 1992, **24**, 1307–1309.

14 B. Liu, G. Wang, W. E. I. Hu, Y. Jin, C. Chen, Z. Jiang, W. Zhang, Z. Wu and Y. E. N. Wei, *J. Polym. Sci., Part A: Polym. Sci*., 2002, 3392–3398.

15 I. Ruppert, K. Schlich and W. Volbach, *Tetrahedron*, 1984, **25**, 2195–2198.

16 G. K. S. Prakash and A. K. Yudin, *Chem. Rev.*, 1997, **97**, 757–786.

17 G. K. S. Prakash, R. Krishnamurti and G. A. Olah, *J. Am. Chem. Soc.*, 1989, **111**, 393–395.

18 R. P. Singh, G. Cao, R. L. Kirchmeier and J. M. Shreeve, *J. Org. Chem.*, 1999, **64**, 2873–2876.

19 R. P. Singh, R. L. Kirchmeier and J. M. Shreeve, *J. Org. Chem.*, 1999, **64**, 2579–2581.

20 R. Krishnamurti, D. R. Bellew and G. K. S. Prakash, *J. Org. Chem.*, 1991, **56**, 984–989.

21 F. Leroux, R. A. Bennett, D. F. Lewis and H. M. Colquhoun, *Macromolecules*, 2018, **51**, 3415–3422.

22 L. Gargallo and M. Russo, *Die Makromol. Chemie*, 1975, **176**, 2735–2744.

23 T. Young, III. An essay to the cohesion of fluids (published 1805), *Phil. Trans. R. Soc.*, **95**, 1997.

24 F. M. Fowkes, *Ind. Eng. Chem.*, 1964, **56**, 40–52.

25 F. M. Fowkes, *J. Colloid Interface Sci.*, 1968, **28**, 493–505.

26 D. K. Owens and R. C. Wendt, *J. Appl. Polym. Sci.*, 1969, **13**, 1741–1747.

27 W. Rabel, *Farbe und Lack*, 1971, **77**, 997–1005.

28 D. H. Kaelble, *J. Adhes.*, 1970, **2**, 66–81.

29 D. M. Mattox, in *Handbook of Physical Vapor Deposition (PVD) Processing*, 1998, pp. 56–126.

30 J. Balart, V. Fombuena, J. M. España, L. Sánchez-Nácher and R. Balart, *Mater. Des.*, 2012, **33**, 1–10.

31 FUJIFILM Inc., *Dimatix™ Materials Printer DMP-2800 Series User Manual*, 2010, 4th edn. pp. 1-150.

32 B. J. de Gans, E. Kazancioglu, W. Meyer and U. S. Schubert, *Macromol. Rapid Commun.*, 2004, **25**, 292–296.

33 B. J. de Gans, P. C. Duineveld and U. S. Schubert, *Adv. Mater.*, 2004, **16**, 203–213.

34 S. J. Haward, G. H. Mckinley and A. Q. Shen, *Nat. Sci. Reports*, 2016, **6**, 1–18.

35 I. Delaby, R. Muller and B. Ernst, *Rheol. Acta*, 1995, **34**, 525–533.

36 G. Odian, *Principles of Polymerisation*, John Wiley and Sons Ltd., Hoboken, New Jersey, 4th edn., 2004.

37 T. G. Fox and P. J. Flory, *J. Appl. Phys.*, 1950, **21**, 581–591.

38 T. G. Fox and P. J. Flory, *J. Polym. Sci.*, 1954, **14**, 315–319.

Chapter 5

Conclusions and Future Perspectives

5.1 Conclusions

The synthesis, characterisation and inkjet deposition of three different classes of functional polymeric materials for inkjet printing has been achieved. The materials produced were investigated for the application of i) self-assembling inkjet formulations, ii) UV-curable polymer formulations and iii) soluble, hydrophobic polymers for printable, hydrophobic polymer coatings.

A novel anthracene-capped PEG polymer was synthesised for use as a soluble, π-electron rich polymer component for the formation of π-π stacking supramolecular polymer networks with a π-electron deficient NDI polymer. PEG backbones were employed as they exhibit good solubility and are non-toxic, both of which are important properties for ink components intended for packaging materials. The self-assembly of the two π-motifs was investigated using computational modelling, which predicted partial overlap of the anthracene aromatic rings with the NDI moieties. Further model compound studies using ^{1}H NMR spectroscopy demonstrated a 1:1 binding interaction and a very weak association constant ($K_a = 4\ M^{-1}$). Solution complexation studies between the anthracene-capped polymer and the NDI polymer also showed only minor complexation shifts in ^{1}H NMR spectroscopic analysis and the absence of a charge transfer absorption in UV-vis analysis. The weak π-stacking interaction observed between anthracene-capped PEG and the NDI polymer was attributed to the weak binding between these π-motifs and the entropic tendency of polymer chains to favour the unbound (free) state. In this case, the entropy of the polymer chains prevailed over the weak π-interaction between the two aromatic systems. Both of the polymers were deposited successfully using a Dimatix™ DOD printer, but overprinting of the materials, unsurprisingly, did not afford sufficient π-stacking interaction to produce a charge-transfer and a coloured image absorption, as observed in related studies reported previously.[1-3]

Anthracene terminated polymers were also employed as UV-curable polymer systems. Both linear and branched anthracene-capped PEGs were produced and exhibited good solubility in a variety of organic solvents allowing facile formulation and deposition using a Dimatix™ DOD printer. The linear system was employed as a model compound for solution state analysis of the UV-irradiation process, which revealed the formation of anthracene dimers upon exposure to UV light above 350 nm. The branched system formed a cross-linked network upon UV irradiation, transitioning from a viscous, soluble material to an elastic, insoluble material, thus indicating potential for its use as a UV-curable polymer coating. The inclusion of dye compounds into the branched anthracene-PEG formulation produced only a minor decrease in cure rate as a result of competitive UV absorption, further highlighting the suitability of the material as a UV-curable component for UV inkjet formulations.

Finally, a series of poly(fluorocarbinol)s (PFO)s has been investigated as a class of soluble, hydrophobic materials with potential as polymer binders or coatings for inkjet printing. Stoichiometric control of the step-growth polymerisation involved in the synthesis of PEKKs enabled very good molecular weight control to produce a range of molecular weights of PEKKs (M_n = 10,000–114,000 g mol^{-1}). This series of PEKKs was converted to the poly(trifluoromethyltrimethylsilyl ether) (PSE) derivatives using Ruppert's reagent and TBAF. The PSEs were then desilylated using excess TBAF to produce the corresponding PFOs (M_n = 11,500–114,500 g mol^{-1}). All of the PFO materials demonstrated consistent hydrophobic film properties that were independent of molecular weight, with films of all FPOs produced exhibiting water contact angles of 88-89°. Despite the hydrophobic properties observed, the PFOs were found to be soluble in a variety of high-polarity organic solvents, including ethanol and MEK to allow facile formulation for inkjet printing. The printability of all the PFOs was tested using a Dimatix™ DOD printer and it was concluded that the lower molecular weight materials (M_n = 11,500–25,200 g mol^{-1}) demonstrated the most suitability for inkjet deposition and further investigation using an Ax-series CIJ printer. Two of the lower molecular weight materials (11,500 and 25,200 g mol^{-1}) were deposited successfully onto a variety of substrates and showed good adhesion to glass, PET, nylon and steel. The materials were also screened to determine their suitability as CIJ inks and it was found that the materials showed Newtonian or near-Newtonian behaviour, good droplet formation and minimal risk of build-up in the printer. The above qualities highlight the suitability for the inclusion of the lower molecular weight PFOs in inkjet formulations as either polymer binders or to produce clear hydrophobic coatings.

5.2 Future Perspectives

Despite the weak binding interaction between anthracene and naphthalene diimide units observed in Chapter 2, the use of π-stacking supramolecular polymers for inkjet printing is a promising concept. As described in Chapter 2 previous studies using alternative π-electron rich groups, pyrene and perylene, showed stronger association constants and the evolution of coloured charge transfer complexes.[1,2] Expansion of the existing colour palette would be of benefit in inkjet printing, as the employment of complementary polymer systems that can produce coloured charge-transfer complexes could eliminate the need for pigments and dyes in inkjet formulations.

The investigation into the complexation of alternative π-electron rich groups with NDI tweezers could result in the formation of complexes that produce novel charge transfer colours. Compounds with different number and sizes of aromatic rings and those that contain alkene functionalities or heteroatoms (Figure 1) would be of interest as they are likely to exhibit different electronic properties that may result in the evolution of a coloured charge-transfer complex.

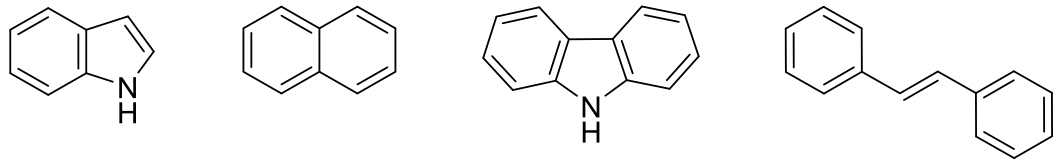

a **b** **c** **d**

Figure 1- Alternative π-electron rich aromatics for the production of π-electron rich polymers including: a) indole, b) naphthalene, c) carbazole and d) stilbene.

The electron rich systems suggested can also be substituted with electron donating and/or withdrawing functionalities to alter the electronics of the system. The charge-transfer absorption of donor-acceptor systems can be tuned by altering the type[4] and location[5] of substituent(s) on the aromatic ring(s). For example, the charge-transfer absorption between NDI compounds with di-substituted naphthalene is directly affected by the position of substituent groups on the aromatic ring of naphthalene.[5] This approach can also be expanded to include existing π-electron donors such as pyrene and perylene to determine the effect of substituents on the colour of the charge-transfer complex produced.

The tuning of the charge-transfer absorption could also be achieved by the production of polymers with alternative π-electron deficient groups (Figure 2).[6] Again, variation of the size of the π-electron deficient system as well as the electron withdrawing groups may produce differently coloured charge-transfer complexes. In particular, the investigation of the π-electron deficient systems with examples of π-electron rich systems in Figure 1 as well as any substituted derivatives would provide a library of charge-transfer complexes, with the potential to produce a variety of differently coloured π-π stacking complexes.

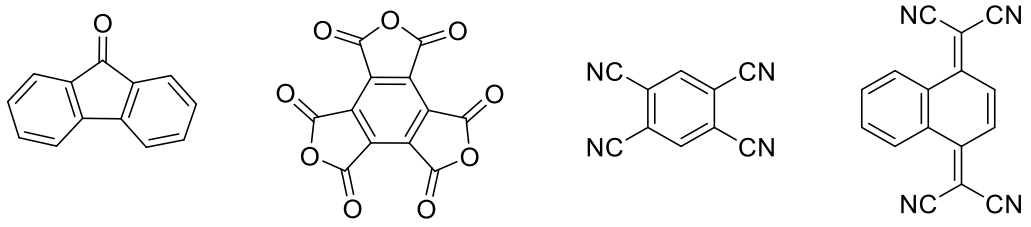

a **b** **c** **d**

Figure 2- Alternative π-electron deficient aromatics for the production of π-electron deficient polymer systems. including: a) fluorenones, b) mellitic trianhydrides, c) tetracyanobenzenes and d) naphthaquinodimethanes.

The application of supramolecular polymers to inkjet printing should not be limited to solely π-stacking interactions, but could also include the investigation of supramolecular polymer networks driven by hydrogen bonding, which tend to exhibit binding energies ranging between 4-120 kJ mol^{-1}.[7] Polymers containing hydrogen bond donors or hydrogen bond acceptors could be sequentially overprinted to produce a hydrogen bonded network on the substrate. Poly(ethylene gycol)s have

already been employed in this work as soluble, printable materials. The ether linkages within the polymer backbone act as hydrogen bond acceptors and therefore the sequential overprinting of PEG with a hydrogen bond donor, such as poly(methyl methacrylate-*co*-methacrylic acid)[8,9] would produce a hydrogen bonded network on the substrate. The ether linkages in the PEG backbone would act as hydrogen bond acceptors, whilst the carboxylic acid functionalities of the methacrylic acid groups in poly(methyl methacrylate-*co*-methacrylic acid) would act as hydrogen bond donors (Figure 3).

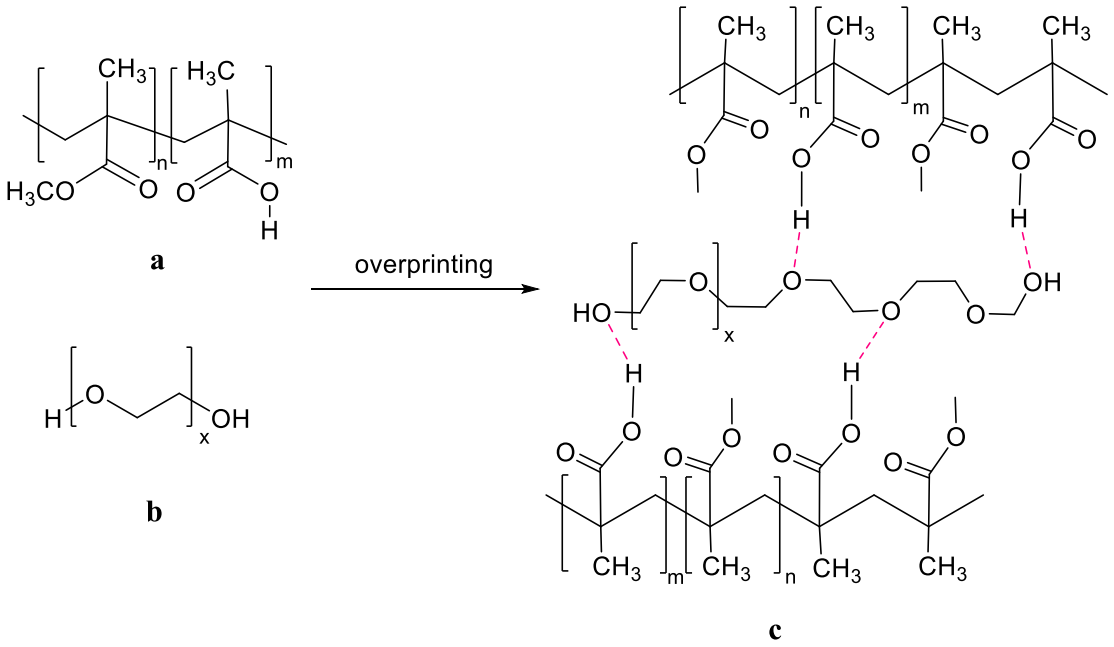

Figure 3- a) poly(methyl methacrylate-*co*-methacrylic acid) as a hydrogen bond donor, b) PEG as a hydrogen bond acceptor and c) the potential formation of supramolecular hydrogen-bonded networks following overprinting using inkjet printing.

The number of hydrogen bond donor (methacrylic acid) units in the poly(methyl methacrylate-*co*-methacrylic acid) could be altered by employing different molar equivalents of co-monomers in the polymerisation reaction. The physical properties of the hydrogen-bonding networks produced such as toughness and rigidity could then be investigated to determine the optimum co-monomer ratio for the formation of tough, but not brittle, supramolecular polymer networks. The synthesis of branched polymeric structures would also increase the extent of the supramolecular hydrogen-bonded network, which would increase the toughness and strength of the materials produced when compared to the linear derivatives.

The anthracene-capped materials described in Chapter 3 demonstrated suitability for the application of UV-curable inkjet polymers. However, employing a polymer backbone with a larger extent of branching would provide more hydroxyl (or similar) terminated ‘arms’ which could be functionalised with anthracene units. The inclusion of more anthracene units into the polymer backbone by

employing a star type, comb-type or dendritic polymer could provide a more densly cross-linked network within the same time frame as the tris-anthracene system seen in Chapter 3 (Figure 4). The number of arms in star or dendritic type polymers could be increased gradually to produce UV-cured materials with increasing extent of cross-linking to provide increased toughness and insolubility of the cured materials. The application of polymers with different numbers of anthracene-capped arms and varying lengths of polymer repeat units would provide a library of materials with different physical properties post-cure which would be beneficial for deposition onto different packaging substrates that would require different degrees of toughness and elasticity.

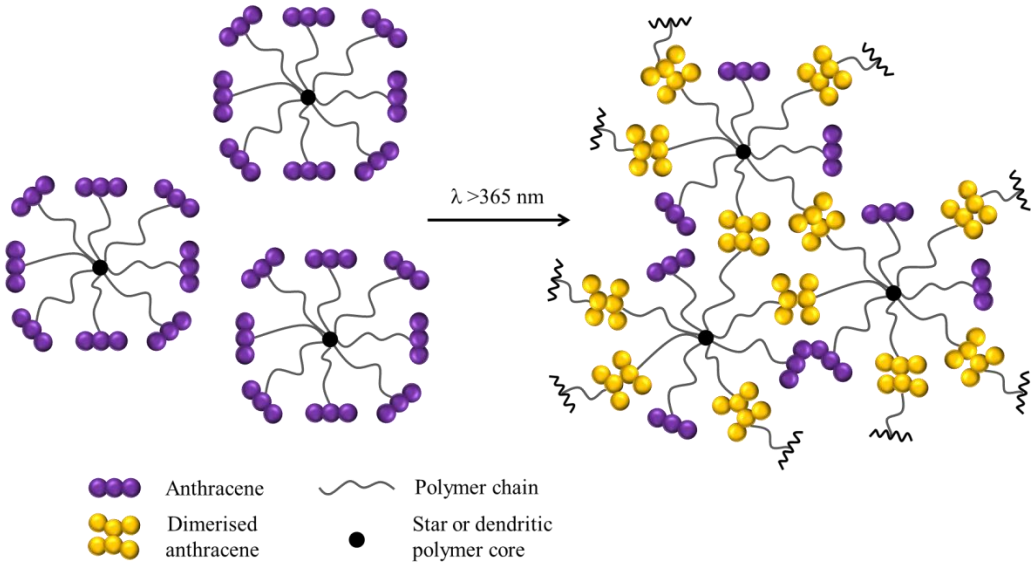

Figure 4- Schematic representation of a highly branched anthracene-containing polymer for the production of highly cross-linked networks upon UV irradiation.

As described in Chapter 4, the PFO films produced demonstrated interesting hydrophobic surface properties despite being readily soluble in polar solvents. The PSE derivatives described in Chapter 4 (Figure 5) were also soluble in polar solvents such as MEK, despite yielding more hydrophobic films (103–106°) than both the PFO (88–89°) and PEKK derivatives.

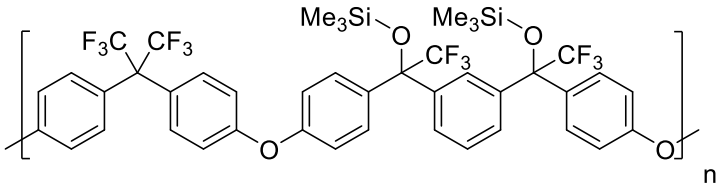

Figure 5- The structure of the poly(trifluoromethyltrimethyl silane) produced in Chapter 4, which may exhibit improved adhesion to glass compared to the poly(fluorocarbinol) derivatives.

Rheological testing of the silyl ethers could be undertaken to predict the rheological behaviour of these materials in the printhead. Furthermore the PSE materials could be tested for their potential

application in inkjet formulations using both DOD and CIJ printheads. The adhesion of the PSEs could also be investigated as they may produce polymer films that exhibit enhanced adhesion to glass compared to the PFO derivatives. This is because the presence of silyl ether functionalities in polymeric materials is known to result in polymer films which exhibit stronger adhesion to glass, through reaction with surface hydroxyl groups on the glass substrate. The PSE materials could therefore provide a stronger, more hydrophobic material than the PFOs.

5.3 References

1 L. R. Hart, J. L. Harries, B. W. Greenland, H. M. Colquhoun and W. Hayes, *ACS Appl. Mater. Interfaces*, 2015, **7**, 8906–8914.

2 L. R. Hart, N. A. Nguyen, J. L. Harries, M. E. Mackay, H. M. Colquhoun and W. Hayes, *Polymer*, 2015, **69**, 293–300.

3 L. R. Hart, J. L. Harries, B. W. Greenland, H. M. Colquhoun and W. Hayes, *Polym. Chem.*, 2015, **6**, 7342–7352.

4 F. Biedermann and O. a Scherman, *J. Phys. Chem.*, 2005, **116**, 1–32.

5 P. Mukhopadhyay, Y. Iwashita, M. Shirakawa, S. I. Kawano, N. Fujita and S. Shinkai, *Angew. Chem. Int. Ed.*, 2006, **45**, 1592–1595.

6 R. Foster, *Organic Charge-Transfer Complexes*, Academic Press, London, UK, 1969.

7 J. Steed and J. L. Atwood, *Supramolecular Chemistry*, John Wiley and Sons Ltd., Chichester, 2nd edn., 2009.

8 Y. Cao, Y. Guan, J. Du, J. Luo, Y. Peng, C. W. Yip and A. S. C. Chan, *J. Mater. Chem.*, 2002, **12**, 2957–2960.

9 Y. Yokoyama and S. I. Yusa, *Polym. J.*, 2013, **45**, 985–992.